
Doctoral Dissertations

Student Theses and Dissertations

Spring 2021

Investigation of packed bed and moving bed reactors with benchmarking using advanced measurement and computational techniques

Binbin Qi

Follow this and additional works at: https://scholarsmine.mst.edu/doctoral_dissertations

 Part of the [Chemical Engineering Commons](#)

Department: Chemical and Biochemical Engineering

Recommended Citation

Qi, Binbin, "Investigation of packed bed and moving bed reactors with benchmarking using advanced measurement and computational techniques" (2021). *Doctoral Dissertations*. 2980.
https://scholarsmine.mst.edu/doctoral_dissertations/2980

This thesis is brought to you by Scholars' Mine, a service of the Missouri S&T Library and Learning Resources. This work is protected by U. S. Copyright Law. Unauthorized use including reproduction for redistribution requires the permission of the copyright holder. For more information, please contact scholarsmine@mst.edu.

INVESTIGATION OF PACKED BED AND MOVING BED REACTORS WITH
BENCHMARKING USING ADVANCED MEASUREMENT AND
COMPUTATIONAL TECHNIQUES

by

BINBIN QI

A DISSERTATION

Presented to the Graduate Faculty of the
MISSOURI UNIVERSITY OF SCIENCE AND TECHNOLOGY

In Partial Fulfillment of the Requirements for the Degree

DOCTOR OF PHILOSOPHY

in

CHEMICAL ENGINEERING

2021

Approved by:

Muthanna H. Al-Dahhan, Advisor
Daniel Forciniti
Fateme Rezaei
Joseph Smith
Serhat Hosder

© 2021

Binbin Qi

All Rights Reserved

PUBLICATION DISSERTATION OPTION

This dissertation consists of the following five articles, formatted in the style used by the Missouri University of Science and Technology:

Paper I, found on pages 12–55, has been published in *Chemical Engineering Research and Design*, in December 2020.

Paper II, found on pages 56–91, has been published in *The Canadian Journal of Chemical Engineering*, in July 2020.

Paper III, found on pages 92–123, has been submitted to *Chemical Engineering Journal*.

Paper IV, found on pages 124–162, is intended for submission to *Chemical Engineering Science*.

Paper V, found on pages 163–201, has been submitted to *Chemical Engineering Research and Design*.

ABSTRACT

Trickle bed reactors (TBR), as typical packed bed reactors (PBR), are widely used in various fields. Very limited information regarding the flow behaviors, hydrodynamic, and mathematical models in extrudate catalyst shapes, such as cylinders, trilobes, and quadrilobes, can be found in literatures because the major focus was on spherical shape. Therefore, a hybrid pressure drops and liquid holdup phenomenological model for extrudate catalyst shapes was developed based on two-phase volume averaged equations, which showed high accuracy against experimental data. The maldistribution and dynamic liquid holdup were investigated in quadrilobe catalyst using gamma-ray computed tomography. A pseudo-3D empirical model was developed and compared with deep neural network predictions. Both models were in good agreement with experimental data. The accretion locations of heavy metal contaminants entrained with flow were tracked by the dynamic radioactive particle tracking technique in the packed beds of sphere, cylinder, trilobe, and quadrilobe, respectively. Kernel density estimator was used to indicate the accretion probability distribution, showing that pressure drop played an important role in heavy metal accretions. CFD simulations of random packed trilobe catalyst bed were conducted to obtain the local information and were validated by experimental data.

Moving bed reactors (MBR), as a relatively new type of reactor, encounter many challenges due to the bed expansion because of the concurrent gas-liquid upflow. DEM simulation was used to generate expanded bed. A porosity distribution correlation was developed and implemented in CFD simulations to investigate the hydrodynamics.

ACKNOWLEDGMENTS

First and foremost, I would like to express my deepest gratitude to my advisor and mentor, Dr. Muthanna H. Al-Dahhan, for his constant support and guidance during my Ph.D. His active and optimistic personality has inspired me greatly. His encouragement and freedom of thought enabled me to think creatively and be self-driven.

I would like to thank my advising committee, Dr. Daniel Forciniti, Dr. Fateme Rezaei, Dr. Joseph Smith, and Dr. Serhat Hosder for their critical comments and interest in evaluating my Ph.D. research.

I would like to thank my research group members and friends, particularly Omar Farid, whose cooperation and useful discussion contributed the success of my work. I would also like to thank the amazing technicians in our department, Dean and Michael, who offered great help on my experimental setup design and manufacture. I extend my thanks to the department office staff for their supports whenever I needed.

I would like to thank all the people that I met in my life. All of them have either tangible or intangible impacts on my life decisions.

Finally, I would like to thank my parents, who are always supporting my decisions and dream without reserve and hesitation. I would also like to thank my sister, brother in law, my niece Yi Dou, and my newborn niece Xinfei Dou, for their unconditional encouragement.

TABLE OF CONTENTS

	Page
PUBLICATION DISSERTATION OPTION	iii
ABSTRACT.....	iv
ACKNOWLEDGMENTS	v
LIST OF ILLUSTRATIONS.....	xii
LIST OF TABLES	xvi
NOMENCLATURE	xviii
 SECTION	
1. INTRODUCTION.....	1
1.1. TRICKLE BED REACTORS.....	1
1.1.1. Investigations on Liquid Distribution and Holdup.....	1
1.1.2. Mathematical Models to Predict Hydrodynamics.....	3
1.1.3. Computational Fluid Dynamics (CFD) Simulations.....	7
1.1.4. Heavy Metal Contaminants.....	5
1.1.5. Motivations and Objectives.....	8
1.2. MOVING BED REACTORS	10
1.2.1. Bed Expansion.....	10
1.2.2. Motivations and Objectives.....	11

PAPER

I. MALDISTRIBUTION AND DYNAMIC LIQUID HOLDUP QUANTIFICATION OF QUADRILOBE CATALYST IN A TRICKLE BED REACTOR USING GAMMA-RAY COMPUTED TOMOGRAPHY: PSEUDO-3D MODELLING AND EMPIRICAL MODELLING USING DEEP NEURAL NETWORK	12
ABSTRACT	12
1. INTRODUCTION	13
2. EXPERIMENTAL WORK	16
2.1. TRICKLE BED REACTOR SYSTEM	16
2.2. GAMMA-RAY COMPUTED TOMOGRAPHY	19
2.3. DEMONSTRATION OF CT	27
3. RESULTS AND DISCUSSION	29
3.1. LIQUID MALDISTRIBUTION FACTOR	30
3.2. DYNAMIC LIQUID HOLDUP	36
4. DYNAMIC LIQUID HOLDUP MODELS	37
4.1. MODELING USING DEEP NEURAL NETWORK (DNN)	39
4.2. PSEUDO-3D MODEL OF DYNAMIC LIQUID HOLDUP	42
4.3. EVALUATION OF MODELS	48
5. REMARKS	50
FUNDING	51
REFERENCES	51
II. DEVELOPMENT OF A HYBRID PRESSURE DROP AND LIQUID HOLDUP PHENOMENOLOGICAL MODEL FOR TRICKLE BED REACTORS BASED ON TWO-PHASE VOLUME AVERAGED EQUATIONS	56
ABSTRACT	56

1. INTRODUCTION.....	57
2. EXPERIMENTAL SETUP	61
3. DEVELOPMENT OF THE MODEL	63
3.1. VOLUME AVERAGED EQUATIONS	63
3.2. PHASE PERMEABILITY ESTIMATION	68
3.3. VISCOUS DRAG PARAMETER ESTIMATION	70
4. HYBRID MODEL FOR SIMULTANEOUS PRESSURE DROP AND LIQUID HOLDUP ESTIMATION	76
5. APPLICATIONS.....	80
5.1. COMPARISON WITH LITERATURE DATA	82
6. REMARKS.....	86
FUNDING.....	87
REFERENCES	88
III. ACCRETION OF HEAVY METAL CONTAMINANTS ENTRAINED WITH FLOW INTO A TRICKLE BED HYDROTREATING REACTOR PACKED WITH DIFFERENT CATALYST SHAPES USING NEWLY DEVELOPED NONINVASIVE DYNAMIC RADIOACTIVE PARTICLE TRACKING	92
ABSTRACT	92
1. INTRODUCTION.....	93
2. EXPERIMENTAL SETUPS	96
2.1. RADIOACTIVE PARTICLE REPRESENTING THE HEAVY METAL CONTAMINANTS	96
2.2. TRICKLE BED REACTOR SYSTEM	97
2.3. PARTICLE INJECTION SYSTEM	99
2.4. LOCATION IDENTIFICATION SYSTEM OF DYNAMIC RADIOACTIVE PARTICLE TRACKING TECHNIQUE	100

3. PROCEDURE AND VALIDATION.....	100
3.1. EXPERIMENTAL PROCEDURE.....	100
3.2. VALIDATION OF THE LOCATION IDENTIFICATION SYSTEM OF DYNAMIC RADIOACTIVE PARTICLE TRACKING TECHNIQUE	107
4. RESULTS AND DISCUSSION	113
5. REMARKS.....	121
FUNDING.....	121
REFERENCES.....	122
IV. EXPERIMENTAL AND MATHEMATICAL MODELLING INVESTIGATION OF HYDRODYNAMICS IN TRICKLE BED REACTORS OF RANDOM PACKED TRILOBE CATALYST BED	124
ABSTRACT	124
1. INTRODUCTION.....	125
2. RANDOM PACKING OF TRILOBES	128
3. MESH GENERATION	131
4. CFD SIMULATIONS	134
4.1. GOVERNING EQUATIONS.....	134
4.2. SURFACE TENSION MODEL	135
4.3. WALL ADHESION	136
4.4. SOLUTION PROCEDURE.....	137
5. EXPERIMENTAL WORK	138
5.1. EXPERIMENTAL SETUP.....	138
5.2. OPTICAL FIBER PROBE	139
6. RESULTS AND DISCUSSION	140

6.1. PRESSURE DROPS.....	140
6.2. LOCAL LIQUID SATURATION.....	143
6.3. LOCAL VELOCITY	145
7. REMARKS.....	157
FUNDING	158
REFERENCES.....	158
V. POROSITY DISTRIBUTION MODEL AND HYDRODYNAMICS IN MOVING BED REACTORS: CFD SIMULATION AND EXPERIMENTS.....	163
ABSTRACT	163
1. INTRODUCTION.....	164
2. POROSITY DISTRIBUTION MODEL	168
2.1. GOVERNING EQUATIONS.....	168
2.2. PACKING AND EXPANSION SIMULATION	170
2.3. DEVELOPMENT OF MODEL.....	172
2.4. POROSITY DISTRIBUTION FUNCTIONS ASSESSMENT	175
3. CFD SIMULATION COUPLED WITH POROSITY DISTRIBUTION CORRELATION	182
3.1. GOVERNING EQUATIONS.....	185
3.2. SURFACE TENSION MODEL	187
3.3. WALL ADHESION	187
4. EXPERIMENTAL WORK	190
5. RESULTS AND DISCUSSION	192
5.1. PRESSURE DROPS.....	192
5.2. VELOCITY FIELD	193

5.3. GAS SATURATION	194
5.4. GAS HOLDUP	196
6. REMARKS.....	197
FUNDING	198
REFERENCES	198
SECTION	
3. CONCLUSIONS AND RECOMMENDATIONS.....	202
3.1. CONCLUSIONS	202
3.1.1. Maldistribution and Liquid Holdup in Trilobe Catalyst.....	202
3.1.2. Hybrid Pressure Drop and Liquid Holdup Model.	203
3.1.3. CFD Simulations in Random Packed Trilobe Catalyst Bed.....	205
3.1.4. Heavy Metal Contaminants Accretion	204
3.1.5. Mathematical Modeling and CFD Simulation in Moving Bed Reactor.....	206
3.2. RECOMMENDATIONS.....	207
BIBLIOGRAPHY	208
VITA.....	215

LIST OF ILLUSTRATIONS

PAPER I	Page
Figure 1. Trickle bed reactor inside Gamma-ray CT	17
Figure 2. Single phase distribution and holdup profiles comparison between CT scan and real profile	28
Figure 3. Schematic of maldistribution quantification module ($N = 32$).....	30
Figure 4. Maldistribution factors at different bed heights and flowrates.....	32
Figure 5. (a) Dynamic liquid distribution from CT; (b) 3-D mapping of dynamic liquid distribution; (c) Dynamic liquid distribution bar chart with trendline at selected levels, $Q_{\beta} = 0.025 \text{ Kg} / \text{m}^2\text{s}$, $Q_{\gamma} = 4 \text{ Kg} / \text{m}^2\text{s}$	38
Figure 6. Dynamic liquid holdup profiles with regard to radius at different heights at flowrate, $Q_{\beta} = 0.025 \text{ Kg} / \text{m}^2\text{s}$, $Q_{\gamma} = 4 \text{ Kg} / \text{m}^2\text{s}$	39
Figure 7. (a) Schematic of DNN algorithm structure (b) Schematic of K-fold cross-validation	40
Figure 8. (a) Prediction vs. experiments plot for DNN model (b) Prediction vs. experiment plot for pseudo-3D model	47
Figure 9. Experimental data, DNN model predictions, and pseudo-3D model predictions $Q_{\beta} = 0.025 \text{ Kg} / \text{m}^2\text{s}$, $Q_{\gamma} = 4 \text{ Kg} / \text{m}^2\text{s}$	49
PAPER II	
Figure 1. Details of the experimental setup	62
Figure 2. Representative porous media within the bed.....	64
Figure 3. Experimentally determined pressure drop with labels showing the corresponding superficial liquid inlet velocity in mm/s, (a) Cylinders, (b) Trilobes, (c) Quadrilobes.....	71
Figure 4. Experimentally estimated and modelled viscous drag parameter (a) Cylinders, (b) Trilobes, (c) Quadrilobes	73
Figure 5. Average absolute relative error in the prediction of the viscous drag parameters by the proposed empirical model.....	76

Figure 6. Average absolute relative error in the prediction of experimentally measured liquid holdup and dimensionless pressure drop by extended-slit, slit and an empirical model.	78
Figure 7. Parity plot of the model predicted and experimentally measured dimensionless pressure drops for cylinders, trilobes and quadrilobes particles.....	81
Figure 8. Parity plot of the model predicted and experimentally measured liquid holdup for cylinders, trilobes and quadrilobes particles	82
Figure 9. Parity plot of the model predicted total liquid holdup and extracted experimental dynamic liquid holdup from literature for cylinders and trilobes.....	83
Figure 10. Parity plot of the model predicted and extracted dimensionless pressure drops from literature for cylinders and trilobes	85
 PAPER III	
Figure 1. MiniCNC machine and micro drill bits	98
Figure 2. Details of the experimental setup	99
Figure 3. Schematic of the Dynamic Radioactive Particle Tracking system.....	101
Figure 4. Flowchart of experimental procedure.....	101
Figure 5. Sample results of coarse seeking and fine seeking procedure.....	104
Figure 6. Comparisons between 1 mm and 2 mm step sizes for fine coordinates seeking.....	105
Figure 7. Magnetic fishing tool.....	107
Figure 8. Co-60 in a capsule	108
Figure 9. Top view picture of validation	109
Figure 10. Schematic of the Co-60 location for validation.....	109
Figure 11. Coarse coordinates of the Co-60 location for validation.....	110
Figure 12. Fine coordinate of the Co-60 particle with 2 mm step size before and after averaging	112
Figure 13. Particle distribution inside different catalyst beds.....	116

Figure 14. Kernel density estimation of heavy metal accretion locations	118
Figure 15. Pressure drop and liquid holdup in different catalyst beds for various liquid velocities at gas velocity 0.06 m/s	120

PAPER IV

Figure 1. Schematic of decomposition of friction cone and contact velocity	129
Figure 2. Random packing of trilobe particles	131
Figure 3. Showcase of generated mesh	133
Figure 4. Schematic of contact angle on the walls	137
Figure 5. Schematic of experimental setup and optical fiber probe configuration	141
Figure 6. Sample result of 2 tip optical probe signal	142
Figure 7. Comparison of pressure drops between CFD simulations and experiments at different combination of flowrates	142
Figure 8. Schematic of azimuthally averaged data points at different radius	144
Figure 9. Cut plan of liquid saturation at different velocities	145
Figure 10. Liquid saturations comparisons between CFD and experimental results in terms of radius at different combination of flowrates	146
Figure 11. Cut plan of velocity fields at different velocities	151
Figure 12. Velocity vectors of 5 cm zone at different velocities	151
Figure 13. Schematic of velocity field at radius $r/R = 0, 0.24, 0.48, 0.72, 0.96$	153
Figure 14. KDE of both positive and negative velocities for experimental and CFD results at $v_\beta = 0.2 \text{ m/s}$, $v_\gamma = 0.016 \text{ m/s}$	153

PAPER V

Figure 1. Catalyst packed bed inside the column with cone distributor	171
Figure 2. Discrete element method module	172
Figure 3. Schematic of porosity calculation module	174
Figure 4. Porosity distribution in terms of radius at different levels	176

Figure 5. Average porosity distribution	180
Figure 6. Parameter values for different expansions	181
Figure 7. Comparison of overall averaged porosity between CFD simulation and model	182
Figure 8. Comparison of the average porosity distribution under 10% expansion.....	183
Figure 9. Comparison of the local porosity obtained by the DEM simulations and the proposed model	184
Figure 10. Porosity distribution of the catalyst bed inside MBR.....	186
Figure 11. Schematic of contact angle on the walls.....	189
Figure 12. Schematic of experimental setup	191
Figure 13. Pressure drops at different locations along the reactor in CFD and experiments	193
Figure 14. Velocity field on a cut plane in CFD	195
Figure 15. Gas saturation on a cut plane in CFD	195
Figure 16. Gas saturation at different bed heights	196
Figure 17. Gas holdup at different bed heights	197

LIST OF TABLES

PAPER I	Page
Table 1. TBR dimensions, catalyst information and operation conditions.....	18
Table 2. The perturbation rank of inputs	43
Table 3. Models for prediction of liquid holdup and saturation in trickle bed reactors	43
PAPER II	
Table 1. Geometrical properties of the experimental setup and operation conditions.....	62
Table 2. Geometrical properties of the solid particles and bed.....	70
Table 3. Fitting parameters for the empirical model to estimate the viscous drag parameters	75
PAPER III	
Table 1. Geometrical properties of the solid particles and bed.....	102
Table 2. Kernel density functions	117
PAPER IV	
Table 1. Random packing simulation parameters.....	131
Table 2. Mesh generation specifications.....	133
Table 3. Simulation specifications.....	137
Table 4. Experimental operation conditions	139
Table 5. Absolute relative errors of local liquid saturations of CFD and experimental results.....	148
Table 6. Absolute relative errors of cross-sectional average liquid saturations of CFD and experimental results	149
Table 7. Velocities of CFD (average value) and experimental results (modal number)	156

PAPER V

Table 1. CFD-DEM simulation parameters	173
Table 2. Parameters estimation for different bed expansions	179
Table 3. Simulation specifications	188
Table 4. MBR information and operation conditions	191

NOMENCLATURE

Symbol	Description
A_i	Cross-sectional area of each compartment
A_σ	Projected area of the particle
a_{ij}, b_{ij}	Fitting parameters for viscous drag parameter
b_0	Bias
C_d	Drag force coefficient
C_{fs}	Static friction coefficient
d	Characteristic length scale of the porous media
d_e	Volumetric equivalent diameter
d_c	Diameter of the column
d_n	Overlap at contact point
d_p	Particle diameter
f_s	Shear slip factor
\mathbf{F}_b	Resultant of the body forces
\mathbf{F}_d	Drag force
\mathbf{F}_g	Gravity force
\mathbf{F}_p	Pressure gradient force
\mathbf{F}_s	Resultant of the forces on the particle surface

\mathbf{F}_{vm}	Virtual mass force
Ga_γ	Galileo number $\left(\mathbf{g}d_e^3\varepsilon_B^3\rho_\gamma^2/\mu^2(1-\varepsilon_B)^2\right)$
h	Unit height
H	Total bed height
K	Kernel density function
K	Bed permeability
\mathbf{K}_i	i -phase permeability tensor
\mathbf{K}_{ij}	Viscous drag tensor for phase i over phase j
K_n	Normal spring stiffness
l	Characteristic length scale of the bed
L_C	Column height
m_σ	Particle mass
M	Mass of each particle
M_{eq}	Equivalent mass
M_f	Maldistribution factor
N	Number of compartments
n	Number of phases
P	Pressure
$\langle P_i \rangle^i$	Intrinsic average pressure of phase i
Q	Phase mass flux

V	Liquid volumetric flowrate
$\langle \mathbf{v}_i \rangle$	Superficial average velocity vector of phase i
\mathcal{V}	Average volume
r	Observation radius
R	Radius
Re	Reynolds number, $\text{Re} = \frac{\rho u d_p}{\mu(1-\varepsilon)}$
R_{eq}	Equivalent radius
S	Arc length
w	Weight factor
We	Weber number, $We = \frac{\rho v^2 l}{\sigma}$
X_i	Value of i th observation
y	Output or results
Z	Observation level height
Greek letter	
β	Gas phase
δ_i	Unit vector in the i direction
δ_{ij}	Kronecker delta
ΔP	Pressure drop
ϕ	Phase saturation
φ	Sphericity

γ	Liquid phase
ε_i	Holdup (volume fraction) of phase i
μ_i	Dynamic viscosity of phase i
$\mu_{i,j}$	Attenuation of pixel at location (i, j)
$\mu_{i,j}$	Pure phase attenuation coefficient
ρ_i	Density of phase i
σ	Solid phase
θ	Kozeny parameter for permeability correlation
ψ	Any field variable
χ	Lockhart-Martinelli number, $\chi = \frac{m_\gamma}{m_\beta} \sqrt{\frac{\rho_\beta}{\rho_\gamma}}$
Subscript	
d	Dynamic
st	Static
st_int	Internal static
st_ext	External static

1. INTRODUCTION

1.1. TRICKLE BED REACTORS

Trickle bed reactors (TBR), as one of the typical packed bed reactors, are gas-liquid-solid interaction equipment utilized in various fields such as petroleum hydrotreating (hydrodesulfurization, hydrodenitrification, hydrodemetallization, hydrocracking, etc.), hydrogenation reactions, oxidation reactions, esterification, as well as Fischer-Tropsch reactions [1]. The most common type of trickle bed reactors is that the gas and liquid phases concurrently flow downward through the porous solid catalysts, in which the flow behaviors mainly depend on the catalyst particle type, size, shape, which directly affect the hydrodynamics, mass and heat transfers, and reactions [2]. Different types of catalysts are used in trickle bed reactors such as spheres, cylinders, trilobes, and quadrilobes [3]. Comparing to spherical particles, the extrudate particles show better pressure drops and liquid holdup as well as the phase distributions. In the last few decades, vast work has focused on the hydrodynamics studies in the beds packed with sphere and cylindrical catalysts [2,4–7]. Limited work contributed to the hydrodynamics and computational fluid dynamics (CFD) simulations of trilobe or quadrilobe particles [8–10].

1.1.1. Investigations on Liquid Distribution and Holdup. As the dispersed phase (liquid) distribution, also referred as the dynamic liquid flow, dominates the performance of trickle bed reactors because it indicates the flow patterns inside the packed bed and determines the utilization of catalysts. Liquid maldistribution, which can be categorized as gross maldistribution and local distribution [11], may cause unexpected contacting of gas and liquid over the solid catalysts which affects the heat and mass transfer rate, and hence

the temperature distribution and the reaction rate [12]. The most common way to quantify the liquid maldistribution is using a multi-compartment collector at the outlet of the bed to obtain the maldistribution factor based on the volumetric flowrates [9,13,14]. However, the collector method can only identify the liquid distribution near the outlet of the reactor. In fact, the liquid distribution in the upper region of the packed bed discloses more information indicating the fluid flow behaviors inside the reactor. A modified collector method was used to obtain the liquid distribution of extrudate trilobe catalyst at different axial locations by separating the reactor into several sections and putting the collectors in between these sections to get maldistribution factors along the bed height [9]. However, there is a high chance that these collectors will affect the catalyst bed continuity, therefore affecting the flow behaviors inside the reactor.

There are some other works using electrical resistance tomography (ERT) [15] or electrical capacitance tomography (ECT) [16] as non-invasive techniques to investigate the maldistribution at different axial locations, which had the same issue that the media of the reactor system should have enough conductivity for ERT or ECT detection and quantification. Otherwise it is difficult to obtain proper results. Another issue is that ERT or ECT have very low spatial resolution which makes it hard to get accurate local information. Another non-invasive technique is gamma-ray computed tomography (CT) which has been widely utilized on multiphase reactor systems [17–20]. Boyer et. al. [17] used CT to get the liquid saturation and distribution of glass beads bed in a TBR. Kuzeljevic [19] proposed a scaled maldistribution factor based on the liquid holdup of cylindrical porous catalyst bed in a TBR and compared with the results calculated from Marcandelli's equation [13]. It showed that the absolute values of maldistribution factors from

Marcandelli's equation are much larger than that based on liquid holdup. This was because in that work the liquid holdup referred to the total liquid holdup, which included the static liquid, both inside and outside the catalysts, instead of only the dynamic liquid holdup, leading to a misunderstanding that the liquid was more uniformly distributed. For porous catalytic packed bed reactors, the total liquid holdup refers to the overall volume of the liquid phase divided by the reactor volume. The total amount of liquid consists of two parts which are dynamic liquid and static liquid. The static liquid includes the liquid inside porous catalyst (internal static liquid) and the stagnant liquid attached on the catalyst surfaces and/or between the catalyst particles (external static liquid) after completely draining the reactor. The dynamic liquid, which dominates the flow behavior, means the freely flowing liquid under operating conditions.

1.1.2. Mathematical Models to Predict Hydrodynamics. It has been recognized that the hydrodynamics of TBR, which is also regarded as the multiphase interactions, play a determining role in the mass and heat transfer phenomena, kinetics and performance throughput of these systems. Hence, vast contributions in literature have devoted to the characterization and understanding of the TBR hydrodynamics, focusing on determining/measuring and predicting the key hydrodynamic parameters required for design and scaling of these systems, such as pressure drops and overall liquid holdup. With different approaches, and using different experimental techniques, the key macroscopic hydrodynamic parameters have been determined [14,17,21–23].

Two main kind of models have been developed to predict pressure drops and holdups in TBR, i.) empirical models and ii.) phenomenological models. The empirical models are expressions that fit experimental observations as a function of parameters

related to some of the fluids' physical properties, operation conditions, and bed characteristics, such as bed tortuosity and porosity, without a fundamental physical reason [23,24]. On the other hand, the phenomenological models seek to find a relationship between the system physical and geometrical characteristics and the observed pressure drops, but based on a physical principle, such as a force balance [25–28], or a mechanistic concept and its fundamental principle, such as the relative permeability concept [29]. However, these models are not fully mechanistic (theoretical) models and require the estimation of closure parameters according to experimental observations, which means that phenomenological models are semi-empirical and are also constrained by experimental observations.

Another important limitation in the use of the empirical and phenomenological models reported in the literature is that there is limited information of the particle shape effects over the predictive capability of the models. In fact, a vast number of experimental studies have been conducted for spherical particles, and thus the determined closure parameters for the models should be constrained to such geometry [30]. Al-Ani [30] made a comprehensive comparison between two phenomenological models, slit [25] and double-slit [27], and an empirical model reported by Larachi et al [23] against experimentally determined pressure drops and liquid holdup on a TBR packed with spheres, cylinders, trilobes and quadrilobes. The results showed that the double-slit model has the highest predictive quality among those models, suggesting that the current understanding and predictive quality of the available models is limited, and that a new model that has an enhanced predictability is yet required.

1.1.3. Computational Fluid Dynamics (CFD) Simulations. In the past few decades, vast research efforts have been devoted to study the hydrodynamics of these systems, such as characterizing the gas/liquid holdups and their distributions, pressure drops, and wetting efficiency, either through experiments or by mathematical modeling through computational fluid dynamics (CFD) techniques [43–45]. In general, most experimental work focuses on measuring the macroscopic hydrodynamic behaviors in these reactors, such as overall pressure drops, overall holdups, and residence time distribution. On these investigations, scarce information was obtained regarding the local scale hydrodynamic phenomena due to the limitations of the applied measurement techniques, such as systematic errors in the measurements under harsh operation conditions.

In order to overcome the limitations in the experimental studies of TBRs, mathematical modeling through CFD techniques has gained increasing interest in recent years. This CFD modeling approach to study TBRs allows to provide predictions of the local scale multiphase flow phenomena. However, due to the complexity of the multiphase flow in these systems, which results in a highly non-linear mathematical model, and the intricate porous media generated by the packing, the level of detail in the predictions is limited by both the assumptions to deal with the textural characteristics of the bed and the available computational resources [46,47]. In general, there are two main approaches to represent the geometrical characteristics of TBRs in CFD modeling, i) effective porous media approach and ii) discrete particle approach.

The effective media approach uses a porosity distribution function to macroscopically represent the porosity distribution inside the packed beds, typically with

oscillatory correlations [48–51] or exponential correlations [52,53]. As so far, the majority of the CFD modeling works rely on the effective media approach, as it can simulate pilot scale reactors with a low computational cost. However, by implementing this approach the level of detail in the local predictions is compromised. These models can only provide predictions of overall or average parameters, such as the liquid distribution and average phase holdups inside the packed beds without detailed local information such as local liquid velocities. This implies that certain undesired phenomena caused by the random packing of the beds, such as bypass channeling, backmixing and dead zones, cannot be predicted.

On the other hand, the discrete particle approach explicitly incorporated the intricate bed structure through the inclusion of the solid-fluid interfacial area in the computational domain. By incorporating such level of detail, fundamental understanding of the effects of bed geometry on transport phenomena of the two-phase flow and the multiphase interactions, as well as detailed local information of each phase, can be obtained. Despite the advantages of this approach, scarce contributions have been conducted using discrete particle approach in multiphase (gas-liquid-solid) CFD modeling, and mostly have only considered the ordered packing of spherical particles [54–58]. However, extrudate catalyst shapes are more commonly used in real industries because they provide better pressure drops, therefore better liquid holdups distributions, and the solids distribution is random. The lack of works implementing discrete particle approach for TBRs randomly packed with extrudates can be attributed to two main challenges, i) the generation of the random packing, and ii) the meshing of the intricate computational domain.

A promising technique to simulate the bed packing is the discrete element method (DEM). One of the common approaches to simulate complex shapes such as cylinders, trilobes, and quadrilobes, is to approximate their shapes by overlapping large number of spheres as representations, then using DEM to conduct random packing, which requires vast computational resources. Because these complex shapes are made of overlapping spheres, there are continuous curvatures on the surfaces of these particle which result in difficulties when meshing the geometries for the CFD model. In addition, during the DEM simulation, there are chances that these particles have overlaps creating acute angles, which also represent important challenges in the mesh generation.

1.1.4. Heavy Metal Contaminants. Contaminants are inevitably delivered into the TBR, especially in hydroprocessing applications, where heavy residual oils are converted into lighter fuel oils. These contaminants (e.g., nickel, vanadium, arsenic, sodium, iron, lead) are usually associated with the produced crude oil, the remaining heavy metals in the liquid feed, or residues from the additives (silicon, lead) used during refining operations, as well as corrosion (iron) [31]. These contaminants directly or indirectly result in catalyst deactivation due to a chemical, mechanical, or thermal effect, such as poisoning, fouling, thermal degradation, or attrition [32] which leads to hot spots, high pressure drops, and even the need for emergency shutdowns. Currently, vast literature work are related to the catalysts aging, deactivation and regeneration including mechanisms and kinetical investigation [31–34]. All the work is in micro perspective that relies on the prerequisite that the contaminants already exist in the catalyst bed. There is no doubt that the contaminants are entrained through the liquid feed flow into the trickle beds hence get stuck and accret. However, there is no such work that discloses how these contaminants are

carried by the liquid fluid, the distribution of the accretion locations, and especially the effects of the catalyst bed structure, such as the catalyst shape, on the contaminant's accretion.

Various particle tracking methodologies have been reported to aid in the identification of the contaminants' locations inside the packed beds. Single particle tracking (SPT) [35] is a methodology that uses computer-enhanced video microscopy to track the single particle motion in a system. However, it requires the system to be totally visible at least at the surface so that it can be captured by a camera. Laser doppler anemometry (LDA) and particle imaging velocimetry (PIV) [36] are another two typical techniques to track particles. However, both techniques are optical methods based on the light reflection from the seeded particles hence tracking large amount of the particles to measure the velocity field in fluid dynamics. Another non-invasive particle tracking technique that does not require the transparency or visibility, which is radioactive particle tracking (RPT) [37–42], become a well-reasoned option. There are two types of RPT which are Static RPT (SRPT) and Dynamic RPT (DRPT). The main difference between these two RPT systems is that, SRPT tracks the trajectory of a dynamic object that is represented by the radioactive particle which mimics the moving phase to be tracked (liquid, solid), hence the Lagrangian trajectory is determined. From the Lagrangian trajectory, the velocity fields can be obtained and hence the fluctuation and turbulent parameters. While DRPT determines the location of a static object which is represented by the radioactive particle by dynamically moving the detectors to determine the coordinates of this object.

1.1.5. Motivations and Objectives. The experimental investigation on the dynamic liquid distribution and holdup of porous quadrilobe catalyst in a TBR was

conducted using advanced gamma-ray CT to fill in the blank. The quantification and mapping of the maldistribution based on the dynamic liquid holdup were achieved. Deep neural network (DNN) was implemented to predict the dynamic liquid holdup inside quadrilobe catalyst bed, comparing with a newly developed pseudo-3D empirical model.

A new highly predictive phenomenological model was developed to estimate pressure drops and liquid holdup in extrudate shape catalysts, which is based on results of the volume averaging of a two-phase flow through porous media [59]. The closure parameters are estimated for cylinders, trilobes and quadrilobes, for a wide range of liquid and gas superficial inlet velocities. To provide closure for the developed model to enable the simultaneous prediction of pressure drop and liquid holdup, the developed model is coupled with a modification of the extended slit model.

The accretion locations of the heavy metal contaminants entrained through the liquid flow inside a TBR were investigated by a newly modified dynamic radioactive particle tracking (DRPT) system. Four catalyst shapes, sphere, cylinder, trilobe, and quadrilobe, were used to identify the effects of the bed structure difference on the heavy metal contaminants accretion locations. Kernel density estimation (KDE) was used to determine the probability distribution of the contaminant final position, in terms of bed radius and height in each type of catalyst.

In order to develop a modeling scheme to implement discrete particle approach for a TBR packed with extrudate catalysts, in this work, first an efficient packing scheme was implemented to randomly pack a vast number of extruded catalysts to represent the TBR, based on a rigid body approach. Then, the generated geometry was used to define the computational domain for the two-phase hydrodynamics simulation. A work scheme to

avoid overlapping of the solid particles, and to avoid issues in the mesh generation is presented. Finally, the obtained computational domain is used for implementing a two-phase hydrodynamics model based on the volume of fluids (VOF) approach. This hydrodynamics modelling study is paired with an experimental study using our in-house developed advanced measurement techniques based on optical fiber probes, which allowed to determine local liquid velocity and saturation profiles. The experimental measurements were used for local validation of the implemented model.

1.2. MOVING BED REACTORS

As a relatively new multiphase phase reactor, moving bed reactors (MBR) have been utilized in selected hydrotreating processes due to some inherent advantages such as processing higher metal feeds, outputting lower Sulphur products and enhancing the economic efficiency [60]. MBR enables continuous replacement of spent catalyst from the bottom of the reactor and adding fresh catalyst from the top of the reactor without shutdown. In MBR, the gas and liquid flow co-currently upward through a catalyst bed supported by a cone shape distributor, leading to a slight expansion of the catalyst bed (around 10% in volume) without fluidization [61–63].

1.2.1. Bed Expansion. In MBR, the catalysts are suspended by the two phase flow which is able to enhance the catalyst performance, mitigate coking, and improve the pressure drop along the reactor [64]. In practice, the suspended catalysts are not stationary but vibrating due to the fluid flow. This slight expansion and vibration of the catalyst creates a special scenario in between Packed Bed Reactors and Fluidized Bed Reactors. Vast contributions in literature have addressed on either the hydrodynamics or the reaction

kinetics in packed bed reactors (PBR) and fluidized bed reactors (FBR). However, researches on this special case are hardly found, except for some works that studied on the hydrodynamics within the operation conditions that maintain the catalysts as packed bed without expansion [65–67].

1.2.2. Motivations and Objectives. Porosity distribution correlations describing the catalyst bed characteristics on a MBR under different expansions, 5%, 10%, and 15%, respectively, as well as for a MBR without bed expansion, were developed. Such porosity distributions were developed based bed structures predicted by an implemented DEM model. The applicability of the developed model was tested by setting an Euler-Euler model using the developed 10% expansion porosity distribution model. The overall experimental flow pattern and pressure drops along the reactor were observed to compare with the simulation for validation. However, further experimental work is required to validate the other local hydrodynamics fields predictions.

PAPER

I. MALDISTRIBUTION AND DYNAMIC LIQUID HOLDUP QUANTIFICATION OF QUADRILOBE CATALYST IN A TRICKLE BED REACTOR USING GAMMA-RAY COMPUTED TOMOGRAPHY: PSEUDO-3D MODELLING AND EMPIRICAL MODELLING USING DEEP NEURAL NETWORK

Binbin Qi¹, Omar Farid¹, Muthanna Al-Dahhan^{1,2*}

¹ Chemical and Biochemical Engineering Department, Missouri University of Science and Technology, Rolla, MO 65409 USA

² Mining and Nuclear Engineering Department, Missouri University of Science and Technology, Rolla, MO 65409, USA

* Corresponding author: aldahhanm@mst.edu

ABSTRACT

The dynamic liquid distribution and holdup in a TBR packed with porous quadrilobe catalyst were studied using advanced gamma-ray computed tomography. A multi-compartment module is used to quantify the maldistribution factor which shows that there is a transition region from high maldistribution to relatively uniform distribution depending on the flowrates. The 3D maldistribution maps show that there is more dynamic liquid close to the column center at high bed height and there is no high correlation between the average dynamic liquid holdup and the bed height. If the gas flowrate increases while keeping the liquid flowrate fixed, the average dynamic liquid holdup decreases; however, if the gas flowrate is fixed, there is no dominant increasing or decreasing trend showing up. A deep neural network model and a pseudo-3D model are developed showing high

accuracy for predicting the local dynamic liquid holdup at different bed heights, radius, and flowrates.

Keywords: Trickle bed reactor, Gamma-ray CT, Maldistribution, Liquid holdup modeling, Deep Neural Network, Quadrilobe catalyst

1. INTRODUCTION

Trickle bed reactor (TBR) is one of the typical packed bed reactors where gas and liquid reactants flow over a solid catalytic bed. They have quite versatile applications in petrochemical, chemical and refinery fields such as oxidation reactions, petroleum processing, hydrogenation reactions, esterification, and F-T synthesis [1], among others. Most of the catalyst particles in trickle bed reactors are porous and have different shapes such as sphere, cylindrical, extrudate trilobes, and quadrilobes [2]. The distribution of the interstitial voids of packed bed are highly related to the particle size and shape [3], which will affect the hydrodynamics of a TBR. The extrudate particles show much better pressure drop and liquid holdup as well as the phase distributions. During the last few decades, vast works reported on literature have focused on the hydrodynamics studies beds packed with sphere and cylindrical catalysts [3–7]. Limited works have contributed on the hydrodynamics and computational fluid dynamics (CFD) simulations of extrudate trilobe or quadrilobe particles [8–10], except some CFD studies [2,11–13] predicting the void fraction, wetting efficiencies and pressure drop in very small scales without experimental validations due to the complex bed characteristics and limitation of measurement techniques. Therefore, better understanding of the flow behavior inside complex geometry

catalysts is imperative since trilobes and quadrilobes catalysts are the most commonly used ones in industries, particularly petroleum industries.

As the dispersed phase (liquid) distribution, also referred as the dynamic liquid flow, dominates the performance of trickle bed reactors because it indicates the flow patterns inside the packed bed and determines the utilization of catalysts. Liquid maldistribution may cause unexpected contacting of gas and liquid over the solid catalysts which affect the heat and mass transfer rate, and hence the temperature distribution and the reaction rate [14]. There are two types of liquid maldistribution: gross maldistribution and local maldistribution [15]. The gross maldistribution can be improved by modifying the inlet of liquid. However, the local maldistribution is related to the catalyst configuration, type, size, and shape. This makes it rather difficult to quantify the liquid maldistribution. The most common way to quantify the liquid maldistribution is using a multi-compartment collector at the outlet of the bed to obtain the maldistribution factor based on the volumetric flowrates [9,16,17]. However, the collector method has an obvious defect that it can only identify the liquid distribution near the outlet of the reactor. In fact, the liquid distribution in the upper region of the packed bed discloses more information indicating the fluid flow behaviors inside the reactor. The identification of where liquid fully spreads over the radius is rather significant for understanding the real industrial issues such as hot spot inside reactors [14]. Bazmi et al. (2013) modified the collector method to obtain the liquid distribution of extrudate trilobe catalyst at different axial locations by separating the reactor into several sections and putting the collectors in between these sections to get maldistribution factors along the bed height. However, there is a high chance that these collectors will affect the catalyst bed continuity, therefore affecting the flow behaviors

inside the reactor. Moreover, any resistance to the flow streams, such as collectors, will redistribute the gas and liquid flows.

There are some other works using electrical resistance tomography (ERT) [18] or electrical capacitance tomography (ECT) [19] as non-invasive techniques to investigate the maldistribution at different axial locations. They had the same issue that the media of the reactor system should have enough conductivity for ERT or ECT detection and quantification. Otherwise it is difficult to obtain proper results. Another issue is that ERT or ECT have very low spatial resolution which makes it hard to get accurate local information.

Another advanced non-invasive technique is gamma-ray computed tomography (CT) which has been widely utilized on multiphase reactor systems [20–23]. Boyer (2005) used CT to get the liquid saturation and distribution of glass beads bed in a TBR. Kuzeljevic (2010) proposed a scaled maldistribution factor based on the liquid holdup of cylindrical porous catalyst bed in a TBR and compared with the results calculated from Marcandelli's equation [16]. It showed that the absolute values of maldistribution factors from Marcandelli's equation are much larger than that based on liquid holdup. This was because in that work the liquid holdup referred to the total liquid holdup, which included the static liquid, both inside and outside the catalysts, instead of only the dynamic liquid holdup, leading to a misunderstanding that the liquid was more uniformly distributed. In packed bed systems, liquid holdup is one of the most important hydrodynamic parameters which significantly affects the mass, heat transfer and temperature distribution, as well as the wetting efficiency. Liquid holdup also affects the liquid residence time, and therefore the reaction conversion [15]. For porous catalytic packed bed reactors, the total liquid holdup

($\varepsilon_{\gamma,t}$) refers to the overall volume of the liquid phase divided by the reactor volume ($\varepsilon_{\gamma} = V_{\gamma}/V_{total}$). The total amount of liquid consists of two parts which are dynamic liquid ($\varepsilon_{\gamma,d}$) and static liquid ($\varepsilon_{\gamma,st}$). The static liquid includes the liquid inside porous catalyst (internal static liquid, $\varepsilon_{\gamma,st_int}$) and the stagnant liquid attached on the catalyst surfaces and/or between the catalyst particles (external static liquid, $\varepsilon_{\gamma,st_ext}$) after completely draining the reactor. The dynamic liquid, which dominates the flow behavior, means the freely flowing liquid under operating conditions.

In this study, the experimental investigation on the dynamic liquid distribution and holdup of porous quadrilobe catalyst in a TBR was conducted using advanced Gamma-ray CT to fill in the blank of this area. The quantification and mapping of the maldistribution based on the dynamic liquid holdup were achieved in this work. Moreover, deep neural network (DNN) is implemented to predict the dynamic liquid holdup, comparing with a pseudo-3D model that was also proposed in this work.

2. EXPERIMENTAL WORK

2.1. TRICKLE BED REACTOR SYSTEM

The lab scale trickle bed reactor system that was mounted inside gamma-ray CT technique is illustrated in Figure 1. The dimensions and catalyst information are listed in Table 1. The system consists of an acrylic glass column of 5.5 inches (0.139 m) inside diameter and 6 feet (1.83 m) in height, a cycling water pump, and a water reservoir tank. A single nozzle was used as the liquid inlet at the center of top of the column, 10 cm away

from the top of the catalyst bed. The single nozzle inner diameter is 9.5 mm and the length is 20 cm. The air was fed by two inlets from the top of the column to create uniform distribution. Porous quadrilobe catalyst was used in this study. These porous catalysts were selected on this work due to their vast use on industrial applications, such as on hydrocarbon treatment. Furthermore, works studying the phases distribution on TBRs packed with porous extruded catalysts are scarce, and further research efforts, such as the one conducted in this work, are required to advance the knowledge of the local scale phenomena on these systems. One layer of inert ceramic balls were set on the top of the catalyst bed as industries usually use it to stabilize the catalyst and filter the impurities from the feed flow to protect the catalyst, which can improve the liquid distribution as well. [24].

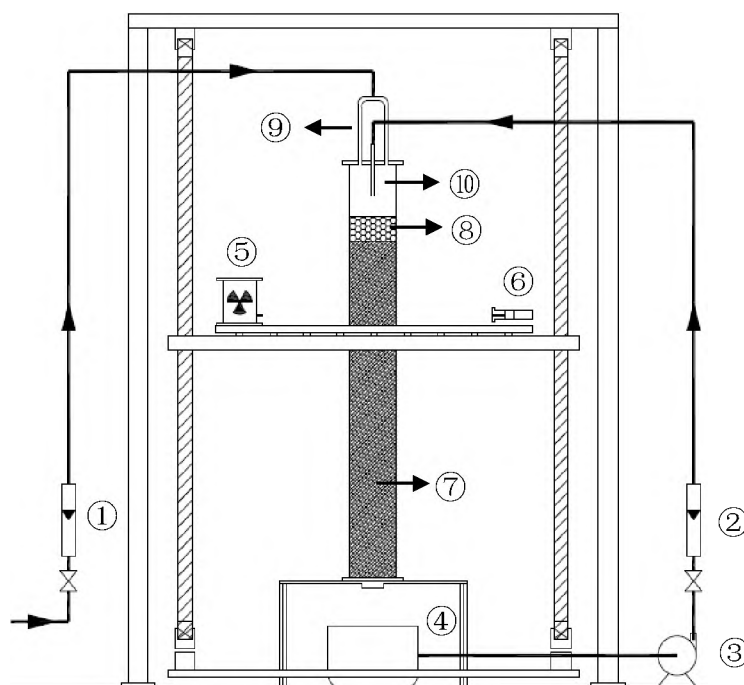


Figure 1. Trickle bed reactor inside Gamma-ray CT: ① air flowmeter; ② water flowmeter; ③ water pump; ④ water tank; ⑤ Cs-137 source; ⑥ NaI (TI) detector array; ⑦ porous quadrilobe catalyst bed; ⑧ inert ceramic balls; ⑨ gas inlet; ⑩ liquid inlet

Table 1. TBR dimensions, catalyst information and operation conditions

Item	Remark
Column height m	1.83
Column I.D. m	0.139
Column O.D. m	0.152
Catalyst shape	Extrudate quadrilobe
Catalyst material	CoMo
Catalyst equivalent diameter m	~0.0025
Catalyst length m	~0.005
Bed height m	1.5
Inert balls height m	0.1
Inert balls diameter m	0.01
Air flow flux kg/m ² s	0.025, 0.05, 0.075
Water flow flux kg/m ² s	4, 6, 8
Scan height Z/H	0.9, 0.85, 0.8, 0.7, 0.65, 0.6, 0.5

The air – water flow system was used as downstream flow in this work. Air was provided by the compressed air supply in the lab. Both air and water flow rates were controlled using calibrated flow meters. According to the flow regime map [25], the trickle flow regime was selected with gas flux ranging from 0.025 – 0.075 kg/m²s and liquid flux from 4 – 6 kg/m²s to investigate the distribution and holdup. Seven axial positions (Z/H from 0.9 – 0.5) were scanned to identify where liquid would fully spread along the cross section. The reason we selected only the upper part of the bed is that relatively uniform

distribution would always be obtained before half of the bed height based on the literature review and experiences.

2.2. GAMMA-RAY COMPUTED TOMOGRAPHY

Gamma-ray computed tomography is a non-invasive technique that provides the cross-sectional images of multiphase flow reactors at different axial levels by rotating the gamma source and its detectors covering the whole 360 degrees around the object. It is able to visualize and quantify the phase distributions and holdup profiles for multiphase flow reactors which are rather difficult to be measured by other techniques. The gamma-ray CT technique in our lab is composed of two collimated gamma ray sources (Cs-137 and Co-60), the collimated detector arrays, the data acquisition system, and the data processing system. In this study, the Cs-137 source was used to identify the two phases (gas-liquid) flow in the Trickle Bed Reactor. The Cs-137 source (193 mCi, 661 keV, 30.07 years half-life) is housed in a lead container with a window facing to the center of an arch of 15 Sodium Iodide (NaI (Tl), 2 inch in diameter) scintillation detectors. The Cs-137 source provides a 40° gamma-ray fan beam with 5 mm height in the horizontal plane. This fan beam can cover objects up to 24 inches (0.6 m) in diameter. In this work, 5 detectors were assigned to cover the Trickle Bed Reactor (6 inches (0.152 m) outside diameter). All the detectors are shielded with lead collimators which have 5×2 mm fine apertures to obtain narrow gamma-ray beams and minimize the scattered gamma-ray in order to achieve better spatial resolution. The gamma ray sources and detectors are mounted on the horizontal plane which can be move vertically up and down to scan different axial positions of the reactors.

The data acquisition system consists of 15 NaI (TI) scintillation detectors (Canberra Model 2007), 30 timing filter amplifiers (Canberra 2111), 32 channel discriminators (Phillips Scientific, CAMAC Model 7106), 32 channel 225 MHz scalars (Phillips Scientific, CAMAC Model 7132H), and CC-USB CAMAC controller (W-IE-NER). All the parameters such as the sample time, sample frequency can be specified to command the motor controller to move the detector array and source. For one CT scan, Cs-137 source has 197 source positions (197 views). At each source position, the detector array moves 20 steps driven by a 3-phase stepper motor starting from the initial position (21 projection measurements). In this work, the measurements were taken with a frequency of 10 Hz for 5 s at each of the locations. The average counts of each projection during the sampling time is written in the output data file until 62055 projections ($197 \text{ views} \times 15 \text{ detectors} \times 21 \text{ projection measurement per detector}$) are finished within about 6 hours. This leads to a total of 3102750 samples, which are enough to minimize the deviations in the time averaging, thus, allowing to capture the attenuation changes caused by the trickling liquid flow. With this thorough procedure, the CT scans resolution is enough to capture detailed phases distribution information, such as the static and dynamic liquid holdup distribution. Furthermore, for each flow condition, experiments were repeated three times, in order to assess the accuracy of the procedure, and the repeatability of the measurements. It was found that the deviations between the replications were under 1% for all cases.

The original data collected from CT scan are processed by alternating minimization (AM) algorithm to depict the attenuation values of the cross-sectional images with 80×80 pixels. Alternating minimization algorithm aims to find the maximum-likelihood estimates of attenuation values in transmission of gamma ray computed tomography. Gamma ray

transmission photon counts with regard to attenuation can be affiliated to two families, exponential family and linear family. AM uses the I-divergence function to describe the discrepancy between these two functions. If the I-divergence value is small enough to converge, the most likely attenuation value of each pixel will be obtained. The details of AM algorithm for gamma ray CT reconstruction have been explained at length by other authors from our research group [26,27]. The attenuation value is a linear sum of the product of the phase holdup and their pure phase attenuation coefficient which is given as:

$$\mu_{i,j} = \sum_n \hat{\mu}_{i,j}(n) \varepsilon_{i,j}(n) \quad (1)$$

where $\mu_{i,j}$ is the total attenuation in one pixel, i,j is the index of pixel, n is the phase number, $\hat{\mu}_{i,j}$ is the pure phase attenuation coefficient, $\varepsilon_{i,j}$ is the phase holdup in this pixel.

Besides, the sum of holdup fractions of the three phases is unity:

$$\sum_n \varepsilon_{i,j}(n) = 1 \quad (2)$$

For porous catalysts, as explained in previous section, the total liquid holdup ($\varepsilon_{\gamma,t}$) includes the dynamic liquid ($\varepsilon_{\gamma,d}$) and static liquid ($\varepsilon_{\gamma,st}$). The static liquid includes the internal static liquid, ($\varepsilon_{\gamma,st_int}$) and external static liquid ($\varepsilon_{\gamma,st_ext}$). For simplicity, the pixel index i,j is omitted from now on. Therefore, a comprehensive scan procedure and methodology were performed as follows to measure the phase holdups and to map the distribution.

1. Scan air without column to obtain the reference intensity of the source in order to calculate the attenuation of each step as follows by using the AM algorithm mentioned above.
2. Scan the empty column to obtain the attenuation due to the reactor wall.

3. Scan the column fully filled with water to get the liquid attenuation.
4. Drain the column from step 3, load the column with dry catalyst and scan to get the attenuation of the gas and solid phases.
5. Fill water inside the column with dry catalyst from step 4, leave it for prewetting for 24 hours, then scan the column to get the attenuation of the liquid and solid phases.
6. Drain the column by gravity from step 5 and wait for 24 hours till there is no flowing water coming out from the bottom outlet, then scan the column to get the attenuation of wet catalyst plus the external static liquid remained inside the bed.
7. Turn on the air/water flow and scan the column to get the attenuations under operation conditions.

The methodology to obtain the dynamic liquid holdup, solid holdup, gas holdup, static liquid holdup (internal static liquid plus external static liquid), and wet void fraction (void fraction after draining the column from Step 6 above) has been developed as follows:

From step 2, the wall attenuation of the reactor (i.e. air inside only) is due to the wall ($\mu_c \varepsilon_c$) of the column and the air ($\mu_\beta \varepsilon_\beta$) inside it. The mass attenuation coefficient of the air is negligible compared to other materials. The attenuation can be described as:

$$\mu_{\beta-c} = \mu_\beta \varepsilon_\beta + \mu_c \varepsilon_c \quad (3)$$

From step 3, the attenuation of the column filled with water (i.e. water inside only) is due to the wall of the column ($\mu_c \varepsilon_c$) and the liquid ($\mu_\gamma \varepsilon_\gamma$) inside it, which is:

$$\mu_{\gamma-c} = \mu_\gamma \varepsilon_\gamma + \mu_c \varepsilon_c \quad (4)$$

From step 4, the attenuation of the column packed with dry catalyst (i.e. dry catalyst inside only) is due to the column wall ($\mu_c \mathcal{E}_c$), the dry catalyst ($\mu_s \mathcal{E}_s$) and the air in the pores of catalyst. As mentioned earlier, the attenuation of air can be neglected. It can be described as:

$$\mu_{s-\beta-c} = \mu_s \mathcal{E}_s + \mu_\beta \mathcal{E}_\beta + \mu_c \mathcal{E}_c \quad (5)$$

From step 5, the attenuation of the column with catalyst and water (i.e. wet catalyst plus the water filling the external void) is due to the column wall ($\mu_c \mathcal{E}_c$), solid catalyst ($\mu_s \mathcal{E}_s$), water absorbed inside catalyst ($\mu_\gamma \mathcal{E}_{\gamma, st_int}$), water inside the external void of the packed bed ($\mu_\gamma \mathcal{E}_{\gamma, ev}$), and small amount of air inside catalyst that cannot be filled with water, which can be neglected. It can be described as:

$$\mu_{s-\gamma-c} = \mu_s \mathcal{E}_s + \mu_\gamma \mathcal{E}_{\gamma, st_int} + \mu_\gamma \mathcal{E}_{\gamma, ev} + \mu_c \mathcal{E}_c \quad (6)$$

From step 6, the attenuation of the column with wet catalyst (i.e. wet catalyst plus the water retained after drainage) is due to the column wall ($\mu_c \mathcal{E}_c$), solid catalyst ($\mu_s \mathcal{E}_s$), water absorbed inside catalyst ($\mu_\gamma \mathcal{E}_{\gamma, st_int}$), water retained on the catalyst surface ($\mu_\gamma \mathcal{E}_{\gamma, st_ext}$) after draining the water from step 5, and air in the void obtained after draining the water. It can be described as:

$$\mu_{ws-\beta-c} = \mu_s \mathcal{E}_s + \mu_\gamma \mathcal{E}_{\gamma, st_int} + \mu_\gamma \mathcal{E}_{\gamma, st_ext} + \mu_\beta \mathcal{E}_\beta + \mu_c \mathcal{E}_c \quad (7)$$

From step 7, the attenuation of the flow conditions (i.e. gas-liquid-solid system) is due to the air and water introduced into the wet packed bed from step 6. It includes the

solid catalyst ($\mu_c \mathcal{E}_c$), water absorbed inside catalyst ($\mu_\gamma \mathcal{E}_{\gamma,st_int}$), water attached on the catalyst surface ($\mu_\gamma \mathcal{E}_{\gamma,st_ext}$), dynamic liquid ($\mu_\gamma \mathcal{E}_{\gamma,d}$) flowing through the void of the packed bed, and air flowing between the dynamic liquid and the catalyst. It can be described as:

$$\mu_{s-\beta-\gamma-c} = \mu_s \mathcal{E}_s + \mu_\gamma \mathcal{E}_{\gamma,st_int} + \mu_\gamma \mathcal{E}_{\gamma,st_ext} + \mu_\gamma \mathcal{E}_{\gamma,d} + \mu_\beta \mathcal{E}_\beta + \mu_c \mathcal{E}_c \quad (8)$$

Besides, in packed bed reactors, the overall holdup of all phases should be unity which is:

$$\mathcal{E}_s + \mathcal{E}_{\gamma,st_int} + \mathcal{E}_{\gamma,st_ext} + \mathcal{E}_{\gamma,d} + \mathcal{E}_\beta = 1 \quad (9)$$

There are total 7 equations listed above (Equation (3) – (9)), from which we can solve 7 unknowns (phase holdups) under flow conditions as follows.

(1) **Total void fraction (\mathcal{E}_{void}):** By subtracting the attenuation of dry catalyst from attenuation of the packed bed filled with water, then divided by attenuation of the column filled with water we can obtain:

$$\begin{aligned} & \frac{\mu_{s-\gamma-c} - \mu_{s-\beta-c}}{\mu_{\gamma-c} - \mu_{\beta-c}} \\ &= \frac{(\mu_s \mathcal{E}_s + \mu_\gamma \mathcal{E}_{\gamma,st_int} + \mu_\gamma \mathcal{E}_{\gamma,ev} + \mu_c \mathcal{E}_c) - (\mu_s \mathcal{E}_s + \mu_\beta \mathcal{E}_\beta + \mu_c \mathcal{E}_c)}{(\mu_\gamma \mathcal{E}_\gamma + \mu_c \mathcal{E}_c) - (\mu_\beta \mathcal{E}_\beta + \mu_c \mathcal{E}_c)} \\ &= \frac{\mu_\gamma \mathcal{E}_{\gamma,st_int} + \mu_\gamma \mathcal{E}_{\gamma,ev}}{\mu_\gamma \mathcal{E}_\gamma} \\ &= \frac{\mathcal{E}_{\gamma,st_int} + \mathcal{E}_{\gamma,ev}}{\mathcal{E}_\gamma} = \mathcal{E}_{void} \end{aligned} \quad (10)$$

(2) **Solid holdup (ε_s):** By subtracting the total void fraction, the solid holdup will be obtained:

$$\varepsilon_s = 1 - \varepsilon_{void} \quad (11)$$

(3) **Gas holdup (ε_β):** By subtracting the attenuation of flow condition from the attenuation of packed bed filled with water, then divided by attenuation of the column filled with water we can obtain:

$$\begin{aligned} & \frac{\mu_{s-\gamma-c} - \mu_{s-\beta-\gamma-c}}{\mu_{\gamma-c} - \mu_{\beta-c}} \quad (12) \\ &= \frac{(\mu_s \varepsilon_s + \mu_\gamma \varepsilon_{\gamma,st_int} + \mu_\gamma \varepsilon_{\gamma,ev} + \mu_c \varepsilon_c) - (\mu_s \varepsilon_s + \mu_\gamma \varepsilon_{\gamma,st_int} + \mu_\gamma \varepsilon_{\gamma,st_ext} + \mu_\gamma \varepsilon_{\gamma,d} + \mu_\beta \varepsilon_\beta + \mu_c \varepsilon_c)}{(\mu_\gamma \varepsilon_\gamma + \mu_c \varepsilon_c) - (\mu_\beta \varepsilon_\beta + \mu_c \varepsilon_c)} \\ &= \frac{\mu_\gamma \varepsilon_{\gamma,ev} - \mu_\gamma \varepsilon_{\gamma,st_ext} - \mu_\gamma \varepsilon_{\gamma,d}}{\mu_\gamma \varepsilon_\gamma} \\ &= \frac{\varepsilon_{\gamma,ev} - \varepsilon_{\gamma,st_ext} - \varepsilon_{\gamma,d}}{\varepsilon_\gamma} = \varepsilon_\beta \end{aligned}$$

(4) **Static liquid holdup ($\varepsilon_{\gamma,st}$):** As explained in previous sections, static liquid consists of internal static liquid and external static liquid. In this work, we are focusing on the dynamic liquid, so both of the internal and external static liquid are considered as being lumped together. The separation of the internal and external static liquid holdup will be introduced in another work which is not mentioned in this work. By subtracting the attenuation of column with dry catalyst from the attenuation of column with wet catalyst, then divided by attenuation of the column filled with water we can obtain:

$$\frac{\mu_{ws-\beta-c} - \mu_{s-\beta-c}}{\mu_{\gamma-c} - \mu_{\beta-c}} \quad (13)$$

$$= \frac{(\mu_s \mathcal{E}_s + \mu_\gamma \mathcal{E}_{\gamma,st_int} + \mu_\gamma \mathcal{E}_{\gamma,st_ext} + \mu_\beta \mathcal{E}_\beta + \mu_c \mathcal{E}_c) - (\mu_s \mathcal{E}_s + \mu_\beta \mathcal{E}_\beta + \mu_c \mathcal{E}_c)}{(\mu_\gamma \mathcal{E}_\gamma + \mu_c \mathcal{E}_c) - (\mu_\beta \mathcal{E}_\beta + \mu_c \mathcal{E}_c)}$$

$$= \frac{\mu_\gamma \mathcal{E}_{\gamma,st_int} + \mu_\gamma \mathcal{E}_{\gamma,st_ext}}{\mu_\gamma \mathcal{E}_\gamma}$$

$$= \frac{\mathcal{E}_{\gamma,st_int} + \mathcal{E}_{\gamma,st_ext}}{\mathcal{E}_\gamma} = \mathcal{E}_{\gamma,st}$$

(5) **Dynamic liquid holdup ($\mathcal{E}_{\gamma,d}$):** With gas holdup, solid holdup and static liquid holdup calculated above, the dynamic liquid holdup can be calculated as:

$$\mathcal{E}_{\gamma,d} = 1 - \mathcal{E}_\beta - \mathcal{E}_s - \mathcal{E}_{\gamma,st} \quad (14)$$

(6) **Void fraction of column with wet catalyst ($\mathcal{E}_{v,wet}$):** After draining the water from step 6, the void fraction in the wet packed bed can be calculated by subtracting the attenuation of column with wet packed bed from the attenuation of packed bed filled with water, then divided by attenuation of the column filled with water we can obtain:

$$\frac{\mu_{s-\gamma-c} - \mu_{ws-\beta-c}}{\mu_{\gamma-c} - \mu_{\beta-c}} \quad (15)$$

$$= \frac{(\mu_s \mathcal{E}_s + \mu_\gamma \mathcal{E}_{\gamma,st_int} + \mu_\gamma \mathcal{E}_{\gamma,ev} + \mu_c \mathcal{E}_c) - (\mu_s \mathcal{E}_s + \mu_\gamma \mathcal{E}_{\gamma,st_int} + \mu_\gamma \mathcal{E}_{\gamma,st_ext} + \mu_\beta \mathcal{E}_\beta + \mu_c \mathcal{E}_c)}{(\mu_\gamma \mathcal{E}_\gamma + \mu_c \mathcal{E}_c) - (\mu_\beta \mathcal{E}_\beta + \mu_c \mathcal{E}_c)}$$

$$= \frac{\mu_\gamma \mathcal{E}_{\gamma,ev} - \mu_\gamma \mathcal{E}_{\gamma,st_ext}}{\mu_\gamma \mathcal{E}_\gamma}$$

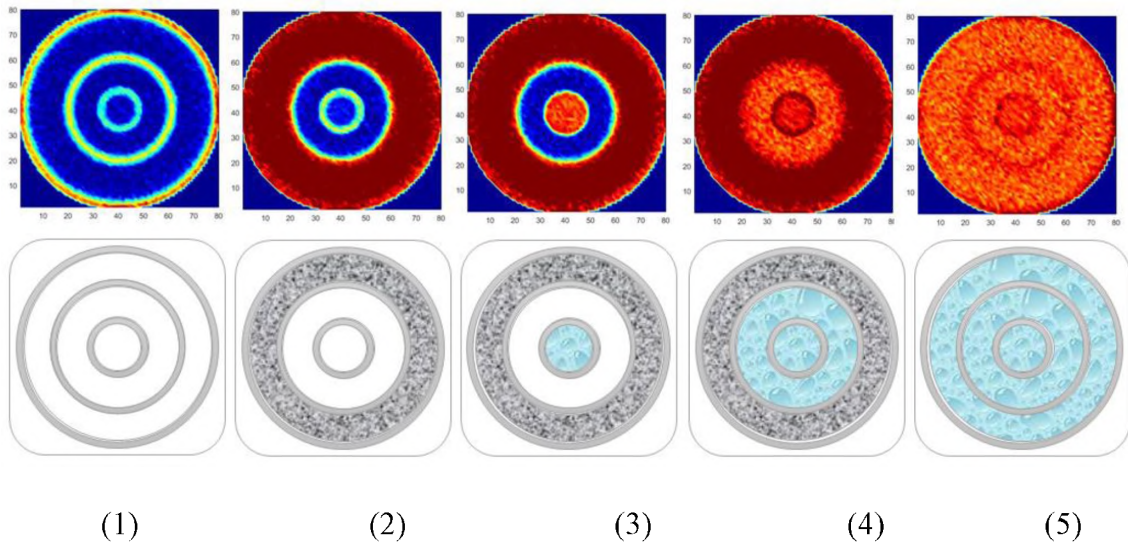
$$= \frac{\mathcal{E}_{\gamma, ev} - \mathcal{E}_{\gamma, st-ext}}{\mathcal{E}_{\gamma}} = \mathcal{E}_{v, wet}$$

(7) **Total liquid holdup ($\mathcal{E}_{\gamma, t}$):** The total liquid holdup is the summation of dynamic liquid holdup and static liquid holdup:

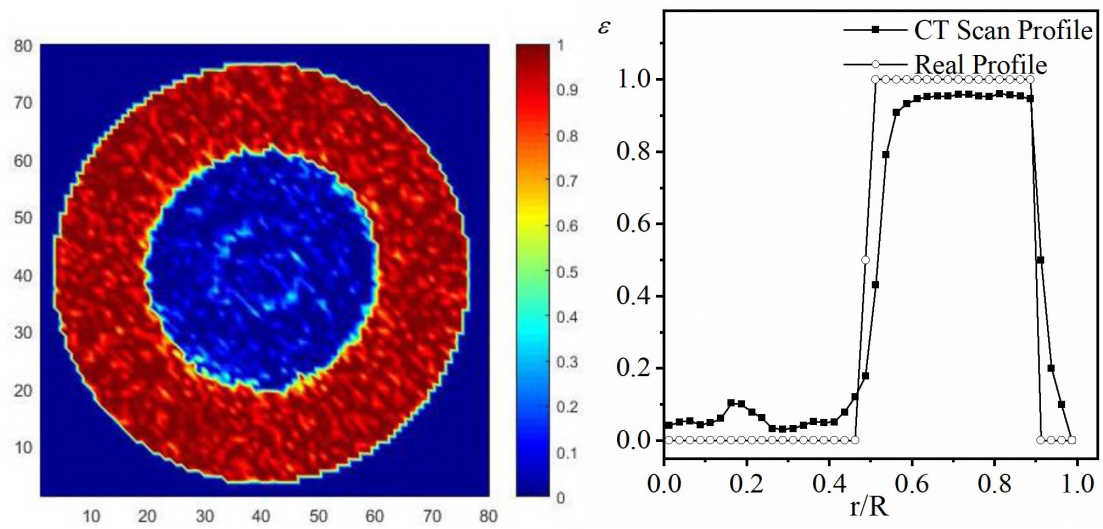
$$\mathcal{E}_{\gamma, t} = \mathcal{E}_{\gamma, int} + \mathcal{E}_{\gamma, d} \quad (16)$$

2.3. DEMONSTRATION OF CT

In order to demonstrate the capability and reproducibility of CT scan identifying the gas – liquid – solid system, the validation experiments were conducted using a pre-designed synthetic phantom. The phantom is made of three acrylic-glass columns: inside column (O.D. 31.75 mm), middle column (O.D. 82.55 mm) and outside column (O.D. 152.4 mm). The same procedure and calculation methodology explained in previous section were followed. The crossed-sectional images reconstructed by AM algorithm with comparison to the schematics are shown in in Figure 2 (a). In the meanwhile, case (3) is the one we need to validate since it contains gas, liquid and solid phase. The single-phase distribution and holdup profiles for case (3) obtained from CT compared with the actual phase holdup profiles are shown in Figure 2 (b - d). The relative errors for gas phase holdup, liquid phase holdup and solid phase holdup phase are 7.63%, 5.11% and 9.86%, respectively.

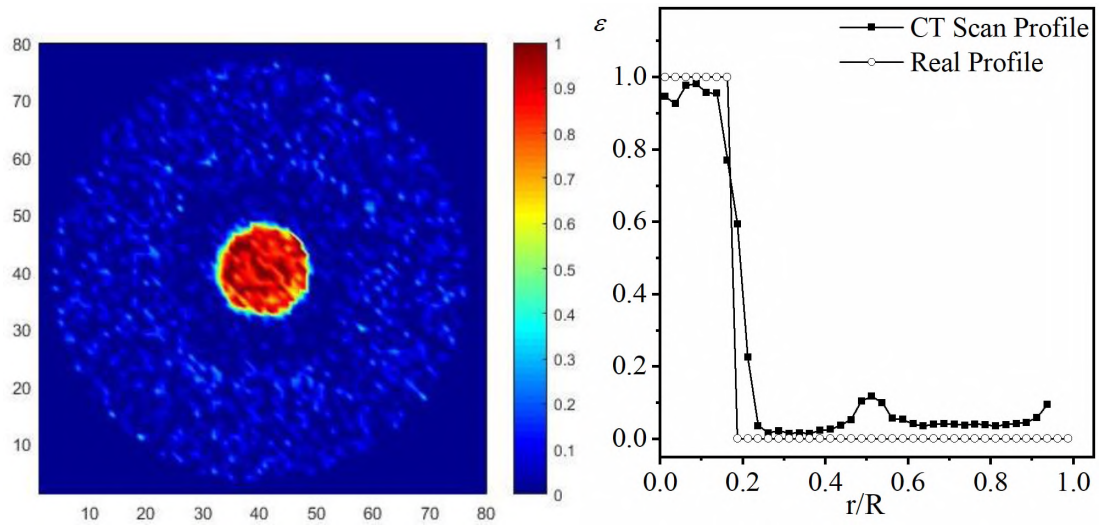


(a) The cross-sectional images reconstructed by AM algorithm

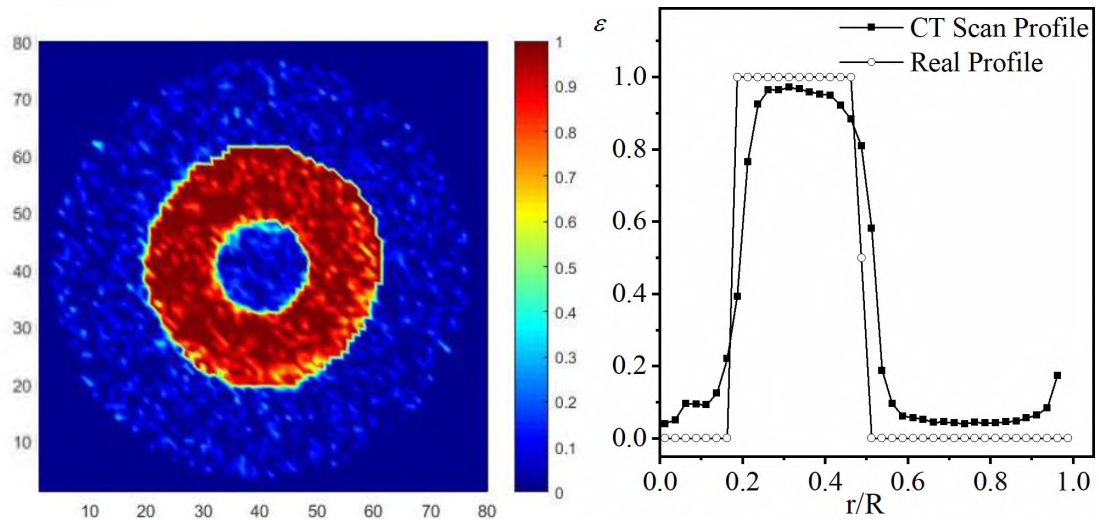


(b) Solid phase

Figure 2. Single phase distribution and holdup profiles comparison between CT scan and real profile



(c) Liquid phase



(d) Gas phase

Figure 2. Single phase distribution and holdup profiles comparison between CT scan and real profile (cont.)

3. RESULTS AND DISCUSSION

From CT scans, we are able to reconstruct the cross-sectional images indicating the phase distributions and holdup profiles at different axial levels for the Trickle Bed Reactor

with quadrilobes catalyst. In order to better qualify and quantify the dynamic liquid distribution and holdup, the 3-D map based on a 32-compartments ($N = 32$, shown in Figure 3) module, as well as the maldistribution factor were introduced in this section. Each compartment has the same area to ensure the uniformly distributed probability of occurrences. The number of compartments was determined based on the resolution and representative quality after several trials with different number of compartments.

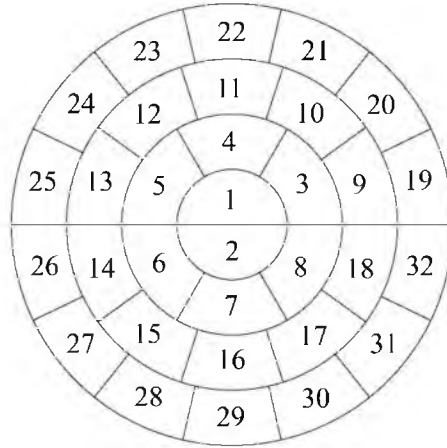


Figure 3. Schematic of maldistribution quantification module ($N = 32$)

3.1. LIQUID MALDISTRIBUTION FACTOR

As mentioned earlier, the most common way to quantify the liquid maldistribution is using a multi-compartment collector at the outlet of the bed to obtain the maldistribution factor, which ranges from 0 to 1. Less maldistribution factor means better distribution. If maldistribution factor is 0, it means ideally perfect distribution. The maldistribution factor can be expressed by:

$$M_f = \sqrt{\frac{1}{N(N-1)} \sum \left(\frac{Q_i - Q_{mean}}{Q_{mean}} \right)^2} \quad (17)$$

where $Q_i[m^3/s]$ is the liquid volume flow rate through compartment i , N is the compartment number, $Q_{mean}[m^3/s]$ is the mean volume flow rate of all compartments. Considering a certain level of the reactor, if we take the cross section with a unit height of the reactor, it is reasonable to describe the liquid volume as the liquid proportion of the whole cross-sectional volume. Then we can take dimensionality deduction due to the unity of height to use the liquid volume fraction (holdup) of the cross-sectional area to describe the liquid volume which can be explained mathematically as follows.

$$M_f = \sqrt{\frac{1}{N(N-1)} \sum \left(\frac{\varepsilon_{\gamma,d,i} V_i - (\varepsilon_{\gamma,d} V)_{mean}}{(\varepsilon_{\gamma,d} V)_{mean}} \right)^2} \quad (18)$$

$$= \sqrt{\frac{1}{N(N-1)} \sum \left(\frac{\varepsilon_{\gamma,d,i} A_i h - \left(\frac{\sum \varepsilon_{\gamma,d,i} A_i h}{N} \right)_{mean}}{\left(\frac{\sum \varepsilon_{\gamma,d,i} A_i h}{N} \right)_{mean}} \right)^2} \quad (19)$$

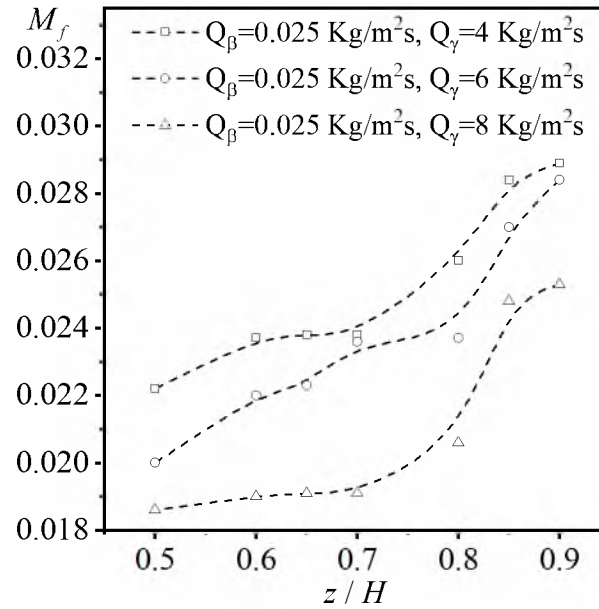
$$= \sqrt{\frac{1}{N(N-1)} \sum \left(\frac{\varepsilon_i - \varepsilon_{mean}}{\varepsilon_{mean}} \right)^2} \quad (20)$$

where V_i is the volume of the i th compartment, A_i is the cross-sectional area of the i th compartment, h is the unit height, $\varepsilon_{\gamma,d,i}$ is the dynamic liquid holdup of each compartment. The maldistribution factors of each velocity combination at different heights are plotted in Figure 4.

For all the flowrates, the maldistribution factors decrease along the height getting lower. We can also observe that there is a transition region to get better distribution for each flowrate. The cases with lower liquid flowrate ($4 \leq Q_\gamma \leq 6 \text{ Kg} / \text{m}^2 \text{s}$) and higher gas

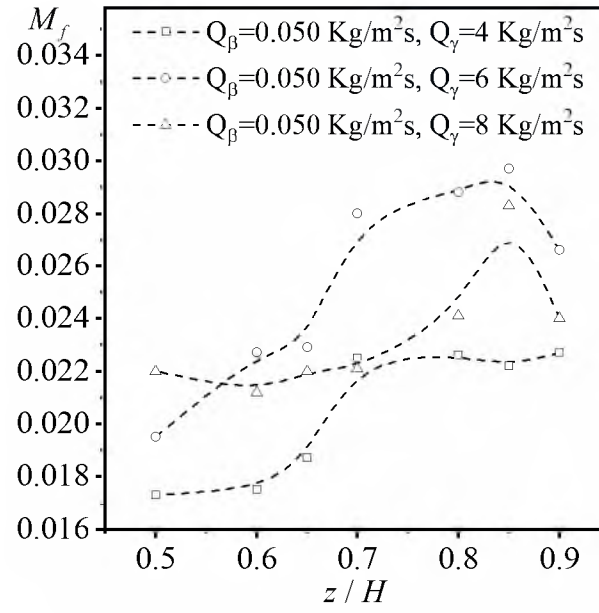
flowrate ($0.05 \leq Q_\beta \leq 0.075 \text{ Kg/m}^2\text{s}$) have the transition in between $Z/H = 0.65 \sim 0.7$.

At lower gas flowrates, the transition happens in between $Z/H = 0.8 \sim 0.85$. With both high gas flowrates and high liquid flowrates, the transition is relatively hard to capture from the experiments. However, it can be concluded that all the cases tend to get better distribution at level $Z/H = 0.6$. At the same gas flowrate, the maldistribution factor decreases with increasing the liquid flowrate, which means better distribution is obtained. In addition, both of liquid and gas flowrate can affect the dynamic liquid distribution inside a packed bed reactor while it is difficult to conclude which one has higher impact.

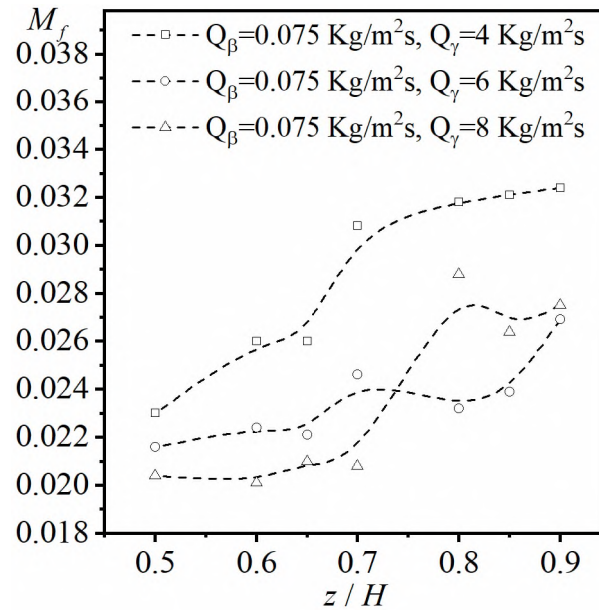


(a) Gas flowrates $Q_\beta = 0.025 \text{ kg/m}^2\text{s}$

Figure 4. Maldistribution factors at different bed heights and flowrates

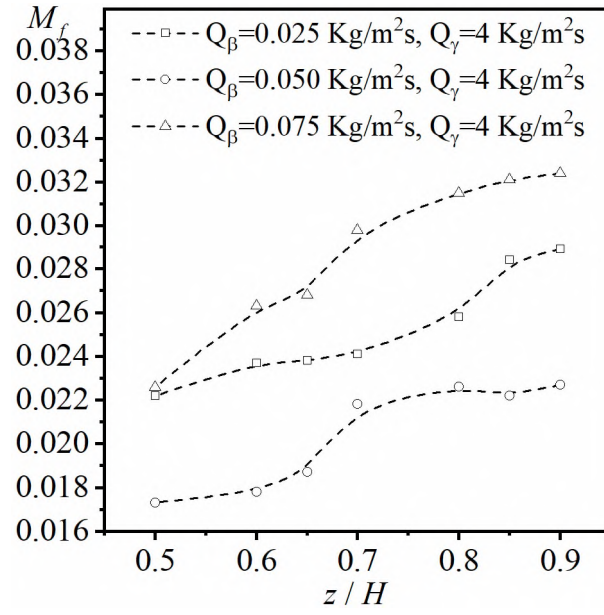


(b) Gas flowrates $Q_\beta = 0.050 \text{ kg/m}^2\text{s}$

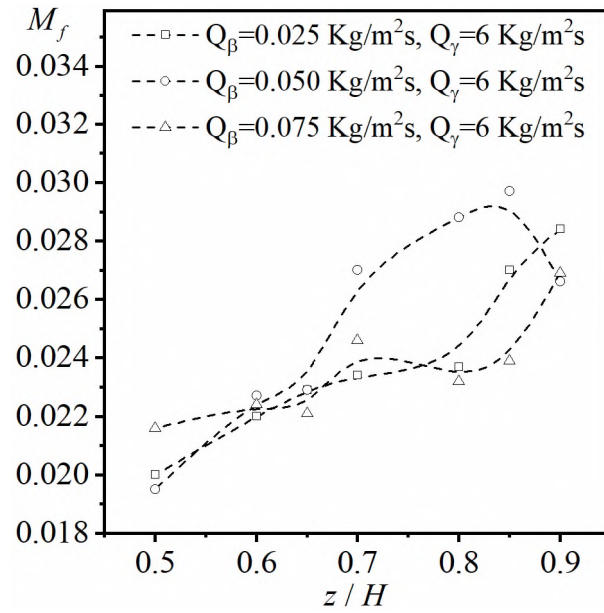


(c) Gas flowrates $Q_\beta = 0.075 \text{ kg/m}^2\text{s}$

Figure 4. Maldistribution factors at different bed heights and flowrates (cont.)

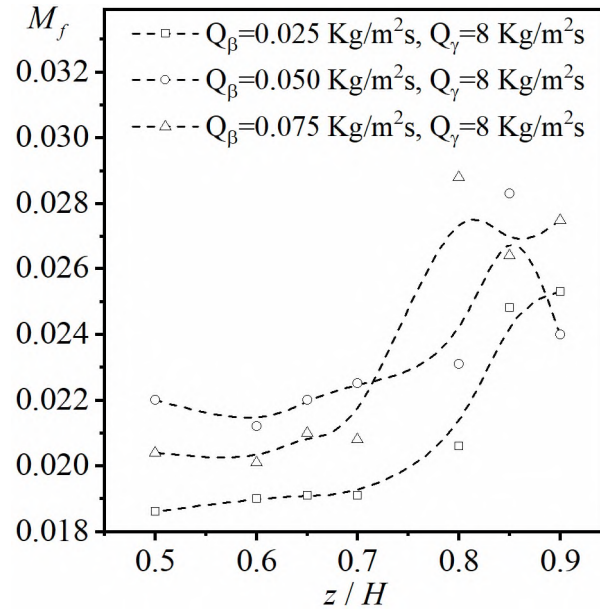


(d) Liquid flowrate $Q_\gamma = 4 \text{ kg/m}^2 \text{ s}$



(e) Liquid flowrate $Q_\gamma = 6 \text{ kg/m}^2 \text{ s}$

Figure 4. Maldistribution factors at different bed heights and flowrates (cont.)



(f) Liquid flowrate $Q_\gamma = 8 \text{ kg/m}^2 \text{ s}$

Figure 4. Maldistribution factors at different bed heights and flowrates (cont.)

A showcase ($Q_\beta = 0.025 \text{ kg/m}^2 \text{ s}$, $Q_\gamma = 4 \text{ kg/m}^2 \text{ s}$) is discussed here. The dynamic liquid distribution images of different levels obtained from CT are shown in Figure 5 (a). In order to better visualize the distribution, the corresponding 3D mapping images are generated in Figure 5 (b). It can be seen that at $Z/H = 0.9$, there is more dynamic liquid in the center of the column. With decreasing the level height, the dynamic liquid proportion difference reduces gradually to maximize the uniform distribution. This can also be observed in the trendline in Figure 5 (c), where the X-axis represents the compartment number in Figure 3 and Y-axis represents the dynamic liquid proportion of each compartment over the whole cross section. These trendlines indicate the dynamic liquid distribution along the radius of the reactor. At $Z/H = 0.9$, the trendline is quite slant since

the dynamic liquid flowrate in the center is around 1.5 times that close to the wall. Comparing $Z/H = 0.7$ and $Z/H = 0.5$, the trendlines are almost the same flat even with quite different maldistribution factors. This can be explained from the bar chart in Figure 5 (c) that at $Z/H = 0.7$, the large variance of the dynamic liquid proportion of each compartment happens more frequently than that at $Z/H = 0.5$. It means that $Z/H = 0.5$ has better distribution than that of $Z/H = 0.7$. In the meanwhile, it also discloses the information that around this level ($Z/H = 0.5$), the dynamic liquid starts spreading to the region near the wall of the reactor. Similar conclusions can be obtained for all the other flow conditions which will not be discussed at length here.

3.2. DYNAMIC LIQUID HOLDUP

It was observed that there is no high correlation between the cross-sectional average dynamic liquid holdup and the bed height. The standard deviations of the average dynamic holdup for each flowrate at different heights is around 0.01. It can also be observed that if the gas flowrate increases while keeping the liquid flowrate fixed, the average dynamic liquid holdup decreases. However, if the gas flowrate is fixed, there is no dominant increasing or decreasing trend showing up for different liquid flowrates at different heights.

If we look at the dynamic liquid holdup profiles with respect to column radius in Figure 6, for each flowrate, the profiles of different heights are approximately matching each other which proves again that the bed height is not the determining factor affecting the dynamic liquid holdup. What can be clearly seen in these profiles is that the dynamic liquid holdup at heights above $Z/H = 0.8$ close to the center ($r/R < 0.3$) is visibly higher than that close to the wall indicating the maldistribution trend discussed in previous

sections. On the other hand, some holdup values are extremely small right around the wall region due to the limitation of CT technique to distinguish with high resolution the wall from the flow region.

4. DYNAMIC LIQUID HOLDUP MODELS

Proper numerical models to predict the dynamic liquid holdup for quadrilobes catalyst inside the Trickle Bed Reactor are necessary. Typically, there are two types of models, empirical model and phenomenological model. Since part of the dynamic liquid flows through the space inside the packed bed without contacting the catalyst, it is impractical to develop a phenomenological model based on fundamental physical principles such as force balance etc. An empirical model by including certain physical properties, such as gas/liquid flowrate, radial position, axial position etc., would be a better option to predict the dynamic liquid holdup. However, it is hard to determine which physical properties have more significant effect on the dynamic liquid holdup. Hence, deep neural network (DNN) was used to compare the importance of each physical property as a guidance for the development of the empirical model. Therefore, a pseudo-3D empirical model predicting the dynamic liquid holdup for quadrilobes catalyst in a Trickle Bed Reactor was proposed in this work. The reason why naming the model ‘pseudo-3D’ is that this model is able to predict the dynamic liquid holdup in terms of r/R (azimuthally averaged at radius of r) and Z/H (relative bed height). After that, both of DNN model and the pseudo-3D model predictions were compared against the experimental data.

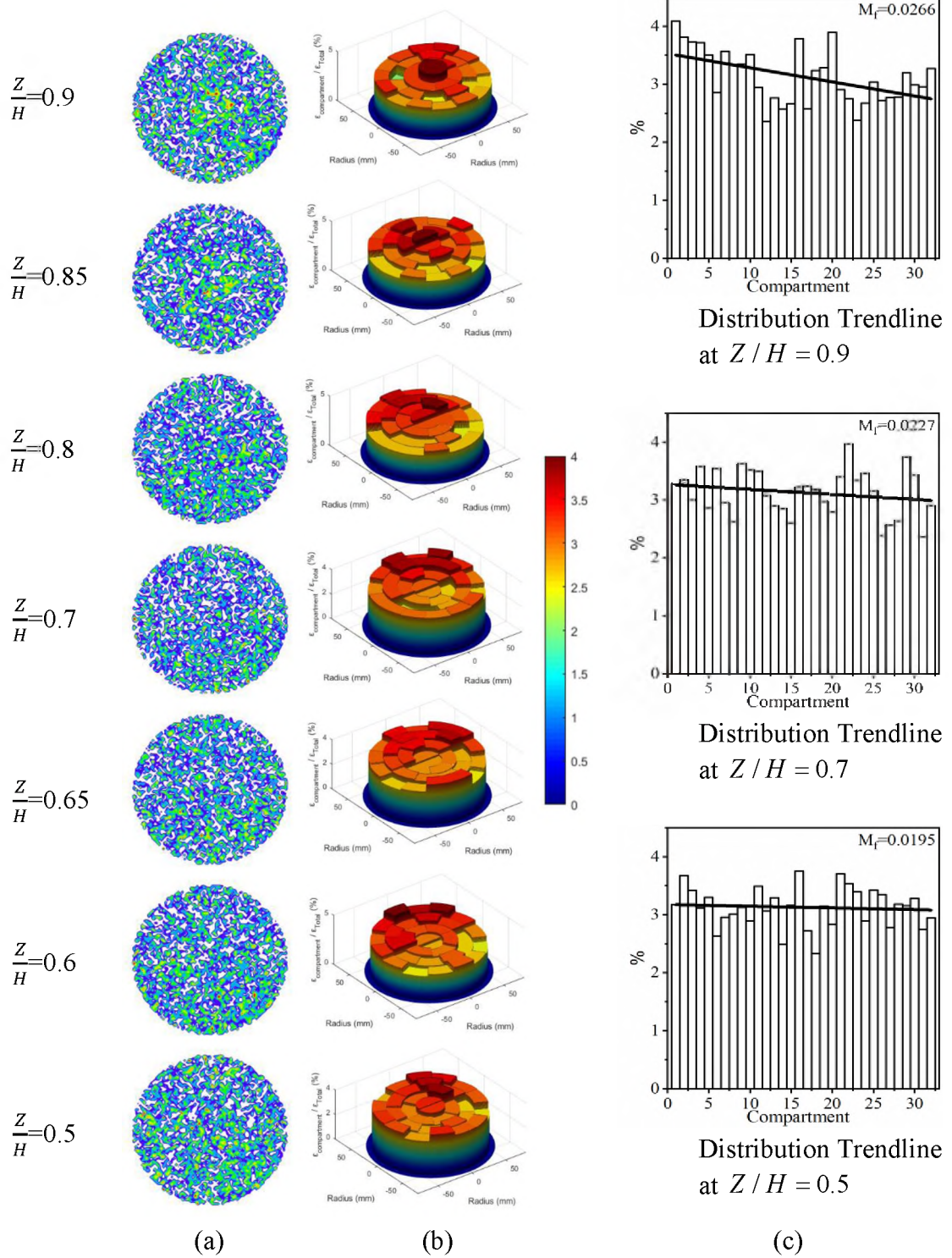


Figure 5. (a) Dynamic liquid distribution from CT; (b) 3-D mapping of dynamic liquid distribution; (c) Dynamic liquid distribution bar chart with trendline at selected levels,

$$Q_\beta = 0.025 \text{ Kg} / \text{m}^2 \text{s}, Q_\gamma = 4 \text{ Kg} / \text{m}^2 \text{s}$$

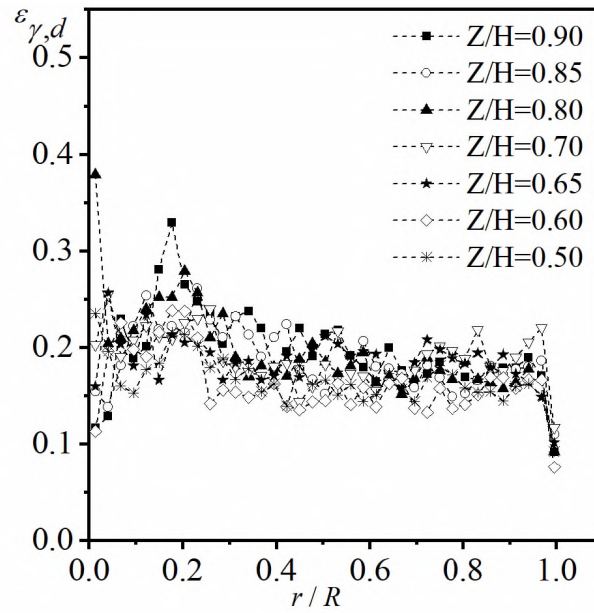


Figure 6. Dynamic liquid holdup profiles with regard to radius at different heights at flowrate, $Q_\beta = 0.025 \text{ Kg} / \text{m}^2 \text{s}$, $Q_\gamma = 4 \text{ Kg} / \text{m}^2 \text{s}$

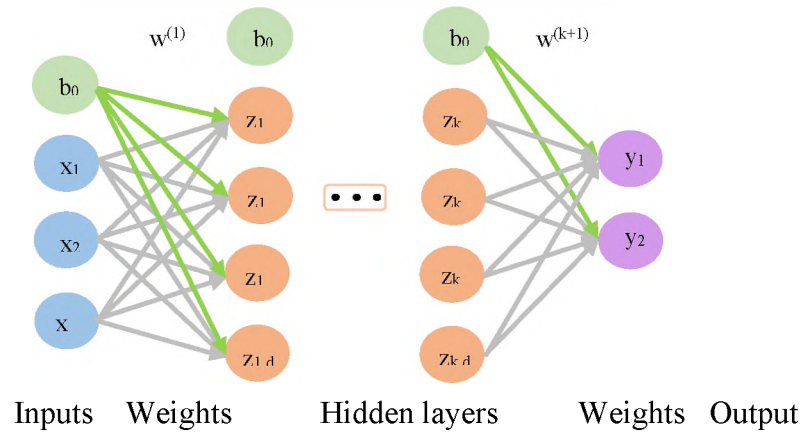
4.1. MODELING USING DEEP NEURAL NETWORK (DNN)

Deep neural network (DNN) extracts the features or representations directly from the input data and map it into one or more outputs with multiple hidden layers [28]. One of the great advantages of DNN is the pliability towards the chaotic or turbulent occurrences following the law of nature and giving the reliable models and predictions. The typical DNN algorithm structure is illustrated in Figure 7 (a). DNN is basically the stack of the simplest standard neural network which is called Perceptron. The idea of perceptron is multiplying the inputs by their corresponding weight vectors and then passing the summation of these weighted combinations through a nonlinear activation function to get the output [29]. Instead that one perceptron has only one hidden layer, DNN has multiple hidden layers. From one layer to the next layer, DNN usually takes many epochs (iteration) to process the data. Once the processes reach the last layer, DNN generates the

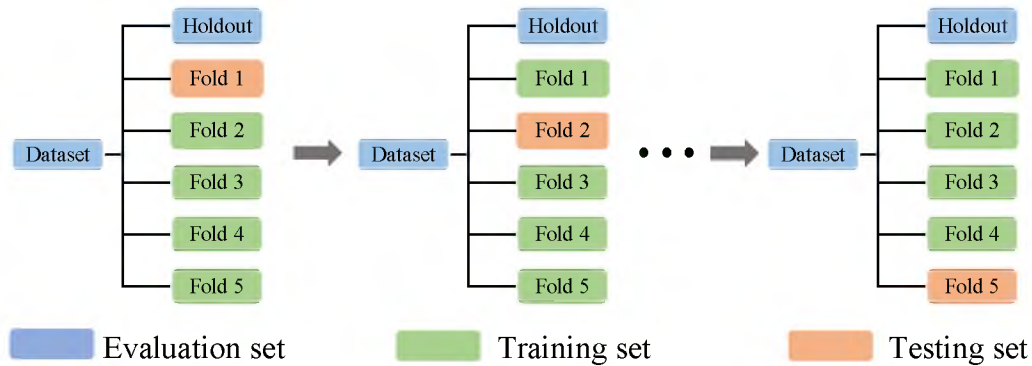
outputs comparing with the expected data to check the error and then updates the weights of the previous layer which is called backpropagation process. After that, a loss function is used to judge the performance of the model and then the next epoch continues until it reaches the minimum error. The DNN algorithm can be expressed as follows:

$$z_{k,i} = b_{0,i}^{(k-1)} w_{0,i}^{(k-1)} + \sum_{j=1}^{d_{k-1}} \phi(z_{k-1,j}) w_{j,i}^{(k)} \quad (21)$$

$$y = \phi(b_{0,i}^{(k)} w_{0,i}^{(k)} + \sum_{j=1}^{d_k} \phi(z_{k,j}) w_{j,i}^{(k+1)}) \quad (22)$$



(a) Schematic of DNN algorithm structure



(b) Schematic of K-fold cross-validation

Figure 7. (a) Schematic of DNN algorithm structure (b) Schematic of K-fold cross-validation

In the equations, b_0 is the bias, w is the weight, z_k is the hidden neuron at k layer, $\phi(x)$ is the nonlinear activation function. Activation function aims to determine whether the output is within the desired range mapped by the activation function itself [29]. Commonly used activation functions are Sigmoid function, TanH function, Rectified Linear Unit (ReLU) function etc. For engineering progression and prediction problems, ReLU is the proper choice [30].

Neural network has been utilized as a handy tool to do rapid predictions and parameters assessment in multiphase flow systems [9,31]. In this study, DNN is used to model and predict the dynamic liquid holdup at different axial and radial locations under different operating conditions. The free open source software TensorFlow (developed by Google Inc.) based on Python language was used to develop the DNN model.

In this case, we have four inputs, gas flowrate ($Q_g [Kg / m^2s]$), liquid flowrate ($Q_l [Kg / m^2s]$), bed height (Z / H), and radius (r / R) with dynamic liquid holdup ($\varepsilon_{l,d}$) as output. Based on the amount of the experimental data, three hidden layers were used in the model to obtain better prediction performance with low computational cost. Each layer contains 60, 30, and 15 neurons, respectively. To evaluate and improve the performance of the model, the K-fold Cross Validation (K-fold CV) was implemented, which divides the data set into folds and each fold is used as a testing group at a certain validation step [32,33]. In this work, the whole data set is split into 6 parts, one holdout fold (10% of the data set) and five cross-validation folds (90% of the data set, $K = 5$). The purpose of holdout fold is to evaluate the accuracy of the model after K-fold CV as shown in Figure 7 (b). In order to achieve better performance but to avoid overfitting, the Adam backpropagation

algorithm [34] with relatively low patience (Patience = 5, the steps without improvement can be tolerated) for early stopping were considered.

The model loss and root mean squared error (RMSE) were calculated respectively. The model loss reveals how good the model's prediction is in terms of being able to predict the expected output. Less loss value means better prediction performance. The mean squared error (MSE) loss function and the root mean squared error (RMSE) are given as:

$$MSE = \frac{\sum_{i=1}^N (y_i - y_i^p)^2}{N} \quad (23)$$

$$RMSE = \sqrt{\frac{\sum_{i=1}^N (y_i - y_i^p)^2}{N}} \quad (24)$$

where y_i is the expected output while y_i^p is the model prediction and N is the sample numbers. From the DNN results, the model loss is 0.0038 and the overall RMSE is 0.042 after converging. From the Experiment vs. Prediction plot we can see that the model shows reasonable accuracy. In addition, the Input Perturbation Ranking Algorithm [35,36] that evaluates the importance of inputs by doing sensitivity analysis based on the experimental data is implemented. The results in **Table 2** show that radius position have hundred percent importance in the dynamic liquid holdup in a trickle bed reactor, then the gas flowrate, liquid flowrate and bed height. This conclusion is exactly the same as the holdup profiles show earlier.

4.2. PSEUDO-3D MODEL OF DYNAMIC LIQUID HOLDUP

The commonly used empirical models to predict the liquid holdup and saturation are listed in Table 3.

Table 2. The perturbation rank of inputs

Name	Error	Importance
r / R	0.003719	1.000000
$Q_\beta, Kg / m^2 s$	0.002166	0.582444
$Q_\gamma, Kg / m^2 s$	0.002026	0.544605
Z / H	0.001955	0.525605

Table 3. Models for prediction of liquid holdup and saturation in trickle bed reactors

Author	Description	Models
Specchia and Baldi 1977	Dynamic liquid holdup	$\varepsilon_{L,d} = 3.86 Re_L^{0.545} (Ga^*)^{-0.42} \left(\frac{a_s d_p}{\varepsilon}\right)^{0.65}, 3 < Re < 470$ $Ga^* = d_p^3 \rho_L g + \frac{\Delta P}{\Delta Z \mu_L^2}$ <p><i>for low interaction regime</i></p> $\varepsilon_{L,d} = 0.125 \left(\frac{Z}{\psi^{1.1}}\right)^{-0.312} \left(\frac{a_s d_p}{\varepsilon}\right)^{0.65}, 3 < \frac{Z}{\psi^{1.1}} < 470$ $\psi = \left(\frac{\delta_g}{\delta_l}\right) \left[\left(\frac{\mu_L}{\mu_G}\right) \left(\frac{\rho_G}{\rho_L}\right)^2\right]^3$ <p><i>for high interaction regime</i></p>
Burghardt et al. 1995	Dynamic liquid holdup	$\varepsilon_{L,d} = 1.125 (Re_G + 2.28)^{-0.1} (Ga'_L)^{-0.5} \left(\frac{a_s d_p}{\varepsilon}\right)^{0.3}$ $\times \tanh(48.9 (Ga'_L)^{-1.16} Re_L^{0.41})$ $Ga'_L = d_p / (\mu_L^2 / (g \rho_L^2))^{1/3}$ $2 < Re_L < 62, 0 < Re_G < 103, 51 < Ga'_L < 113$

Table 3. Models for prediction of liquid holdup and saturation in trickle bed reactors (cont.)

Author	Description	Models
Wammes et al. 1991	Non-capillary liquid saturation	$\beta_{nc} = 16.3 Re_L^c Ga_L^d$ $c = 0.36 \text{ and } d = -0.39 \text{ for } Re < 11$ $c = 0.55 \text{ and } d = -0.42 \text{ for } Re > 15$
Morsi et al. 1982	Total liquid saturation	$\beta_t = \frac{0.66\chi^{0.81}}{1 + 0.66\chi^{0.81}}, 0.1 < \chi < 80$ $\beta_t = \frac{0.92\chi^{0.3}}{1 + 0.92\chi^{0.3}}, 0.05 < \chi < 100$ $\beta_t = \frac{4.83\chi^{0.58}}{1 + 4.83\chi^{0.58}}$ $\chi = (dP/dZ)_L / (dP/dZ)_G$
Larachi et al. 1991	External liquid saturation	$\log(1 - \beta_e) = -\frac{1.22 We_L^{0.15}}{Re_L^{0.2} X_G^{0.15}}$
Ellman et al. 1990	Non-capillary liquid saturation	$\log(\beta_{nc}) = -R \chi_G^m Re_L^n We_L^p \left(\frac{a_v d_k}{1 - \varepsilon}\right)^q$ $R = 0.16, m = 0.325, n = 0.163, p = -0.13, q = -0.163$ <p><i>for high interaction regime</i></p> $R = 0.42, m = 0.24, n = 0.14, p = -0, q = -0.14$ <p><i>for low interaction regime</i></p>

Table 3. Models for prediction of liquid holdup and saturation in trickle bed reactors (cont.)

Author	Description	Models
Al-Naimi, Al-Sudani, and Halabia 2011	Dynamic liquid holdup	$\varepsilon_{L,d} = 0.13676 Re_L'^{0.27946} Re_G^{-0.03643}$ $\times (Ga_L(1 + \frac{\Delta P/H}{\rho_L g}))^{-0.44184} We_L^{0.25458}$
Lange, Schubert, and Bauer 2005	Total liquid holdup and dynamic liquid holdup	$\varepsilon_{L,d} = 0.002(d_R/d_P)^{1.28} Re_L^{0.38}$ $\varepsilon_t = 0.16(d_R/d_P)^{0.33} Re_L^{0.14}$
M. Bazmi, Hashemabadi, and Bayat 2013	Dynamic liquid holdup	$\varepsilon_{L,d} = 0.07 + (HB)^{0.17} \exp(HB)$ $HB = \frac{We_L^{0.5}}{\chi_L} \left(\frac{\varepsilon^3}{1 - \varepsilon} \right)^{3.5} \left(\frac{Re_L}{Re_L} \right)^2$

In the last two decades, many phenomenological (semi-empirical and semi-mechanistic) models predicting the total liquid holdup instead of the dynamic liquid were proposed. Hence, it is imperative to develop a model to predict the local dynamic liquid holdup. However, as mentioned earlier, most part of the dynamic liquid flow through the void space inside the catalyst bed without contacting the solid phase. It is impractical to develop a phenomenological model for dynamic liquid holdup based on slit model or force balanced model. But still, it is possible to develop an empirical model based on the

experimental data. Some empirical models of dynamic liquid holdup or liquid saturation are listed in Table 3. All of these models predict the macro scale holdup over the whole reactor bed. Even at the same operating conditions, these models have significant errors while predicting the liquid holdup or saturation [15]. In fact, dynamic liquid spreading along the radius and axis of the catalyst bed is more significant than the overall information. In addition, most of these models are suitable for sphere catalysts and very few of them are applicable for cylindrical and trilobe catalysts. In this work, a comprehensive pseudo-3D non-linear local dynamic liquid holdup model is proposed as follows:

$$\varepsilon_{\gamma,d} = f\left(Z/H, r/R, \text{Re}_{\gamma}, \text{Re}_{\beta}, \text{We}, \chi, d_p/d_r, \varepsilon_{bed}\right) \quad (25)$$

where Z/H is observation level over total bed height, r/R is observation radius over the inner radius of reactor, d_p/d_r is the characteristic diameter of catalyst over the diameter of reactor, Re : Reynolds number, ratio of fluid inertial and viscous forces, χ : Lockhart–Martinelli number, liquid fraction of a flowing fluid, $\varepsilon_{v,ext}$: external void fraction after draining the reactor from pre-wetting. Based on the experimental data from gamma-ray CT technique, the model is proposed as:

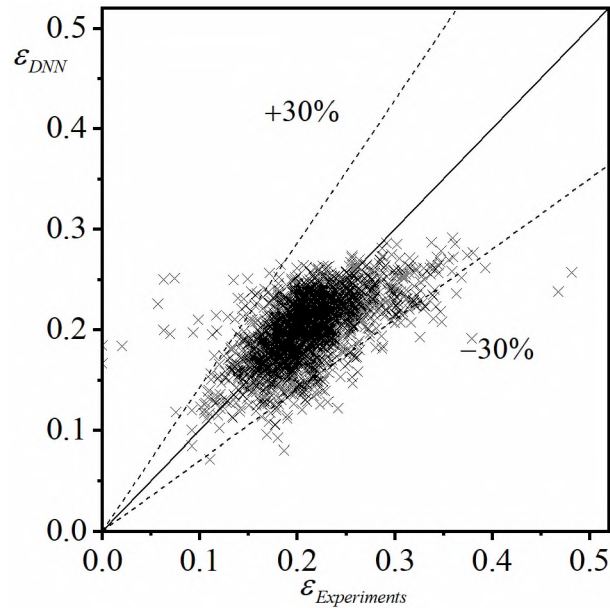
$$\begin{aligned} \varepsilon_{\gamma,d} &= A + (G)^B \exp(G^C) \\ G &= \left(\frac{z}{H}\right)^a \left(\frac{r}{R}\right)^b \left(\frac{d_p}{d_r}\right)^c \left(\frac{\varepsilon_{bed}}{1-\varepsilon_{bed}}\right)^d \left(\frac{\text{Re}_{\gamma}}{\text{Re}_{\beta}}\right)^e \chi^f \end{aligned} \quad (26)$$

After fitting the experimental data and comparing the weight of each parameter, the following model is obtained.

$$\varepsilon_{\gamma,d} = -2.5 + G \exp(G^{0.37})$$

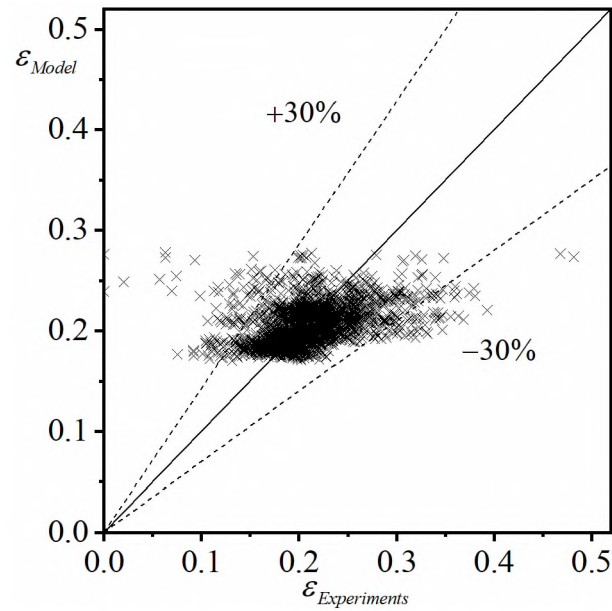
$$G = \left(\frac{z}{H}\right)^{0.002} \left(\frac{r}{R}\right)^{-0.05} \left(\frac{d_p}{d_r}\right)^{0.58} \left(\frac{\varepsilon_{bed}}{1-\varepsilon_{bed}}\right)^{-2.205} \left(\frac{\text{Re}_\gamma}{\text{Re}_\beta \chi}\right)^{-0.35} \quad (27)$$

Similarly, the Experiment vs. Prediction plot for this pseudo-3D model is shown in Figure 8 (b). Unlike DNN model, this model predicts the general trend of the dynamic liquid holdup instead of oscillation details. However, the model still shows reasonable accuracy with RMSE = 0.067.



(a) Prediction vs. experiments plot for DNN model

Figure 8. (a) Prediction vs. experiments plot for DNN model (b) Prediction vs. experiment plot for pseudo-3D model



(b) Prediction vs. experiment plot for pseudo-3D model

Figure 8. (a) Prediction vs. experiments plot for DNN model (b) Prediction vs. experiment plot for pseudo-3D model (cont.)

4.3. EVALUATION OF MODELS

In order to better evaluate the performance of these two models, the results of some showcases are discussed. In Figure 9, it can be seen that both DNN model and pseudo-3D model can predict the local dynamic liquid holdup quite well. Both of them are able to indicate the maldistribution at high levels such as at $Z/H = 0.9$. However, DNN model shows better predicting performance than the pseudo-3D model. DNN model gives more details such as the variations along the column radius and is able to distinguish the difference between different bed heights. The pseudo-3D model is able to predict the main trend of dynamic liquid distribution instead of oscillation variations. However, both of the models have quite accurate prediction performance for local dynamic liquid holdup of porous quadrilobe catalyst in a trickle bed reactor.

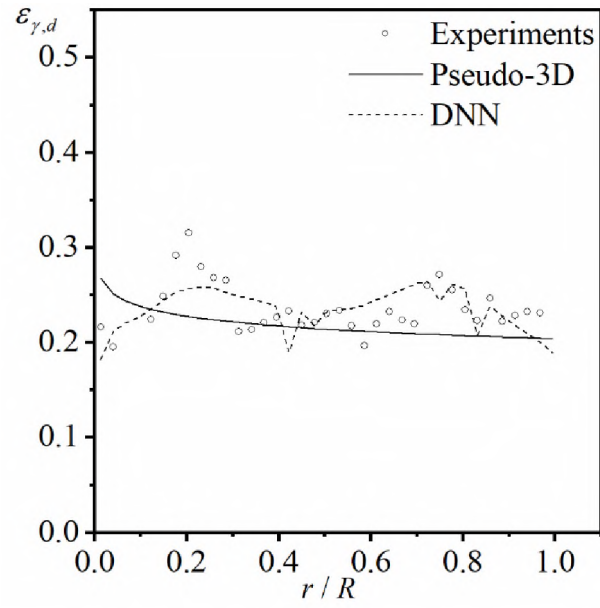
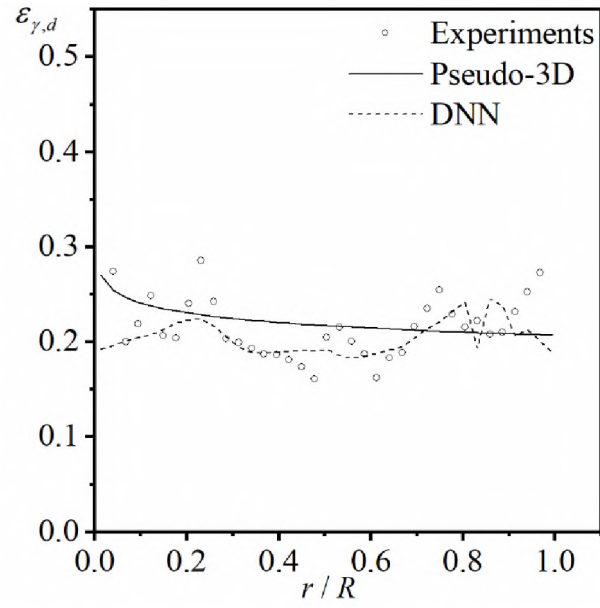
(a) $Z/H = 0.5$ (b) $Z/H = 0.7$

Figure 9. Experimental data, DNN model predictions, and pseudo-3D model predictions $Q_\beta = 0.025 \text{ Kg/m}^2\text{s}$, $Q_\gamma = 4 \text{ Kg/m}^2\text{s}$

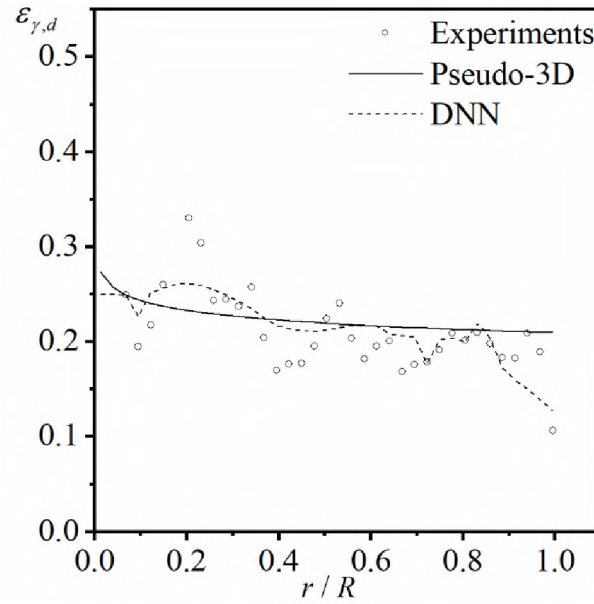
(c) $Z / H = 0.9$

Figure 9. Experimental data, DNN model predictions, and pseudo-3D model predictions $Q_{\beta} = 0.025 \text{ Kg} / \text{m}^2 \text{s}$, $Q_{\gamma} = 4 \text{ Kg} / \text{m}^2 \text{s}$ (cont.)

5. REMARKS

In this work, the dynamic liquid distribution and holdup of porous quadrilobe catalyst in a TBR are for the first time being studied using advanced Gamma-ray CT. The quantification and mapping of the maldistribution are discussed. The dynamic liquid holdup is modelled using deep neural network (DNN) as well as the pseudo-3D model. Here are the main remarks of this study:

- (1) A 32-compartment module is used to quantify the maldistribution factor. The maldistribution factors decrease from the higher level to lower level which means more uniform distribution show up at lower bed heights. There is a transition region from maldistribution to uniform distribution depending on the flowrates.

- (2) The 3D mapping figures of the dynamic liquid distribution are presented showing that there is more dynamic liquid in the center of the column at high levels. With decreasing the level height, the liquid proportion difference reduces gradually to maximize the uniform distribution.
- (3) There is no high correlation between the average dynamic liquid holdup and the bed height. If the gas flowrate increases while keeping the liquid flowrate fixed, the average dynamic liquid holdup decreases. However, if the gas flowrate is fixed, there is no dominant increasing or decreasing trend showing up.
- (4) The empirical model using Deep Neural Network and the pseudo-3D model are developed and compared with the experimental data. Both of them show high accuracy for predicting the local dynamic liquid holdup with regard to bed height, radius, and flowrates.

FUNDING

This research did not receive any specific grant from funding agencies in the public, commercial, or not-for-profit sectors.

REFERENCES

- [1] V. V. Ranade, R. V. Chaudhari, P.R. Gunjal, Introduction, Trickle Bed React. React. Eng. Appl. (2011) 1–23. <https://doi.org/10.1016/b978-0-444-52738-7.10001-4>.

- [2] E. Palmisano, P.A. Ramachandran, K. Balakrishnan, M. Al-Dahhan, Computation of effectiveness factors for partially wetted catalyst pellets using the method of fundamental solution, *Comput. Chem. Eng.* (2003). [https://doi.org/10.1016/S0098-1354\(03\)00033-4](https://doi.org/10.1016/S0098-1354(03)00033-4).
- [3] M.E. Trivizadakis, D. Giakoumakis, A.J. Karabelas, A study of particle shape and size effects on hydrodynamic parameters of trickle beds, *Chem. Eng. Sci.* 61 (2006) 5534–5543. <https://doi.org/10.1016/j.ces.2006.03.025>.
- [4] D. Janecki, A. Burghardt, G. Bartelmus, Parametric sensitivity of a CFD model concerning the hydrodynamics of trickle-bed reactor (tbr), *Chem. Process Eng. - Inz. Chem. i Proces.* 37 (2016) 97–107. <https://doi.org/10.1515/cpe-2016-0010>.
- [5] G.S. Honda, P. Gase, D.A. Hickman, A. Varma, Hydrodynamics of trickle bed reactors with catalyst support particle size distributions, *Ind. Eng. Chem. Res.* (2014). <https://doi.org/10.1021/ie403491x>.
- [6] S. Sundaresan, Role of hydrodynamics on chemical reactor performance, *Curr. Opin. Chem. Eng.* (2013). <https://doi.org/10.1016/j.coche.2013.06.003>.
- [7] R. Lange, M. Schubert, T. Bauer, Liquid holdup in trickle-bed reactors at very low liquid reynolds numbers, *Ind. Eng. Chem. Res.* 44 (2005) 6504–6508. <https://doi.org/10.1021/ie048906r>.
- [8] M. Bazmi, S.H. Hashemabadi, M. Bayat, CFD simulation and experimental study for two-phase flow through the trickle bed reactors, sock and dense loaded by trilobe catalysts, *Int. Commun. Heat Mass Transf.* 38 (2011) 391–397. <https://doi.org/10.1016/j.icheatmasstransfer.2010.11.003>.
- [9] M. Bazmi, S.H. Hashemabadi, M. Bayat, Flow Maldistribution in Dense- and Sock-Loaded Trilobe Catalyst Trickle-Bed Reactors: Experimental Data and Modeling Using Neural Network, *Transp. Porous Media.* 97 (2013) 119–132. <https://doi.org/10.1007/s11242-012-0114-x>.
- [10] G. Boccardo, F. Augier, Y. Haroun, D. Ferré, D.L. Marchisio, Validation of a novel open-source work-flow for the simulation of packed-bed reactors, *Chem. Eng. J.* 279 (2015) 809–820–820. <https://doi.org/10.1016/j.cej.2015.05.032>.
- [11] A.D. Rakotonirina, J.-Y. Delenne, M. Rolland, A. Wachs, J.L. Barrios Goicetty, A. Devouassoux, Predicting average void fraction and void fraction uncertainty in fixed beds of poly-lobed particles, *Ind. Eng. Chem. Res.* (2019). <https://doi.org/10.1021/acs.iecr.8b05557>.
- [12] A. Pavlišić, R. Ceglar, A. Pohar, B. Likozar, Comparison of computational fluid dynamics (CFD) and pressure drop correlations in laminar flow regime for packed bed reactors and columns, *Powder Technol.* (2018). <https://doi.org/10.1016/j.powtec.2018.01.029>.

- [13] F. Augier, A. Koudil, A. Royon-Lebeaud, L. Muszynski, Q. Yanouri, Numerical approach to predict wetting and catalyst efficiencies inside trickle bed reactors, *Chem. Eng. Sci.* (2010). <https://doi.org/10.1016/j.ces.2009.06.027>.
- [14] F. Mousazadeh, Hot spot formation in trickle bed reactors, 2013.
- [15] V. V. Ranade, R. V. Chaudhari, P.R. Gunjal, *Hydrodynamics and Flow Regimes*, 2011. <https://doi.org/10.1016/b978-0-444-52738-7.10002-6>.
- [16] C. Marcandelli, A.S. Lamine, J.R. Bernard, G. Wild, Liquid Distribution in Trickle-Bed Reactor, *Oil Gas Sci. Technol.* (2000). <https://doi.org/10.2516/ogst:2000029>.
- [17] Z. Solomenko, Y. Haroun, M. Fourati, F. Larachi, C. Boyer, F. Augier, Liquid spreading in trickle-bed reactors: Experiments and numerical simulations using Eulerian-Eulerian two-fluid approach, *Chem. Eng. Sci.* 126 (2015) 698–710. <https://doi.org/10.1016/j.ces.2015.01.013>.
- [18] A. SAPKOTA, M. TAKEI, M. NISHIO, J. HARUTA, T. EDA, Experimental Study on Liquid Spread and Maldistribution in the Trickle Bed Reactor Using Electrical Resistance Tomography, *J. Power Energy Syst.* 7 (2013) 94–105. <https://doi.org/10.1299/jpes.7.94>.
- [19] G. Liu, J. an Lan, Y. Cao, Z. Huang, Z. Cheng, Z. Mi, New insights into transient behaviors of local liquid-holdup in periodically operated trickle-bed reactors using electrical capacitance tomography (ECT), *Chem. Eng. Sci.* 64 (2009) 3329–3343. <https://doi.org/10.1016/j.ces.2009.04.008>.
- [20] C. Boyer, A. Koudil, P. Chen, M.P. Dudukovic, Study of liquid spreading from a point source in a trickle bed via gamma-ray tomography and CFD simulation, in: *Chem. Eng. Sci.*, 2005. <https://doi.org/10.1016/j.ces.2005.03.049>.
- [21] M. Schubert, G. Hessel, C. Zippe, R. Lange, U. Hampel, Liquid flow texture analysis in trickle bed reactors using high-resolution gamma ray tomography, *Chem. Eng. J.* (2008). <https://doi.org/10.1016/j.cej.2007.10.006>.
- [22] Z. Kuzeljevic, *Hydrodynamics of Trickle Bed Reactors: Measurements and Modeling*, Washington University, 2010. <http://dx.doi.org/10.7936/K7WQ01V5>.
- [23] M.K. Al Mesfer, A.J. Sultan, M.H. Al-Dahhan, Impacts of dense heat exchanging internals on gas holdup cross-sectional distributions and profiles of bubble column using gamma ray Computed Tomography (CT) for FT synthesis, *Chem. Eng. J.* 300 (2016) 317–333. <https://doi.org/10.1016/j.cej.2016.04.075>.
- [24] L.B. Møller, C. Halken, J.A. Hansen, J. Bartholdy, Liquid and gas distribution in trickle-bed reactors, *Ind. Eng. Chem. Res.* (1996). <https://doi.org/10.1021/ie950478p>.

- [25] S.T. Sie, R. Krishna, Process development and scale up: III. Scale-up and scale-down of trickle bed processes, *Rev. Chem. Eng.* (1998). <https://doi.org/10.1515/REVCE.1998.14.3.203>.
- [26] R. Varma, S. Bhusarapu, J.A. O'Sullivan, M.H. Al-Dahhan, A comparison of alternating minimization and expectation maximization algorithms for single source gamma ray tomography, *Meas. Sci. Technol.* 19 (2008). <https://doi.org/10.1088/0957-0233/19/1/015506>.
- [27] J.A. O'Sullivan, J. Benac, Alternating minimization algorithms for transmission tomography, *IEEE Trans. Med. Imaging.* 26 (2007) 283–297. <https://doi.org/10.1109/TMI.2006.886806>.
- [28] A.I. Georgevici, M. Terblanche, Neural networks and deep learning: a brief introduction, *Intensive Care Med.* (2019). <https://doi.org/10.1007/s00134-019-05537-w>.
- [29] J. Schmidhuber, Deep Learning in neural networks: An overview, *Neural Networks.* 61 (2015) 85–117. <https://doi.org/10.1016/j.neunet.2014.09.003>.
- [30] J. Heaton, An empirical analysis of feature engineering for predictive modeling, in: *Conf. Proc. - IEEE SOUTHEASTCON*, 2016. <https://doi.org/10.1109/SECON.2016.7506650>.
- [31] A. Shaikh, M. Al-Dahhan, Development of an artificial neural network correlation for prediction of overall gas holdup in bubble column reactors, *Chem. Eng. Process. Process Intensif.* (2003). [https://doi.org/10.1016/S0255-2701\(02\)00209-X](https://doi.org/10.1016/S0255-2701(02)00209-X).
- [32] M. Kuhn, K. Johnson, *Applied predictive modeling*, 2013. <https://doi.org/10.1007/978-1-4614-6849-3>.
- [33] G. James, D. Witten, T. Hastie, R. Tibshirani, *An Introduction to Statistical Learning*, 2013. <https://doi.org/10.1007/978-1-4614-7138-7>.
- [34] T. Dozat, Incorporating Nesterov Momentum into Adam, *ICLR Work.* (2016).
- [35] J.D. Olden, M.K. Joy, R.G. Death, An accurate comparison of methods for quantifying variable importance in artificial neural networks using simulated data, *Ecol. Modell.* (2004). <https://doi.org/10.1016/j.ecolmodel.2004.03.013>.
- [36] J. Heaton, S. McElwee, J. Fraley, J. Cannady, Early stabilizing feature importance for TensorFlow deep neural networks, in: *Proc. Int. Jt. Conf. Neural Networks*, 2017. <https://doi.org/10.1109/IJCNN.2017.7966442>.
- [37] V. Specchia, G. Baldi, Pressure drop and liquid holdup for two phase concurrent flow in packed beds, *Chem. Eng. Sci.* (1977). [https://doi.org/10.1016/0009-2509\(77\)87008-5](https://doi.org/10.1016/0009-2509(77)87008-5).

- [38] A. Burghardt, G. Bartelmus, M. Jaroszyński, A. Kołodziej, Hydrodynamics and mass transfer in a three-phase fixed-bed reactor with cocurrent gas-liquid downflow, *Chem. Eng. J. Biochem. Eng. J.* (1995). [https://doi.org/10.1016/0923-0467\(94\)02956-3](https://doi.org/10.1016/0923-0467(94)02956-3).
- [39] W.J.A. Wammes, J. Middelkamp, W.J. Huisman, C.M. DeBass, K.R. Westerterp, Hydrodynamics in a cocurrent gas-liquid trickle bed at elevated pressures, *AIChE J.* (1991). <https://doi.org/10.1002/aic.690371210>.
- [40] B.I. Morsi, N. Midoux, A. Laurent, J.C. Charpentier, Hydrodynamics and interfacial areas in downward cocurrent gas-liquid flow through fixed beds. Influence of the nature of the liquid, *Int. Chem. Eng.* (1982).
- [41] F. Larachi, A. Laurent, N. Midoux, G. Wild, Experimental study of a trickle-bed reactor operating at high pressure: two-phase pressure drop and liquid saturation, *Chem. Eng. Sci.* (1991). [https://doi.org/10.1016/0009-2509\(91\)85051-X](https://doi.org/10.1016/0009-2509(91)85051-X).
- [42] M.J. Ellman, N. Midoux, G. Wild, A. Laurent, J.C. Charpentier, A new, improved liquid hold-up correlation for trickle-bed reactors, *Chem. Eng. Sci.* (1990). [https://doi.org/10.1016/0009-2509\(90\)87046-U](https://doi.org/10.1016/0009-2509(90)87046-U).
- [43] S.A. Al-Naimi, F.T.J. Al-Sudani, E.K. Halabia, Hydrodynamics and flow regime transition study of trickle bed reactor at elevated temperature and pressure, *Chem. Eng. Res. Des.* 89 (2011) 930–939. <https://doi.org/10.1016/j.cherd.2010.11.008>.
- [44] M. Bazmi, S.H. Hashemabadi, M. Bayat, Extrudate Trilobe Catalysts and Loading Effects on Pressure Drop and Dynamic Liquid Holdup in Porous Media of Trickle Bed Reactors, *Transp. Porous Media.* 99 (2013) 535–553. <https://doi.org/10.1007/s11242-013-0199-x>.

II. DEVELOPMENT OF A HYBRID PRESSURE DROP AND LIQUID HOLDUP PHENOMENOLOGICAL MODEL FOR TRICKLE BED REACTORS BASED ON TWO-PHASE VOLUME AVERAGED EQUATIONS

Binbin Qi¹, Sebastián Uribe¹, Muthanna Al-Dahhan^{1,2*}

¹ Chemical and Biochemical Engineering Department, Missouri University of Science and Technology, Rolla, MO 65409 USA

² Mining and Nuclear Engineering Department, Missouri University of Science and Technology, Rolla, MO 65409, USA

* Corresponding author: aldahhanm@mst.edu

ABSTRACT

A model with a high predictive quality to estimate pressure drops and liquid holdups in trickle bed reactors (TBR), is yet necessary to assist in design, up scaling and implementation of new processes tasks. The currently available models to estimate pressure drops and liquid holdups on trickle bed reactors (TBR) exhibit important deviations, which arise uncertainties in their applicability. To overcome the limitations in prediction deviations in the currently available models, a new model is developed based on the volume averaged two-phase transport equations in a porous media, as developed by Whitaker [1]. In order to develop a model that could simultaneously predict pressure drops and liquid holdup with a high accuracy, the developed model was coupled with a modification of the extended slit model reported on literature, leading to a new hybrid model with enhanced predictability. Experimentally determined pressure drops and liquid holdup on a column of 0.14 m internal diameter and 2 m in height, packed with different extrudate geometries, cylinders, trilobes and quadrilobes, were used to determine the model

parameters and to verify the quality of the proposed hybrid model predictions. The developed model, when compared with the experimentally determined data of pressure drops showed a mean squared error (MSE) of 0.89%, 2.31% and 1.22% for cylinders, trilobes and quadrilobes particles, respectively; while the liquid holdups were predicted with an MSE of 0.03%, 0.16% and 0.01% for cylinders, trilobes and quadrilobes particles, respectively.

Keywords: Trickle Bed Reactors; Two-Phase Hydrodynamics; Pressure Drop Model; Holdup Model

1. INTRODUCTION

Over the past decades, vast contributions on the study of trickle bed reactors (TBR) hydrodynamics [2–8] and mass transfer [9–14] phenomena can be found in the literature. In these contributions, it has been recognised that the hydrodynamics of TBR, and therefore, the multiphase interactions, play a determining role in the mass and heat transfer phenomena, kinetics and performance throughput of these systems. Hence, vast contributions in literature have devoted to the characterization and understanding of the TBR hydrodynamics, focusing on determining/measuring and predicting the key hydrodynamic parameters required for design and scaling of these systems, such as pressure drops and overall liquid holdup $(\varepsilon_\gamma = V_\gamma / V_{total})$. With different approaches, and using different experimental techniques, the key macroscopic hydrodynamic parameters have been determined, and hence, extensive information is available in reported literature [2,4,15–18].

The main challenge that remains is the development of predictive models that can estimate such hydrodynamic parameters and that can be useful in design and scale-up of multiphase reactors. In this sense, two main kind of models have been developed to predict pressure drops and holdups in TBR, *i.*) empirical models and *ii.*) phenomenological models. The empirical models are expressions that fit experimental observations as a function of parameters related to some of the fluids' physical properties, operation conditions, and bed characteristics, such as bed tortuosity and porosity, without a fundamental physical reason [18–20]. On the other hand, the phenomenological models also seek to find a relationship between the system physical and geometrical characteristics and the observed pressure drops, but based on a physical principle, such as a force balance [21–24], or a mechanistic concept and its fundamental principle, such as the relative permeability concept [25]. However, these models are not fully mechanistic (theoretical) models and require the estimation of closure parameters according to experimental observations, which means that phenomenological models are semi-empirical and are also constrained by experimental observations.

Hence, it can be seen that an empirical model, despite of being useful and have a good predictive quality for a particular set of data and conditions that are developed for, these models will be fully constrained to the range of those experimental observations. While a phenomenological model could be used to extrapolate outside the range of the experimental observations that are used to validate them, even though the uncertainty on such predictions cannot be *a priori* assessed, and could be limited by the assumptions made in the derivation of the model. Another important limitation in the use of the empirical and phenomenological models reported in the literature is that there is limited information of

the particle shape effects over the predictive capability of the models. In fact, a vast number of experimental studies have been conducted for spherical particles, and thus the determined closure parameters for the models should be considered to be constrained to such geometry [26]. A fully mechanistic model could overcome such limitations, however, due to the highly complex multiphase and multiscale nature of these TBR systems, the development of such model is a remaining challenge to overcome.

On a recent study by Al-Ani [26], a comprehensive comparison between two phenomenological models, slit [21] and double-slit [23], and an empirical model reported by Larachi *et al* [18] against experimentally determined pressure drops and liquid holdup on a TBR of 6 inch internal diameter, packed with spheres, cylinders, trilobes and quadrilobes was presented. The results showed that the double-slit model has the highest predictive quality between those models, with average relative error in pressure drop predictions of 55.9%, 31.0%, 25.51% and 14.78% for spheres, cylinders, trilobes and quadrilobes, respectively. The overall average relative error for the models was found to be 31.8%, 35.26% and 37.5% for double-slit, slit and the empirical model, respectively. These results suggest that the current understanding and predictive quality of the available models is limited, and that a new model that has an enhanced predictability is yet required.

An alternative to deal with the complexity of the two-phase flow through the porous media that represent the bed of the TBR, is the use of the method of Volume Averaging [27]. This method seeks to develop macroscopic transport equation by applying averaging theorems on the pointwise transport equations on a representative porous media [28]. The averaging of the equations also lead to expression to estimate the effective transport coefficients based on a closure problem that captures the essential information of the

porous structure [29]. Whitaker developed the averaging procedure for the two-phase flow on a porous media [1], and determined that the averaged macroscopic transport equations for such case include a phase permeability tensor (\mathbf{K}_i) and a viscous drag tensor (\mathbf{K}_{ij}) that account for the multiphase interaction within the pores. To estimate these parameters, a closure boundary values problem was developed, and an extensive discussion on the mathematical development was presented. However, no results of the closure problem were presented, mainly due to the mathematical and computation procedure complexity. Hence, despite of the advantages of this rigorous mechanistic development, it also arises further challenges in the computation procedure.

Thus, so far, there is no theory or model that can fully describe the hydrodynamic behaviour of TBR in a straightforward way. The current descriptions of the TBR hydrodynamics are either the use of empirical and phenomenological models with high deviations, or the use of rigorous models with high computational requirements.

Therefore, in this work, an effort is conducted to develop a new highly predictive phenomenological model to estimate pressure drops and liquid holdup on trickle bed reactors. The developed phenomenological model is based on results of the volume averaging of a two-phase flow through porous media, as developed by Whitaker [1]. The closure parameters are estimated for different commercial extrudate particle shapes of cylinders, trilobes and quadrilobes, for a wide range of liquid and gas superficial inlet velocities, as reported by Al-Ani [26]. In this way, the developed model will have a mechanistic development on the description of the governing equations and will be closed by empirical models that overcome the high computational cost of the fully mechanistic model. To provide closure for the developed model to enable the simultaneous prediction

of pressure drop and liquid holdup, the developed model is coupled with a modification of the extended slit model available in the literature [30]. In this way, a new hybrid highly predictive model for simultaneous prediction of liquid holdup and dimensionless pressure drop is developed.

2. EXPERIMENTAL SETUP

The experimental setup, as previously reported by Al-Ani [26], consists of a column of 6-inch internal diameter and 2 m in length, packed with different industrial extruded catalysts, cylinders, trilobes and quadrilobes. Experiments were conducted at seven different superficial gas inlet velocities $\left(\left\langle v_{\beta} \right\rangle_0\right)$, ranging from 0.03 – 0.27 m/s, and seven different superficial liquid inlet velocities $\left(\left\langle v_{\gamma} \right\rangle_0\right)$, ranging from 0.004 – 0.016 m/s. The geometrical features of the experimental setup and operation conditions are summarized on Table 1.

Pressure drops were determined on the system by a high-frequency differential pressure transducer (DPT) mounted on the column wall. A series of automated solenoid valves that allowed to stop the flow in/out of the column, and a digital load cell equipped with high sensitivity sensors to measure changes in the column weight, were used to determine the overall liquid holdup by the drainage method [26].

Further details of the experimental setup and the implemented measurement techniques can be seen in Figure 1 and can be found elsewhere [26].

Table 1. Geometrical properties of the experimental setup and operation conditions

Geometry	
$D_C [cm]$	14
$L_C [cm]$	200
Operation conditions	
$\langle V_\beta \rangle_0 [m/s]$	0.03 – 0.27
$\langle V_\gamma \rangle_0 [m/s]$	0.004 – 0.016
$P_0 [atm]$	1

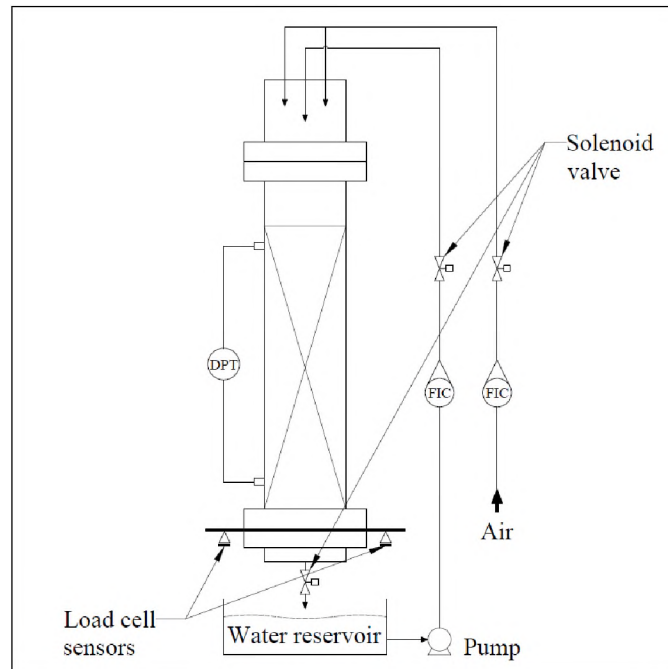


Figure 1. Details of the experimental setup

3. DEVELOPMENT OF THE MODEL

3.1. VOLUME AVERAGED EQUATIONS

Considering an averaging volume \mathcal{V} in a representative region within the bed that contains a representative amount of the three phases, solid (σ -phase), gas (β -phase) and liquid (γ -phase), (as shown in Figure 2) the two-phase flow averaged transport equations can be described by Equations (1) to (4), according to the previous developments by Whitaker [1].

$$\langle \mathbf{v}_\beta \rangle = -\frac{\mathbf{K}_\beta}{\mu_\beta} \cdot \left(\nabla \langle P_\beta \rangle^\beta - \rho_\beta \mathbf{g} \right) + \mathbf{K}_{\beta\gamma} \cdot \langle \mathbf{v}_\gamma \rangle \quad (1)$$

$$\frac{\partial \varepsilon_\beta}{\partial t} + \nabla \cdot \langle \mathbf{v}_\beta \rangle = 0 \quad (2)$$

$$\langle \mathbf{v}_\gamma \rangle = -\frac{\mathbf{K}_\gamma}{\mu_\gamma} \cdot \left(\nabla \langle P_\gamma \rangle^\gamma - \rho_\gamma \mathbf{g} \right) + \mathbf{K}_{\gamma\beta} \cdot \langle \mathbf{v}_\beta \rangle \quad (3)$$

$$\frac{\partial \varepsilon_\gamma}{\partial t} + \nabla \cdot \langle \mathbf{v}_\gamma \rangle = 0 \quad (4)$$

where the Equations (1) and (3) represent the volume averaged equations of motion for gas (β) and liquid (γ) phase, respectively; and Equations (2) and (4) represent the volume averaged continuity equations for gas (β) and liquid (γ) phase, respectively. In these, $\langle \mathbf{v}_i \rangle$ represents the superficial phase average velocity vector, and $\langle P_i \rangle^i$ represents the intrinsic phase average pressure [1,31].

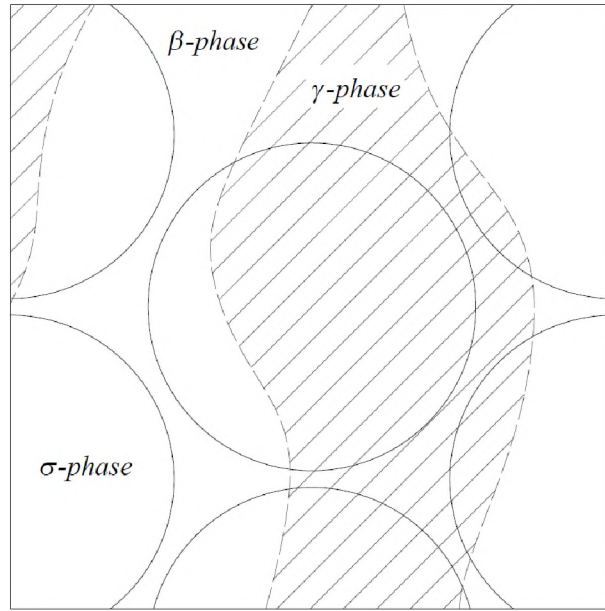


Figure 2. Representative porous media within the bed

The superficial phase average of a random variable (ψ) can be defined according to Equation (5); while the intrinsic phase average of a random variable is defined by Equation (6). These two quantities can be related as shown in Equation (7) [27,31].

$$\langle \psi_i \rangle = \frac{1}{\mathcal{V}} \int_{V_i} \psi_i dV \quad (5)$$

$$\langle \psi_i \rangle^i = \frac{1}{V_i} \int_{V_i} \psi_i dV \quad (6)$$

$$\langle \psi_i \rangle = \varepsilon_i \langle \psi_i \rangle^i \quad (7)$$

where \mathcal{V} is the averaging volume, and ε_i is the overall holdup of each phase in the representative volume ($\varepsilon_i = V_i / \mathcal{V}$). This overall holdup represents both the static and dynamic phase holdup.

The volume averaged equations described by Equations (1) and (3) resemble Darcy's law transport equation with an additional term that involves the second phase velocity. In this sense, it can be identified that the tensors \mathbf{K}_β and \mathbf{K}_γ are the permeability tensors for the gas and liquid phase, respectively; while the additional terms $\mathbf{K}_{\beta\gamma}$ and $\mathbf{K}_{\gamma\beta}$ are interaction terms. These interaction terms arise from the superficial averaging of the pointwise transport equation on the representative porous media and can be interpreted as viscous drag tensors.

Considering that on a trickle bed reactor (TBR) the pressure gradient is mainly generated on the axial direction, and therefore the radial variations of the pressure can be discarded as per the scale estimate of Equation (8), then, on a difference form, the pressure gradient can be approximated as per Equation (9). It should be kept in mind that the intrinsic phase average pressure $\left(\langle P_i \rangle^i\right)$ is a variable that represents the partial pressure of the phase within the porous media. Hence, if a total pressure of the system is desired to be estimated, then, the intrinsic phase average pressures should be added as shown in Equation (10). To estimate the gradient of Equation (10), it can be considered that the average phase holdup within the averaging volume remains constant, and then the terms involving the gradient of the holdup can be discarded, leading to Equation (11). Accordingly, the total pressure drop can be estimated by Equation (12).

$$\mathbf{O}\left(\frac{\partial \langle P_i \rangle^i}{\partial z}\right) \gg \left[\mathbf{O}\left(\frac{\partial \langle P_i \rangle^i}{\partial x}\right) - \mathbf{O}\left(\frac{\partial \langle P_i \rangle^i}{\partial x}\right) \right] \quad (8)$$

$$\nabla \langle P_i \rangle^i = \frac{\Delta \langle P_i \rangle^i}{\Delta z} = \frac{\Delta \langle P_i \rangle^i}{L_c} \quad (9)$$

$$\langle P \rangle = \varepsilon_\beta \langle P_\beta \rangle^\beta + \varepsilon_\gamma \langle P_\gamma \rangle^\gamma \quad (10)$$

$$\begin{aligned} \nabla \langle P \rangle &= \nabla \left(\varepsilon_\beta \langle P_\beta \rangle^\beta \right) + \nabla \left(\varepsilon_\gamma \langle P_\gamma \rangle^\gamma \right) \\ &= \varepsilon_\beta \nabla \langle P_\beta \rangle^\beta + \varepsilon_\gamma \nabla \langle P_\gamma \rangle^\gamma + \langle P_\beta \rangle^\beta \cancel{\nabla \varepsilon_\beta} + \langle P_\gamma \rangle^\gamma \cancel{\nabla \varepsilon_\gamma} \end{aligned} \quad (11)$$

$$\frac{\Delta \langle P \rangle}{L_C} = \frac{\varepsilon_\beta \Delta \langle P_\beta \rangle^\beta + \varepsilon_\gamma \Delta \langle P_\gamma \rangle^\gamma}{L_C} \quad (12)$$

Equations (1) and (3) show the terms that characterize the phase permeability and viscous drag tensors are the ones contained in the main diagonal $\left(\mathbf{K}_\gamma = \sum_j \sum_i K_{ij}^\gamma \delta_{ij} \delta_i \delta_j \right)$.

Hence, assuming that the porous media generated in the catalytic bed can be considered as isotropic, and that therefore, the viscous drag force is also isotropic, then, the phase permeability and viscous drag tensors can be approximated as isotropic tensors according to Equation (13) and (14), respectively.

$$\mathbf{K}_\beta = \sum_j \sum_i K_{ij}^\beta \delta_{ij} \delta_i \delta_j \approx K_\beta \mathbf{I}; \quad \mathbf{K}_\gamma = \sum_j \sum_i K_{ij}^\gamma \delta_{ij} \delta_i \delta_j \approx K_\gamma \mathbf{I} \quad (13)$$

$$\mathbf{K}_{\beta\gamma} = \sum_j \sum_i K_{ij}^{\beta\gamma} \delta_{ij} \delta_i \delta_j \approx K_{\beta\gamma} \mathbf{I}; \quad \mathbf{K}_{\gamma\beta} = \sum_j \sum_i K_{ij}^{\gamma\beta} \delta_{ij} \delta_i \delta_j \approx K_{\gamma\beta} \mathbf{I} \quad (14)$$

According to these assumptions and estimates, Equations (1) and (3) can be rearranged as shown in Equations (15) and (16).

$$\frac{\Delta \langle P_\beta \rangle^\beta}{L_C} = - \frac{\mu_\beta \left(\langle \mathbf{v}_\beta \rangle - K_{\beta\gamma} \langle \mathbf{v}_\gamma \rangle \right)}{K_\beta} + \rho_\beta \mathbf{g} \quad (15)$$

$$\frac{\Delta \langle P_\gamma \rangle^\gamma}{L_C} = - \frac{\mu_\gamma \left(\langle \mathbf{v}_\gamma \rangle - K_{\gamma\beta} \langle \mathbf{v}_\beta \rangle \right)}{K_\gamma} + \rho_\gamma \mathbf{g} \quad (16)$$

Estimating the total dimensionless pressure drop $(\Delta\langle P\rangle/L_c\rho_\gamma\mathbf{g})$ by adding Equations (15) and (16) according to Equation (12), and rewriting the volume fractions in terms of the liquid holdup $(\varepsilon_B = \varepsilon_\beta + \varepsilon_\gamma)$, leads to Equation (17). Solving Equation (17) to estimate the liquid holdup leads to Equation (18). In these correlations/models described by Equations (17) and (18) it is assumed that the superficial phase average velocity can be characterized by the superficial phase inlet velocity $(\langle v_i \rangle_0)$.

$$\frac{\Delta\langle P\rangle}{\rho_\gamma\mathbf{g}L_c} = (\varepsilon_B - \varepsilon_\gamma) \left[\frac{\mu_\beta(K_{\beta\gamma} - 1)}{K_\beta\rho_\gamma\mathbf{g}} \langle v_\beta \rangle_0 + \frac{\rho_\beta}{\rho_\gamma} \right] + \varepsilon_\gamma \left[\frac{\mu_\gamma(K_{\gamma\beta} - 1)}{K_\gamma\rho_\gamma\mathbf{g}} \langle v_\gamma \rangle_0 + 1 \right] \quad (17)$$

$$\varepsilon_\gamma = \frac{\frac{\Delta\langle P\rangle}{\rho_\gamma\mathbf{g}L_c} - \varepsilon_B \left[\frac{\mu_\beta(K_{\beta\gamma} - 1)}{K_\beta\rho_\gamma\mathbf{g}} \langle v_\beta \rangle_0 + \frac{\rho_\beta}{\rho_\gamma} \right]}{1 + \frac{\mu_\gamma(K_{\gamma\beta} - 1)}{K_\gamma\rho_\gamma\mathbf{g}} \langle v_\gamma \rangle_0 - \frac{\mu_\beta(K_{\beta\gamma} - 1)}{K_\beta\rho_\gamma\mathbf{g}} \langle v_\beta \rangle_0 - \frac{\rho_\beta}{\rho_\gamma}} \quad (18)$$

where ε_B is the bed average porosity $(\varepsilon_B = 1 - V_\sigma/\mathcal{V})$.

The expressions shown in Equation (17) and (18) can be used to estimate the overall pressure drop and liquid holdup, provided that one of these parameters is known or using a second expression as closure to estimate the other parameter, such as using another mechanistic expression to estimate liquid holdup or pressure drop leading to a hybrid model. Further discussion on the application of these expressions will be presented on the next section.

Equation (17) and (18) require then the estimation of the closure parameters K_β , K_γ , $K_{\beta\gamma}$ and $K_{\gamma\beta}$. These parameters can be estimated by solving the closure problem presented by Whitaker [1], which implies a high computational complexity. In a different

approach, experimental data of pressure drop and overall liquid holdup can be used to estimate such parameters. In this last approach, the main challenge is determining the relationship between the textural characteristics of the bed with the determined parameters. In this work, an empirical development is presented to estimate the viscous drag parameters.

3.2. PHASE PERMEABILITY ESTIMATION

We will first direct our attention to estimate the Darcy-like closure parameters, the phase permeability K_β and K_γ . These parameters incorporate the resistances generated by the porous media to the momentum transfer, which implicitly include the textural characteristics, such as the tortuosity and bed porosity.

It is possible to state that, according to several experimental observations, the permeability mostly depends on the porous media characteristics rather than on the fluid physical properties or the phase superficial velocities [32–34]. In this sense, it is safe to assume that the permeability of each phase (K_β and K_γ) would be the same, or that their order of magnitude would be within the same range. Hence, in the current development the gas and liquid phase permeability will be considered to be the same ($K_\beta = K_\gamma = K$)

From the early pioneering work of Kozeny [35], Carman [36] developed a modified correlation to estimate the permeability of a porous media which relies only on information regarding the porous media structure. According to these works, the permeability coefficient can be estimated according to Equation (19), where d is a characteristic dimension of the media, which can be estimated by Equation (20); and θ is the Kozeny

parameter, which is a closure parameter depend on the pore structure of the bed [32–34]. For the current development, the Kozeny parameter is set as $\theta = 5$, according to Whitaker [27].

$$K = \frac{\varepsilon_B^3}{36\theta(1-\varepsilon_B)^2} d^2 \quad (19)$$

$$d = \frac{d_e \varepsilon_B}{1-\varepsilon_B}; d_e = \left(\frac{6}{\pi} V_p \right)^{1/3} \quad (20)$$

where, d_e is the volume-equivalent sphere diameter.

Despite that the correlation described by Equation (19) is an empirical expression, it has been extensively used to estimate permeabilities of porous media, and its predictability has been recognized to be within acceptable ranges [27,34]. Nonetheless, it should be kept in mind that for the current development this represents an approximation, and that further efforts should be taken in the development of a mechanistic (or a phenomenological) model to estimate the actual phase permeability. The underlying assumption in the present work is that, according to the experimental observations reported in literature [32–34], and the scale estimate derived by Whitaker [1] ($K_i \sim \mathbf{O}(\varepsilon_i^3 l^2)$), it could be expected that the actual phase permeability is within the same order of magnitude as the predicted by Kozeny-Carman correlation (Equation (19)).

Table 2 shows the estimated permeabilities for each of the particle shapes used in this work, as well as other geometrical characteristics of the solid particles and bed, such as the bed porosity (ε_B), volume-equivalent diameter (d_e) and sphericity (φ).

Table 2. Geometrical properties of the solid particles and bed

Geometry	ε_B	$d_e [mm]$	ϕ	$K [m^2]$	E_1	E_2
Cylinders	0.451	4.13	0.82	2.8424×10^{-8}	838.9	3.04
Trilobes	0.526	3.93	0.62	5.5579×10^{-8}	1421.34	2.32
Quadrilobes	0.544	3.35	0.72	1.9976×10^{-8}	629.44	0.89

3.3. VISCOUS DRAG PARAMETER ESTIMATION

With the phase permeability approximated by Equation (19), the only remaining parameter to estimate the pressure drop and liquid holdup as per the model shown in Equations (17) and (18) are the viscous drag parameters, $K_{\beta\gamma}$ and $K_{\gamma\beta}$. These terms represent the viscous drag of one fluid upon the other through their interphase. Hence, these parameters incorporate, up to a certain extent, the multiphase interactions.

Currently, there is no available experimental or theoretical data regarding the determination of the viscous drag parameters. Therefore, considering the expressions in Equations (17) and (18), and the estimate of Equation (19), experimental data of pressure drops and holdup can be used to determine these parameters. Figures 3a-c show the measured dimensionless pressure drops $(\Delta P / \rho_\gamma g L_C)$ against the measured liquid holdup of the experimental setup described in the previous section for the column packed with cylinder, trilobes and quadrilobes particles, respectively, at the different superficial liquid and gas inlet velocities. A random selection of this data will be selected to estimate the viscous drag parameters by fitting Equation (17) to the experimental observations.

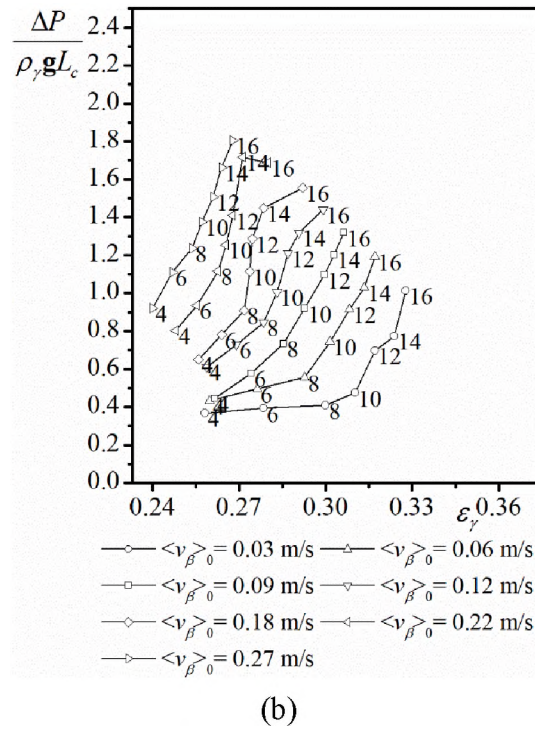
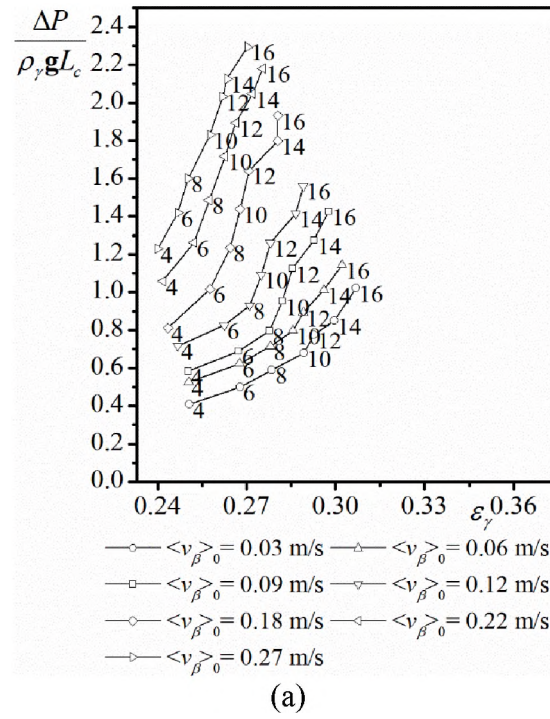


Figure 3. Experimentally determined pressure drop with labels showing the corresponding superficial liquid inlet velocity in mm/s, (a) Cylinders, (b) Trilobes, (c) Quadrilobes

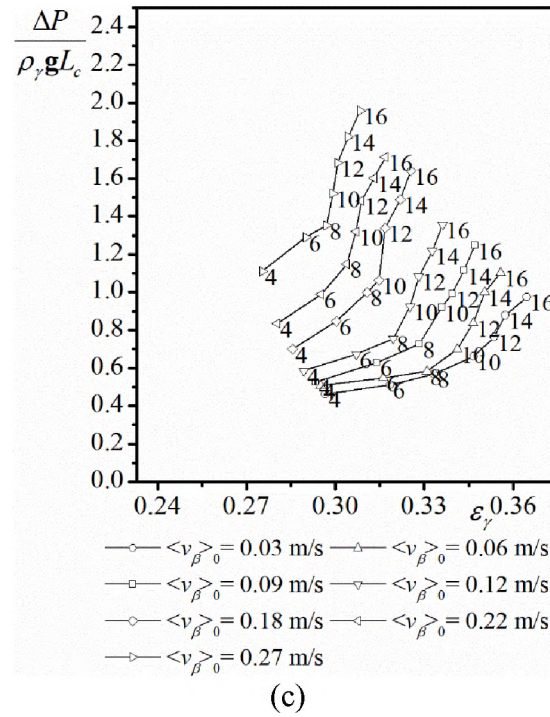


Figure 3. Experimentally determined pressure drop with labels showing the corresponding superficial liquid inlet velocity in mm/s, (a) Cylinders, (b) Trilobes, (c) Quadrilobes (cont.)

It could be intuitive to assume that $K_{\beta\gamma} = -K_{\gamma\beta}$, however there are no arguments that support such assumption. Therefore, both parameters need to be estimated, and a relation between them cannot be *a priori* expected. Also, since these parameters capture, in a certain extent, the multiphase interaction and the interphase phenomena, it can be expected that these parameters are not constants but rather depend on the phases velocities, $K_{\beta\gamma} = K_{\beta\gamma}(\langle \mathbf{v}_\beta \rangle, \langle \mathbf{v}_\gamma \rangle)$ and $K_{\gamma\beta} = K_{\gamma\beta}(\langle \mathbf{v}_\beta \rangle, \langle \mathbf{v}_\gamma \rangle)$. Since the primary fluid phase in the trickle flow regime of the TBR is the gas phase, and according to the experimental results that will be presented in the forthcoming, it was considered that the viscous drag parameters depend on the gas velocity, so that $K_{\beta\gamma} = K_{\beta\gamma}(\langle \mathbf{v}_\beta \rangle)$ and $K_{\gamma\beta} = K_{\gamma\beta}(\langle \mathbf{v}_\beta \rangle)$.

Figures 4a-c show the estimated viscous drag parameters ($K_{\beta\gamma}$, $K_{\gamma\beta}$) using the randomly selected measured dimensionless pressure drops shown in Figures 3a-c, for the column packed with cylinder, trilobes and quadrilobes particles, respectively, as a function of the superficial gas inlet velocity. The fitting of these parameters was performed by using a randomly selected set of experimentally determined pressure drop data. The remaining experimental measurements were used to validate the model predictions. From Figures 4a-c, it can be seen that in all cases, the viscous drag parameters increase when the superficial gas inlet velocity increases; also, it can be seen that the gas-liquid ($K_{\beta\gamma}$) and liquid-gas ($K_{\gamma\beta}$) parameters are not equal ($K_{\beta\gamma} \neq K_{\gamma\beta}$), nor is their absolute value ($K_{\beta\gamma} \neq -K_{\gamma\beta}$).

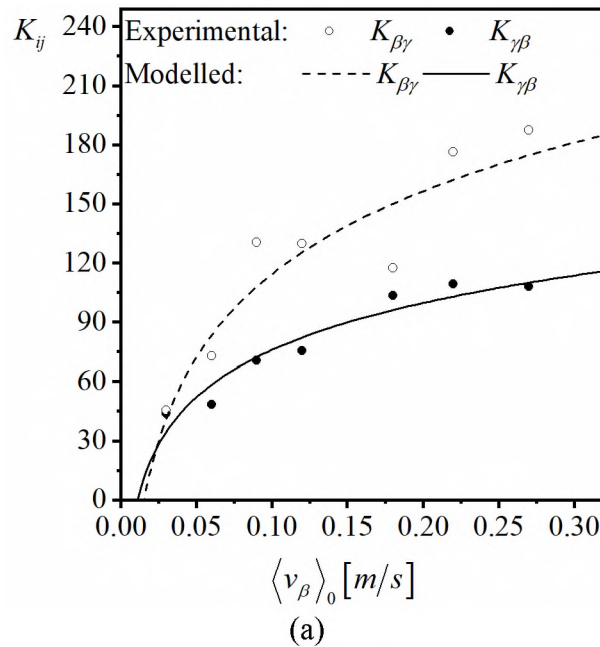


Figure 4. Experimentally estimated and modelled viscous drag parameter (a) Cylinders, (b) Trilobes, (c) Quadrilobes

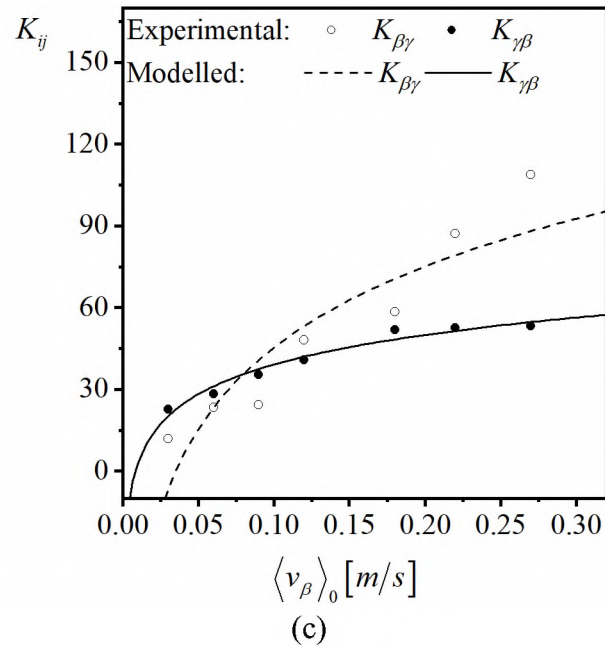
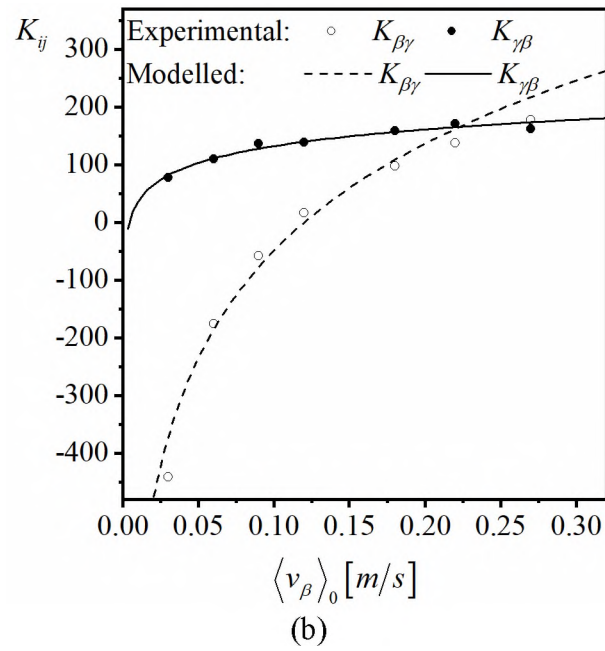


Figure 4. Experimentally estimated and modelled viscous drag parameter (a) Cylinders, (b) Trilobes, (c) Quadrilobes (cont.)

From the observed trends in the experimentally estimated viscous drag parameters, an empirical expression, described by Equation (21), is proposed to fit the estimated values.

The fitting parameters a_{ij} and b_{ij} values for each of the geometries experimentally tested are shown in Table 3.

$$K_{ij} = a_{ij} \ln(b_{ij} \langle v_{\beta} \rangle_0) \quad (21)$$

The predicted viscous drag parameters predicted by the empirical model are also shown in Figures 4a-c.

Table 3. Fitting parameters for the empirical model to estimate the viscous drag parameters

Geometry	$a_{\beta\gamma}$	$b_{\beta\gamma}$	$a_{\gamma\beta}$	$b_{\gamma\beta}$
Cylinders	60.8	65.6	34.3	92.4
Trilobes	268.2	8.3	41.7	235.9
Quadrilobes	43.1	28.6	15.7	120.5

From the predictions shown in Figures 4a-c it can be seen that the liquid-gas ($K_{\gamma\beta}$) viscous drag parameter is closely predicted by the proposed model; while the gas-liquid ($K_{\beta\gamma}$) parameter predictions present slight deviations. Figure 5 shows the average absolute relative error ($AARE = 1/n \sum |(\psi_{Experimental} - \psi_{Modelled}) / \psi_{Experimental}|$) . liquid-gas ($K_{\gamma\beta}$) viscous drag parameters are predicted with deviations of 9.8%, 3.6% and 5.9% for cylinders, trilobes and quadrilobes, respectively; while the gas-liquid ($K_{\beta\gamma}$) parameters are predicted with higher deviations of 12.5%, 17.9% and 12.1% for cylinders, trilobes and quadrilobes, respectively. Despite the higher deviation on the prediction of the gas-liquid

$(K_{\beta\gamma})$ parameter, these will be shown to be within an acceptable range according to the predicted pressure drops and liquid holdup as per the developed volume averaged models.

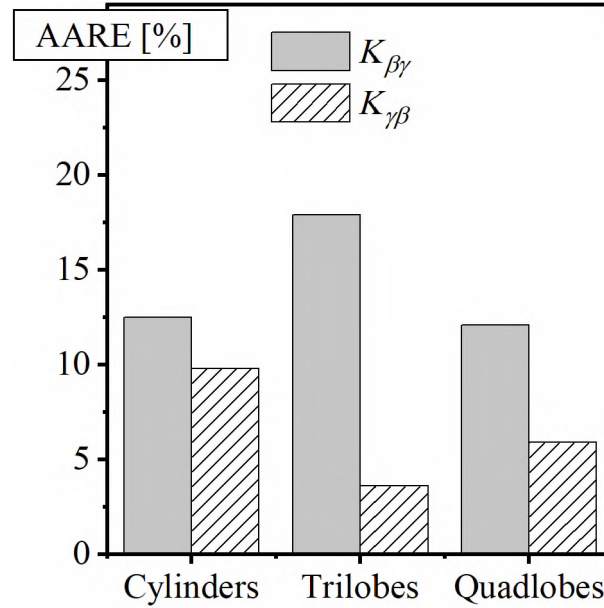


Figure 5. Average absolute relative error in the prediction of the viscous drag parameters by the proposed empirical model.

4. HYBRID MODEL FOR SIMULTANEOUS PRESSURE DROP AND LIQUID HOLDUP ESTIMATION

Estimating the pressure drop and liquid holdup of a TBR is of paramount importance in design tasks, such as up scaling and implementing new processes. However, the estimation of such parameters is a complex task because of the highly non-linear multiphase interaction in these systems. In this sense, it can be seen that the currently available models, as well as the proposed model in this work, require that one of these parameters is known to estimate the other one. Hence, in order to provide a model that enables the simultaneous prediction of pressure drops and holdup with high accuracy, a

second phenomenological model with high predictability needs to be developed or selected to be simultaneously solved with the proposed model in this work, thus providing closure for both variables.

Through the last decades, different developments can be found in reported literature, such as the slit model [21] and its modifications, as the extended slit model [30] and the double-slit model [23], and other empirical models, such as the reported by Larachi *et al* [18]. However, in most of these reported models, important deviations have been found in the prediction of the key hydrodynamic parameters. Recently, in a previous contribution by our research group, a comparison between the predicted pressure drops and liquid holdup by the slit [21], extended slit [30] and the empirical model by Larachi *et al* [18], was presented, and it was observed that the empirical model led to the highest deviations, with an AARE of 75.5% and 35.3% in the prediction of experimentally determined liquid holdup and dimensionless pressure drop, respectively; while the model with the highest accuracy was the extended slit model, with an AARE of 10.4% and 31.8% in the prediction of experimentally determined liquid holdup and dimensionless pressure drop, respectively, as shown in Figure 6. As per this comparison, it can be seen that the extended slit model has a good predictive quality to estimate the liquid holdup but exhibits important deviations when predicting pressure drops. Furthermore, it should be pointed out that the extended slit model is based on a mechanistic development, considering a force balance over a representative region of a TBR [30], and thus, the extended slit model is a phenomenological model that has a wide applicability. Such wide applicability is desirable for selecting the extended slit model to obtain the proposed hybrid model, as this coupled model would not overconstrain the volume-averaging-based model previously described.

Hence, by virtue of these results, and the phenomenological development of the extended slit model, the extended slit can be coupled with the developed model in this work in order to obtain a hybrid model that will enable the simultaneous prediction of liquid holdup and dimensionless pressure drop, and will enhance the predictive quality of the available extended slit model. Nevertheless, it should be considered that a different model could also be selected instead of the extended slit model, to further enhance the predictive quality of the hybrid model, or to extend its applicability. However, as far as the authors concern, there are no other available mechanistic or phenomenological models for predicting pressure drops and liquid holdup for a TBR, which can provide better closure in terms of predictive quality and applicability, in comparison with the selected extended slit model.

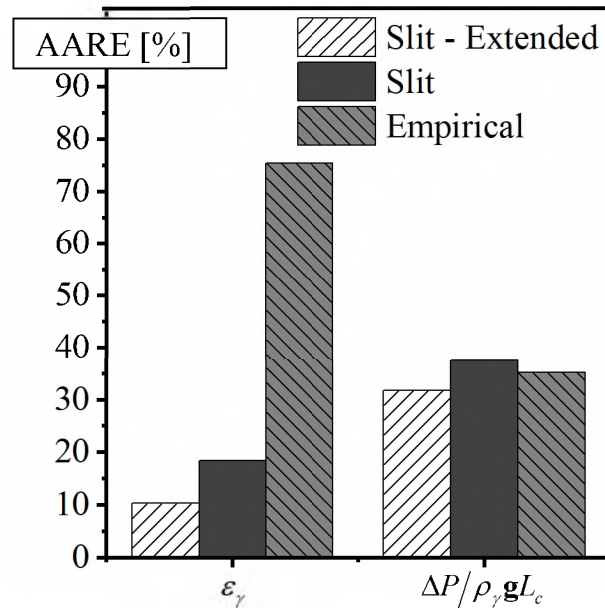


Figure 6. Average absolute relative error in the prediction of experimentally measured liquid holdup and dimensionless pressure drop by extended-slit, slit and an empirical model.

In order to couple the extended slit model with the proposed model (Equation (17) or (18)), the extended slit model can be written and used as shown in Equation (22). Where Re_γ and Ga_γ are the liquid Reynolds number and Galileo number, respectively. E_1 and E_2 are the first and second Ergun constants, respectively, which represent, in a certain extent, the textural characteristics of the bed, and are determined experimentally. For this development, the values of E_1 and E_2 were taken from a previous contribution by Al-Ani [26], and are shown in Table 2.

$$\frac{\Delta\langle P \rangle}{\rho_\gamma \mathbf{g} L_C} + 1 = \left(\frac{\varepsilon_B}{\varepsilon_\gamma} \right)^3 \left(\frac{E_1 Re_\gamma}{Ga_\gamma} + \frac{E_2 Re_\gamma^2}{Ga_\gamma} \right) + f_s \frac{\varepsilon_B}{\varepsilon_\gamma} \left(-\frac{\rho_\beta}{\rho_\gamma} - \frac{\Delta\langle P \rangle}{\rho_\gamma \mathbf{g} L_C} \right) \quad (22)$$

According to the development of the extended slit model [30], the parameter f_s is a shear slip factor, which is related to the shear stress in the gas and liquid phases, and its value has to be determined by two-phase flow experiments. Using a randomly selected set of the experimentally determined pressure drop data shown in Figures 3a-c, the shear slip factor, f_s , was estimated. It was observed that f_s remained the same when changing the catalyst shape at the same superficial gas $\left(\langle v_\beta \rangle_0 \right)$ and liquid $\left(\langle v_\gamma \rangle_0 \right)$ inlet velocities: also, for all catalyst shapes f_s remained constant for different superficial liquid inlet velocities $\left(\langle v_\gamma \rangle_0 \right)$ at the same superficial gas inlet velocity $\left(\langle v_\beta \rangle_0 \right)$. It was observed that f_s has an important linear dependence on the superficial gas inlet velocity $\left(\langle v_\beta \rangle_0 \right)$ regardless of the geometry or the superficial liquid inlet velocity $\left(\langle v_\gamma \rangle_0 \right)$. Thus, a good estimate of the value

of f_s for any geometry and any liquid velocity can be estimated by using the following empirical Equation (23).

$$f_s = 7.9422 \langle v_\beta \rangle_0 - 4.0505 \quad (23)$$

Equation (23) is developed based on the empirical fitting of the shear slip factor needed for the extended slit model, as reported on literature [30]. Nevertheless, it should be noted that the empirical fitting is based on a wide range of superficial gas and liquid inlet velocities and different catalyst geometries, and thus, it is widely applicable.

Hence, in order to use the hybrid model, Equations (17) and (22) have to be solved simultaneously to estimate the liquid holdup and dimensionless pressure drop. Equations (19), (21) and (23) should be used to estimate the corresponding parameters in Equations (17) and 22.

5. APPLICATIONS

Using the set of equations as outlined allows to estimate simultaneously the liquid holdup and dimensionless pressure drop without the need of a priori knowing one or the other parameter. The model was applied to estimate the liquid holdup and dimensionless pressure drop of all the experimental cases shown in Figures 3a-c.

Figure 7 shows the parity plot of the predicted dimensionless pressure drop by the model against the experimentally measured dimensionless pressure drop for cylinders, trilobes and quadrilobes particles. In this figure, it can be seen that all the model predictions fall within a deviation of 15%. This leads to an AARE of 6.9%, 11.5% and 11% for cylinders, trilobes and quadrilobes predictions, respectively; and a mean squared error

$\left(MSE = 1/n \sum (\psi_{Experimental} - \psi_{Modelled})^2\right)$ of 0.89%, 2.31% and 1.22%, respectively. This represents an overall AARE of 9.81%, and an overall MSE of 1.47% for all pressure drop predictions.

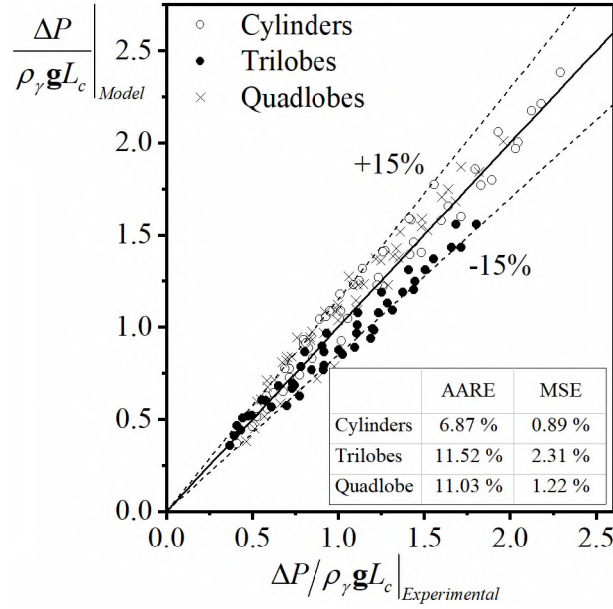


Figure 7. Parity plot of the model predicted and experimentally measured dimensionless pressure drops for cylinders, trilobes and quadrilobes particles

Similarly, Figure 8 shows the parity plot of the predicted liquid holdup by the model against the experimentally determined liquid holdup for cylinders, trilobes and quadrilobe particles. It can be seen that the model predictions for liquid holdup also fall within a deviation of 15%, and that most of the cases were slightly overpredicted rather than underpredicted. The AARE was found to be 6.24%, 13.57%, and 2.74% for cylinders, trilobes and quadrilobes, respectively; while the MSE was found to be 0.03%, 0.16% and 0.01% also for cylinders, trilobes and quadrilobes, respectively. This represents an overall AARE of 7.52% and an overall MSE of 0.07% in the prediction of the liquid holdup.

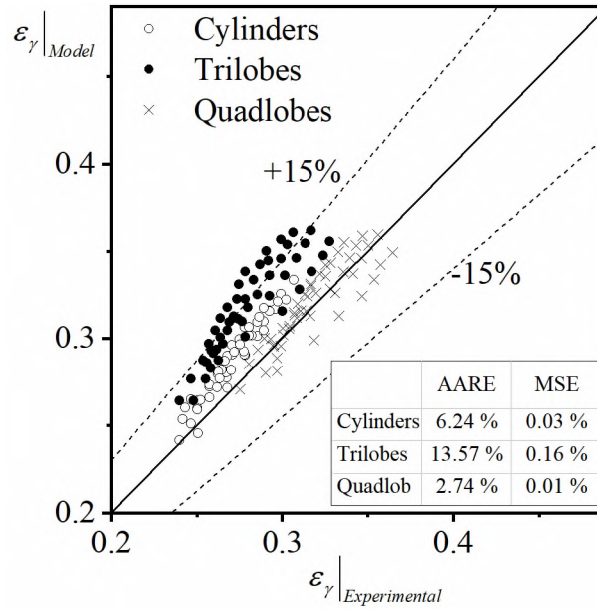


Figure 8. Parity plot of the model predicted and experimentally measured liquid holdup for cylinders, trilobes and quadrilobes particles

5.1. COMPARISON WITH LITERATURE DATA

In order to provide a further insight into the applicability and limitations of the developed hybrid model, the model was used to predict benchmarking experimental cases found in literature. The selected reported experiments corresponded to the contributions of Trivizadakis *et al.* [37] for a TBR packed with cylindrical catalyst, and the contributions of Bazmi *et al.* [19] for a TBR packed with trilobes. In both of these contributions, the pressure drop and dynamic liquid holdup were reported. It should be noted that the developed hybrid model allows to determine the overall liquid holdup, which consist of the dynamic liquid holdup and static liquid holdup. The static liquid holdup can also be separated into the external static liquid holdup, which corresponds to the retained liquid in the interstitial space between the packing, adhered to the catalyst surface; and the internal static liquid holdup, which is the liquid retained in the porous structure inside the catalysts. Hence, the reported experimental dynamic liquid holdup cannot be directly compared with

the model predictions, as the static liquid holdup is not accounted by the experimental measurements. In order to allow the comparison between the data from Trivizadakis *et al.* [37] and Bazmi *et al.* [19] with the model predictions, a value of 0.06 for the static liquid holdup in those systems can be considered a good estimate, according to the contributions of Kramer [38] and Saez *et al.* [39]. However, it should be noted that the actual static liquid holdup will be determined by the contact angle and local bed textural characteristics, such as the local void phase distribution, and hence, its actual value for the experimental setup and conditions of Trivizadakis *et al.* [37] and Bazmi *et al.* [19] remain unknown. Considering such estimate, Figure 9 shows the parity plot of the predicted liquid holdup by the model against the experimental data of Trivizadakis *et al.* [37] and Bazmi *et al.* [19].

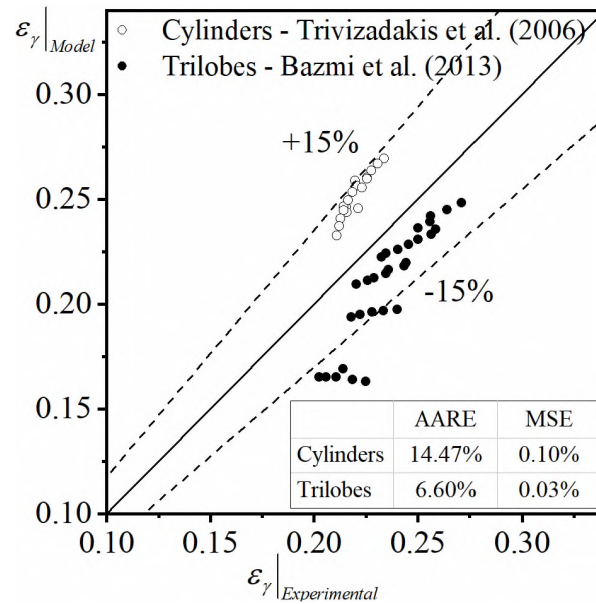


Figure 9. Parity plot of the model predicted total liquid holdup and extracted experimental dynamic liquid holdup from literature for cylinders and trilobes

It can be seen that considering such estimate for the static liquid holdup, the AARE in the predictions are of 14.5% for the experimental data of Trivizadakis *et al.* [37], and 6.6% for the experimental data of Bazmi *et al.* [19]. It can be seen that for these cases, the deviation in the prediction of the liquid holdup for the cylinders case is larger than the one obtained for our experimental data. This can be attributed to the uncertainty in the actual static liquid holdup, and the validity of the estimate considered. Nevertheless, overall, the deviations for our experimental data and the data found in literature are below 15%. This shows that the model has a high predictive quality when applied for other systems.

Figure 10 shows the parity plot of the dimensionless pressure drop predicted by the model, and the reported experimental data of Trivizadakis *et al.* [37] and Bazmi *et al.* [19]. In this, it can be seen that the model exhibits a AARE of 10.9% for the experimental data of Trivizadakis *et al.* [37], and 14.1% for the experimental data of Bazmi *et al.* [19]. Again, this shows that the model has a high predictive quality for the pressure drop predictions when applied for other systems.

It should be noted that experimental studies on TBRs packed with extruded catalysts are scarce, and most of the works reported in literature correspond to TBRs packed with spheres [3,18,40,41]. In this sense, the developed hybrid model as presented in this work is not suitable for application for TBRs packed with spherical catalysts. In order for the model to be applicable for spherical packings, experimentally determined pressure drop and liquid holdup data is needed to estimate new fitting parameters for Equation (21). Nevertheless, it should be pointed out that the model was developed for extruded catalysts due to their vast industrial applications.

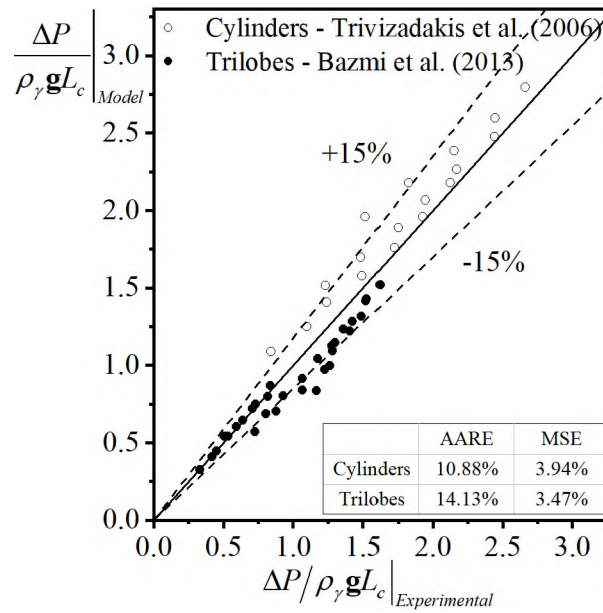


Figure 10. Parity plot of the model predicted and extracted dimensionless pressure drops from literature for cylinders and trilobes

It can be seen that the hybrid model for simultaneous predictions of liquid holdup and dimensionless pressure drop has a high accuracy and is highly predictive. When compared with the other models' deviations shown in Figure 6, it can be noted that the proposed hybrid model provides more accurate predictions than the other models and allows to highly enhance the quality of the predictions of the extended slit model. Furthermore, when applied to other experimental setups found in reported works in literature, this high predictive quality and accuracy is still exhibited. This enhancement in the predictions of the extended slit model could be attributed to the rigorous development that leads to Equation (17), which allows to obtain a mechanistic expression that is coupled to the extended slit model. In a great extent, therefore, it could be considered that the proposed hybrid model has an enhanced predictive quality over other available models reported on literature by virtue of the mechanistic developments to obtain both of the

coupled expressions, and to the use of a comprehensive experimental study to obtain the empirical closures to these mechanistic expressions.

6. REMARKS

Based on volume averaged equations for the two-phase flow on a porous media, a phenomenological model to estimate dimensionless pressure drop or liquid holdup of a Trickle Bed Reactor packed with extrudate particles, cylinders, trilobes and quadrilobes was developed. The model included three closure terms, the bed permeability (K), a gas-liquid ($K_{\beta\gamma}$) and a liquid-gas ($K_{\gamma\beta}$) viscous drag parameter. In this sense, the bed permeability captures the resistances to the momentum transfer imposed by the porous media over the fluids; while the viscous drag parameters capture, in a certain extent, the multiphase interactions. The permeability was approximated according to the generally accepted Kozeny-Carman model; while the viscous drag parameters were estimated according to experimentally determined liquid holdup and pressure drops. Furthermore, an empirical model based on the experimentally estimated viscous drag parameters was developed.

In order to develop a hybrid phenomenological model that can simultaneously predict pressure drops and liquid holdup, expressions from the extended slit model reported on literature [36], were coupled with the expression developed by means of the results of averaging procedure.

The predictive quality of the hybrid model was tested by comparing with experimental measurements of dimensionless pressure drops and liquid holdup in a column

of 0.14 m in diameter and 2 m in height. The proposed model shows a high predictive quality to estimate the dimensionless pressure drop, with an overall AARE of 9.81%, and an overall MSE as low as 1.47%; while the model predictions liquid holdups also exhibits a high predictive quality, with an overall AARE of 7.52%, and an overall MSE as low as 0.07%. The observed deviations show a remarkable enhancement in the quality of the predictions in comparison with currently available models reported in literature. Furthermore, as shown by the comparison with other experimental data reported on literature, and due to the fact that both of the models coupled in the hybrid model development are based on a phenomenological development, the hybrid model has a wide range of applicability with high accuracy. A model with these characteristics is desirable for design and scale up tasks.

It should be noted that the developed hybrid model, as presented, is only applicable for extruded catalysts. The model was developed in this way due to the vast industrial applications and interest on extruded catalysts over spherical catalysts. Nevertheless, the model could be adapted for spherical packings, provided that experimental liquid holdup and pressure data is available to obtain fitting parameters for the viscous drag parameter.

FUNDING

This research did not receive any specific grant from funding agencies in the public, commercial, or not-for-profit sectors.

REFERENCES

- [1] S. Whitaker, Flow in porous media II: The governing equations for immiscible, two-phase flow, *Transp. Porous Media.* 1 (1986) 105–125. <https://doi.org/10.1007/BF00714688>.
- [2] M.H. Al-Dahhan, M.P. Duduković, Pressure drop and liquid holdup in high pressure trickle-bed reactors, *Chem. Eng. Sci.* 49 (1994) 5681–5698. [https://doi.org/10.1016/0009-2509\(94\)00315-7](https://doi.org/10.1016/0009-2509(94)00315-7).
- [3] C. Boyer, C. Volpi, G. Ferschneider, Hydrodynamics of trickle bed reactors at high pressure: Two-phase flow model for pressure drop and liquid holdup, formulation and experimental validation, *Chem. Eng. Sci.* 62 (2007) 7026–7032. <https://doi.org/10.1016/j.ces.2007.08.036>.
- [4] Z. Solomenko, Y. Haroun, M. Fourati, F. Larachi, C. Boyer, F. Augier, Liquid spreading in trickle-bed reactors: Experiments and numerical simulations using Eulerian-Eulerian two-fluid approach, *Chem. Eng. Sci.* 126 (2015) 698–710. <https://doi.org/10.1016/j.ces.2015.01.013>.
- [5] A. Atta, S. Roy, K.D.P. Nigam, Prediction of pressure drop and liquid holdup in trickle bed reactor using relative permeability concept in CFD, *Chem. Eng. Sci.* 62 (2007) 5870–5879. <https://doi.org/10.1016/j.ces.2007.06.008>.
- [6] H. Nadeem, I. Ben Salem, M. Sassi, Experimental Visualization and Investigation of Multiphase Flow Regime Transitions in Two-Dimensional Trickle Bed Reactors, *Chem. Eng. Commun.* 204 (2017) 388–397. <https://doi.org/10.1080/00986445.2016.1205982>.
- [7] A. Jindal, V. V. Buwa, Effect of Bed Characteristics on Local Liquid Spreading in a Trickle Bed, *AIChE J.* 63 (2017) 347–357. <https://doi.org/10.1002/aic>.
- [8] M.E. Cordero, S. Uribe, L.G. Zárate, J.A. Hernandez-Servin, E.P. Reyes, A. Regalado-Méndez, R. Natividad, CFD analysis of BED textural characteristics on TBR behavior: Hydrodynamics and scaling-up, *Int. J. Chem. React. Eng.* 15 (2017). <https://doi.org/10.1515/ijcre-2017-0095>.
- [9] F.S. Mederos, J. Ancheyta, Mathematical modeling and simulation of hydrotreating reactors: Cocurrent versus countercurrent operations, *Appl. Catal. A Gen.* 332 (2007) 8–21. <https://doi.org/10.1016/j.apcata.2007.07.028>.
- [10] R. Chacón, A. Canale, A. Bouza, Y. Sánchez, Modeling of a three-phase reactor for bitumen-derived gas oil hydrotreating, *Brazilian J. Chem. Eng.* 29 (2012) 135–146. <https://doi.org/10.1590/S0104-66322012000100015>.

- [11] M. De Sousa Duarte, M. Rolland, C. Sagnard, D. Suire, F. Flacher, O. Delpoux, C.P. Lienemann, High-Pressure High-Temperature Transparent Fixed-Bed Reactor for Operando Gas-Liquid Reaction Follow-up, *Chem. Eng. Technol.* 42 (2019) 655–660. <https://doi.org/10.1002/ceat.201800090>.
- [12] S. Uribe, M.E. Cordero, L.G. Zárate, J.J. Valencia López, R. Natividad, CFD analysis of bed textural characteristics on TBR behaviour: Kinetics, scaling-up, multiscale analysis, and wall effects, *Can. J. Chem. Eng.* (2018). <https://doi.org/10.1002/cjce.23298>.
- [13] C. Botchwey, A.K. Dalai, J. Adjaye, Product Selectivity during Hydrotreating and Mild Hydrocracking of Bitumen-Derived Gas Oil, (2003) 1372–1381.
- [14] S. Uribe, M.E. Cordero, E.P. Reyes, A. Regalado-Méndez, L.G. Zárate, Multiscale CFD modelling and analysis of TBR behavior for an HDS process: Deviations from ideal behaviors, *Fuel*. (2019) 1162–1172. <https://doi.org/10.1016/j.fuel.2018.11.104>.
- [15] S.A. Ghenni, M.H. Al-Dahhan, Assessing the Feasibility of Optical Probe in Phase Holdup Measurements and Flow Regime Identification, *Int. J. Chem. React. Eng.* 13 (2015) 369–379. <https://doi.org/10.1515/ijcre-2014-0147>.
- [16] C. Boyer, A. Koudil, P. Chen, M.P. Dudukovic, Study of liquid spreading from a point source in a trickle bed via gamma-ray tomography and CFD simulation, *Chem. Eng. Sci.* 60 (2005) 6279–6288. <https://doi.org/10.1016/j.ces.2005.03.049>.
- [17] M.H. Al-Dahhan, F. Larachi, M.P. Dudukovic, A. Laurent, High-Pressure Trickle-Bed Reactors: A Review, *Ind. Eng. Chem. Res.* 36 (1997) 3292–3314. <https://doi.org/10.1021/ie9700829>.
- [18] F. Larachi, A. Laurent, N. Midoux, G. Wild, Experimental study of a trickle-bed reactor operating at high pressure: two-phase pressure drop and liquid saturation, *Chem. Eng. Sci.* 46 (1991) 1233–1246. [https://doi.org/10.1016/0009-2509\(91\)85051-X](https://doi.org/10.1016/0009-2509(91)85051-X).
- [19] M. Bazmi, S.H. Hashemabadi, M. Bayat, Extrudate Trilobe Catalysts and Loading Effects on Pressure Drop and Dynamic Liquid Holdup in Porous Media of Trickle Bed Reactors, *Transp. Porous Media.* 99 (2013) 535–553. <https://doi.org/10.1007/s11242-013-0199-x>.
- [20] J.L. Turpin, R.L. Huntington, Prediction of pressure drop for two-phase, two-component concurrent flow in packed beds, *AIChE J.* 13 (1967) 1196–1202. <https://doi.org/10.1002/aic.690130630>.
- [21] R.A. Holub, M.P. Dudukovic, P.A. Ramachandran, A Phenomenological Model for Pressure Drop, Liquid Holdup, and Flow Regime Transition in gas-liquid Trickle Flow, *Chem. Eng. Sci.* 47 (1992) 2343–2348.

- [22] R.A. Holub, M.P. Duduković, P.A. Ramachandran, Pressure drop, liquid holdup, and flow regime transition in trickle flow, *AIChE J.* 39 (1993) 302–321. <https://doi.org/10.1002/aic.690390211>.
- [23] I. Iliuta, F. Larachi, M.H. Al-Dahhan, Double-Slit Model for Partially Wetted Trickle Flow Hydrodynamics, *AIChE J.* 46 (2000) 597–609. <https://doi.org/10.1205/026387600528256>.
- [24] A. Attou, G. Ferschneider, A two-fluid model for flow regime transition in gas-liquid trickle-bed reactors, *Chem. Eng. Sci.* 54 (1999) 5031–5037. [https://doi.org/10.1016/S0009-2509\(99\)00226-2](https://doi.org/10.1016/S0009-2509(99)00226-2).
- [25] A.E. Sáez, R.G. Carbonell, Hydrodynamic Parameters for Gas-Liquid Cocurrent Flow in Packed Beds, *AIChE J.* 31 (1985) 52–62. <https://doi.org/10.1002/aic.690310105>.
- [26] M.J. Al-ani, Hydrodynamics of trickle bed reactors (TBRs) packed with industrial catalyst using advanced measurement techniques, Missouri University of Science and Technology, 2019.
- [27] S. Whitaker, *The Method of Volume Averaging*, 1st ed., Kluwer Academic Publishers, Dordrecht, 1999. <https://doi.org/10.1007/978-94-017-1114-2>.
- [28] I. Battiatto, P.T. Ferrero V, D. O' Malley, C.T. Miller, P.S. Takhar, F.J. Valdés-Parada, B.D. Wood, Theory and Applications of Macroscale Models in Porous Media, *Transp. Porous Media.* (2019). <https://doi.org/10.1007/s11242-019-01282-2>.
- [29] M.E. Cordero, R. Natividad, L.G. Zárate, J.A. Hernandez-Servin, J. Salas, Estimation of effective diffusion coefficient and its effect on effectiveness factor for HDS catalytic process: A multi-scale approach, *Catal. Today.* 220–222 (2014) 113–123. <https://doi.org/10.1016/j.cattod.2013.07.020>.
- [30] M.H. Al-Dahhan, M.R. Khadilkar, Y. Wu, M.P. Dudukovic, prediction of Pressure Drop and Liquid Holdup in High-Pressure Trickle-Bed Reactors, 5885 (1998) 793–798.
- [31] S. Whitaker, Flow in porous media I: A theoretical derivation of Darcy's law, *Transp. Porous Media.* 1 (1986) 3–25. <https://doi.org/10.1007/BF01036523>.
- [32] A. Bejan, I. Dincer, S. Lorente, A.F. Miguel, A.H. Reis, *Porous and Complex Flow Structures in Modern Technologies*, Springer-Verlang, New York, 2004.
- [33] D.A. Nield, A. Bejan, *Convection in Porous Media*, Springer-Verlang, New York, 1999.

- [34] M.M. Ahmadi, S. Mohammadi, A.N. Hayati, Analytical derivation of tortuosity and permeability of monosized spheres: A volume averaging approach, *Phys. Rev. E - Stat. Nonlinear, Soft Matter Phys.* 83 (2011). <https://doi.org/10.1103/PhysRevE.83.026312>.
- [35] J. Kozeny, *Über Kapillare Leitung des Wassers im Boden*, *Akad. Wiss. Wien.* 136 (1927) 271–306.
- [36] P.C. Carman, *Flow of Gases Through Porous Media*, Butterworths, London, 1956.
- [37] M.E. Trivizadakis, D. Giakoumakis, A.J. Karabelas, A study of particle shape and size effects on hydrodynamic parameters of trickle beds, *Chem. Eng. Sci.* 61 (2006) 5534–5543. <https://doi.org/10.1016/j.ces.2006.03.025>.
- [38] G.J. Kramer, Static liquid hold-up and capillary rise in packed beds, *Chem. Eng. Sci.* 53 (1998) 2985–2992. [https://doi.org/10.1016/S0009-2509\(98\)80001-8](https://doi.org/10.1016/S0009-2509(98)80001-8).
- [39] A.E. Sáez, M.M. Yépez, C. Cabrera, E.M. Soria, Static liquid holdup in packed beds of spherical particles, *AIChE J.* 37 (1991) 1733–1736. <https://doi.org/10.1002/aic.690371117>.
- [40] S. Uribe, M. Al-Ani, M.E. Cordero, M. Al-Dahhan, Modelling and validation of TBR Hydrodynamics: Local comparison between CFD and experiments, *Fuel*. 277 (2020) 118244. <https://doi.org/10.1016/j.fuel.2020.118244>.
- [41] D. Nemec, J. Levec, Flow through packed bed reactors: 2. Two-phase concurrent downflow, *Chem. Eng. Sci.* 60 (2005) 6958–6970. <https://doi.org/10.1016/j.ces.2005.05.069>.

III. ACCRETION OF HEAVY METAL CONTAMINANTS ENTRAINED WITH FLOW INTO A TRICKLE BED HYDROTREATING REACTOR PACKED WITH DIFFERENT CATALYST SHAPES USING NEWLY DEVELOPED NONINVASIVE DYNAMIC RADIOACTIVE PARTICLE TRACKING

Binbin Qi¹, Omar Farid¹, Muthanna Al-Dahhan^{1,2*}

¹ Multiphase flow and Reactor Engineering and Education Laboratory (mFReel), Chemical and Biochemical Engineering Department, Missouri University of Science and Technology, Rolla, MO 65409 USA

² Mining and Nuclear Engineering Department, Missouri University of Science and Technology, Rolla, MO 65409, USA

* Corresponding author: aldahhanm@mst.edu

ABSTRACT

A newly developed modified dynamic radioactive particle tracking system (DRPT) was used to investigate the heavy metal contaminants accretion locations in different catalyst beds, sphere, cylinder, trilobe, and quadrilobed in trickle bed reactors. In the present paper, kernel density estimator (KDE) was used to estimate the probability density distributions of heavy metal contaminants accretion in terms of bed radius height. The result shows that the four cases have similar probability density distribution in terms of radius, while the spherical catalyst has the larger distribution range in terms of bed height. The heavy metal accretion is directly related to the pressure drops along the bed height which indicate the bed porosity and intricate bed structure in catalyst packed beds. Heavy metals have more chance to deposit at higher levels of packed beds with higher pressure drops.

Keywords: Trickle Bed Reactors; Heavy metal contaminants, RPT, Kernel Density Estimation

1. INTRODUCTION

Trickle bed reactors (TBR) are the most used gas-liquid-solid interacting equipment in various processing such as petroleum hydrotreating processing (hydrodesulfurization, hydrodenitrification, hydrodemetallization, hydrocracking, etc.), hydrogenation reactions, oxidation reactions, esterification, as well as Fischer-Tropsch reactions [1]. In these processes, there are inevitably contaminants being delivered into the TBR, especially in hydroprocessing applications, where heavy residual oils are converted into lighter fuel oils. These contaminants (e.g., nickel, vanadium, arsenic, sodium, iron, lead) are usually associated with the produced crude oil, the remaining heavy metals in the liquid feed, or residues from the additives (silicon, lead) used during refining operations, as well as corrosion (iron) [2]. These contaminants directly or indirectly result in catalyst deactivation due to a chemical, mechanical, or thermal effect, such as poisoning, fouling, thermal degradation, or attrition [3] which leads to hot spots, high pressure drops, and even the need for emergency shutdowns. Currently, there is vast literature related to the catalysts aging, deactivation and regeneration including mechanisms and kinetical investigation [2–5]. All the work is in micro perspective that relies on the prerequisite that the contaminants already exist in the catalyst bed. There is no doubt that the contaminants are entrained through the liquid feed flow into the trickle beds hence get stuck and deposit. However, to the best of authors' knowledge, there is no such work that discloses how these contaminants

are carried by the liquid fluid, the distribution of the accretion locations, and especially the effects of the catalyst bed structure, such as the catalyst shape, on the contaminant's accretion. Hence, in order to obtain insights into the interaction of the liquid fluid and the contaminant particles, and to provide guidance for industries to diagnose the common issues in TBRs such as hot spot or high pressure drops, it is essential to track the contaminants locations. The challenge of tracking the contaminants locations becomes more complex, since the size of the contaminants varies in a large range, from nanometer level to millimeter level, which precludes their visual identification, furthermore in the intricate interstitial space between the packing.

There have been various particle tracking methodologies reported in literature, which can aid in the identification of the contaminants' locations inside the packed beds. Single particle tracking (SPT) [6] is a methodology that uses computer-enhanced video microscopy to track the single particle motion in a system. However, it requires the system to be totally visible at least at the surface so that it can be captured by a camera. Laser doppler anemometry (LDA) and particle imaging velocimetry (PIV) [7] are another two typical techniques to track particles. However, both techniques are optical methods based on the light reflection from the seeded particles hence tracking large amount of the particles to measure the velocity field in fluid dynamics. All these techniques are not feasible for the TBR system due to the impossible visual identification of the void space inside the bed. Hence, another non-invasive particle tracking technique that does not require the transparency or visibility, which is radioactive particle tracking (RPT) [8–13], become a well-reasoned option. There are two types of RPT which are Static RPT (SRPT) and Dynamic RPT (DRPT). The SRPT aims to determine the Lagrangian trajectories,

instantaneous and time averaged velocity field and various turbulent parameters (Reynolds stresses, turbulent kinetic energy, turbulent eddy diffusivities etc.) [9–13] based on a priori calibration data obtained when the tracer radioactive particle is placed statically inside the system under normal operation conditions. The tracer radioactive particle is made up of a gamma-ray isotope particle by either coating a layer with chemical and thermal resistant materials or embedding in a larger particle to match the substance density that needs to be measured depending on the system. The system is surrounded by an array of non-collimated scintillation (NaI (Tl)) detectors. Before the actual experiments, the SRPT system is calibrated by placing the isotope particle at various known positions under the desired operation to develop the correlation of counts in terms of distance for each detector. During the actual experiments, the instantaneous locations of the free moving particle can be reconstructed based on the correlation developed in the static calibration step, therefore the velocity field and various turbulent parameters can be found. Khane et al. [8] developed a dynamic radioactive particle tracking (DRPT) to perform calibration for the RPT as a hybrid RPT system. The DRPT uses three moveable collimated scintillation (NaI (Tl)) detectors to seek the coordinate of the radioactive particle under motion. The main difference between these two RPT systems is that, SRPT tracks the trajectory of a dynamic object that is represented by the radioactive particle which mimics the moving phase to be tracked (liquid, solid), hence the Lagrangian trajectory is determined. From the Lagrangian trajectory, the velocity fields can be obtained and hence the fluctuation and turbulent parameters. While DRPT determines the location of a static object which is represented by the radioactive particle by dynamically moving the detectors to determine the coordinates of this object.

Therefore, in this work, the accretion locations of the heavy metal contaminants entrained through the liquid flow inside a TBR were investigated by a newly modified Dynamic Radioactive Particle Tracking system. It is worth to note here that the different catalyst shapes, sphere, cylinder, trilobe, and quadrilobed, have significant impacts on the flow behaviors inside a TBR [14–16]. Hence, these four catalyst shapes will be tested to identify the effects of the bed structure difference on the heavy metal contaminants accretion locations. Kernel density estimation (KDE) was used to determine the probability distribution of the contaminant final position, in terms of bed radius and height in each type of catalyst. This information can benefit not just industries to diagnose the common issues in TBRs such as contaminants accretion, hot spot or high pressure drop, it could also benefit the hydrodynamics investigation in computational fluid dynamics (CFD) simulations as it provides valuable benchmarking data for CFD validation. The probability density information can be coupled with the packed bed porosity distribution function giving more realistic bed structure so that researchers can investigate the flow behaviour or hydrodynamics under the case of contaminant accretion which can be extended for the beds with catalyst coking or sintering scenarios when the bed structure can be determined or assumed.

2. EXPERIMENTAL SETUPS

2.1. RADIOACTIVE PARTICLE REPRESENTING THE HEAVY METAL CONTAMINANTS

As mentioned earlier, the heavy metal contaminants could be any size and shape. In order to balance the maneuverability and representativeness, a spherical particle with

500 μm in diameter and 2000-3000 kg/m^3 in density was considered to be used for the experiments. Therefore, a Co-60 ($\phi 300 \mu\text{m}$, 18.5 MBq (500 μCi), with main yield energies of 1173.2 keV and 1332.5 keV, 5.27 half-life years) radioactive particle was embedded in a PMMA particle ($\phi 500 \mu\text{m}$, 1200 kg/m^3). A MiniCNC machine with a 0.3 mm drill bit was used to drill the hole in the PMMA particle. The Co-60 particle was placed inside the hole of the PMMA particle under the microscope and then it was sealed with Epoxy glue. After drying out, the particle was spray painted with orange color in order to be easily found during the experiments. The tools that were used are shown in Figure 1. The theoretical density (maximum) after the calculation is 2863.2 kg/m^3 .

2.2. TRICKLE BED REACTOR SYSTEM

The schematic of the trickle bed reactor (TBR) system is shown in Figure 2. The TBR is made of an acrylic column which is 1 foot (30.48 cm) in height and 5.5 inch (13.97 cm) in inner diameter. At the bottom of the column, a mesh gate valve was used to support the catalyst pack bed and to enable water and air passing through freely with negligible pressure drop. This mesh gate valve can be opened easily to remove the catalysts from the column in order to fish the particle or clean the system. A single nozzle pipe with 9 mm inner diameter was used as liquid inlet while two gas inlets (9 mm inner diameter) were attached to the top flange to obtain better distribution. The bottom of the liquid inlet is 2 cm away from the top of the packed bed. Both liquid and gas flowrates were controlled by the flowmeters. A particle injection system was attached to the liquid inlet pipe with a Y connector. The full description and operation procedure of the particle injection system will be explained at length later. A water tank with two sections was used in order to

prevent the radioactive particle from being sucked by the pump, in case that it had passed through the packed bed and drop inside the tank. A sump pump was used to help circulate the water in the system.



Figure 1. MiniCNC machine and micro drill bits

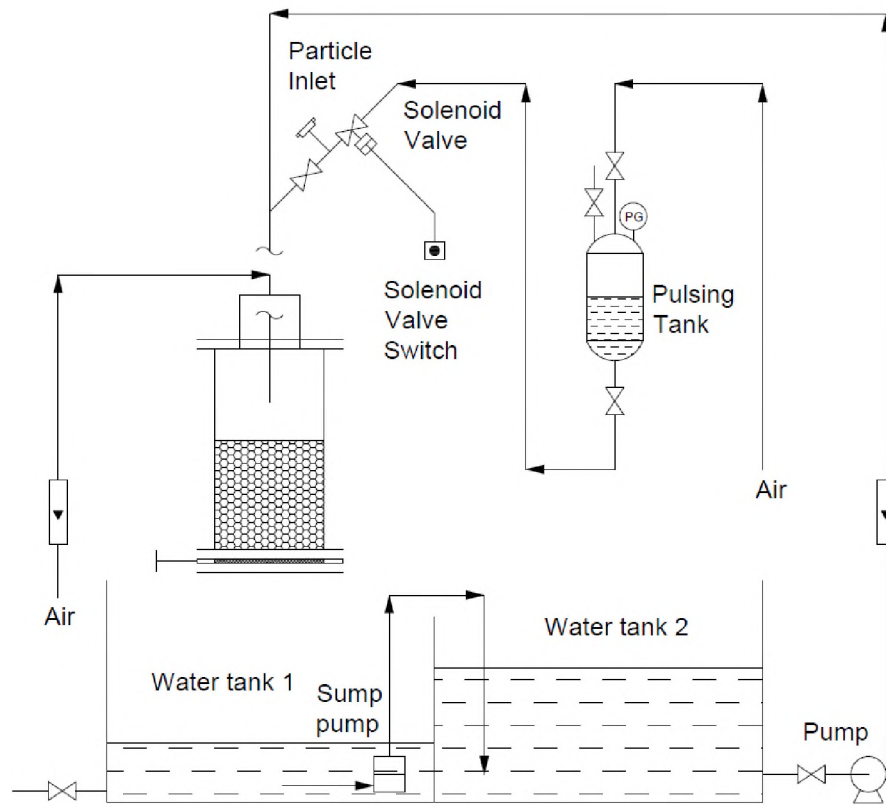


Figure 2. Details of the experimental setup

2.3. PARTICLE INJECTION SYSTEM

The particle injection system includes a pressurized pulsing tank, a normally closed solenoid valve controlled by a switch, a particle inlet, and a normal valve. Before experiments, the pulsing tank will be filled with water up to about half of the tank. Then the high-pressure air will be injected into the pulsing tank to pressurize the tank to no more than 30 Psi (206.843 KPa) in order to minimize the effects on the inlet liquid flow. The normally closed solenoid valve can prevent the water getting inside the system unless the switch is turned on. After that, the radioactive particle will be placed inside the particle inlet. To avoid that the particle flows directly inside the system, the normal valve will not be open until running the gas and liquid flow.

2.4. LOCATION IDENTIFICATION SYSTEM OF DYNAMIC RADIOACTIVE PARTICLE TRACKING TECHNIQUE

The modified DRPT system uses 3 collimated Sodium Iodide (NaI (Tl), $\phi 5 \times 5$ cm) scintillation detectors (Canberra Model 2007, named as X, Y, Z, respectively) to seek the coordinates of the radioactive particle. As shown in Figure 3, X Y and Z detectors are located at the same level and can be moved vertically by a 2-phase stepping motor to locate the Z coordinate of the radioactive particle. X and Y detectors are driven by a 2-phase stepping motors to move horizontally. These two detectors are perpendicular to each other so that X and Y coordinates can be easily determined. It is noted that all the detector crystals are fully covered by the lead collimators only with narrow slots (0.1 cm wide, 5 cm long). For the Z detector, the slot in the collimator is horizontally oriented while for the X and Y detectors, the slots are vertically oriented. As the detectors move in discrete steps, the photon counts of all the detectors will be tracked and recorded for 30 seconds at each position. The data acquisition system consists of 3 timing filter amplifiers (Canberra 2111), a channel discriminators (PhillipsScientific, CAMAC Model 7106, 32 channels), 225 MHz scalers(Phillips Scientific, CAMAC Model 7132 H, 32 channels), and CC-USB CAMACcontroller (W-IE-NER). The operation procedure and validation of this system will be described in the following section.

3. PROCEDURE AND VALIDATION

3.1. EXPERIMENTAL PROCEDURE

The complete experimental procedure is summarized in the flowchart below shown in Figure 4.

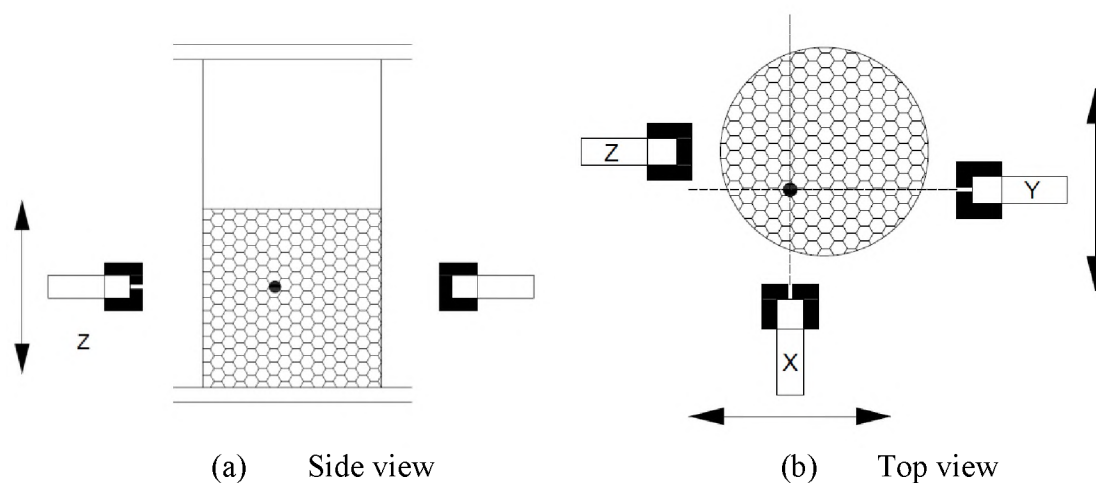


Figure 3. Schematic of the Dynamic Radioactive Particle Tracking system

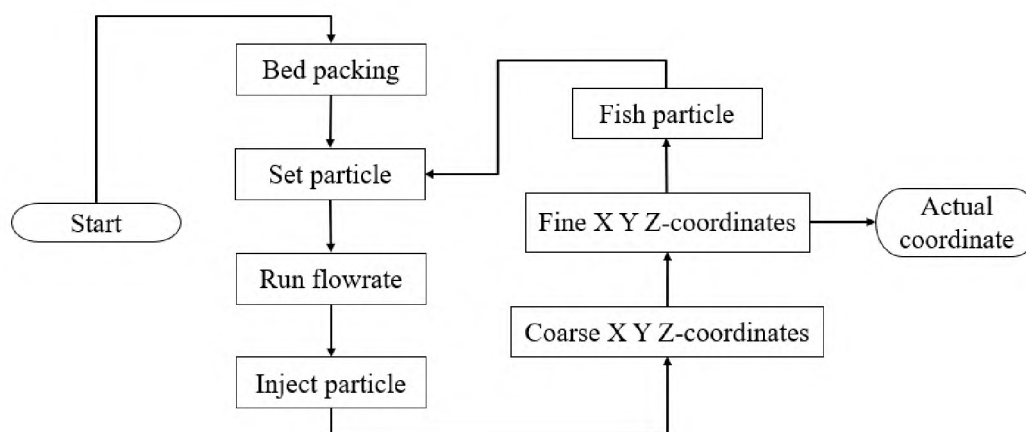


Figure 4. Flowchart of experimental procedure

(1) Bed packing

Four types of catalysts, sphere, cylinder, trilobe, and quadrilobed, were used in this work. The geometrical characteristics [14,16] of these catalysts and the packed beds are listed in Table 1. The purpose of this work is to assess the impacts of different catalyst shapes on heavy metal contaminants accretion. Hence, the gas and liquid flowrates are the same for all tested catalyst shapes. The packed bed was set to be 15 cm in height, by virtue

of preliminary experiments that showed that the 500 μm radioactive particle almost had no chance to pass through a packed bed of such height for all the catalyst shapes.

Table 1. Geometrical properties of the solid particles and bed

Shape	ε_B	$d_e [mm]$	ϕ	Actual size [mm]
Spheres	0.36	4.7	1	4.7
Cylinders	0.451	4.13	0.82	5.5×3
Trilobes	0.526	3.93	0.62	6×3
Quadrilobes	0.544	3.35	0.72	6×2.5

Where ε_B is bed porosity, d_e is volume equivalent diameter, ϕ is sphericity

(2) Setting the particle

Before running the gas and liquid flow, the radioactive particle will be placed inside the particle inlet in the particle injection system as explained earlier. During this step, the normal valve should always be kept closed to prevent the particle from dropping inside the packed bed before it is injected. After putting the particle inside the inlet, the gamma-ray survey meter will be used to check if the particle is at the right place.

(3) Running the flowrate

The air valve is open, and the superficial velocity is set at 0.05 m/s, later on the water pump is turned on and the superficial velocity is set at 0.0065 m/s. The system is kept running for 5 minutes in order to stabilize the flow of air and water into the trickle bed.

(4) Injecting the particle

The normal valve on the particle injection line is then opened, and the solenoid valve switch is quickly pressed to enable the pressurized water to push the particle into the system in a very short time to minimize the effect on the system. The gas/liquid flowrates are kept running for another 5 minutes before turning off the pump and air flow.

(5) Identifying the coarse X Y Z-coordinates of the particle location (coarse seeking coordinates)

The particle location seeking procedure is divided into two steps, coarse seeking and fine seeking coordinates. For coarse seeking coordinates, the step size is 1 cm. In Z direction, starting from the top of the packed bed and moving downward, the detector will collect the counts at each centimeter for 30 seconds until reaching the 14 cm-depth that there are total 15 data points. The coarse position at Z-axis can be determined from the data plot that the point has the highest counts should be the coarse Z coordinate as shown in Figure 5 (a). Then the collimated detectors of the DRPT system will be moved up to that particular position (highest counts) for X and Y coordinates seeking. Since the TBR column has 5.5 inch (13.97 cm) inner diameter and 6 inch (15.24 cm) outer diameter, 15 cm horizontal moving range is enough for the X and Y detectors to cover the whole column diameter in X and Y directions. Similarly, starting from the left edge, the X and Y detectors will collect counts at each centimeter for 30 seconds until reaching the right edge that total 15 data points will be generated to obtain the peak, therefore the coarse X and Y coordinates.

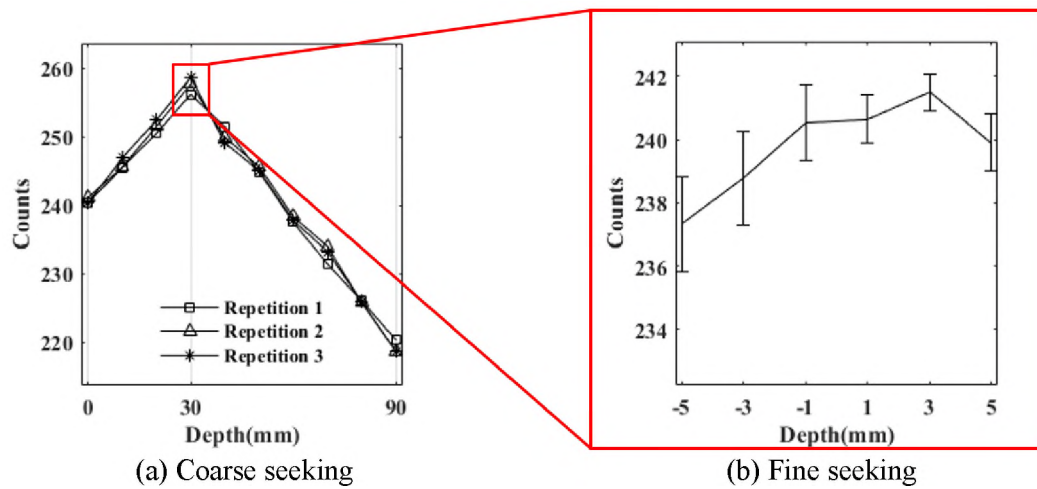


Figure 5. Sample results of coarse seeking and fine seeking procedure

(6) Identifying the fine X Y Z- coordinates of the particle location (fine seeking coordinates)

Once the coarse coordinates are found, all the detectors will be moved to their coarse coordinates as the base reference to seek the fine coordinates. The reference coarse coordinates plus and minus 5 mm will be the moving range (Figure 5(b)). By recalling that the slots on the collimators covering the detectors are 1 mm wide and 5 cm long. It is reasonable to make the initial assumption of the step size as 1 mm for fine seeking. However, from the plots in Figure 6, the indication of a peak is quite ambiguous for 1 mm step size, which cannot be used to identify the fine coordinates. Therefore, 2 mm step size was assessed by following the same procedure. In this way, clear indications of peaks can be identified. In order to minimize the error and achieve the repeatability and reproducibility, three repetitions of data collections are conducted, hence pinpointing the fine coordinates by averaging the 3 repetition results. Based on the plot of the average of 3

repetitions and error bars, the fine X Y and Z coordinates can be located with tolerance of ± 1 mm.

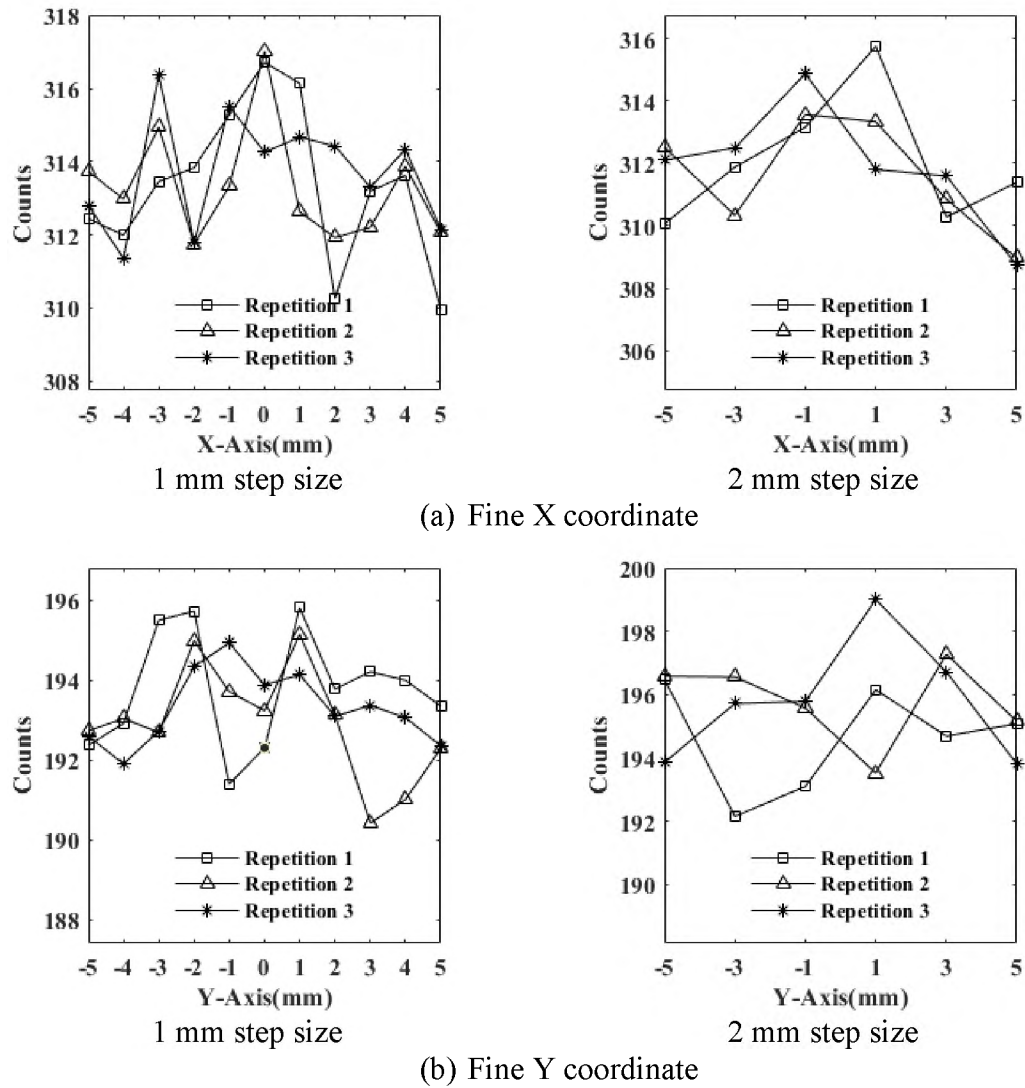


Figure 6. Comparisons between 1 mm and 2 mm step sizes for fine coordinates seeking

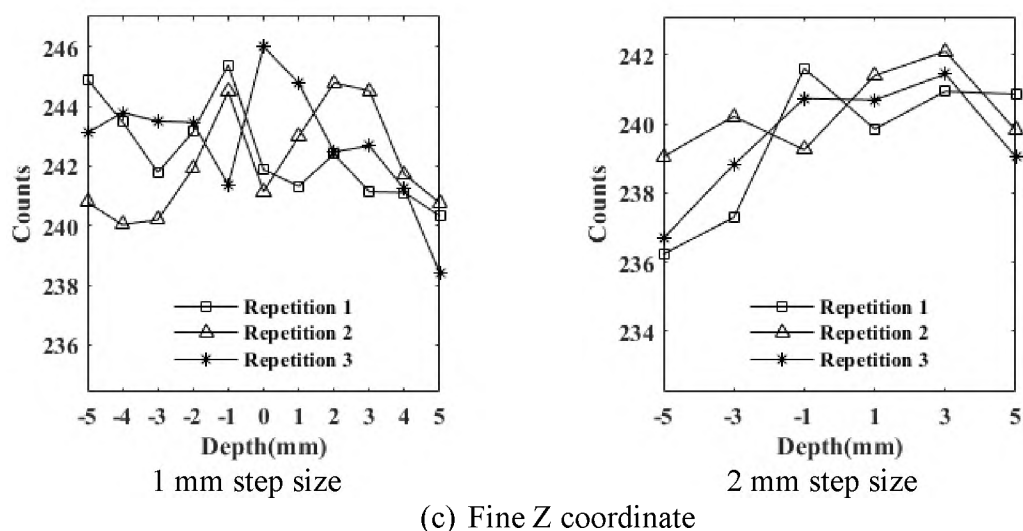


Figure 6. Comparisons between 1 mm and 2 mm step sizes for fine coordinates seeking (cont.)

(7) Determining the actual coordinate

From the coarse seeking and fine seeking coordinates, the actual coordinate can be determined. For example, in Figure 5, the coarse depth of the radioactive particle is 30 mm from the top of the packed bed. From the fine seeking coordinate ranging in 25 – 35 mm, it can be seen that at +3 mm position it has the highest counts with minimum error bar. Hence, the actual coordinate (depth) of Z direction would be 33 ± 1 mm.

(8) Fishing the particle

A fishing tool with a magnetic head (7.63 mm in diameter, Figure 7) is used to fish the radioactive particle since the Co-60 is magnetic. From the actual coordinates obtained from coarse and fine seeking coordinates, it is easy to locate and insert this tool inside the packed bed to fish the particle. The advantage of this tool is that there is no necessary to remove all the catalysts and load them again. In this way, it is able to minimize the disturbance to the packed bed configuration. However, sometimes when the particle goes

very deep inside the packed bed, where it is very difficult to use the fishing tool, removing all the catalysts from the bottom by opening the mesh gate valve would be a better option. After that, the whole procedure will be repeated for the next experiment.

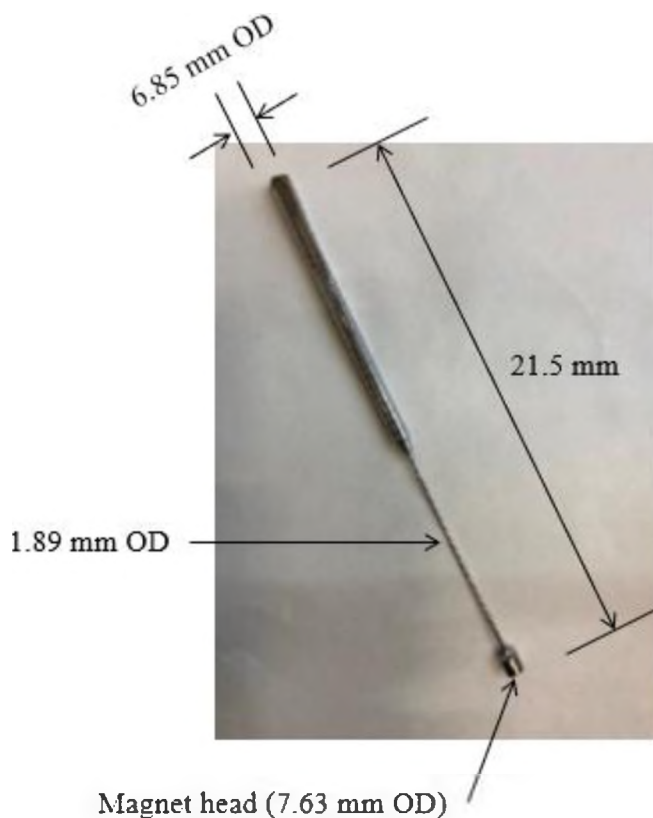


Figure 7. Magnetic fishing tool

3.2. VALIDATION OF THE LOCATION IDENTIFICATION SYSTEM OF DYNAMIC RADIOACTIVE PARTICLE TRACKING TECHNIQUE

Validation of the capability and reliability, as well as the accuracy is always necessary for a newly developed experimental system. In order to validate the newly developed DRPT system, the Co-60 particle was placed in a known location by putting it in a capsule as shown in Figure 8. The capsule is around 4 cm long and the Co-60 particle is

located at around 38 mm due to the thickness of the tip. The capsule was vertically inserted into the bed at a random location with around 5 mm left above the top line of the bed for better visualization and taking a picture. Based on the picture (Figure 9) that was taken from the top view, with AutoCAD it can be found that the actual coordinate of the Co-60 particle is $[-23, 26.6, 33]$ mm as shown in Figure 10.

For validation, even coarse seeking coordinate step was repeated 3 times to show the accuracy of the system as shown in Figure 11. All 3 repetitions give exact the same coarse coordinate which is $[-20, 30, 30]$ mm. In view of this, it is not necessary to repeat 3 times for the coarse seeking coordinate steps during real experiments. The fine coordinate of the Co-60 particle is $[-3, -3, 3]$ mm as shown in Figure 12. By combining the coarse and fine coordinates, the actual coordinate of the Co-60 particle for validation is $[-23 \pm 1, 27 \pm 1, 33 \pm 1]$ mm, which is solid validation of the newly developed DRPT system.

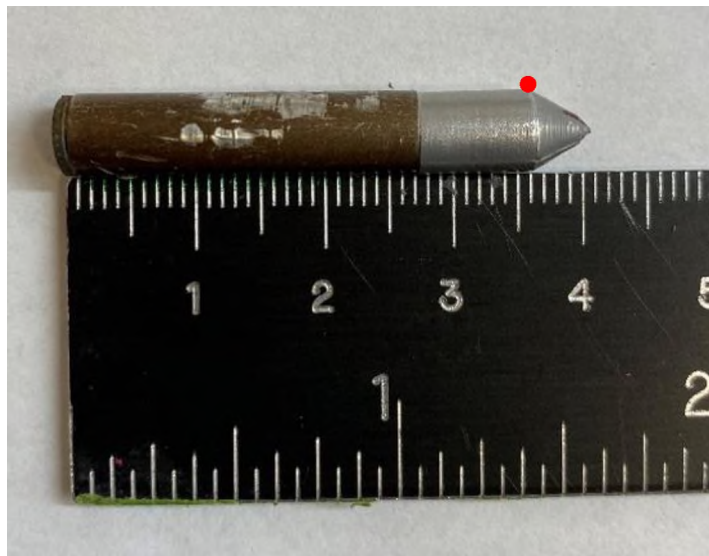


Figure 8. Co-60 in a capsule

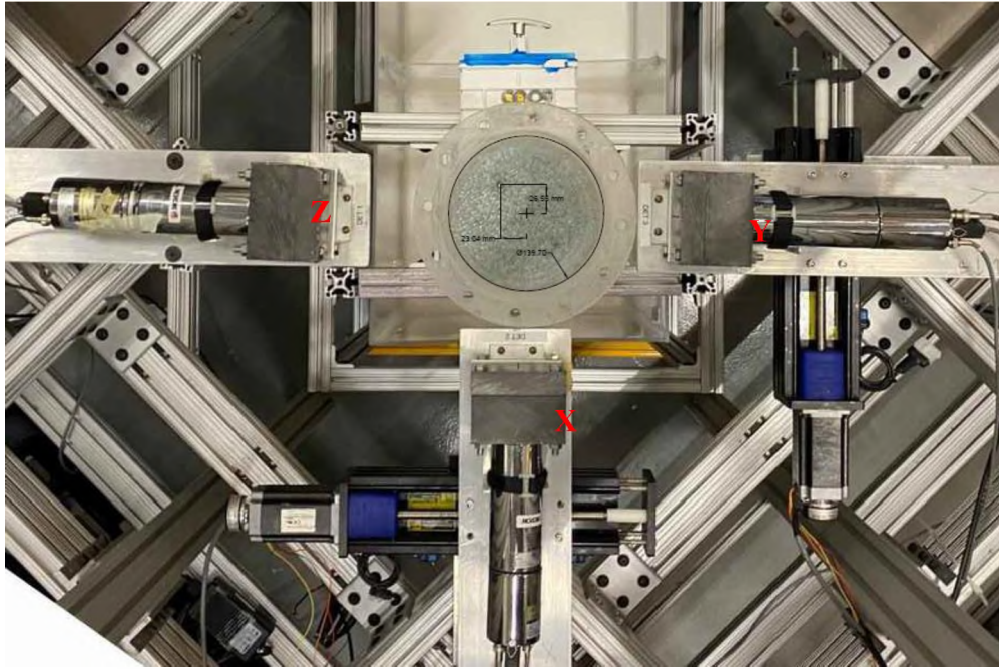
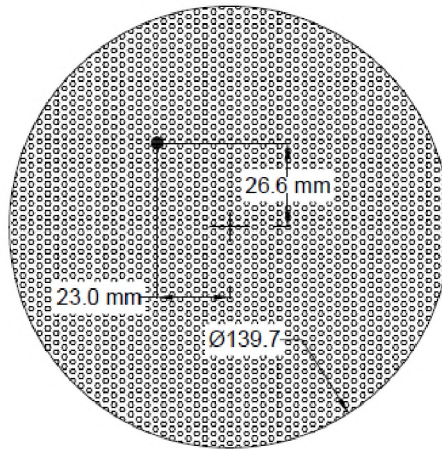
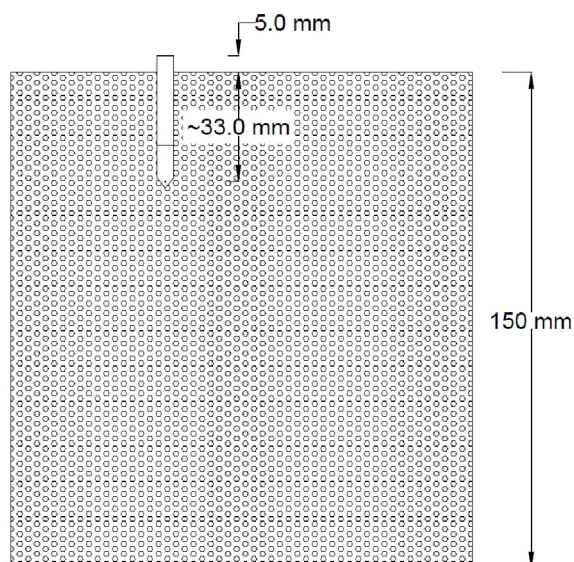


Figure 9. Top view picture of validation



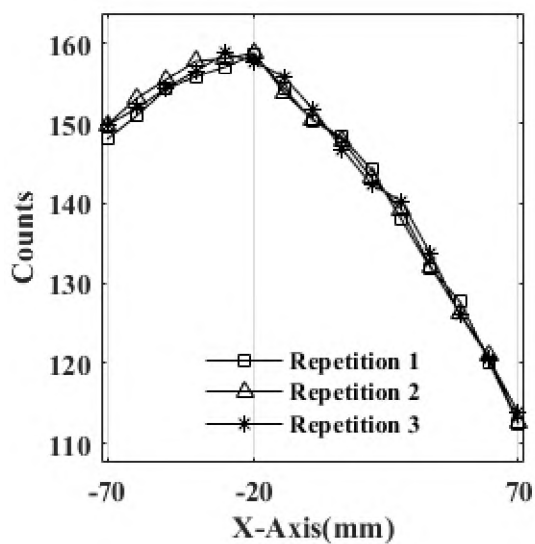
(a) Top view of the schematic of the Co-60 location

Figure 10. Schematic of the Co-60 location for validation



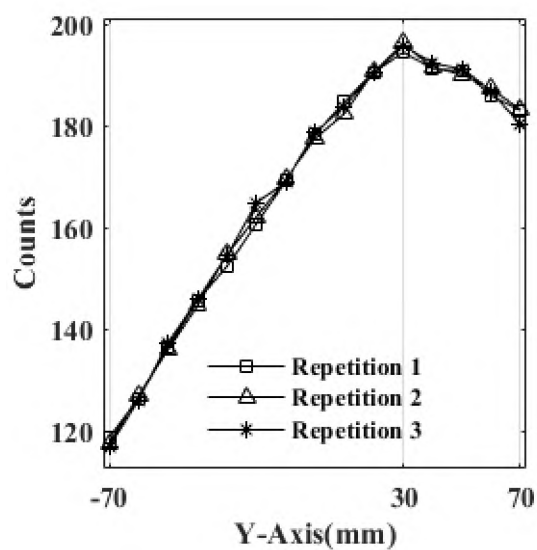
(b) Side view of the schematic of the Co-60 location

Figure 10. Schematic of the Co-60 location for validation (cont.)

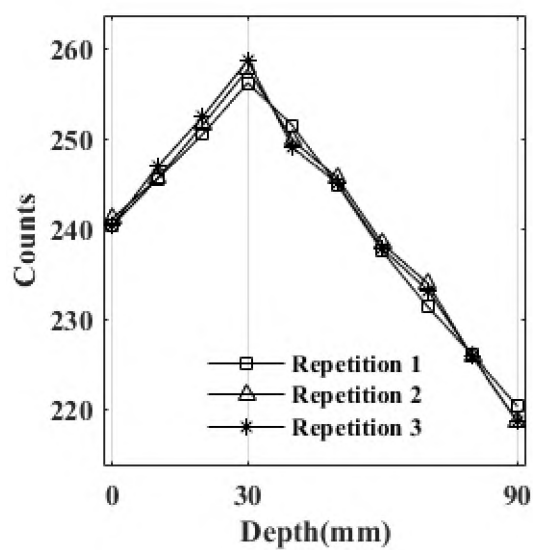


(a) Coarse X coordinate

Figure 11. Coarse coordinates of the Co-60 location for validation

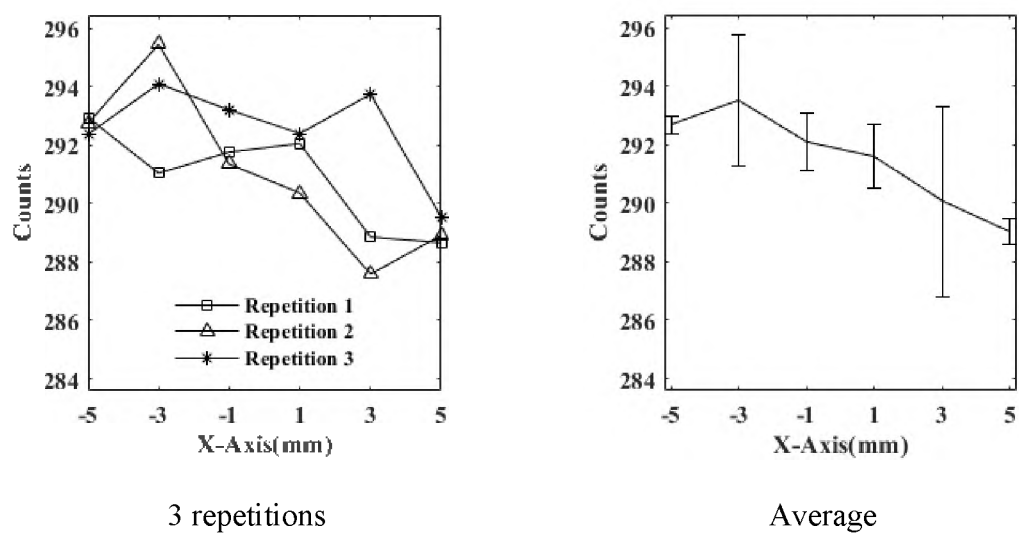


(b) Coarse Y coordinate

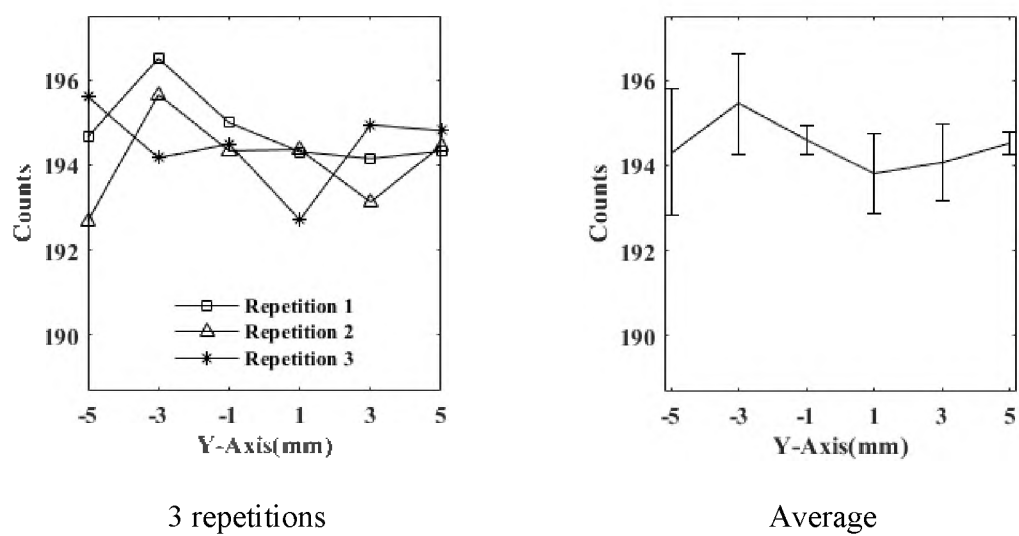


(c) Coarse Z coordinate

Figure 11. Coarse coordinates of the Co-60 location for validation (cont.)

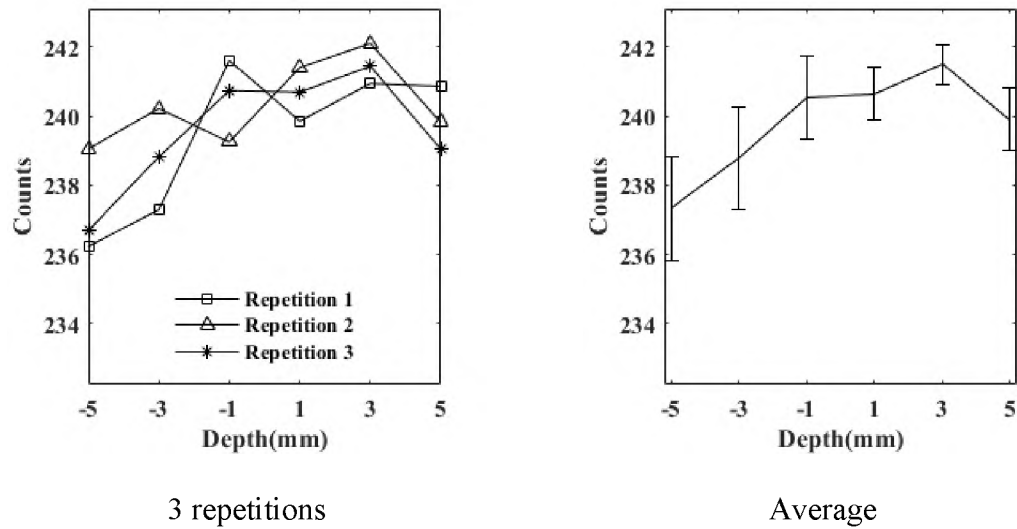


(a) Fine X coordinate



(b) Fine Y coordinate

Figure 12. Fine coordinate of the Co-60 particle with 2 mm step size before and after averaging



(c) Fine Z coordinate

Figure 12. Fine coordinate of the Co-60 particle with 2 mm step size before and after averaging (cont.)

4. RESULTS AND DISCUSSION

For each catalyst shape, 30 experiments were repeated by following the procedure described in the previous section. All the coordinates of the heavy metal accretion locations are projected in the 3D plots as shown in Figure 13. It can be observed that all catalyst shapes have similar radius distribution, while spherical catalyst has larger axial distribution range. In order to characterize the uncertain data due to the randomness of this experimental work, probability density distribution was estimated based on the results. There are two statistical analysis methodologies which are parametric and nonparametric procedures [17]. Parametric analysis is based on large amount of sample data which can give the statistical parameters such as mean, standard deviation, and variance. In other words, the parametric analysis assumes that data is normally distributed. However, nonparametric

analysis has no assumption about the population, which is not based on the parameters of a normal distribution. The most common way to do nonparametric estimation is the histogram. However, the histogram has difficulties to represent smooth continuous function and bivariate or trivariate data [18]. Therefore, in this work, kernel density estimator (KDE) [18,19] was used to estimate the probability density distribution as a continuous function, which is feasible for small population as in such work. The KDE is defined as Equation (1):

$$f(x) = \frac{1}{nh^d} \sum_{i=1}^n K\left(\frac{x - X_i}{h^d}\right) \quad (1)$$

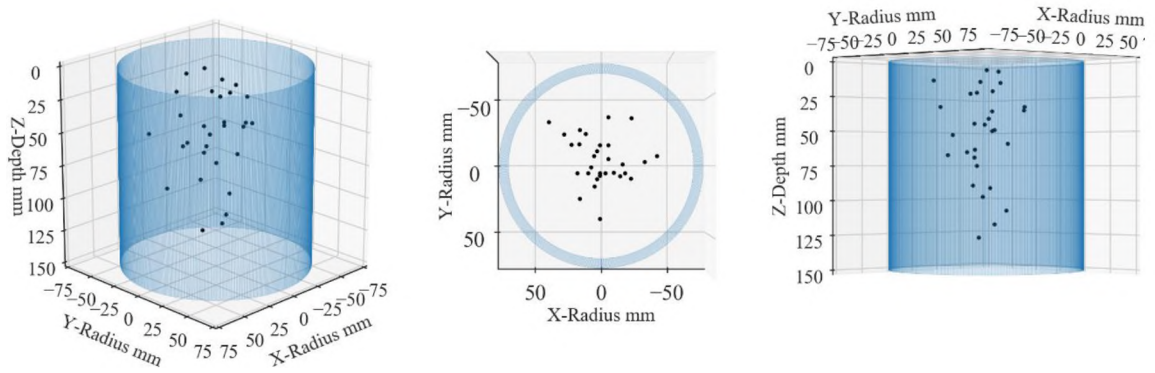
where n is the total sample number, h^d is the bandwidth for d dimensions multivariate KDE, K is the kernel density function and the common ones are listed in Table 2, X_i is the value of i th observation.

In this case, the Gaussian kernel density function was used as plotted in Figure 14. The probability density distributions of four catalyst shapes are quite similar to the observation.

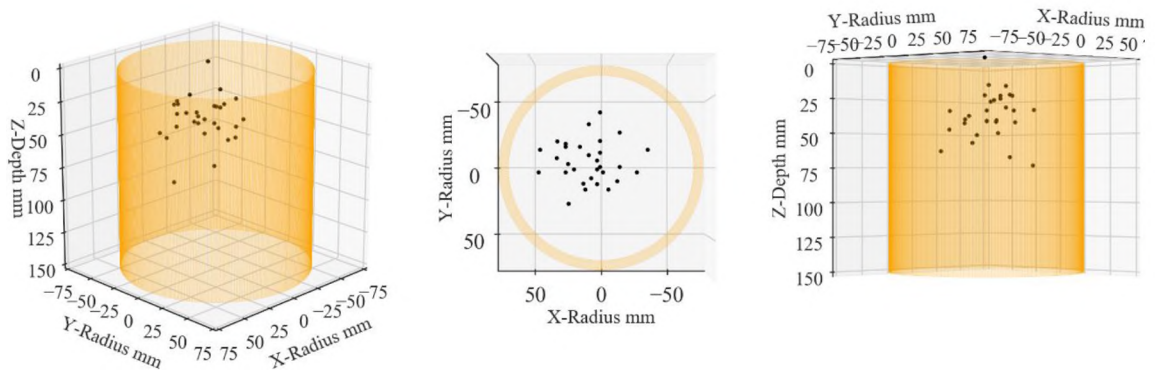
In terms of radius, all of them have similar probability density distribution and the highest probability is at around $r = 20 \text{ mm}$. In terms of height, spherical catalyst has larger distribution range than the other types do. However, all of them have the highest probability at around $z = 50 \text{ mm}$. Recalling the bed porosity of each catalyst shape in Table 1, spherical shape has the lowest bed porosity while trilobe and quadrilobe shapes have similar bed porosity, which means, theoretically the heavy metal should have more chance to pass through and deposit at lower locations in the trilobe or quadrilobe beds, however, the experimental data indicate otherwise. The particles get stuck in a higher position in

extrudate catalysts (tri, quad, cylinders), because the void space distribution is more tortuous. This means, the free paths for the particle to flow through are more intricate. In spherical catalyst, such free paths are longer and less intricate. Therefore, the void space distribution on a bed packed with spheres is less tortuous. An indicative of the tortuosity and the intricate of such porous matrix can be found to be related to the pressure drop. Al-Ani et al. [16] investigated the effects of all these 4 catalyst shapes on the pressure drop and liquid holdup in a 6 inch TBR, indicating that spherical shape has the lowest liquid holdup and pressure drop along the bed height while the other shapes have similar holdups and pressure drops as shown in Figure 15. Extruded catalysts have a higher pressure drop, which is physically explained due to the fact that these shapes provide higher resistances for the liquid to flow (because of the intricate porous structure). Hence, it can be observed that an insight into the contaminants final position in a TBR can be obtained by looking at tortuosity of the bed, which can be inferred by the pressure drop of the system and the bed structure and porosity. The reason why all catalyst shapes have similar radial probability density distributions can be explained similarly. When liquid flows inside the cylindrical, trilobe and quadrilobe beds, due to the random packing, the horizontal oriented catalysts act as guides leading the water to disperse further in the radial direction. However, because of high pressure drop, in other words, high momentum loss, the liquid velocity (kinetic energy) is not high enough to push the particle sideways. When the liquid flows inside the spherical bed, since there are no horizontal guides leading water to flow sideways, the liquid flows along the least resistant path. However, because of the compact structure of spheres which leads to low porosity, it is hard for the particle to pass through the little space among these spherical catalysts. Instead, the liquid wave might be able to push the particle

away from the center towards to the wall until reaching the maximum liquid distribution location. Therefore, the combination of pressure drop and tortuosity determine the phenomena showing in the results.

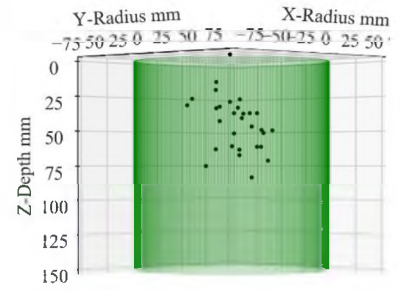
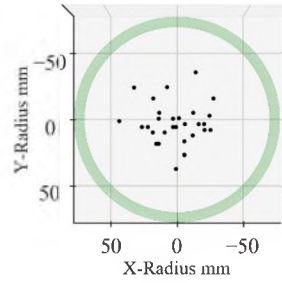
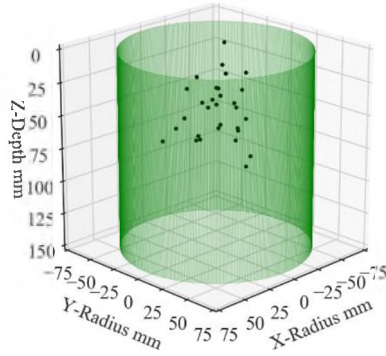


(a) Particle distribution inside spherical catalyst bed

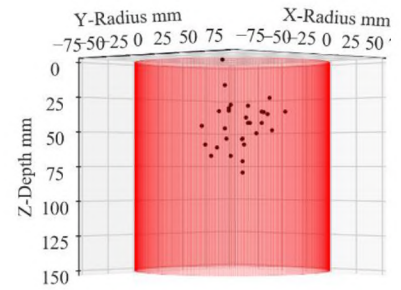
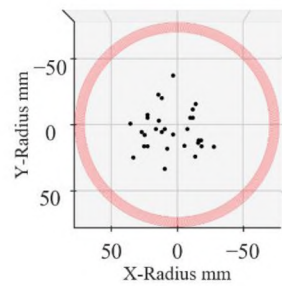
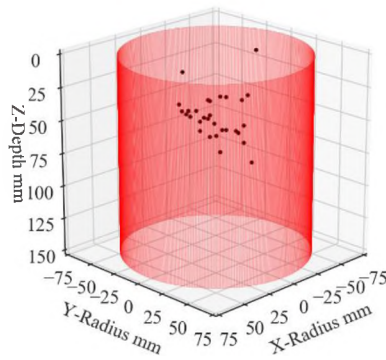


(b) Particle distribution inside cylindrical catalyst bed

Figure 13. Particle distribution inside different catalyst beds



(c) Particle distribution inside trilobe catalyst bed



(d) Particle distribution inside quadrilobe catalyst bed

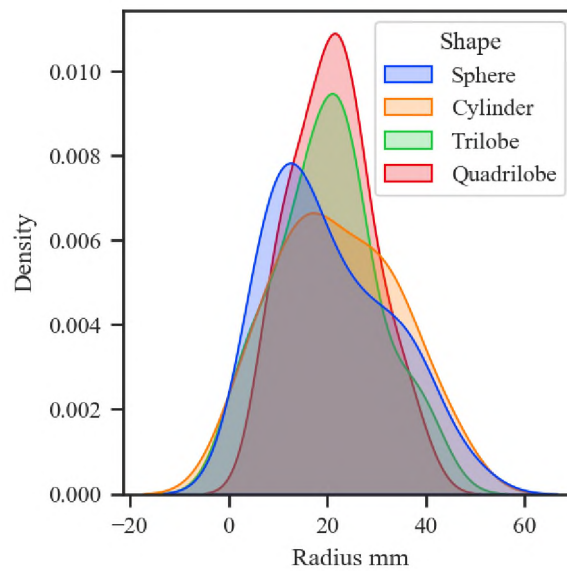
Figure 13. Particle distribution inside different catalyst beds (cont.)

Table 2. Kernel density functions

Name	$K(x)$
Epanechnikov	$\frac{3}{4} \left(1 - \frac{1}{5} x^2\right) / \sqrt{5}$ for $ x < \sqrt{5}$
	0 otherwise
Biweight	$\frac{5}{6} (1 - x^2)^2$ for $ x < 1$
	0 otherwise

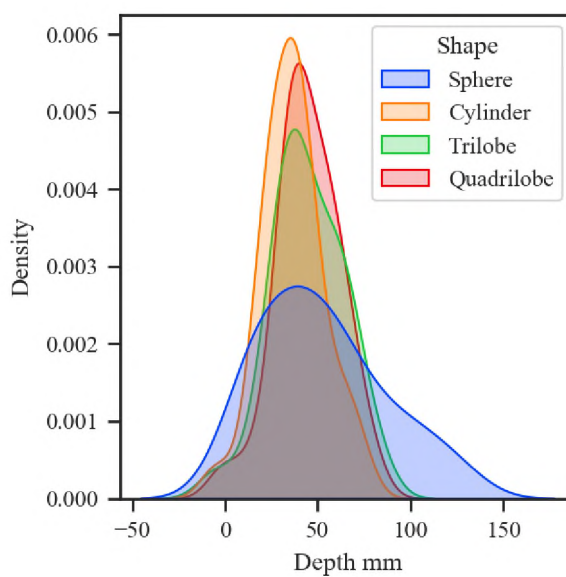
Table 2. Kernel density functions (cont.)

Name	$K(x)$
Triangular	$1 - x $ for $ x < 1$
	0 otherwise
Gaussian	$\frac{1}{\sqrt{2\pi}} \exp -\frac{1}{2} x^2$
Rectangular	$\frac{1}{2}$ for $ x < 1$
	0 otherwise

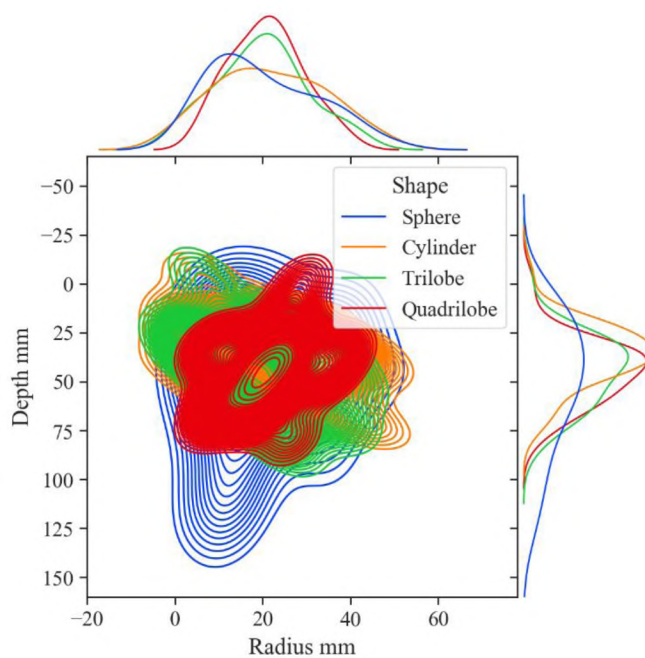


(a) Kernel density estimation of heavy metal accretion locations in terms of radius

Figure 14. Kernel density estimation of heavy metal accretion locations

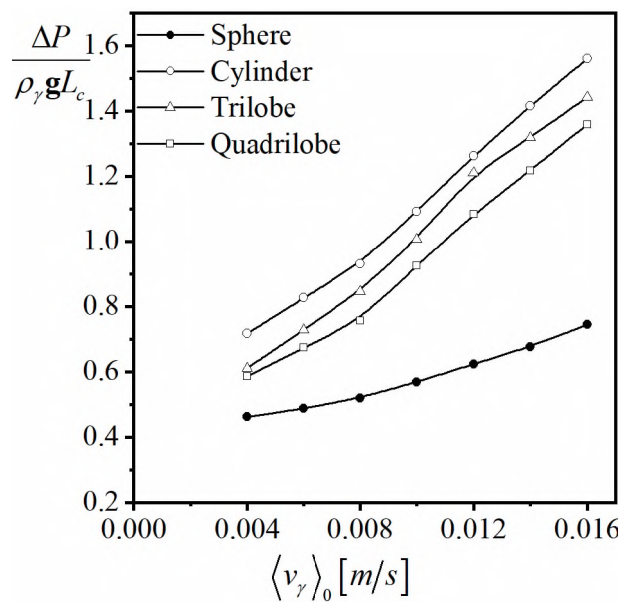


(b) Kernel density estimation of heavy metal accretion locations in terms of depth

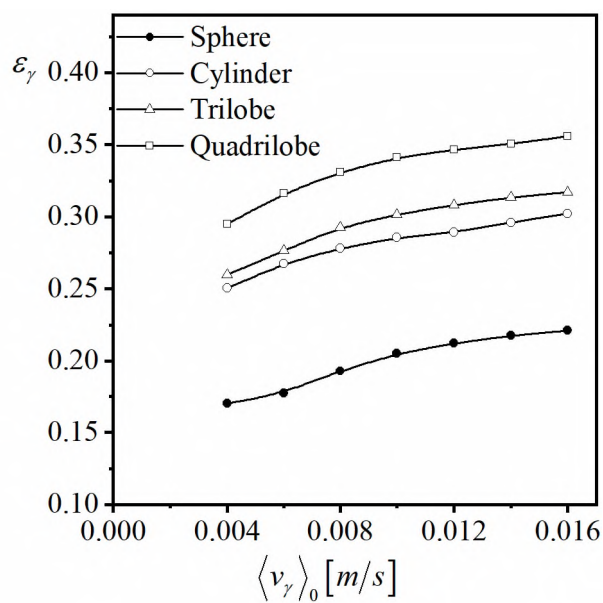


(c) Jointplot of Kernel density estimation of heavy metal accretion locations

Figure 14. Kernel density estimation of heavy metal accretion locations (cont.)



(a) Pressure drop in different catalyst beds at gas velocity 0.06 m/s



(b) Liquid holdup in different catalyst beds at gas velocity 0.06 m/s

Figure 15. Pressure drop and liquid holdup in different catalyst beds for various liquid velocities at gas velocity 0.06 m/s

5. REMARKS

We have developed a new method to seek the coordinates of the radioactive particle mimicking the heavy metal accretion inside a Trickle Bed Hydrotreating Reactor, using a modified dynamic radioactive particle tracking system (DRPT). The resolution obtained by the coarse and fine coordinates is high enough to clearly identify the location of the radioactive particle and to validate the capacity and reliability of this newly developed DRPT system. We have identified the location of the radioactive using a study on different catalysts shapes by accurately determining:

(1) The probability density distributions by using Kernel Density Estimator (KDE).

The results show that in terms of:

- Radius: all the catalysts have similar probability density distribution, and the highest probability is at around $r = 20 \text{ mm}$.
- Height: the spherical catalyst has larger distribution range than the other types do.

(2) The heavy metal accretion is directly related to the pressure drops along the bed height which indicate the bed porosity and intricate bed structure in catalyst packed beds. Heavy metals have more chance to deposit at higher levels of packed beds with higher pressure drops for the extrudate catalyst shapes such as cylinder, trilobe, and quadrilobed.

FUNDING

This research did not receive any specific grant from funding agencies in the public, commercial, or not-for-profit sectors.

REFERENCES

- [1] V. V. Ranade, R. V. Chaudhari, P.R. Gunjal, Introduction, Trickle Bed React. React. Eng. Appl. (2011) 1–23. <https://doi.org/10.1016/b978-0-444-52738-7.10001-4>.
- [2] P. Dufresne, Hydroprocessing catalysts regeneration and recycling, Appl. Catal. A Gen. 322 (2007) 67–75. <https://doi.org/10.1016/j.apcata.2007.01.013>.
- [3] M.D. Argyle, C.H. Bartholomew, Heterogeneous catalyst deactivation and regeneration: A review, Catalysts. 5 (2015) 145–269. <https://doi.org/10.3390/catal5010145>.
- [4] P.W. Tamm, H.F. Harnsberger, A.G. Bridge, Effects of Feed Metals on Catalyst Aging in Hydroprocessing Residuum, Ind. Eng. Chem. Process Des. Dev. 20 (1981) 262–273. <https://doi.org/10.1021/i200013a014>.
- [5] B.M. Vogelaar, S. Eijsbouts, J.A. Bergwerff, J.J. Heiszwolf, Hydroprocessing catalyst deactivation in commercial practice, Catal. Today. 154 (2010) 256–263. <https://doi.org/10.1016/j.cattod.2010.03.039>.
- [6] M.J. Saxton, K. Jacobson, Single-particle tracking: Applications to membrane dynamics, Annu. Rev. Biophys. Biomol. Struct. 26 (1997) 373–399. <https://doi.org/10.1146/annurev.biophys.26.1.373>.
- [7] H.G. Maas, A. Gruen, D. Papantoniou, Particle tracking velocimetry in three-dimensional flows - Part 1. Photogrammetric determination of particle coordinates, Exp. Fluids. 15 (1993) 133–146. <https://doi.org/10.1007/BF00190953>.
- [8] V. Khane, M.H. Al-Dahhan, Hybrid dynamic radioactive particle tracking (RPT) calibration technique for multiphase flow systems, Meas. Sci. Technol. 28 (2017). <https://doi.org/10.1088/1361-6501/aa5c27>.
- [9] V. Khane, I.A. Said, M.H. Al-Dahhan, Experimental investigation of pebble flow dynamics using radioactive particle tracking technique in a scaled-down Pebble Bed Modular Reactor (PBMR), Nucl. Eng. Des. (2016). <https://doi.org/10.1016/j.nucengdes.2016.03.031>.
- [10] V.B. Khane, M.H. Al-Dahhan, Study of solids movement in pebble bed/moving bed reactors using radioactive particle tracking (RPT) technique, in: 7th World Congr. Ind. Process Tomogr., 2014.
- [11] V. Khane, I.A. Said, M.H. Al-Dahhan, Assessment of performing experimental investigation on a pebble bed modular reactor (PBMR) as a static packed bed approximation, Ann. Nucl. Energy. (2017). <https://doi.org/10.1016/j.anucene.2016.11.020>.

- [12] M.K. Al Mesfer, A.J. Sultan, M.H. Al-Dahhan, Study the effect of dense internals on the liquid velocity field and turbulent parameters in bubble column for Fischer–Tropsch (FT) synthesis by using Radioactive Particle Tracking (RPT) technique, *Chem. Eng. Sci.* 161 (2017) 228–248. <https://doi.org/10.1016/j.ces.2016.12.001>.
- [13] T. Al-Juwaya, N. Ali, M. Al-Dahhan, Investigation of hydrodynamics of binary solids mixture spouted beds using radioactive particle tracking (RPT) technique, *Chem. Eng. Res. Des.* (2019). <https://doi.org/10.1016/j.cherd.2019.05.051>.
- [14] B. Qi, S. Uribe, O. Farid, M. Al-Dahhan, Development of a hybrid pressure drop and liquid holdup phenomenological model for trickle bed reactors based on two-phase volume averaged equations, *Can. J. Chem. Eng.* (2020). <https://doi.org/10.1002/cjce.23892>.
- [15] B. Qi, O. Farid, S. Uribe, M. Al-Dahhan, Maldistribution and dynamic liquid holdup quantification of quadrilobe catalyst in a trickle bed reactor using gamma-ray computed tomography: Pseudo-3D modelling and empirical modelling using deep neural network, *Chem. Eng. Res. Des.* 164 (2020) 195–208. <https://doi.org/10.1016/j.cherd.2020.09.024>.
- [16] M. Al-Ani, M. Al-Dahhan, Effect of catalyst shape on pressure drop and liquid holdup in a pilot plant trickle bed reactor, *Fuel*. (2021). <https://doi.org/10.1016/j.fuel.2020.118860>.
- [17] D.J. Sheskin, *Parametric and non parametric statistical procedures: Third edition*, 2003.
- [18] U. Diwekar, A. David, *BONUS Algorithm for Large Scale Stochastic Nonlinear Programming Problems*, 2015.
- [19] B.W. Silverman, *Density estimation: For statistics and data analysis*, 2018. <https://doi.org/10.1201/9781315140919>.

IV. EXPERIMENTAL AND MATHEMATICAL MODELLING INVESTIGATION OF HYDRODYNAMICS IN TRICKLE BED REACTORS OF RANDOM PACKED TRILOBE CATALYST BED

Binbin Qi¹, Sebastián Uribe¹, Muthanna Al-Dahhan^{1,2*}

¹ Chemical and Biochemical Engineering Department, Missouri University of Science and Technology, Rolla, MO 65409 USA

² Mining and Nuclear Engineering Department, Missouri University of Science and Technology, Rolla, MO 65409, USA

* Corresponding author: aldahhanm@mst.edu

ABSTRACT

An efficient packing scheme was implemented to randomly pack a vast number of trilobe catalyst to represent the TBR based on the rigid body approach. The generated geometry was used to define the computational domain for the two-phase hydrodynamics simulation based on the volume of fluids (VOF) approach. This hydrodynamics modelling study is paired with an experimental study using our in-house developed advanced measurement techniques based on optical fiber probes, which allowed to determine local liquid velocity and saturation profiles. The experimental measurements were used for local validation of the implemented model.

Keywords: Trickle Bed Reactor, CFD, Trilobe, Random packing, Optical probe, Hydrodynamics.

1. INTRODUCTION

Trickle bed reactors (TBRs) are widely used in petrochemical, chemical and refinery fields such as petroleum processing, hydrogenation reactions, oxidation reactions, esterification, and F-T synthesis etc. [1] In the past few decades, vast research efforts have been devoted to study the hydrodynamics of these systems, such as characterizing the gas/liquid holdups and their distributions, pressure drops, and wetting efficiency, either through experiments or by mathematical modeling through computational fluid dynamics (CFD) techniques [1–11]. In general, most experimental work focuses on measuring the macroscopic hydrodynamic behaviors in these reactors, such as overall pressure drops, overall holdups, and residence time distribution. On these investigations, scarce information was obtained regarding the local scale hydrodynamic phenomena due to the limitations of the applied measurement techniques, such as systematic errors in the measurements under harsh operation conditions.

In order to overcome the limitations in the experimental studies of TBRs, mathematical modeling through CFD techniques has gained increasing interest in recent years. This CFD modeling approach to study TBRs allows to provide predictions of the local scale multiphase flow phenomena. However, due to the complexity of the multiphase flow in these systems, which results in a highly non-linear mathematical model, and the intricate porous media generated by the packing, the level of detail in the predictions is limited by both the assumptions to deal with the textural characteristics of the bed and the available computational resources [12,13]. In general, there are two main approaches to

represent the geometrical characteristics of TBRs in CFD modeling, i) effective porous media approach and ii) discrete particle approach.

The effective media approach uses a porosity distribution function to macroscopically represent the porosity distribution inside the packed beds, typically with oscillatory correlations [14–17] or exponential correlations [18,19]. As so far, the majority of the CFD modeling works rely on the effective media approach, as it can simulate pilot scale reactors with a low computational cost. However, by implementing this approach the level of detail in the local predictions is compromised. These models can only provide predictions of overall or average parameters, such as the liquid distribution and average phase holdups inside the packed beds without detailed local information such as local liquid velocities. This implies that certain undesired phenomena caused by the random packing of the beds, such as bypass channeling, backmixing and dead zones, cannot be predicted.

On the other hand, the discrete particle approach explicitly incorporated the intricate bed structure through the inclusion of the solid-fluid interfacial area in the computational domain. By incorporating such level of detail, fundamental understanding of the effects of bed geometry on transport phenomena of the two-phase flow and the multiphase interactions, as well as detailed local information of each phase, can be obtained. Despite the advantages of this approach, scarce contributions have been conducted using discrete particle approach in multiphase (gas-liquid-solid) CFD modeling, and mostly have only considered the ordered packing of spherical particles [3,20–24]. However, extrudate catalyst shapes are more commonly used in real industries because they provide better pressure drops, therefore better liquid holdups distributions [9,25], and the solids distribution is random. The lack of works implementing discrete particle

approach for TBRs randomly packed with extrudates can be attributed to two main challenges, i) the generation of the random packing, and ii) the meshing of the intricate computational domain.

A promising technique to simulate the bed packing is the discrete element method (DEM) [26], which was developed for modelling the granular flow such as sand, particles or powders based on spherical shapes. One of the common approaches to simulate complex shapes such as cylinders, trilobes, and quadrilobes, is to approximate their shapes by overlapping large number of spheres as representations, then using DEM to conduct random packing, which requires vast computational resources. Because these complex shapes are made of overlapping spheres, there are continuous curvatures on the surfaces of these particle which result in difficulties when meshing the geometries for the CFD model. In addition, during the DEM simulation, there are chances that these particles have overlaps creating acute angles, which also represent important challenges in the mesh generation.

In order to develop a modeling scheme to implement discrete particle approach for a TBR packed with extrudate catalysts, in this work, first an efficient packing scheme was implemented to randomly pack a vast number of extruded catalysts to represent the TBR, based on a rigid body approach. Then, the generated geometry was used to define the computational domain for the two-phase hydrodynamics simulation. A work scheme to avoid overlapping of the solid particles, and to avoid issues in the mesh generation is presented. Finally, the obtained computational domain is used for implementing a two-phase hydrodynamics model based on the volume of fluids (VOF) approach. This hydrodynamics modelling study is paired with an experimental study using our in-house developed advanced measurement techniques based on optical fiber probes, which allowed

to determine local liquid velocity and saturation profiles. The experimental measurements were used for local validation of the implemented model.

2. RANDOM PACKING OF TRILOBES

As mentioned above, DEM has been widely implemented to generate random packed bed structures, which takes into consideration of deformation by treating particles as soft bodies due to the acting forces [26,27]. It calculates the contacting forces between the particles using momentum balance equation by taking into account of Young's modulus, restitution, and friction etc. leading to very high computational cost. The details of DEM have been reported at length in many literatures [17,26–32]. Recently, there is growing interests in rigid body approach that treat particles as idealized bodies that no deformations happen even with acting forces [33]. Since most catalyst materials are robust and rigid, it is reasonable to assume that rigid body approach is feasible for catalyst packing. The rigid body approach uses the Newton-Euler equation (Equation (1)), which is obtained by applying Newton's second law twice considering rotational motion and translational motion, to describe the net force \mathbf{f} acting on the body (Equation (2)) and net rotation moment (torque) τ (Equation (3)) [33].

$$\begin{pmatrix} \mathbf{f} \\ \tau \end{pmatrix} = \begin{pmatrix} m\mathbf{I}_3 & 0 \\ 0 & \mathbf{I} \end{pmatrix} \begin{pmatrix} \mathbf{a} \\ \alpha \end{pmatrix} + \begin{pmatrix} 0 \\ \omega \times \mathbf{I}\omega \end{pmatrix} \quad (1)$$

$$\mathbf{f} = \frac{d(m \cdot \mathbf{v})}{dt} \quad (2)$$

$$\tau = \frac{d(\mathbf{I} \cdot \omega)}{dt} \quad (3)$$

where m is the mass of the body, \mathbf{I}_3 is the 3×3 identity matrix, \mathbf{I} is the moment of inertia, ω is the angular velocity, α is the angular acceleration, \mathbf{a} is the acceleration, \mathbf{v} is the velocity of the body.

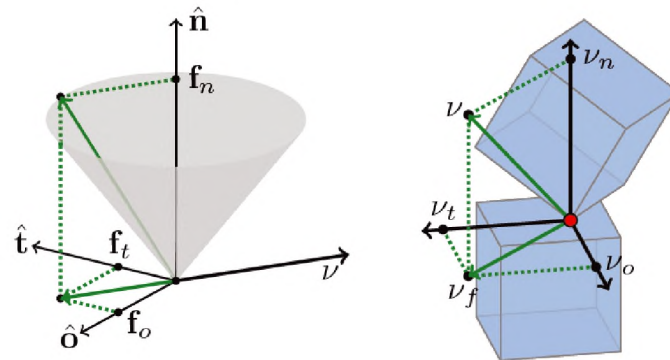
The contact force between bodies is described by the Coulomb friction model (Equation (4)) that contains one normal component \mathbf{f}_n and two tangential components, \mathbf{f}_t and \mathbf{f}_o as shown in Figure 1. Correspondingly, the relative velocity at the touching point \mathbf{v} is decomposed into v_n , v_t , and v_o .

$$F(\mathbf{f}_n, \mu) = \mu^2 \cdot \mathbf{f}_n^2 - \mathbf{f}_t^2 - \mathbf{f}_o^2 \quad (4)$$

$$\mathbf{f}_t = \frac{-\mu \cdot \mathbf{f}_n \cdot v_t}{\beta} \quad (5)$$

$$\mathbf{f}_o = \frac{-\mu \cdot \mathbf{f}_n \cdot v_o}{\beta} \quad (6)$$

where μ is the friction coefficient, $\beta = \sqrt{v_t^2 + v_o^2}$ is the sliding velocity at the contacting point.



(a) Friction cone

(b) Contact velocity

Figure 1. Schematic of decomposition of friction cone and contact velocity

A comprehensive comparison between using rigid body approach and DEM to generate random packings of sphere, cylinder, Raschig ring, and other complex particles has been conducted by Flaischlen and Wehinger [34] in terms of porosity distribution, particle alignment, and simulation time. They concluded that both methods have satisfying accuracy to predict porosity distribution against the experimental data from literatures. However, rigid body approach presents the particle orientations more accurately than DEM does. Most importantly, rigid body approach is way more efficient than DEM simulations, especially for packing complex particles.

It has been claimed in literature [35–38] that the open source software Blender (based on Python language) has promising performance in simulating random packings of complex particles using rigid body approach. Hence, in this work, Blender was used to realistically generate the random packing of trilobe particles ($d_p=3.93$ mm) in a cylinder of 5 cm (2 inch) in diameter and the bed height is 10 cm. A total of 2917 trilobe particles were required to fill the column as shown in Figure 2, where the column-to-particle diameter ratio as 12.5.

In Blender, four main parameters need to be specified and tuned to generate the packings, particle triangle number, restitution factor, friction factor, and simulation time step. Blender presents the particle shapes with “watertight” meshes by splitting the surfaces into triangles (refinement level) leading to smoother surfaces [36]. Restitution factor indicates the kinetic energy ratio between post-collision and pre-collision, while friction factor determines the sliding resistance besides collision between particles [36]. The simulation parameters are listed in Table 1.

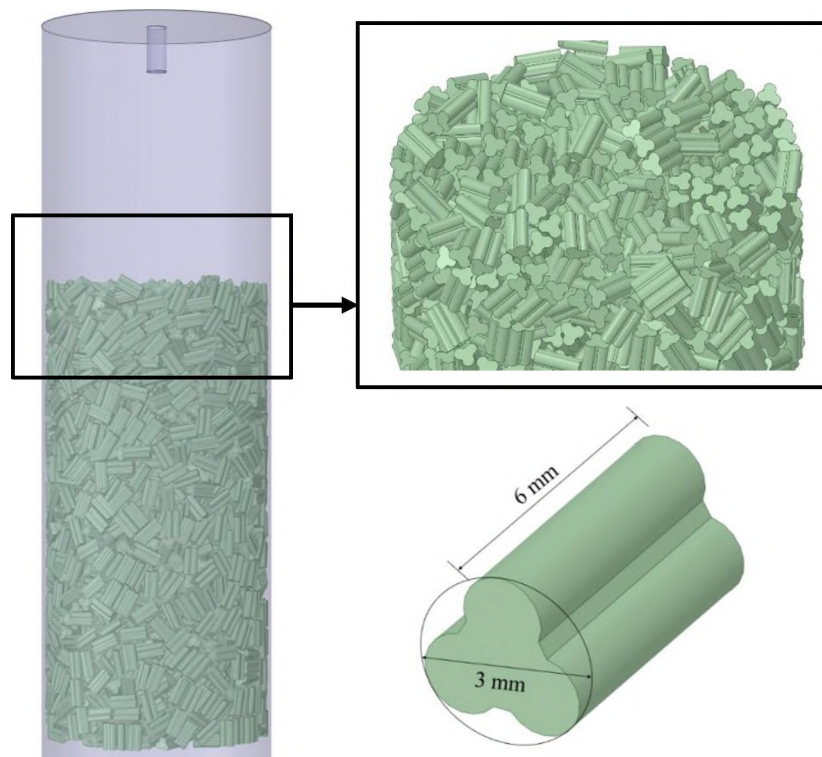


Figure 2. Random packing of trilobe particles

Table 1. Random packing simulation parameters

Property	Value
Refinement level (No. of particle triangles)	1000
Friction factor	0.15
Restitution factor	0.85
Simulation time step [s]	0.05

3. MESH GENERATION

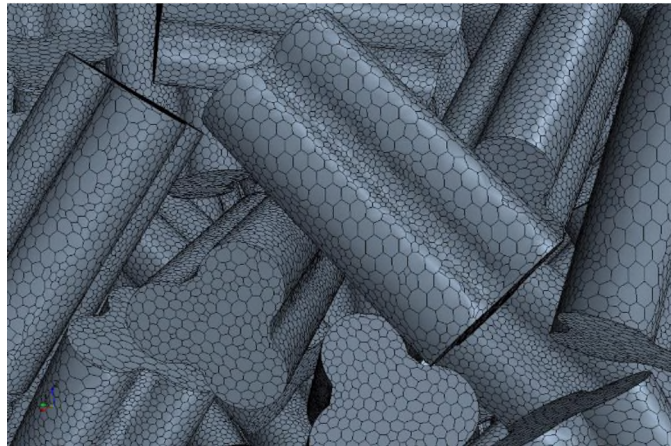
The generated geometry was then exported as STereoLithography (STL) file, which was then imported into StarCCM+ 13.04 to generate the computational domain.

However, one main challenge was the overlap or contact between particles and defective surfaces, which is so-called “dirty geometry” that may cause high skewness in the generated mesh, resulting in the failure in mesh generation. A common approach to deal with this issue is to shrink the particles to avoid the contact or overlap. However, the particle shrinkage, η , which is defined in terms of the actual particle diameter (d) and the diameter after shrinkage (d_{CFD}) as per Equation (7), directly affects the bed porosity in linear correlation [39]. It has been observed that a 1% shrinkage can cause the bed porosity to increase 3%. A 10% porosity deviation can result in over 30% error in pressure drop, while it is desired to have pressure drop error within 10%, which suggests the particle shrinkage to be no more than 1% [39]. Therefore, before importing the STL file into mesh generation, all the particles were shrunk by 1% to eliminate most contacts or overlaps. However, even with 1% overall shrinkage, still there were very few overlaps or contacts existing. The STL file was then imported into Ansys SpaceClaim to adjust the particle orientation or shrink manually and to fix some surface defects using the automatic repair tools. The bed overall porosity after shrinkage is 0.4594 which is 3.7% less than the original bed porosity 0.4428. The clean geometry was then imported into StarCCM+ to generate mesh in the flow domain. The mesh generation specifications for the packed bed are listed in Table 2.

$$\eta = \frac{d - d_{CFD}}{d} \quad (7)$$

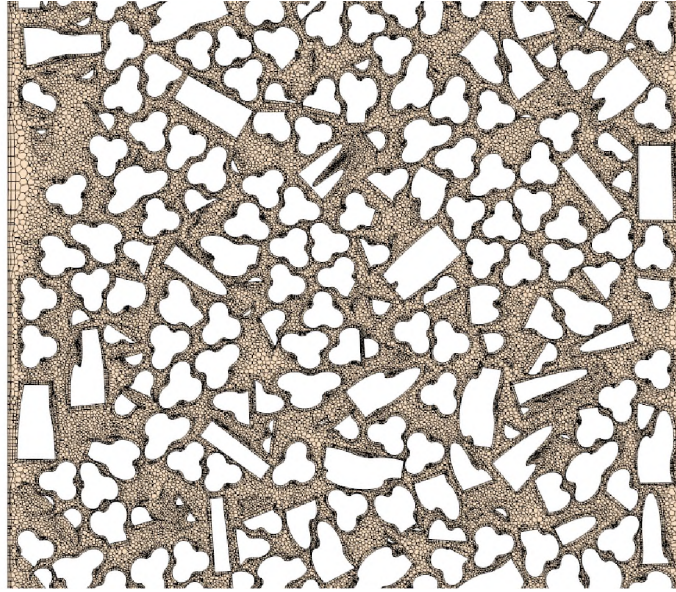
Table 2. Mesh generation specifications

Property	Value/Remark
Mesh type	Polyhedral mesh
Base size [mm]	0.25
Minimum surface size [mm]	0.05
Number of thin layers	2
Number of prism layers	2
Prism layer stretching	1.5
Prism layer total thickness	33.33% of base size
Surface grow rate	1.3
Total cells number	3.13×10^7



(a) Polyhedral mesh

Figure 3. Showcase of generated mesh



(b) Cut plan of generated mesh

Figure 3. Showcase of generated mesh (cont.)

4. CFD SIMULATIONS

4.1. GOVERNING EQUATIONS

In this work, volume of fluid (VOF) multiphase model [40] was implemented due to its genuine efficiency and flexibility. The VOF method is an interface capturing technique by defining the total volume fraction of two or more immiscible phases is unity in a fixed mesh system [41,42]. A single set of transport equations is shared by each phase and the volume fraction of each phase in each cell is calculated. It should be noted that in porous media part of the computational cell is occupied by solid phase that fluids can only flow through the rest of the space which is presented mathematically by porosity in each cell. Hence, the continuity equation and momentum equation are expressed as follows:

$$\frac{\partial \rho}{\partial t} + \nabla \cdot (\rho \vec{u}_i) = 0 \quad (8)$$

$$\rho = \sum \varepsilon_i \rho_i \quad (9)$$

$$\frac{\partial}{\partial t} (\rho \vec{u}) + \nabla \cdot (\rho \vec{u} \vec{u}) = -\nabla p + \nabla \cdot \left[\mu (\nabla \vec{u} + \nabla \vec{u}^T) \right] + \rho \vec{g} + \vec{F} \quad (10)$$

$$\sum \varepsilon_i = 1 \quad (11)$$

where ρ is the density of phase mixture, ρ_i is the density of each phase, \vec{u}_i is the velocity vector, ε_i is the volume fraction of each phase in the empty space of each computational cell, ∇p is the pressure gradient, μ is the viscosity, \vec{F} represents the interaction forces.

4.2. SURFACE TENSION MODEL

The surface tension has to be included along the interface between each two phases as well as between the phases and the walls because the fluid molecules close to the interfaces are under uneven attraction forces [43]. The surface tension plays a fundamental role in transport phenomena. Brackbill et al. proposed the continuum surface force (CSF) method [43] by modeling the interfacial surface force as a volumetric force, where the surface pressure is proportional to the surface curvature that determines the surface tension force. The surface tension force can be resolved into normal and tangential components which can be expressed by:

$$F_\sigma = F_{\sigma,n} + F_{\sigma,t} = \sigma \kappa \vec{n} + \frac{\partial \sigma}{\partial t} \vec{t} \quad (12)$$

where σ is the surface tension which is 0.072 N/m in this case, \vec{n} is the unit vector normal to the surface, \vec{t} is the unit vector tangential to the surface, κ is the surface curvature.

According to the CSF model, the vector normal to the interface is:

$$\vec{n} = \nabla \varepsilon_i \quad (13)$$

The curvature of the interface will be:

$$\kappa = -\nabla \cdot \frac{\nabla \varepsilon_i}{|\nabla \varepsilon_i|} \quad (14)$$

4.3. WALL ADHESION

The surface tension force between the fluids and the catalyst surfaces and the wall is affected by the contact angle, which is measured by the triple line which is shown in Figure 4. In reality, the triple line moves which means the contact angle changes so it is called dynamic contact angle, which is calculated by the Kistler dynamic contact angle model coupled with Hoffman function [44,45] as shown below:

$$\theta_d = f_{Hoff} \left(Ca + f_{Hoff}^{-1}(\theta_e) \right) \quad (15)$$

$$f_{Hoff} = \cos^{-1} \left(1 - 2 \tanh \left(5.16 \left(\frac{x}{1 + 1.31x^{0.99}} \right)^{0.706} \right) \right) \quad (16)$$

where θ_e is the equilibrium (static) contact angle, Ca is the capillary number which is defined as:

$$Ca = \frac{V \mu_p}{\sigma} \quad (17)$$

where μ_p is the dynamic viscosity of the primary phase, σ is the surface tension, V is the triple line characteristic velocity which is defined as:

$$V = -(\vec{V} \cdot \vec{n}_t) \quad (1)$$

where \vec{V} is the relative velocity between the fluid and the wall, \vec{n}_t is the unit vector in the tangential direction pointing to the direction normal to the interface.

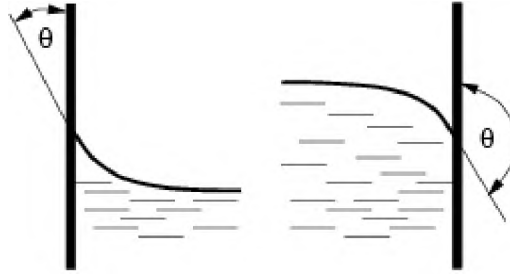


Figure 4. Schematic of contact angle on the walls

Table 3. Simulation specifications

Item	Value/Remark
Gas	Air, $\rho_\beta = 1.18415 \text{ kg} / \text{m}^3$, $\mu_\beta = 1.855 \times 10^{-5} \text{ Pa} \cdot \text{s}$
Liquid	Water, $\rho_\gamma = 997.561 \text{ kg} / \text{m}^3$, $\mu_\gamma = 8.887 \times 10^{-4} \text{ Pa} \cdot \text{s}$
Surface tension [N/m]	0.072
Wall boundary condition	No-slip
Operating pressure [MPa]	0.1
Operating temperature [K]	293.15

4.4. SOLUTION PROCEDURE

The CFD commercial package StarCCM+ 13.04 was used to simulate the two-phase flow in this random packed trilobe bed using finite control volume scheme. Gas was set as primary phase while liquid was set as secondary phase. The simulation specifications

are shown in Table 3 and the flow conditions are listed in Table 4. Both gas and liquid inlets were set as uniform velocity. No-slip conditions were set for walls and catalyst surfaces. The outlet boundary condition was set for the exit. Steady state was simulated in this case.

5. EXPERIMENTAL WORK

5.1. EXPERIMENTAL SETUP

The purpose of the experiments is to measure the local liquid saturation and local liquid velocity inside the trilobe packed bed, as well as the pressure drop to validate the CFD simulation results. However, for 10 cm bed height, the pressure drops values measured by the differential manometer (Dwyer wet/wet Digital Manometer Serious 490) were very low and varied wildly. Therefore, a 40 cm bed height instead of 10 cm was used to measure the pressure drops to obtain reasonable and robust data. It has been approved that in packed beds, the pressure drop per unit length remains the same independently on the bed height [35,39], hence it is equivalent to use the pressure drop data from 40 cm bed height to validate the CFD simulation. The schematic of this case is shown in Figure 5 case 1. However, for local information such as liquid velocity and saturation, there is no basis being reported that such information is identical at the same locations in different bed heights. Therefore, a 10 cm bed height was used to measure the local liquid saturation and liquid velocity by using 2-tip optical probe in the middle level of the bed, as shown in Figure 5 case 2. The diameter of the reactor is 5 cm (2 inch). The diameter of liquid inlet

is 0.45 cm, which is 5 cm above the catalyst bed, while the gas inlet is attached to the top flange. The operation conditions are listed in Table 4.

Table 4. Experimental operation conditions

No.	Gas superficial velocity $v_g [m/s]$	Liquid superficial velocity $v_l [m/s]$
1	0.1	0.008
2	0.1	0.016
3	0.2	0.008
4	0.2	0.016

5.2. OPTICAL FIBER PROBE

Optical fiber probe has been widely used in multiphase flow reactors to measure the phase velocity and saturation and the reliability and accuracy have been proven in many studies [8,11,46,47]. It is based on the internal reflection of light inside the optical fiber. When the medium around the optical fiber tip changes, the reflective light intensity inside the fiber changes due to the difference of refractive index in different media, which is presented by converting the light signals to analog signals. For instance, when the optical fiber tip is immersed into water from air, which means the surrounding media has higher density therefore higher refractive index leading to less reflective light inside the optical fiber, hence the analog signal indicates low values. For measuring the local liquid velocity and liquid saturation in the packed bed, the optical probe with 2 tips (Figure 5) that are vertically aligned with distance 1 mm was used. The two optical fibers were fixed inside a

rigid tube of 2 mm in diameter to minimize the disturbance on the flow behaviors. The optical probe was moved along the diameter using a high accuracy ball screw adjuster to obtain 9 data points. At each point, 3 repetitions were conducted with each repetition lasting for 60 seconds. A sample results is shown in Figure 6. The local liquid velocity can be calculated based on the tip distance and time difference from Equation (19).

$$v_{\gamma} = \frac{1mm}{t_T - t_B} \quad (19)$$

where t_T and t_B are the time of top and bottom tip receiving signal perturbation due to the phase change.

Accordingly, the liquid saturation can be obtained based on the assumption of ergodic hypothesis [11,46], that the time that the probe tips is surrounded by water t_{γ} over the total measurement time t_m is the liquid saturation, which is expressed in Equation (20).

$$\phi_{\gamma} = \frac{t_{\gamma}}{t_m} \quad (20)$$

6. RESULTS AND DISCUSSION

6.1. PRESSURE DROPS

The pressure drops of each flowrate combination was measured by the differential manometer for 1 minute after the system reached steady state. As explained above, the pressured drops measured in the experiments were for 40 cm packed beds. Therefore, in order to compare with the CFD results, the dimensionless pressure drop ($\Delta P / \rho_{\gamma} g L_c$) was used to compare the results between experimental data and CFD simulations. Figure 7

shows the comparison of pressure drops between the CFD simulation results and experimental results at different combination of flowrates (Table 3). It can be observed that for all the cases, the CFD results are lower than experimental results because of the decrease of bed porosity. The absolute relative errors ($ARE = \left| \psi_{Experiments} - \psi_{CFD} \right| / \psi_{CFD}$) are listed in Figure 7 showing the maximum error is 10.5% which is within the acceptable range.

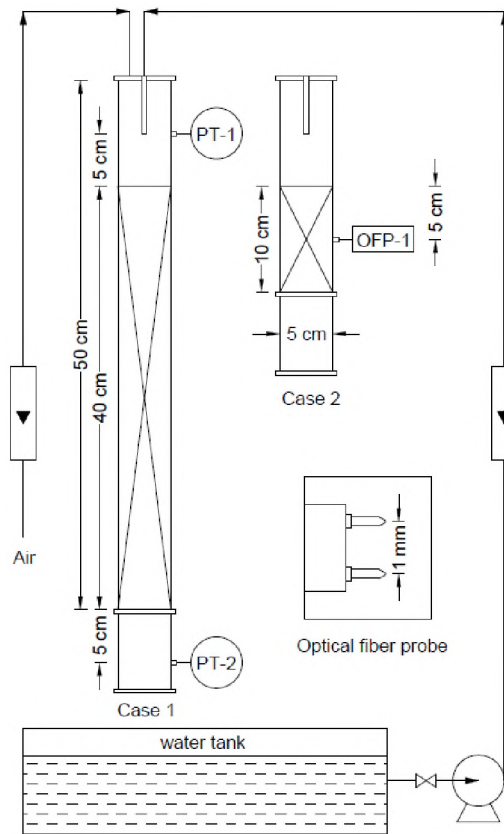


Figure 5. Schematic of experimental setup and optical fiber probe configuration

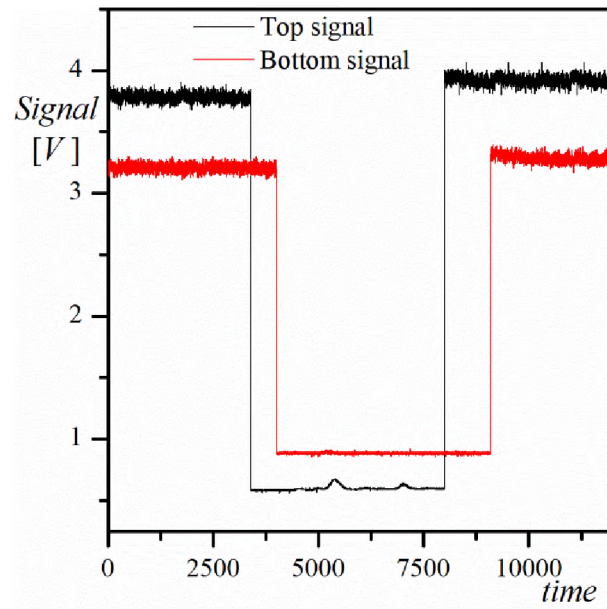


Figure 6. Sample result of 2 tip optical probe signal

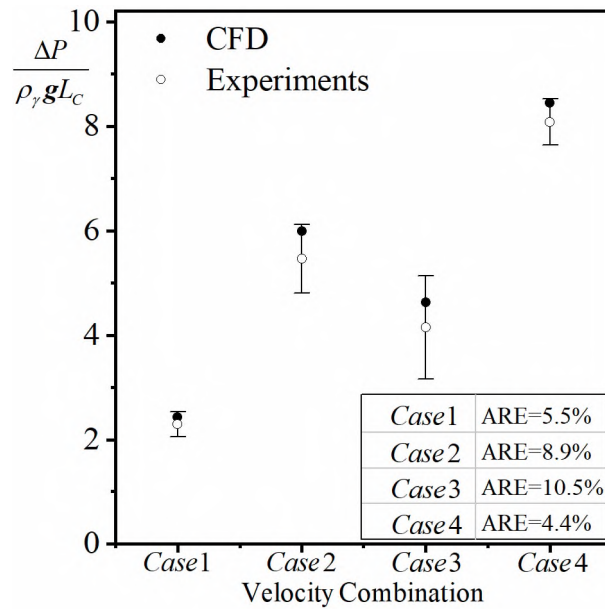


Figure 7. Comparison of pressure drops between CFD simulations and experiments at different combination of flowrates: Case1 $v_{\beta} = 0.1 \text{ m/s}$, $v_{\gamma} = 0.008 \text{ m/s}$, Case 2 $v_{\beta} = 0.1 \text{ m/s}$, $v_{\gamma} = 0.016 \text{ m/s}$, Case 3 $v_{\beta} = 0.2 \text{ m/s}$, $v_{\gamma} = 0.008 \text{ m/s}$, Case 4 $v_{\beta} = 0.2 \text{ m/s}$, $v_{\gamma} = 0.016 \text{ m/s}$

6.2. LOCAL LIQUID SATURATION

As explained earlier, 9 data points along the diameter at 5 cm bed height were used to measure the local liquid saturations and local liquid velocities. 8 out of 9 of these data points are central symmetric except for the center point. Hence, each two data points at the same radius are averaged by reasonably assuming that the random packed bed is an isotropic system. The liquid saturation was obtained by the ratio of time of probe tip contacting water to the total measurement time, which means that the liquid saturation measurement was based on the time average in steady state. However, since the steady state was simulated in CFD, it is not appropriate to use one data point as representative without temporal consideration. Hence, the azimuthally averaged liquid saturations at different radiuses (Figure 8) were calculated to compare with the time averaged experimental results at the same radiuses at 5 cm bed height. The scalar fields of saturation in CFD simulations at different flowrates are shown in Figure 9. It is noteworthy that in the CFD geometry, the center of the 5 cm cut plan is occupied by the catalyst, therefore the average of a small range (circle of 3 mm in diameter) of data points were used to represent the center point ($r/R=0$) results. Figure 10 shows the comparisons of azimuthally averaged liquid saturations in terms of radius at different velocity combinations between the experimental results and CFD results. Generally, in the center region of the column, the liquid saturations of CFD simulations are higher than that of experimental results. While in the area close to the wall, the liquid saturations of CFD simulations are lower than that of experimental results. As explained earlier, the shrinkage of the trilobe particles increases the porosity of the packed bed leading to less resistance of the flowing paths, that it is easier for liquid to flow through the center region of the packed bed comparing to the

actual packed bed. Besides, the gap between the wall and the packed bed also increases, which enables the gas phase to push the liquid directly through the gaps. While in experiments, the real packed bed is closely contacting the wall giving more resistance to the liquid flow, hence higher liquid saturation. The absolute average errors of all the cases are listed in Table 5, while the average absolute relative error ($AARE = 1/n \sum |\psi_{Experiments} - \psi_{CFD}| / \psi_{CFD}$) is 19.18%. Some of the errors are quite high because it is a random packed bed, that it is highly impossible for the intricate internal bed structure to match the real packed bed. Hence, it is not fair to judge the performance of the CFD simulations only based on the local liquid saturations. The cross-sectional average liquid saturation at each velocity combination was also calculated to assess the CFD simulations and the AREs are listed in Table 6, showing satisfying results.

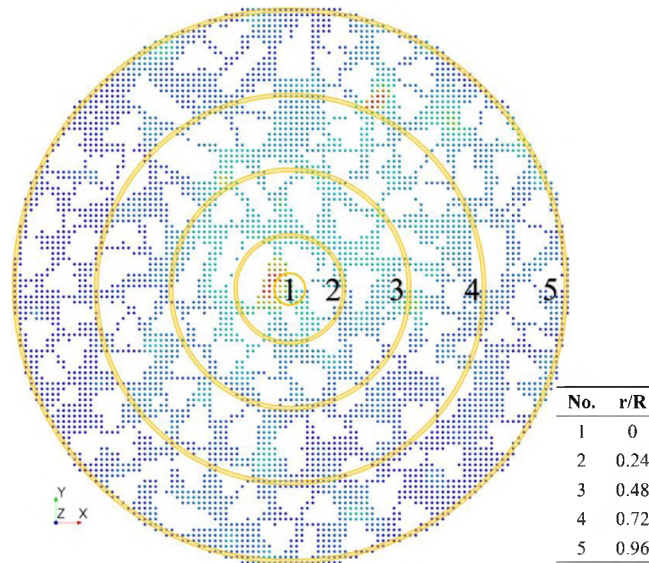


Figure 8. Schematic of azimuthally averaged data points at different radius

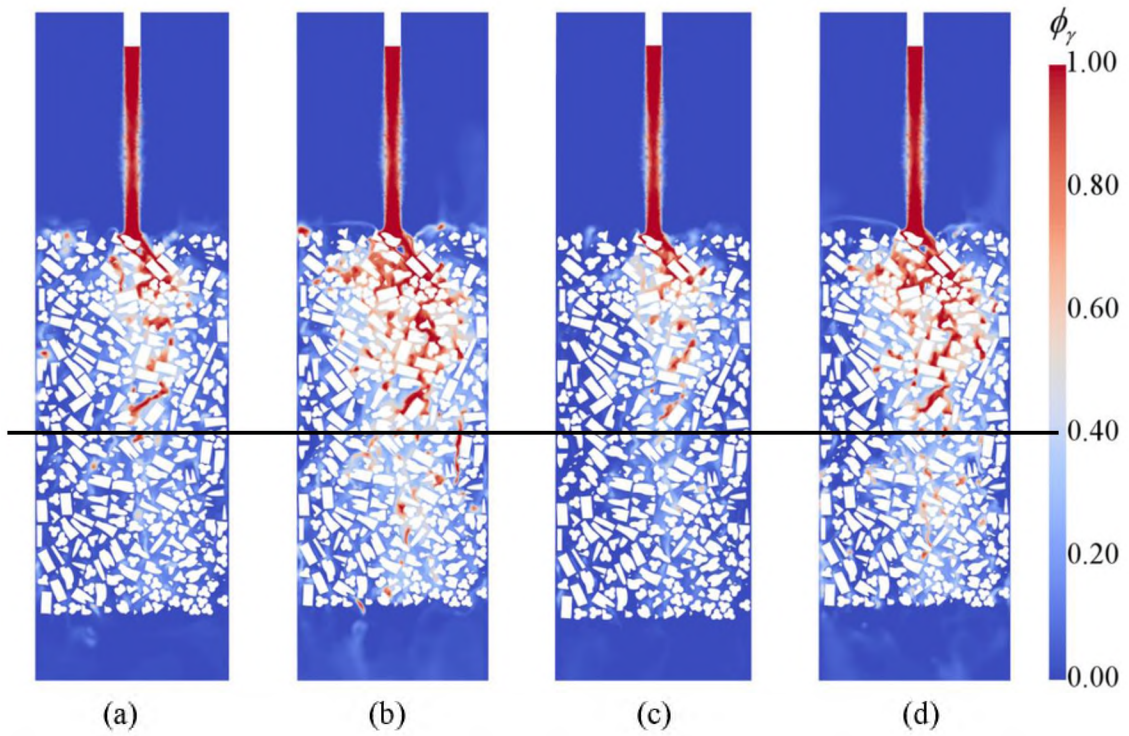
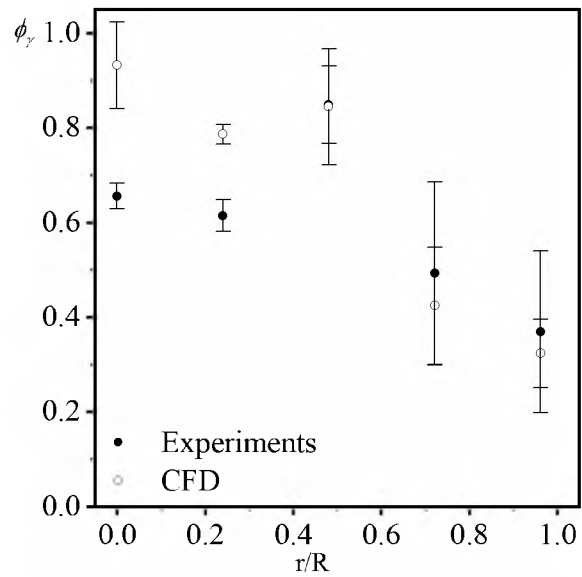


Figure 9. Cut plan of liquid saturation at different velocities: (a) $v_\beta = 0.1 \text{ m/s}$, $v_\gamma = 0.008 \text{ m/s}$, (b) $v_\beta = 0.1 \text{ m/s}$, $v_\gamma = 0.016 \text{ m/s}$, (c) $v_\beta = 0.2 \text{ m/s}$, $v_\gamma = 0.008 \text{ m/s}$, (d) $v_\beta = 0.2 \text{ m/s}$, $v_\gamma = 0.016 \text{ m/s}$

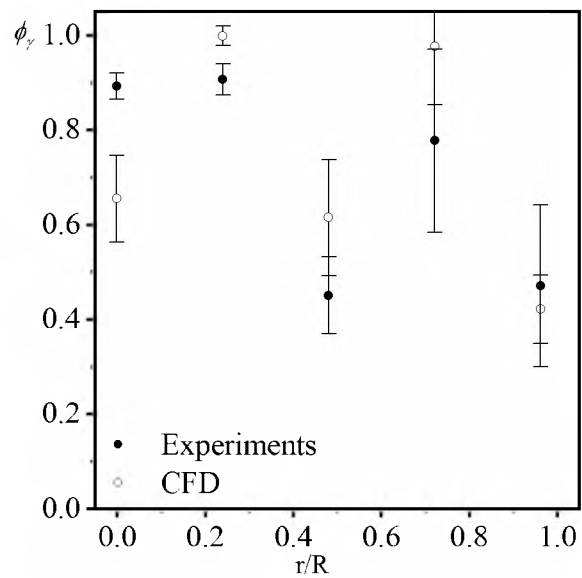
6.3. LOCAL VELOCITY

It is noteworthy that for VOF method, the velocity is the shared velocity between the gas and liquid phase. Hence, the velocity is not necessary the liquid velocity, but could also be the gas velocity depending on the volume fraction at that location. Figure 11 shows the velocity fields and Figure 12 shows the velocity vectors around 5 cm zone (velocity magnitude has been normalized to the scale of 1) at different inlet velocity combinations, respectively. It can be observed that the velocities close to the wall region are much higher than that in the center area, especially for higher gas inlet velocity, which explains why the liquid saturations close to the wall are higher. Clear reverse flows (backmixing) can also

be observed, which seems to be more severe at lower gas inlet velocity and higher liquid inlet velocity ($v_\beta = 0.1 \text{ m/s}$, $v_\gamma = 0.016 \text{ m/s}$), which requires quantifications.

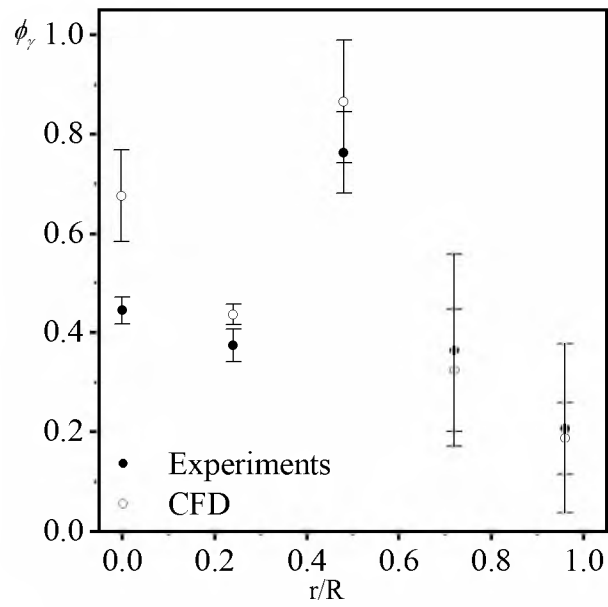


(a) $v_\beta = 0.1 \text{ m/s}$, $v_\gamma = 0.008 \text{ m/s}$

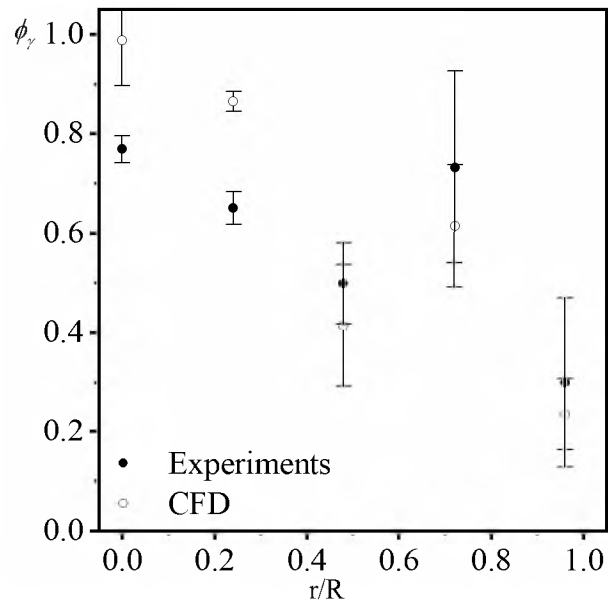


(b) $v_\beta = 0.1 \text{ m/s}$, $v_\gamma = 0.016 \text{ m/s}$

Figure 10. Liquid saturations comparisons between CFD and experimental results in terms of radius at different combination of flowrates



(c) $v_\beta = 0.2 \text{ m/s}, v_\gamma = 0.008 \text{ m/s}$



(d) $v_\beta = 0.2 \text{ m/s}, v_\gamma = 0.016 \text{ m/s}$

Figure 10. Liquid saturations comparisons between CFD and experimental results in terms of radius at different combination of flowrates (cont.)

Table 5. Absolute relative errors of local liquid saturations of CFD and experimental results

r/R	$v_{\beta} [m/s]$	$v_{\gamma} [m/s]$	ARE
0	0.1	0.008	29.62%
	0.1	0.016	36.26%
	0.2	0.008	34.34%
	0.2	0.016	22.07%
0.24	0.1	0.008	21.83%
	0.1	0.016	9.20%
	0.2	0.008	14.20%
	0.2	0.016	24.68%
0.48	0.1	0.008	0.54%
	0.1	0.016	26.65%
	0.2	0.008	11.74%
	0.2	0.016	20.49%
0.72	0.1	0.008	16.13%
	0.1	0.016	20.37%
	0.2	0.008	12.52%
	0.2	0.016	19.20%
0.96	0.1	0.008	14.11%
	0.1	0.016	11.62%
	0.2	0.008	10.90%
	0.2	0.016	27.04%

Table 6. Absolute relative errors of cross-sectional average liquid saturations of CFD and experimental results

$v_{\beta} [m / s]$	$v_{\gamma} [m / s]$	ARE
0.1	0.008	11.03%
0.1	0.016	4.80%
0.2	0.008	15.56%
0.2	0.016	5.59%

In experimental work, the local liquid velocity was calculated based on the time difference when the liquid passed through the two optical probe tips (1 mm distance). During a certain period, the liquid velocity varies quite a bit, including the opposite direction because of the backmixing. Hence, the best way to describe the local liquid velocities is using a statistical model estimating the different velocities' probabilities. In this case, the nonparametric analysis methodology [48] is used because there is no basis to assume the velocity distribution to be normal distribution. The kernel density estimator (KDE) [49,50], which is defined in Equation (21), was used to describe the probability density distribution of the local liquid velocities.

$$f(x) = \frac{1}{nh^d} \sum_{i=1}^n K\left(\frac{x - X_i}{h^d}\right) \quad (21)$$

where n is the total sample number, h^d is the bandwidth for d dimensions multivariate KDE, K is the kernel density function and Gaussian function ($\frac{1}{\sqrt{2\pi}} \exp(-\frac{1}{2}x^2)$) was used in this work, X_i is the value of i th observation.

However, as mentioned earlier, the steady state was simulated in CFD work, therefore no time variations of velocities can be captured. Hence, like the strategy that was used to validate the liquid saturations, all the velocities at different radius was counted (Figure 13) and the density distribution was estimated using KDE as well. It is notable that the experimental velocity vectors are vertically oriented because they were calculated based on the vertically aligned optical probe tips. Hence, for CFD results, only Z direction velocity was used to compare with the experimental results. For both experimental and CFD results, the positive velocities (downward) and negative velocities (upward) are presented separately. The sample results ($v_\beta = 0.2 \text{ m/s}$, $v_\gamma = 0.016 \text{ m/s}$) of KDE estimation are shown in Figure 14 and the other results are listed in Table 7. For experimental results, the modal number of both positive and negative velocities were presented while for CFD results, the average positive and negative velocities are presented because of limited data points. For both positive and negative velocities, the velocity magnitudes of CFD results are larger than that of experimental results. This can be explained by the lower pressure drops in CFD simulations. Lower pressure drop means less energy loss due to the friction when fluids pass through the packed bed, which means more kinetic energy is retained which is indicated as higher velocities. The velocities close to the wall in CFD results are much higher than that of experimental data, because the velocities are mainly the gas velocities since the liquid saturations close to the wall are low while gas and liquid share the same velocity in VOF method. However, all the velocities from CFD results are within the modal range of experimental data.

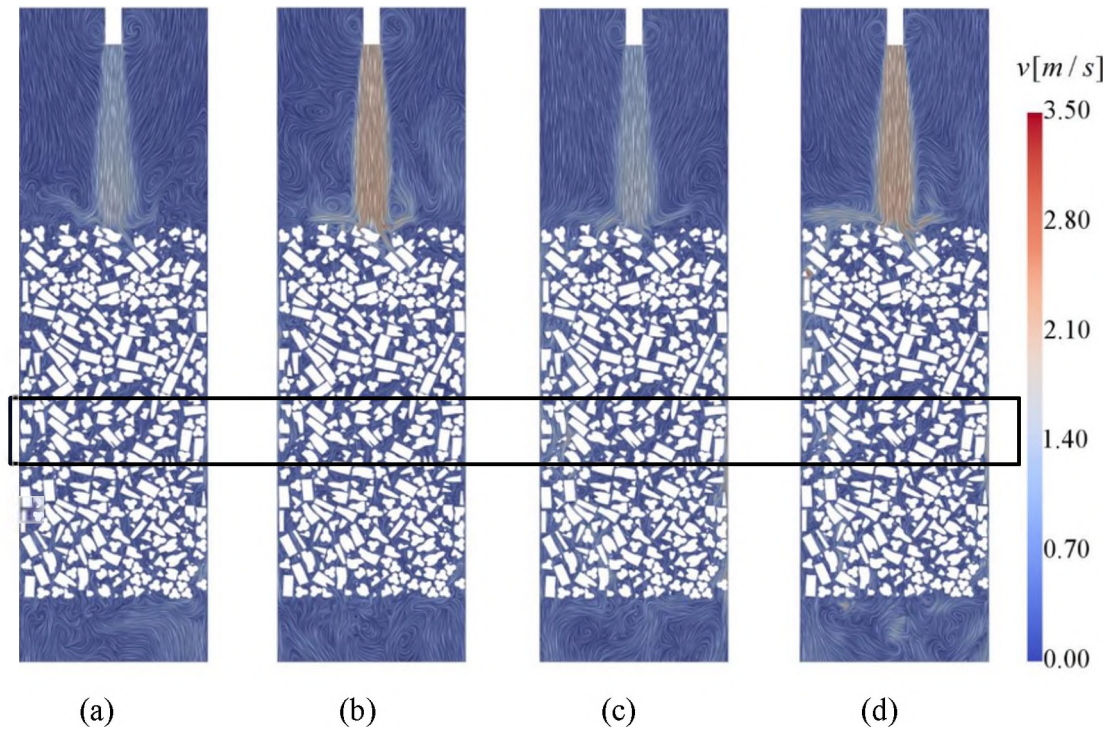
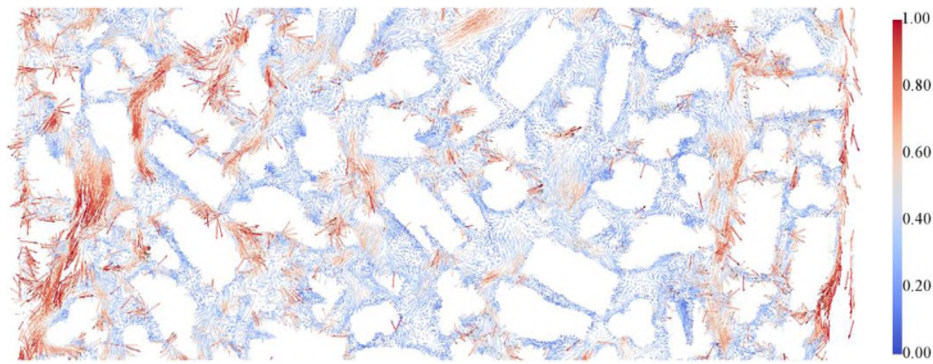
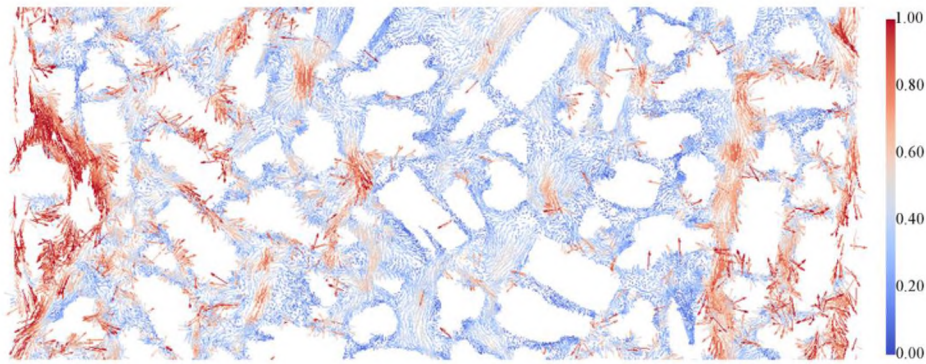


Figure 11. Cut plan of velocity fields at different velocities: (a) $v_\beta = 0.1 \text{ m/s}$, $v_\gamma = 0.008 \text{ m/s}$, (b) $v_\beta = 0.1 \text{ m/s}$, $v_\gamma = 0.016 \text{ m/s}$, (c) $v_\beta = 0.2 \text{ m/s}$, $v_\gamma = 0.008 \text{ m/s}$, (d) $v_\beta = 0.2 \text{ m/s}$, $v_\gamma = 0.016 \text{ m/s}$

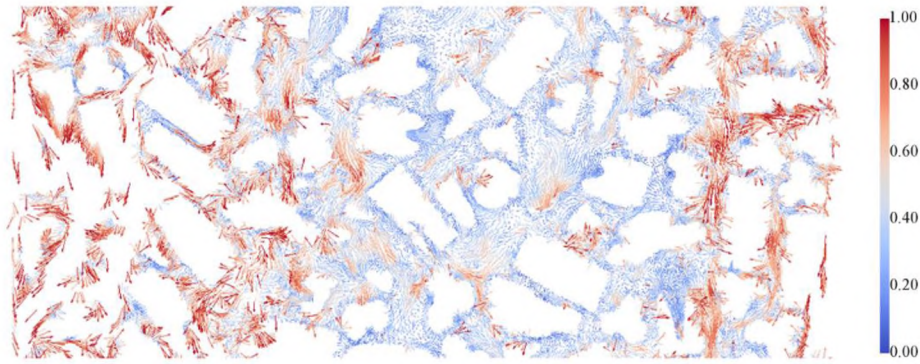


(a) $v_\beta = 0.1 \text{ m/s}$, $v_\gamma = 0.008 \text{ m/s}$

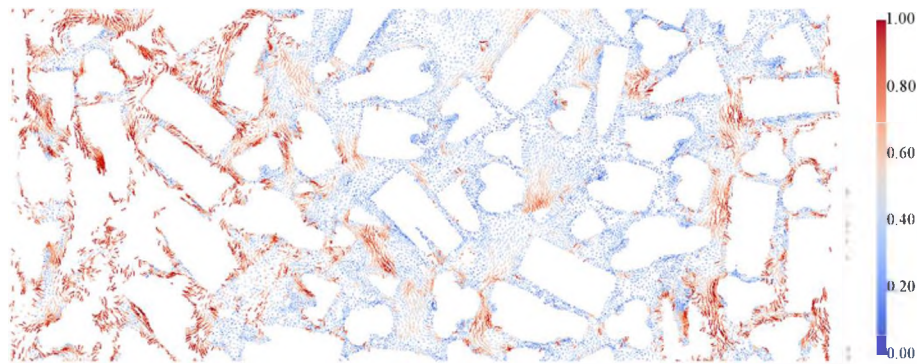
Figure 12. Velocity vectors of 5 cm zone at different velocities



(b) $v_\beta = 0.1 \text{ m/s}, v_\gamma = 0.016 \text{ m/s}$



(c) $v_\beta = 0.2 \text{ m/s}, v_\gamma = 0.008 \text{ m/s}$



(d) $v_\beta = 0.2 \text{ m/s}, v_\gamma = 0.016 \text{ m/s}$

Figure 12. Velocity vectors of 5 cm zone at different velocities (cont.)

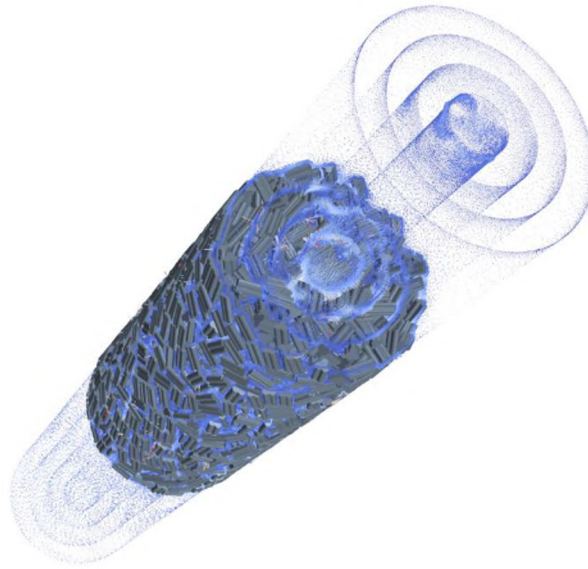
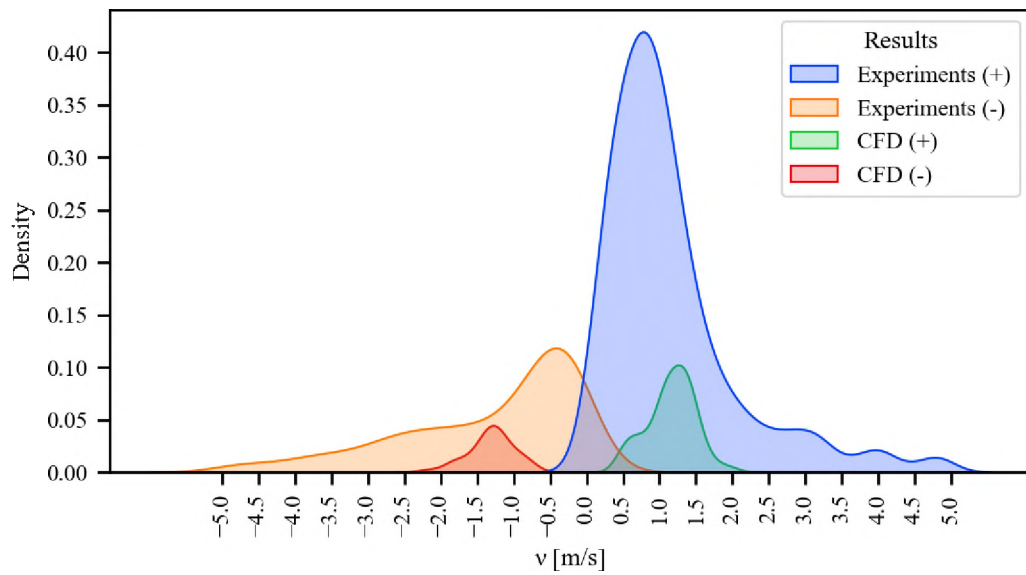


Figure 13. Schematic of velocity field at radius $r/R = 0, 0.24, 0.48, 0.72, 0.96$



(a) $r/R = 0$

Figure 14. KDE of both positive and negative velocities for experimental and CFD results at $v_{\beta} = 0.2 \text{ m/s}$, $v_{\gamma} = 0.016 \text{ m/s}$

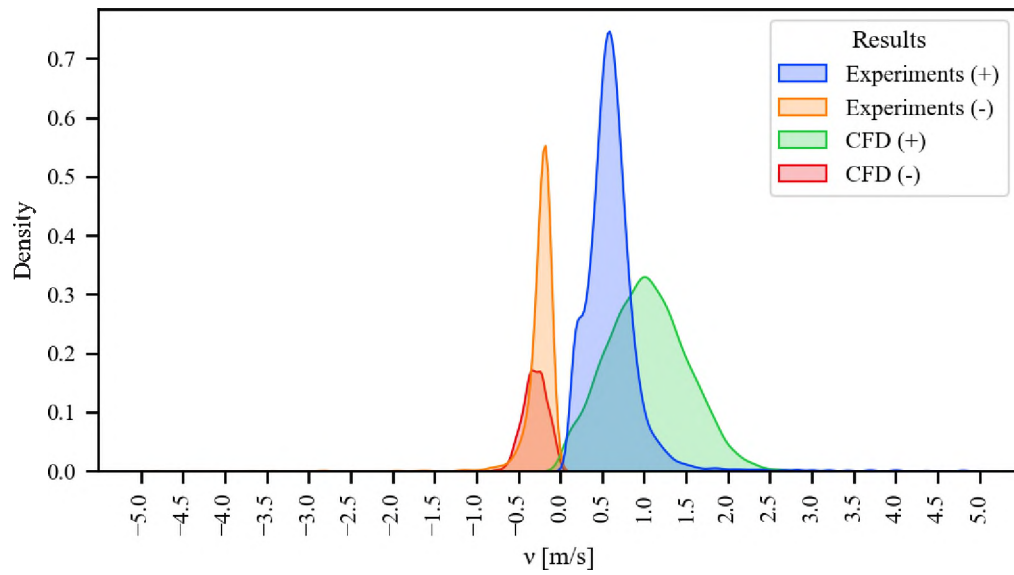
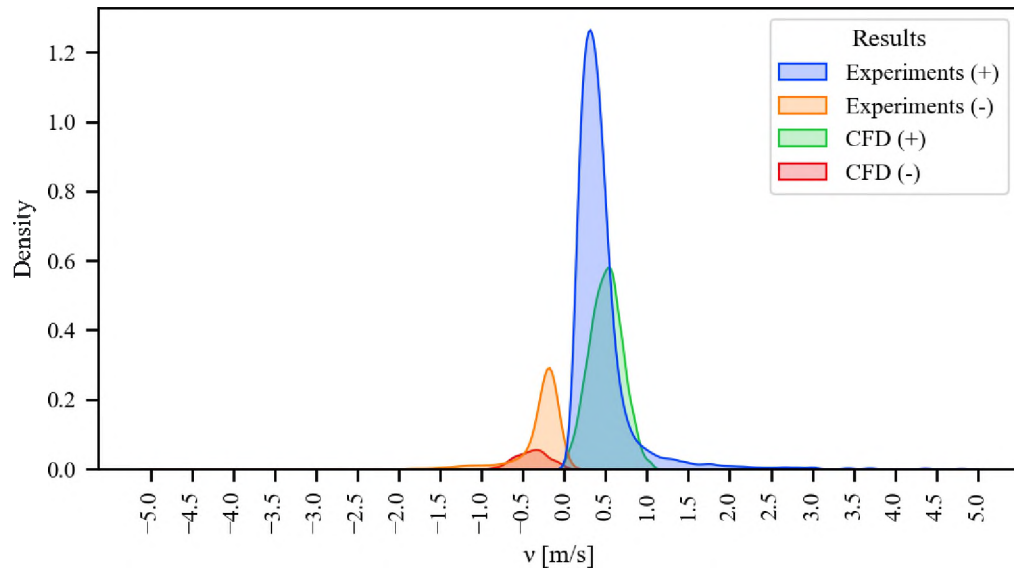
(b) $r/R = 0.24$ (c) $r/R = 0.48$

Figure 14. KDE of both positive and negative velocities for experimental and CFD results at $v_\beta = 0.2 \text{ m/s}$, $v_\gamma = 0.016 \text{ m/s}$ (cont.)

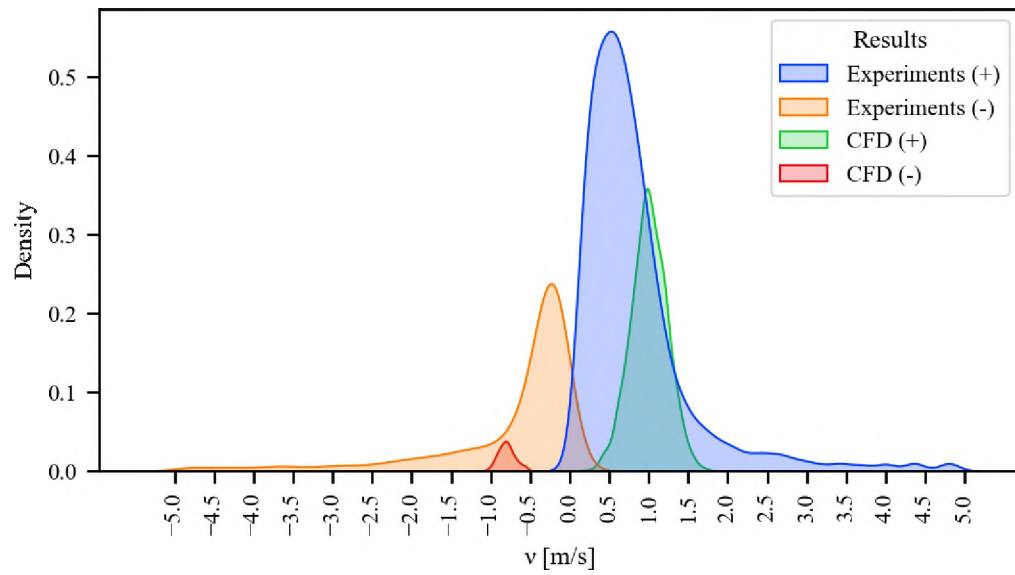
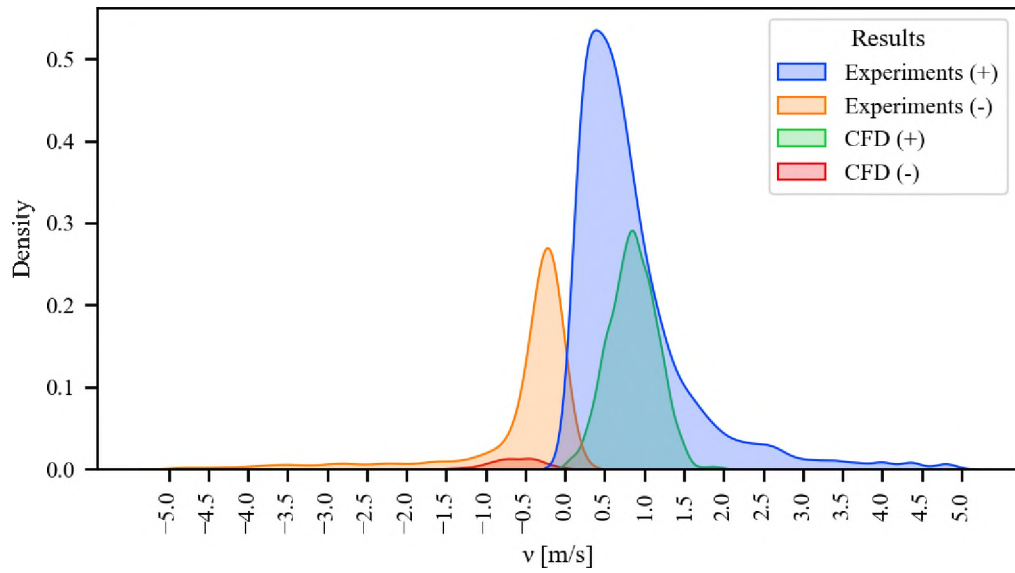
(d) $r/R = 0.72$ (e) $r/R = 0.96$

Figure 14. KDE of both positive and negative velocities for experimental and CFD results at $v_\beta = 0.2 \text{ m/s}$, $v_\gamma = 0.016 \text{ m/s}$ (cont.)

Table 7. Velocities of CFD (average value) and experimental results (modal number)

r / R	$v_{\beta}[m / s]$	$v_{\gamma}[m / s]$	$Exp(+)[m / s]$	$Exp(-)[m / s]$	$CFD(+)[m / s]$	$CFD(-)[m / s]$
0	0.1	0.008	0.14	-0.28	0.17	-0.33
	0.1	0.016	0.17	-0.23	0.20	-0.27
	0.2	0.008	0.15	-0.22	0.15	-0.26
	0.2	0.016	0.97	-0.18	0.76	-1.31
0.24	0.1	0.008	0.16	-0.26	0.19	-0.30
	0.1	0.016	0.07	-0.56	0.07	-0.64
	0.2	0.008	0.17	-0.58	0.19	-0.68
	0.2	0.016	0.57	-0.17	0.72	-0.27
0.48	0.1	0.008	0.33	-0.16	0.32	-0.20
	0.1	0.016	0.15	-0.01	0.16	-0.01
	0.2	0.008	0.16	-0.23	0.19	-0.29
	0.2	0.016	0.37	-0.16	0.41	-0.23
0.72	0.1	0.008	0.17	-0.23	0.23	-0.25
	0.1	0.016	0.15	-0.21	0.17	-0.24
	0.2	0.008	0.19	-0.47	0.23	-0.56
	0.2	0.016	0.18	-0.19	0.96	-0.79
0.96	0.1	0.008	0.19	-0.27	0.23	-0.28
	0.1	0.016	0.16	-0.38	0.19	-0.48
	0.2	0.008	0.18	-0.18	0.22	-0.21
	0.2	0.016	0.15	-0.18	0.91	-0.63

7. REMARKS

An efficient packing scheme was implemented to randomly pack a vast number of trilobe catalyst to represent the TBR based on the rigid body approach. The generated geometry was used to define the computational domain for the two-phase hydrodynamics simulation based on the volume of fluids (VOF) approach. The main remarks of this study are:

- (1) The pressure drops in CFD simulations have been validated by experiments that the maximum absolute relative error is 10.5%.
- (2) The azimuthally averaged liquid saturations in terms of radius in CFD simulations were compared with time averaged liquid saturations from 2-tip optical probe measurements, showing 19.18% average absolute relative error. However, the cross-sectional average liquid saturations in CFD simulations show maximum 15.56% absolute relative error from experimental data.
- (3) The kernel density estimation was used to describe the positive and negative velocities probability distributions. The modal number of experimental velocities are higher than the average velocities in CFD simulations. However, the overall velocity distribution range of CFD simulations are within the experimental velocity distribution range.

FUNDING

This research did not receive any specific grant from funding agencies in the public, commercial, or not-for-profit sectors.

REFERENCES

- [1] M.P.D. M. H. Al-Dahhan,* M. R. Khadilkar, Y. Wu, Prediction of pressure drop and liquid holdup in high-pressure trickle-bed reactors, *Ind. Eng. Chem. Res.* 37 (1998) 193–798.
- [2] M.H. Al-Dahhan, M.P. Duduković, Pressure drop and liquid holdup in high pressure trickle-bed reactors, *Chem. Eng. Sci.* 49 (1994) 5681–5698. [https://doi.org/10.1016/0009-2509\(94\)00315-7](https://doi.org/10.1016/0009-2509(94)00315-7).
- [3] R.J.G. Lopes, V.S.L. de Sousa, R.M. Quinta-Ferreira, CFD and experimental studies of reactive pulsing flow in environmentally-based trickle-bed reactors, *Chem. Eng. Sci.* 66 (2011) 3280–3290. <https://doi.org/10.1016/j.ces.2011.01.058>.
- [4] D. Nemec, J. Levec, Flow through packed bed reactors: 2. Two-phase concurrent downflow, *Chem. Eng. Sci.* 60 (2005) 6958–6970. <https://doi.org/10.1016/j.ces.2005.05.069>.
- [5] K.D.P. Nigam, F. Larachi, Process intensification in trickle-bed reactors, *Chem. Eng. Sci.* 60 (2005) 5880–5894. <https://doi.org/10.1016/j.ces.2005.04.061>.
- [6] C. Boyer, C. Volpi, G. Ferschneider, Hydrodynamics of trickle bed reactors at high pressure: Two-phase flow model for pressure drop and liquid holdup, formulation and experimental validation, *Chem. Eng. Sci.* 62 (2007) 7026–7032. <https://doi.org/10.1016/j.ces.2007.08.036>.
- [7] M. Bazmi, S.H. Hashemabadi, M. Bayat, Extrudate Trilobe Catalysts and Loading Effects on Pressure Drop and Dynamic Liquid Holdup in Porous Media of Trickle Bed Reactors, *Transp. Porous Media.* 99 (2013) 535–553. <https://doi.org/10.1007/s11242-013-0199-x>.
- [8] M.F.B.A. Rahman, Investigation of local velocities and phase holdups, and flow regimes and maldistribution identification i a trickle bed reactor, Missouri University of Science and Technology, 2017.

- [9] B. Qi, O. Farid, S. Uribe, M. Al-Dahhan, Maldistribution and dynamic liquid holdup quantification of quadrilobe catalyst in a trickle bed reactor using gamma-ray computed tomography: Pseudo-3D modelling and empirical modelling using deep neural network, *Chem. Eng. Res. Des.* 164 (2020) 195–208. <https://doi.org/10.1016/j.cherd.2020.09.024>.
- [10] B. Qi, S. Uribe, O. Farid, M. Al-Dahhan, Development of a hybrid pressure drop and liquid holdup phenomenological model for trickle bed reactors based on two-phase volume averaged equations, *Can. J. Chem. Eng.* (2020). <https://doi.org/10.1002/cjce.23892>.
- [11] S. Uribe, M. Al-Ani, M.E. Cordero, M. Al-Dahhan, Modelling and validation of TBR Hydrodynamics: Local comparison between CFD and experiments, *Fuel*. 277 (2020) 118244. <https://doi.org/10.1016/j.fuel.2020.118244>.
- [12] M.E. Cordero, S. Uribe, L.G. Zárate, R.N. Rangel, A. Regalado-Méndez, E.P. Reyes, CFD Modelling of Coupled Multiphysics-Multiscale Engineering Cases, *Comput. Fluid Dyn. - Basic Instruments Appl. Sci.* (2018). <https://doi.org/10.5772/intechopen.70562>.
- [13] S. Uribe, B. Qi, M.E. Cordero, M. Al-Dahhan, Comparison between pseudohomogeneous and resolved-particle models for liquid hydrodynamics in packed-bed reactors, *Chem. Eng. Res. Des.* 166 (2021) 158–171. <https://doi.org/10.1016/j.cherd.2020.12.001>.
- [14] G.E. Mueller, A simple method for determining sphere packed bed radial porosity, *Powder Technol.* 229 (2012) 90–96. <https://doi.org/10.1016/j.powtec.2012.06.013>.
- [15] G.E. Mueller, Radial porosity in packed beds of spheres, *Powder Technol.* 203 (2010) 626–633. <https://doi.org/10.1016/j.powtec.2010.07.007>.
- [16] H. Martin, Low peclet number particle-to-fluid heat and mass transfer in packed beds, *Chem. Eng. Sci.* (1978). [https://doi.org/10.1016/0009-2509\(78\)85181-1](https://doi.org/10.1016/0009-2509(78)85181-1).
- [17] A. De Klerk, Voidage Variation in Packed Beds at Small Column to Particle Diameter Ratio, *AIChE J.* 49 (2003) 2022–2029.
- [18] C.G. Sun, F.H. Yin, A. Afacan, K. Nandakumar, K.T. Chuang, MODELLING AND SIMULATION OF FLOW MALDISTRIBUTION IN RANDOM PACKED COLUMNS, *Trans IChemE.* 78 (2000) 10–12.
- [19] M.L. Hunt, C.L. Tien, Non-darcian flow, heat and mass transfer in catalytic packed-bed reactors, *Chem. Eng. Sci.* (1990). [https://doi.org/10.1016/0009-2509\(90\)87080-C](https://doi.org/10.1016/0009-2509(90)87080-C).

- [20] R.J.G. Lopes, R.M. Quinta-Ferreira, Numerical simulation of trickle-bed reactor hydrodynamics with RANS-based models using a volume of fluid technique, *Ind. Eng. Chem. Res.* 48 (2009) 1740–1748. <https://doi.org/10.1021/ie8014186>.
- [21] R.J.G. Lopes, R.M. Quinta-Ferreira, CFD modelling of multiphase flow distribution in trickle beds, *Chem. Eng. J.* 147 (2009) 342–355. <https://doi.org/10.1016/j.cej.2008.11.048>.
- [22] R.J.G. Lopes, R.M. Quinta-Ferreira, Assessment of CFD Euler-Euler method for trickle-bed reactor modelling in the catalytic wet oxidation of phenolic wastewaters, *Chem. Eng. J.* 160 (2010) 293–301. <https://doi.org/10.1016/j.cej.2010.03.024>.
- [23] R.J.G. Lopes, R.M. Quinta-Ferreira, Evaluation of multiphase CFD models in gas-liquid packed-bed reactors for water pollution abatement, *Chem. Eng. Sci.* 65 (2010) 291–297. <https://doi.org/10.1016/j.ces.2009.06.039>.
- [24] R.J.G. Lopes, R.M. Quinta-Ferreira, Numerical studies of catalyst wetting and total organic carbon reaction on environmentally based trickle-bed reactors, *Ind. Eng. Chem. Res.* 49 (2010) 10730–10743. <https://doi.org/10.1021/ie100563n>.
- [25] M. Al-Ani, M. Al-Dahhan, Effect of catalyst shape on pressure drop and liquid holdup in a pilot plant trickle bed reactor, *Fuel*. (2021). <https://doi.org/10.1016/j.fuel.2020.118860>.
- [26] P.A. Cundall, O.D.L. Strack, A discrete numerical model for granular assemblies, *Geotechnique*. (1979). <https://doi.org/10.1680/geot.1979.29.1.47>.
- [27] B. Majidi, Discrete element method simulation of packing and rheological properties of coke and coke/pitch mixtures, (2018).
- [28] W. Zhang, K.E. Thompson, A.H. Reed, L. Beenken, Relationship between packing structure and porosity in fixed beds of equilateral cylindrical particles, *Chem. Eng. Sci.* 61 (2006) 8060–8074. <https://doi.org/10.1016/j.ces.2006.09.036>.
- [29] A. MAKNICKAS, A. KACENIAUSKAS, R.B. Rimantas KACIANAUSKAS, A. DŽIUGYS, Parallel DEM Software for Simulation of Granular Media, *Informatica*. 17 (2006) 207–224. <http://iospress.metapress.com/index/A9GA03YL2QMVDYKR.pdf>.
- [30] X. Yang, N. Gui, J. Tu, S. Jiang, 3D DEM simulation and analysis of void fraction distribution in a pebble bed high temperature reactor, *Nucl. Eng. Des.* 270 (2014) 404–411. <https://doi.org/10.1016/j.nucengdes.2014.02.010>.
- [31] W. Nan, Y. Wang, Y. Liu, H. Tang, DEM simulation of the packing of rodlike particles, *Adv. Powder Technol.* 26 (2015) 527–536. <https://doi.org/10.1016/j.appt.2014.12.012>.

- [32] X. Luo, L. Zhao, S. Zhang, H. Dong, J. Feng, Experimental and DEM studies on the distribution of voidage in the random filling bed of ellipsoidal particles, *Powder Technol.* 340 (2018) 400–410. <https://doi.org/10.1016/j.powtec.2018.09.042>.
- [33] J. Bender, K. Erleben, J. Trinkle, Interactive simulation of rigid body dynamics in computer graphics, *Comput. Graph. Forum.* 33 (2014) 246–270. <https://doi.org/10.1111/cgf.12272>.
- [34] S. Flaischlen, G.D. Wehinger, Synthetic Packed-Bed Generation for CFD Simulations: Blender vs. STAR-CCM+, *ChemEngineering.* 3 (2019) 52. <https://doi.org/10.3390/chemengineering3020052>.
- [35] G. Boccardo, L. Del Plato, D. Marchisio, F. Augier, Y. Haroun, D. Ferre, M. Icardi, Pore-scale simulation of fluid flow in packed-bed reactors via Rigid-Body simulations and CFD, *Proc. 10th Int. Conf. CFD Oil Gas, Metall. Process Ind. SINTEF, Trondheim, Norway, 17–19 June 2014.* (2014).
- [36] G. Boccardo, F. Augier, Y. Haroun, D. Ferré, D.L. Marchisio, Validation of a novel open-source work-flow for the simulation of packed-bed reactors, *Chem. Eng. J.* 279 (2015) 809–820–820. <https://doi.org/10.1016/j.cej.2015.05.032>.
- [37] B. Partopour, A.G. Dixon, An integrated workflow for resolved-particle packed bed models with complex particle shapes, *Powder Technol.* 322 (2017) 258–272. <https://doi.org/10.1016/j.powtec.2017.09.009>.
- [38] A. Pavlišič, R. Ceglar, A. Pohar, B. Likozar, Comparison of computational fluid dynamics (CFD) and pressure drop correlations in laminar flow regime for packed bed reactors and columns, *Powder Technol.* (2018). <https://doi.org/10.1016/j.powtec.2018.01.029>.
- [39] H. Bai, J. Theuerkauf, P.A. Gillis, P.M. Witt, A coupled DEM and CFD simulation of flow field and pressure drop in fixed bed reactor with randomly packed catalyst particles, *Ind. Eng. Chem. Res.* 48 (2009) 4060–4074. <https://doi.org/10.1021/ie801548h>.
- [40] C.W. Hirt, B.D. Nichols, Volume of Fluid (VOF) Method for the Dynamics of Free Boundaries, *J. Comput. Phys.* 39 (1981) 201–225.
- [41] Y. Wang, J. Chen, F. Larachi, Modelling and simulation of trickle-bed reactors using computational fluid dynamics: A state-of-the-art review, *Can. J. Chem. Eng.* 91 (2013) 136–180. <https://doi.org/10.1002/cjce.20702>.
- [42] B.G.M. van Wachem, A.E. Almstedt, Methods for multiphase computational fluid dynamics, *Chem. Eng. J.* 96 (2003) 81–98. <https://doi.org/10.1016/j.cej.2003.08.025>.

- [43] J.U. Brackbill, D.B. Kothe, C. Zemach, A continuum method for modeling surface tension, *J. Comput. Phys.* 100 (1992) 335–354. [https://doi.org/10.1016/0021-9991\(92\)90240-Y](https://doi.org/10.1016/0021-9991(92)90240-Y).
- [44] Š. Šikalo, H.D. Wilhelm, I. V. Roisman, S. Jakirlić, C. Tropea, Dynamic contact angle of spreading droplets: Experiments and simulations, *Phys. Fluids*. 17 (2005) 1–13. <https://doi.org/10.1063/1.1928828>.
- [45] K. Yokoi, D. Vadillo, J. Hinch, I. Hutchings, Numerical studies of the influence of the dynamic contact angle on a droplet impacting on a dry surface, *Phys. Fluids*. 21 (2009). <https://doi.org/10.1063/1.3158468>.
- [46] S.A. Gheni, M.H. Al-Dahhan, Assessing the Feasibility of Optical Probe in Phase Holdup Measurements and Flow Regime Identification, *Int. J. Chem. React. Eng.* (2015). <https://doi.org/10.1515/ijcre-2014-0147>.
- [47] V. Alexander, Hydrodynamics Related Performance Evaluation of Upflow Moving Bed Hydrotreater Reactor (MBR) Using Developed Experimental Methods and CFD Simulation, Missouri University of Science and Technology, 2018.
- [48] D.J. Sheskin, Parametric and non parametric statistical procedures: Third edition, 2003.
- [49] U. Diwekar, A. David, BONUS Algorithm for Large Scale Stochastic Nonlinear Programming Problems, 2015.
- [50] B.W. Silverman, Density estimation: For statistics and data analysis, 2018. <https://doi.org/10.1201/9781315140919>.

V. POROSITY DISTRIBUTION MODEL AND HYDRODYNAMICS IN MOVING BED REACTORS: CFD SIMULATION AND EXPERIMENTS

Binbin Qi¹, Sebastián Uribe¹, Omar Farid¹, Muthanna Al-Dahhan^{1,2*}

¹ Chemical and Biochemical Engineering Department, Missouri University of Science and Technology, Rolla, MO 65409 USA

² Nuclear Engineering and Radiation Science Department, Missouri University of Science and Technology, Rolla, MO 65409, USA

* Corresponding author: aldahhanm@mst.edu

ABSTRACT

Moving bed reactors (MBR) are newly developed gas-liquid-solid interaction reactor that gas and liquid phase flow concurrently upward pushing the catalyst bed leading to around 10% expansion, which brings challenges to the investigations of hydrodynamics inside MBR because of the uncertainty of the bed porosity due to the expansion. Discrete element model (DEM) coupled with single phase simulation was used to generate expanded bed and a porosity distribution correlation was proposed to predict the porosity distribution for the MBR with a cone distributor with different bed expansions. By implementing the porosity distribution correlation, CFD simulation was conducted using Euler-Euler multiphase model to investigate the hydrodynamics considering the bed as effective porous media. Experimental work was conducted to validate the flow patterns and pressure drops inside the MBR.

Keywords: Moving bed reactor, bed expansion, porosity distribution, DEM, Eulerian-Lagrangian approach, VOF, hydrodynamics

1. INTRODUCTION

As a relatively new multiphase phase reactor, moving bed reactors (MBR) have been utilized in selected hydrotreating processes due to some inherent advantages such as processing higher metal feeds, outputting lower Sulphur products and enhancing the economic efficiency [1]. In MBR, the gas and liquid flow co-currently upward through a catalyst bed supported by a cone shape distributor, leading to a slight expansion of the catalyst bed (around 10% in volume) without fluidization [2–4]. The catalysts are suspended by the two-phase flow which is able to enhance the catalyst performance, mitigate coking, and improve the pressure drop along the reactor [5]. In practice, the suspended catalysts are not stationary but vibrating due to the fluid flow. This slight expansion and vibration of the catalyst creates a special scenario in between Packed Bed Reactors and Fluidized Bed Reactors. Vast contributions in literature have addressed on either the hydrodynamics or the reaction kinetics in packed bed reactors (PBR) and fluidized bed reactors (FBR). However, researches on this special case are hardly found, except for some works that studied on the hydrodynamics within the operation conditions that maintain the catalysts as packed bed without expansion [6,7].

Recently, Alexander et al. [8] studied the gas dispersion inside the MBR under expanded condition. However, due to the limitation of the currently available experimental techniques, no details describing the effects of the characteristics of the bed expansion are provided, such as the porosity distribution along the bed height and radius both in the cone section and cylinder section, which is critical and pivotal to evaluate and determine the hydrodynamics of the reactors. It is also impractical to physically measure the real-time

local porosity distribution inside the expanded packed bed through experimental techniques. Besides, advanced measurement techniques are needed to measure the real-time local hydrodynamics and transport parameters which are not always available. Therefore, mathematical modelling through computational fluid dynamics techniques (CFD) would be a feasible alternative to quantify the bed expansion and related local hydrodynamics in MBR. Nevertheless, despite the advantages of CFD modelling, there is still a need to pair modelling and experimental studies to validate the models' predictions. Due to limited information can be obtained through experimental techniques for MBRs, the validation of the CFD simulation predictions can be conducted by comparison of the overall hydrodynamics parameters, such as pressure drop along the reactor. As well, the flow patterns can be observed to compare with the simulation results as a visualization verification.

A promising technique to simulate the packed bed is to use discrete element method (DEM) [9] which is designed for modelling the granular flow such as sand, particles or powders. In DEM models, solids are treated as a Lagrangian phase, where an equation of motion based on Newton's second law is solved on each of the solid particles, and hence, the particle movement and their interactions are fully resolved. However, implementing DEM models on large scale systems, such as PBR, FBR and MBR, where the number of particles can be in the order of millions, results in high computational costs, and is therefore limited by the available computational resources.

Several contributions in the modelling of single fluid phase PBR or FBR where DEM models are applied can be found in literature [10–14]. In these contributions, the fluid phase interacting with the solid phase is treated as an Eulerian continuous phase. The

multiphase interactions are accounted on surface and body force terms on the solids, and through volumetric momentum sources on the fluid phase. In MBR, gas and liquid flow upward pushing the catalyst to expand, which represents two Eulerian continuous phases (gas and liquid) and one Lagrangian discrete phase (solid catalyst). As far as the authors' concern, there are no reported works in the literature where the coupling of two Eulerian phases and a Lagrangian is developed and implemented. The main reason for the lack of these models can be attributed to the computational complexity in the coupling of these models, and also to the fact that most of the industrial applications where a solid catalyst moves or is fluidized, imply a single-phase flow.

Therefore, the mathematical description of MBR through a detailed DEM model is challenging, and further developments to overcome the complexity of the phases' description is yet required. An alternative to simplify the modelling of a two-phase flow through a packed bed has been widely explored in literature regarding trickle bed reactors (TBR) [15–18]. In such systems, gas and liquid phases concurrently flow downward through a bed packed with solid catalysts; however, in TBR the solid packing is fixed. Despite that the fact that having a fixed solid packing in TBRs reduces the complexity in the mathematical description of the phases, only few works can be found in literature where the solid phase is described with rigorous detail [19], due to the vast computational resources required. Hence, the models incorporating a detailed description of the solid phase are constrained to small-scale systems. In order to enable the modelling of large scale units, it has been a common practice in TRBs to implement a Euler-Euler models to describe the gas and liquid as effective phases flowing through an effective media, which incorporates the effect of the presence of the solids without a detailed description of the

solids. This implies that in such models, the three phases are treated as interpenetrating media. Momentum balances are solved for each of the fluid phases, which incorporate volumetric momentum exchange terms to include the multiphase interactions; while the solid phase is usually described by a porosity distribution model, which is usually an algebraic expression that described the average variations of the void phase along the column radius [17].

Such Euler-Euler models seem to be a promising alternative to model MBRs, by reducing the complexity of the mathematical description of the phases. However, a major challenge that prevents the implementation of such models for MBRs is the proper algebraic description of the solids phase. Due to the conical distributor and the bed expansion, the void phase distribution in a MBR present a specific and challenging case, which has not been addressed in literature. Thus, in order to overcome such shortcoming and enabling the application of Euler-Euler models for MBRs, in this work, porosity distribution correlations describing the catalyst bed characteristics on a MBR under different expansions, 5%, 10%, and 15%, respectively, as well as for a MBR without bed expansion, were developed. Such porosity distributions were developed based bed structures predicted by an implemented DEM model. The applicability of the developed model was tested by setting an Euler-Euler model using the developed 10% expansion porosity distribution model. The overall experimental flow pattern and pressure drops along the reactor were observed to compare with the simulation for validation. However, further experimental work is required to validate the other local hydrodynamics fields predictions.

2. POROSITY DISTRIBUTION MODEL

2.1. GOVERNING EQUATIONS

In order to obtain the bed void phase distribution description under the different expansions, a DEM model was implemented in the commercial software StarCCM+ 13.04. Spherical alumina particles (3 mm in diameter) were packed inside a 3-inch cylinder with a cone bottom as shown in Figure 1. A gas phase was set as the continuous phase that flows upward from the cone distributor with multiple holes on it to push the catalyst bed to expand. In the Lagrangian framework, the exchange of momentum is balanced by the surface force and body force that act on the discrete particles. The momentum conservation equation for a discrete particle of mass m_σ is given by:

$$m_\sigma \frac{d\mathbf{v}_\sigma}{dt} = \mathbf{F}_s + \mathbf{F}_b \quad (1)$$

$$\mathbf{F}_s = \mathbf{F}_d + \mathbf{F}_p \quad (2)$$

$$\mathbf{F}_b = \mathbf{F}_g + \mathbf{F}_c \quad (3)$$

where \mathbf{v}_σ is the particle velocity vector, and m_σ is the mass of each solid particle. \mathbf{F}_s denotes the resultant of the forces that act on the surface on the particle and \mathbf{F}_b is the resultant of the body forces,

$$\mathbf{F}_d = \frac{1}{2} C_d \rho_\beta A_\sigma |\mathbf{v}_{slip}| \mathbf{v}_{slip} \quad \text{Drag force} \quad (4)$$

$$\mathbf{F}_p = V_\sigma \nabla P \quad \text{Pressure gradient force} \quad (5)$$

$$\mathbf{F}_g = m_\sigma \mathbf{g} \quad \text{Gravity force} \quad (6)$$

$$\mathbf{F}_c = \mathbf{F}_n + \mathbf{F}_t \quad \text{Contact force} \quad (7)$$

$$C_d = \begin{cases} \frac{24(1 + 0.15 \text{Re}_p^{0.687})}{\varepsilon_B} \varepsilon^{1-W} & \text{if } \varepsilon_B \text{Re}_p \leq 1000 \\ 0.44 & \text{if } \varepsilon_B \text{Re}_p > 1000 \end{cases} \quad \text{Drag coefficient} \quad (8)$$

where C_d is the drag coefficient, described by Gidaspow model (Equation (8)), W is the Wen-Yu exponent, which was set as $W = -3.65$. ρ_β is the density of continuous phase, which corresponds to air density; A_σ is the projected area of the particle, $\mathbf{v}_{slip} = \mathbf{v}_\beta - \mathbf{v}_\sigma$ represents the slip velocity with \mathbf{v}_β as the velocity of gas phase, V_σ is the volume of the particle, ∇P is the gradient of the static pressure in gas phase, and \mathbf{F}_c is the Hertz-Mindlin no-slip contact model which is the variant of the non-linear spring-dashpot contact model including the normal and tangential force component as shown in Figure 2 and are given by:

$$\mathbf{F}_n = -K_n d_n - N_n v_n \quad (9)$$

$$\mathbf{F}_t = \frac{|K_n d_n| C_{fs} d_t}{|d_t|} \quad (10)$$

where v_n is the relative component of the solids velocity (\mathbf{v}_σ) in the normal direction to the contact point between two spheres, or between a sphere and a wall. d_n and d_t are the normal and tangential overlaps at the contact point, respectively. C_{fs} is the static friction coefficient. K_n and N_n are defined according to the following equations:

$$K_n = \frac{2}{3} \frac{E_A}{1 - \nu_A^2} \sqrt{\frac{d_n R_\sigma}{2}} \quad \text{Normal spring stiffness} \quad (11)$$

$$N_n = N_{n_damp} \sqrt{\left(\frac{5K_n m_\sigma}{2}\right)} \quad \text{Normal damping} \quad (12)$$

$$N_{n_damp} = \frac{-\ln(C_{n_rest})}{\sqrt{\pi^2 + \ln(C_{n_rest})^2}} \quad \text{Normal damping coefficient} \quad (13)$$

where R_σ is the solids particles radius. E_A is the Young's modulus of the solid particles [20]; ν_A is the Poisson ratio of the solid; C_{n_rest} is the normal restitution coefficient.

Two-way coupling scheme was implemented to simulate the interactions between the gas phase and the solids. On this scheme, both phases have influence on each other exchanging momentum through the solids' surface area. With this approach, the momentum balance for the gas-phase (β -phase) can be written as follows:

$$\frac{\partial}{\partial t}(\varepsilon_\beta \rho_\beta) + \nabla \cdot (\varepsilon_\beta \rho_\beta \mathbf{v}_\beta) = 0 \quad (14)$$

$$\begin{aligned} \frac{\partial}{\partial t}(\varepsilon_\beta \rho_\beta \mathbf{v}_\beta) + \nabla \cdot (\varepsilon_\beta \rho_\beta \mathbf{v}_\beta) = & -\varepsilon_\beta \nabla P + \nabla \cdot \left[\varepsilon_\beta \mu_\beta \left(\nabla \mathbf{v}_\beta + (\nabla \mathbf{v}_\beta)^T - \frac{2}{3}(\nabla \cdot \mathbf{v}_\beta) \mathbf{I} \right) \right] \\ & + \varepsilon_\beta \rho_\beta \mathbf{g} + \mathbf{F}_s \end{aligned} \quad (15)$$

where \mathbf{F}_s has been defined by Equation (2). ε_β is the gas volume fraction, which is estimated on each computational cell, based on the ratio of the void volume left by the moving solids particles at a certain time step to the total volume of the computational cell. All the simulation parameters are listed in Table 1.

2.2. PACKING AND EXPANSION SIMULATION

In order to obtain the solid phase distribution under different expansions, two main steps in the simulation scheme were needed. First, the free falling of spheres was simulated

to obtain the packed bed condition. For this step, an injector was set at the top of the column, which fed enough spheres to fill the static height of 5 inches at a constant mass flow rate of 18 kg/s. During this step, the gas inlet was disabled, in order to allow the solid packing to settle. After enough spheres were fed to the column, the injector was stopped, and the computation was continued for 5 seconds in order to allow the solids to reach their final position. From this result, the geometry for the solids distribution under no expansion was extracted.

Afterwards, the gas inlet was enabled. A slowly increasing velocity was set as the inlet condition, feeding air from 0.1 m/s to up 1.5 m/s. The bed expansion was measured with respect to the obtained height of the bed. This means that, for example, a 5% expansion represents that the bed height reached 5.25 inches. When a bed reached a steady expansion, the simulation was stopped and the geometry was extracted.



Figure 1. Catalyst packed bed inside the column with cone distributor

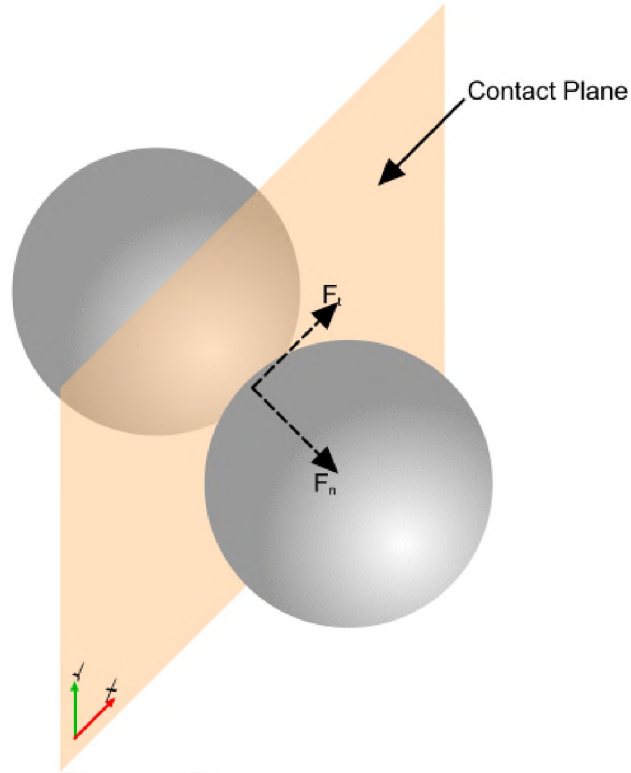


Figure 2. Discrete element method module

2.3. DEVELOPMENT OF MODEL

In order to quantify the radial porosity distribution at different axial positions for all of the expansion cases, Mueller's method [21], which is based on the sphere center coordinates and the arc length, was used to determine the radial porosity distribution profile as shown in Figure 3, which is given by:

$$\varepsilon(r) = 1 - \frac{S_{solid}}{S_{total}} = 1 - \sum_{n=1}^{N(R_\sigma)} \frac{S_n(r)}{S_T(r)} \quad (16)$$

where $N(R_\sigma)$ is the number of particles with cross-sectional radius R_σ at the radial position r , $S_n(r)$ is the total arc length at radial position r , $S_T(r)$ is the perimeter of circle with radius r .

Table 1. CFD-DEM simulation parameters

Item	Remark
Number of particles	3000
Particle diameter [mm]	3
Particle density [kg/m^3]	3950
Gas density [kg/m^3]	1.18415
Gas dynamic viscosity [$\text{Pa} \cdot \text{s}$]	1.855×10^{-5}
Young's modulus [GPa]	375
Poisson ratio	0.27
Coefficient of restitution	0.75
Coefficient of friction	0.5
Time step [s]	1.0×10^{-6}

Many radial porosity distribution models have been proposed for packed bed during the last few decades [22–27], which can be separated into two categories, oscillatory correlations and exponential correlations. The oscillatory correlations capture, to a certain extent, the local variations of the average porosity distribution, predicting local increases and decreases of the porosity along the bed radial position; while on the exponential correlations it is assumed that the bed porosity decays exponentially from the wall [27], predicting a smoothed profile with no strong local variations. In most of these correlations, both oscillatory and exponential, the porosity changes along the bed height are usually neglected.

For beds of a large aspect ratios (Diameter of column over diameter of particles, d_c / d_σ), which is the case of most industrial applications, the solids distribution becomes practically homogeneous away from the walls, and hence, the only important variations on the porosity are observed on the near-wall regions [28]. In these cases, the exponential correlations seem to be enough to capture the main bed textural characteristics.

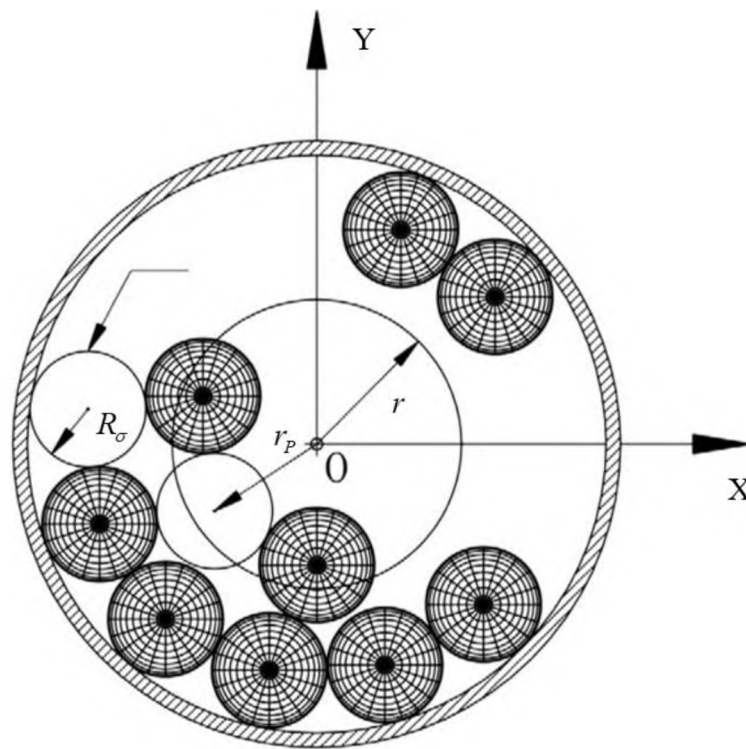


Figure 3. Schematic of porosity calculation module

In our system, the porosity variation along the bed height is considered to be more significant than the radial variation, especially in the cone section due to the flow distribution, and according to the obtained results. In this sense, in order to develop a correlation to capture the bed textural characteristics of the bed under different expansions, a new porosity distribution model integrating both cone and cylinder parts is proposed. The

model considers and exponential formulation to capture radial variations, and an oscillatory formulation to capture the axial variations, as described by Equations (17) to (20).

$$\varepsilon_B = 1 + f(z)f(r) \quad (17)$$

$$f(z) = 1 + a_1 \exp \left[a_2 \left(\frac{z}{H} \right) \right] \cos \left[a_3 \left(\frac{z}{H} \right) + a_4 \right] \quad (18)$$

$$f(r) = 1 - a_5 \exp \left[1 - 2 \left(\frac{R-r}{d_\sigma} \right) \right] \quad (19)$$

$$R = \begin{cases} r_c + z \tan(90 - \theta) & z < H_c \\ R_c & z \geq H_c \end{cases} \quad (20)$$

where z is the observation level height, H is the total bed height, H_c is the cone height, R_c is the radius of the column, r_c is the diameter of the bottom on the cone section, r is the observation radius, d_σ is the particle diameter, θ is the cone angle, and a_1 to a_5 are the constants related to the bed expansion.

2.4. POROSITY DISTRIBUTION FUNCTIONS ASSESSMENT

Figure 4 (a) to (d) shows the local radial porosity distribution profiles obtained by the analysis of the different expanded beds by Muller's method at different axial positions. From these figures, it can be seen that there is an evident oscillatory behavior on the variations of the porosity distribution at the different axial positions for all cases, packed bed and the beds under different expansions. The estimated local porosity distributions were then averaged in order to obtain an average radial and axial porosity distribution. Figure 5 (a) and (b) show the obtained averaged porosity distribution profiles on the radial and axial positions, respectively. From these figures, it can be seen that the oscillatory

profile in the radial porosity variations are smoothed, and that the distribution more closely resembles an exponential behavior. According to this observation, it was considered that to estimate an overall radial porosity distribution, the local oscillations can be overlooked, and then the implementation of an exponential formulation of Equation (18) is in agreement with the DEM results. Nevertheless, due to the especial cone geometry used on the MBR, the oscillatory behavior on the average axial porosity variations seems to prevail. Considering this observed behavior, an oscillatory formulation was implemented on the model, as shown in Equation (17).

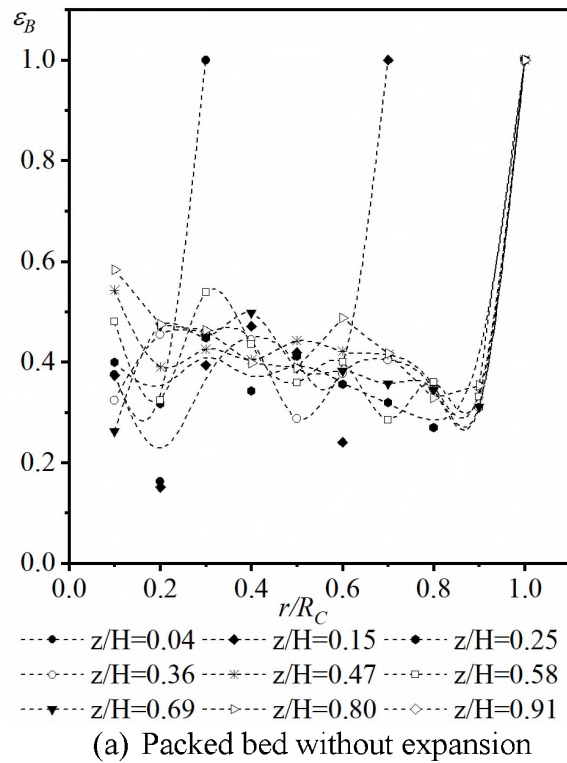


Figure 4. Porosity distribution in terms of radius at different levels

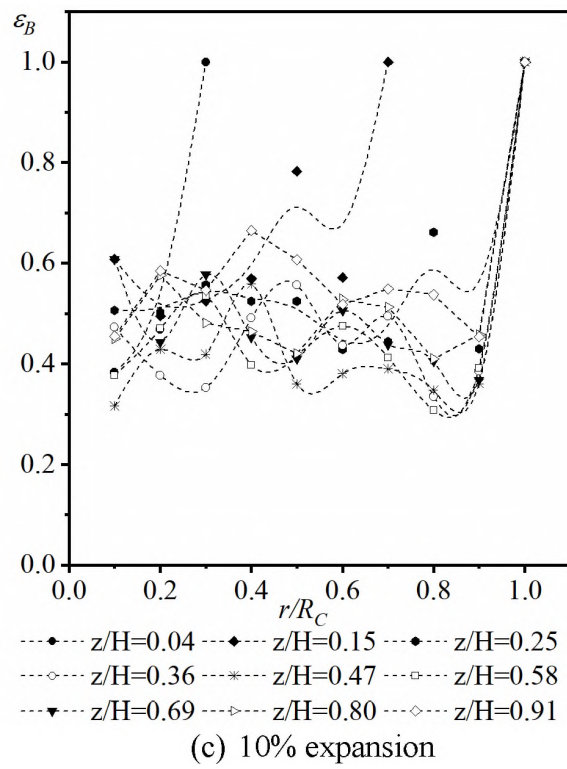
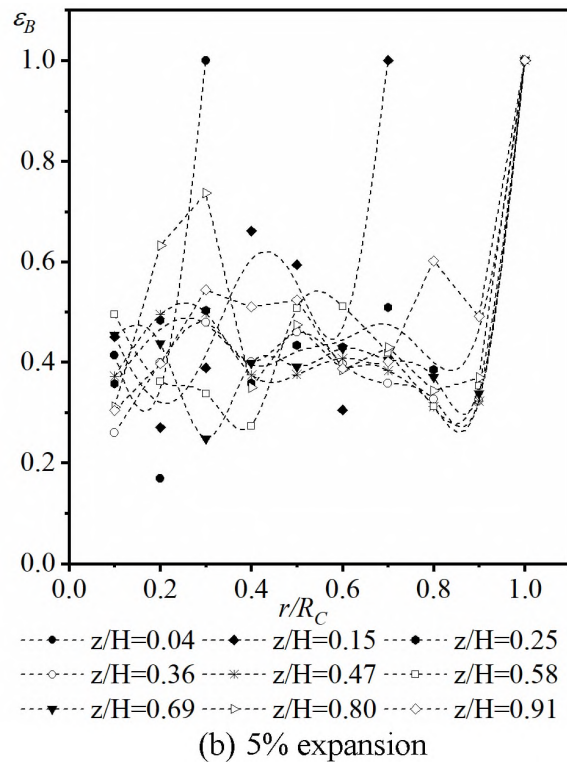


Figure 4. Porosity distribution in terms of radius at different levels (cont.)

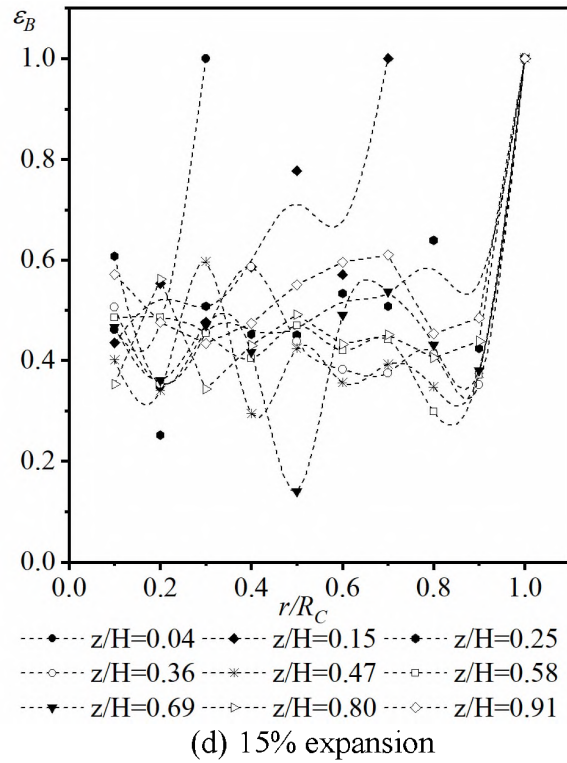


Figure 4. Porosity distribution in terms of radius at different levels (cont.)

Comparing the obtained averaged porosity distributions, it can be seen that the main differences in the distributions are observed when comparing the axial porosity distribution. Comparing the porosity distributions at the different bed expansions with the packed bed one, it can be seen that the radial porosity distribution does not change significantly at the different expansion percentages. This suggests that the bed expansion has a stronger effect over the axial porosity distribution, than its effect over the radial porosity distribution.

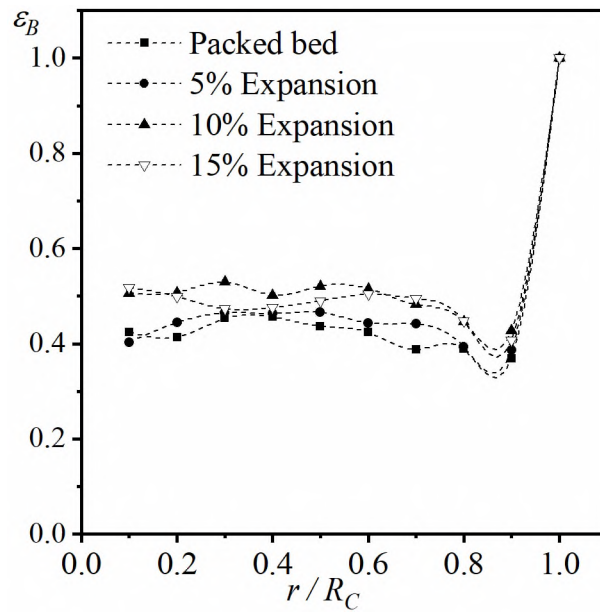
From Figure 5 (b), it can be seen that the main axial porosity distribution differences are observed in the cone section, and that the bed under 10% expansion exhibits the highest porosity. Furthermore, it can be appreciated that the overall axial and radial porosity on the

case under 15% expansion decreases when compared with the porosity obtained on the bed under 10% expansion. This behavior is unexpected, and a possible cause for this would be that under 15% expansion the bed is starting to fluidize, and therefore the solids are no longer suspended, but rather they are free to move within the bed, modifying the measured porosity distribution.

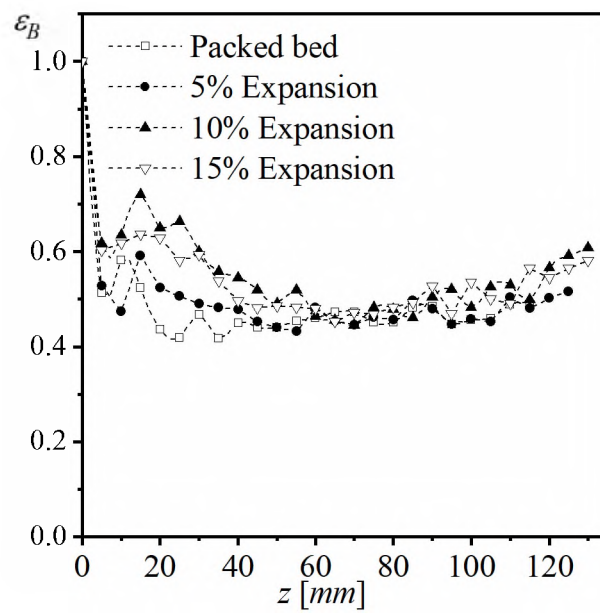
The results shown in Figure 4 were then used to estimate the fitting parameters from the new developed correlation, parameters a_1 to a_5 from Equation (18) and (19). The values of these parameters are listed in Table 2 for all the cases together with the plots in Figure 7. From the plot, it can be seen that parameters a_1 and a_4 decrease as the bed expands, while the other parameters seem to be trivial. Furthermore, the parameters a_2 , a_3 and a_5 do not suffer from significant changes as the bed expands. Both a_1 and a_4 are included in the $f(z)$ part, which indicates that the bed expansion has a greater effect over the axial variations of the porosity distribution .

Table 2. Parameters estimation for different bed expansions

%	a_1	a_2	a_3	a_4	a_5
0	4.4336	-0.0575	-0.0031	10.6107	-0.3355
5	5.1952	0.4696	0.1189	4.4045	-0.3481
10	1.4338	0.7729	0.7498	3.4864	-0.3462
15	-1.4415	0.3847	-0.803	-0.0247	-0.3402



(a) Radial distribution



(b) Axial distribution

Figure 5. Average porosity distribution: (a) Radial distribution, (b) Axial distribution

Figure 6 shows the comparison of the average overall porosity between the DEM simulation and our developed porosity distribution model. The overall root mean squared error $\left(RMSE = \sqrt{1/N \sum (\psi_{DEM} - \psi_{Model})^2}\right)$ was estimated to be 10.15%, 10.58%, 9.70%, and 10.12%, respectively. From the figure it can be seen that the porosity increases when the bed is expanded from packed bed to 10% but decreases when it reaches 15%. It could be reasonably expected that the bed starts to be fluidized after 10% expansion, which could cause the solid particles to circulate in the bed, rather than being suspended as it is desired on the MBR.

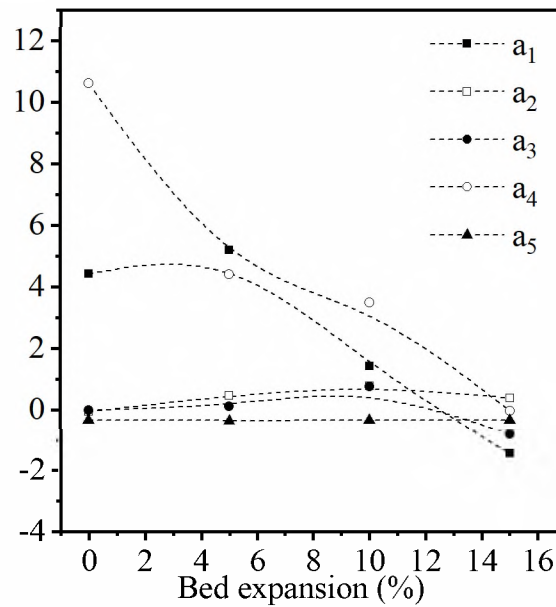


Figure 6. Parameter values for different expansions

Figures 8 (a) and (b) show the average porosity distribution obtained by the DEM results analysis and the predicted distribution by the proposed model on the radial and axial directions, respectively, for a bed under 10% expansion, for comparison purposes. It can

be seen that in both cases, there is a good agreement in the predicted trends by the proposed model and the porosity distribution obtained by analysis of the DEM model results. Instead of predicting all the details, the proposed model predicts a smoothed porosity distribution within reasonable range as shown in Figure 9.

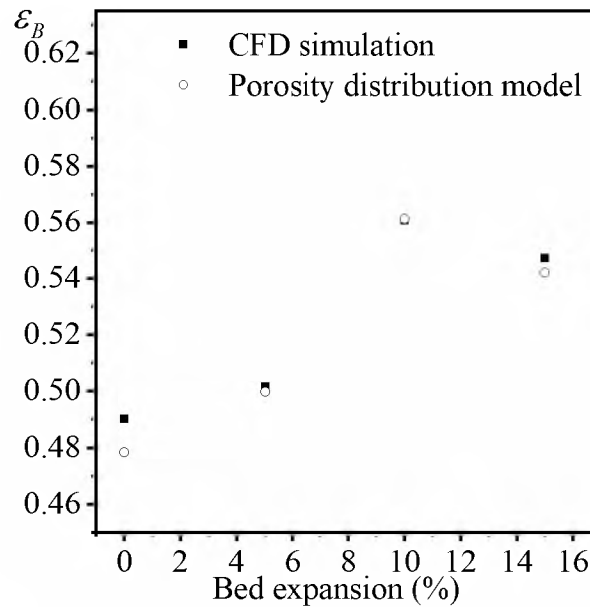


Figure 7. Comparison of overall averaged porosity between CFD simulation and model

3. CFD SIMULATION COUPLED WITH POROSITY DISTRIBUTION CORRELATION

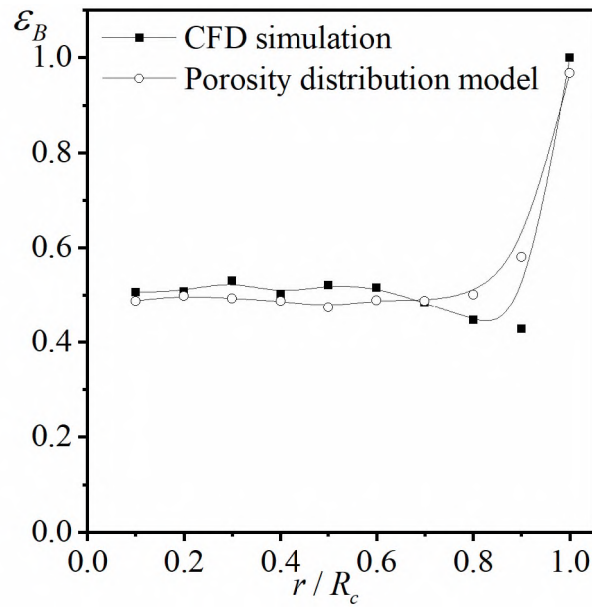
In order to assess the performance and applicability of the proposed porosity distribution model above, a scale-down 11 inch in diameter moving bed reactor was modelled by CFD techniques, considering both of the expanded packed bed and inert packing layer above the chimney tray as effective porous media. The newly developed porosity distribution model (Equation (17) – (20)) was implemented for the expanded packed bed, considering a 10% expansion, as such bed expansion is commonly found on

industrial applications. The porosity distribution of a cut plane can be visualized in Figure 10. For the inert packing layer, the De Klerk [26] oscillatory correlation model was used, which is expressed by:

$$\varepsilon_B = \begin{cases} 2.14Z^2 - 2.53Z + 1 & \text{for } Z \leq 0.637 \\ \varepsilon_b + 0.29e^{-0.6Z} \cos(2.3\pi(Z - 0.16)) + 0.15e^{-0.9Z} & \text{for } Z > 0.637 \end{cases} \quad (21)$$

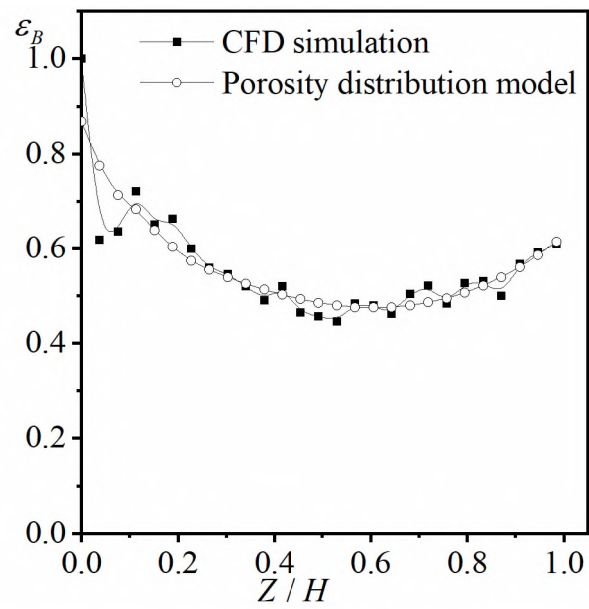
$$Z = \frac{R-r}{d_p}$$

where ε_b is the bed porosity in the absence of wall effects which in this case is 0.41.



(a) Radial distribution

Figure 8. Comparison of the average porosity distribution under 10% expansion



(b) Axial distribution

Figure 8. Comparison of the average porosity distribution under 10% expansion (cont.)

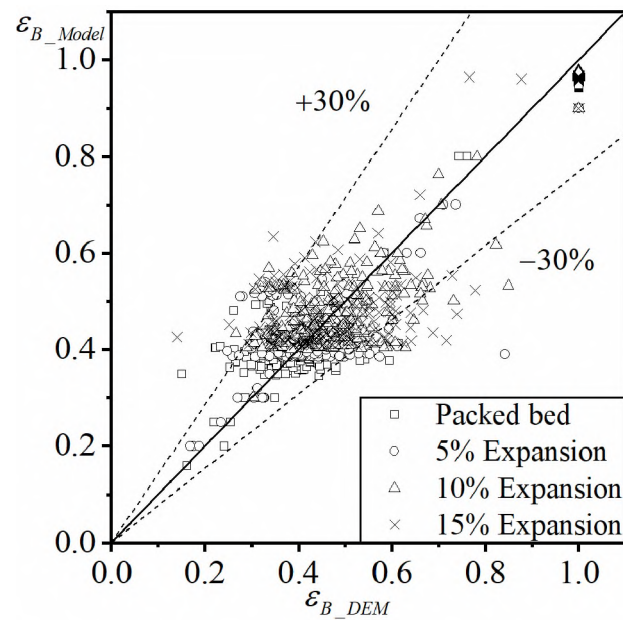


Figure 9. Comparison of the local porosity obtained by the DEM simulations and the proposed model

3.1. GOVERNING EQUATIONS

In this work, volume of fluid (VOF) multiphase model [29] was implemented due to its efficiency and flexibility. The VOF method is an interface tracking technique, which is based on defining the total volume fraction of two or more immiscible phases as an unity in a fixed mesh system [30,31]. A single set of transport equations is shared by both phase and the volume fraction of each phase in each cell is calculated. It should be noted that in porous media part of the computational cell is occupied by solid phase that fluids can only flow through the rest of the space which is presented mathematically by porosity in each cell. Hence, the continuity equation is expressed as follows:

$$\frac{\partial}{\partial t}(\rho \varepsilon_B) + \nabla \cdot (\rho \varepsilon_B \mathbf{u}_i) = 0 \quad (22)$$

$$\rho = \sum \varepsilon_i \rho_i \quad (23)$$

where ρ is the density of phase mixture, ρ_i is the density of each phase, \mathbf{u}_i is the velocity vector, ε_B is the porosity in each computational cell, which can be obtained by the porosity distribution model developed in previous section, ε_i is the volume fraction of each phase in the empty space of each computational cell, where

$$\sum \varepsilon_i = 1 \quad (24)$$

One of the typical ways describing the fluid flow through porous media is Darcy's law, which relates the pressure gradient in terms of fluid velocity and permeability. However, Darcy's law can only be applied to creeping flow ($Re \ll 1$). As the flow velocity increases, the relationship between the pressure gradient and velocity tends to be nonlinear. Hence, a quadratic term was proposed by Dupuit and Forchheimer [32]. The momentum equation is expressed by:

$$\begin{aligned} \frac{\partial}{\partial t}(\rho \varepsilon_B \mathbf{u}) + \nabla \cdot (\rho \varepsilon_B \mathbf{u}) = & -\varepsilon_B \nabla p + \nabla \cdot \left[\varepsilon_B \mu \left(\nabla \mathbf{u} + (\nabla \mathbf{u})^T \right) \right] \\ & + \rho \varepsilon_B \mathbf{g} - \varepsilon_B \mathbf{P}_v \mathbf{u} - \varepsilon_B \mathbf{P}_i |\mathbf{u}| \mathbf{u} + \overline{\mathbf{F}} \end{aligned} \quad (25)$$

where ∇p is the pressure gradient, μ is the viscosity, \mathbf{P}_v and \mathbf{P}_i are viscous resistance tensor and inertial resistance tensor, respectively, in porous media, and $\overline{\mathbf{F}}$ represents the interaction forces. For randomly packed sphere catalysts, it is reasonable to assume that the packed bed is an isotropic system. Therefore, the empirical model of the pressure drops over length of fluid flowing through a packed bed can be expressed based on Ergun equation [33] as follows:

$$-\frac{\Delta p}{L} = \frac{E_1 \mu (1 - \varepsilon_B)^2 \mathbf{u}}{\varepsilon^3 d_\sigma^2} + \frac{E_2 \rho (1 - \varepsilon_B) \mathbf{u}^2}{\varepsilon^3 d_\sigma} \quad (26)$$

where $E_1 = 150$ and $E_2 = 1.75$.

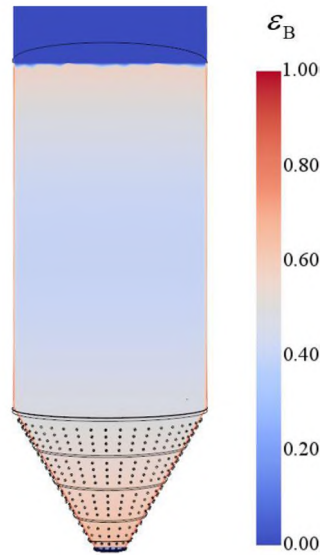


Figure 10. Porosity distribution of the catalyst bed inside MBR

3.2. SURFACE TENSION MODEL

The surface tension has to be included along the interface between each two phases as well as between the phases and the walls because the fluid molecules close to the interfaces are under uneven attraction forces [34]. The surface tension plays a fundamental role in transport phenomena. Brackbill et al. proposed the continuum surface force (CSF) method [34] by modeling the interfacial surface force as a volumetric force, where the surface pressure is proportional to the surface curvature that determines the surface tension force. The surface tension force can be resolved into normal and tangential components which can be expressed by:

$$F_{\sigma} = F_{\sigma,n} + F_{\sigma,t} = \sigma \kappa \mathbf{n} + \frac{\partial \sigma}{\partial t} \mathbf{t} \quad (27)$$

where σ is the surface tension coefficient, \mathbf{n} is the unit vector normal to the surface, \mathbf{t} is the unit vector tangential to the surface, κ is the surface curvature. According to the CSF model, the vector normal to the interface can be expressed as:

$$\mathbf{n} = \nabla \varepsilon_i \quad (28)$$

The curvature of the interface will be:

$$\kappa = -\nabla \cdot \frac{\nabla \varepsilon_i}{|\nabla \varepsilon_i|} \quad (29)$$

3.3. WALL ADHESION

The surface tension force between the fluids and the wall is affected by the contact angle, which is measured by the triple line which is shown in Figure 11. In reality, the triple line moves which means the contact angle changes so it is called dynamic contact angle,

which is calculated by the Kistler dynamic contact angle model coupled with Hoffman function [35,36] as shown below:

$$\theta_d = f_{Hoff} \left(Ca + f_{Hoff}^{-1}(\theta_e) \right) \quad (30)$$

$$f_{Hoff} = \cos^{-1} \left(1 - 2 \tanh \left(5.16 \left(\frac{x}{1 + 1.31x^{0.99}} \right)^{0.706} \right) \right) \quad (31)$$

where θ_e is the equilibrium (static) contact angle, Ca is the capillary number which is defined as:

$$Ca = \frac{V \mu_p}{\sigma} \quad (32)$$

where μ_p is the dynamic viscosity of the primary phase, σ is the surface tension, V is the triple line characteristic velocity which is defined as:

$$V = -(\mathbf{v} \cdot \mathbf{n}_t) \quad (33)$$

where \mathbf{v} is the relative velocity between the fluid and the wall, \mathbf{n}_t is the unit vector in the tangential direction pointing to the direction normal to the interface. All the simulation specifications are shown in Table 3.

Table 3. Simulation specifications

Item	Value/Remark
Gas	Air, $\rho_g = 1.18415 \text{ kg/m}^3$, $\mu_g = 1.855 \times 10^{-5} \text{ Pa}\cdot\text{s}$
Liquid	Water, $\rho_l = 997.561 \text{ kg/m}^3$, $\mu_l = 8.887 \times 10^{-4} \text{ Pa}\cdot\text{s}$
Surface tension [N/m]	0.072
Wall boundary condition	No-slip

Table 3. Simulation specifications (cont.)

Item	Value/Remark
Operating pressure [MPa]	0.1
Operating temperature [K]	293.15
Mesh type	Polyhedral mesh
Base size [cm]	2
Minimum surface size [mm]	0.5
Number of thin layers	2
Number of prism layers	2
Prism layer stretching	1.5
Prism layer total thickness	33.33% of base size
Surface grow rate	1.3
Total cells number	2.943463×10^7

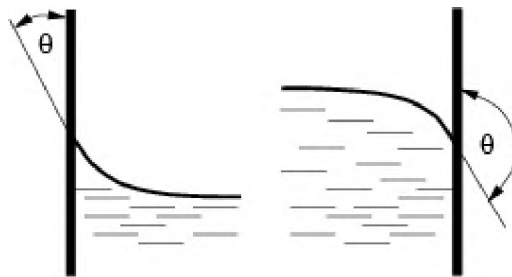


Figure 11. Schematic of contact angle on the walls

4. EXPERIMENTAL WORK

The purpose of the experiments is to observe the flow behavior and patterns at steady state during the operation, and to measure the pressure drop along the reactor wall at different locations as general validation of the model predictions.

The schematic of the scaled-down MBR is shown in Figure 12. It includes three sections which are chimney section, cone section and catalyst bed section, respectively. The inner diameter of the reactor is 29.7 cm while the heights of the three sections are 0.2 m, 0.3 m, and 1 m, respectively. A deflector is used to uniformly disperse the inlet flow. The chimney acts as a stream guidance that liquid flows through the pipe while the gas flows through the side holes on the chimney pipes. The ratio of the diameter of pipe to the diameter of the side hole is 3 in this case. Above the chimney tray, a 5 cm layer of the inert balls (1 cm in diameter) is used as fluid flow distributor. The cone is divided into five sections by the skirts in order to obtain the identical pressure drop and phase volume fraction in each section. There are two local pressure gauges at the inlet and outlet monitoring the overall pressure drop. In addition, five pressure detecting ports were reserved for pressure drop measurement along the reactor wall by Dwyer wet/wet Digital Manometer Serious 490. The other information and operations conditions can be found in Table 4.

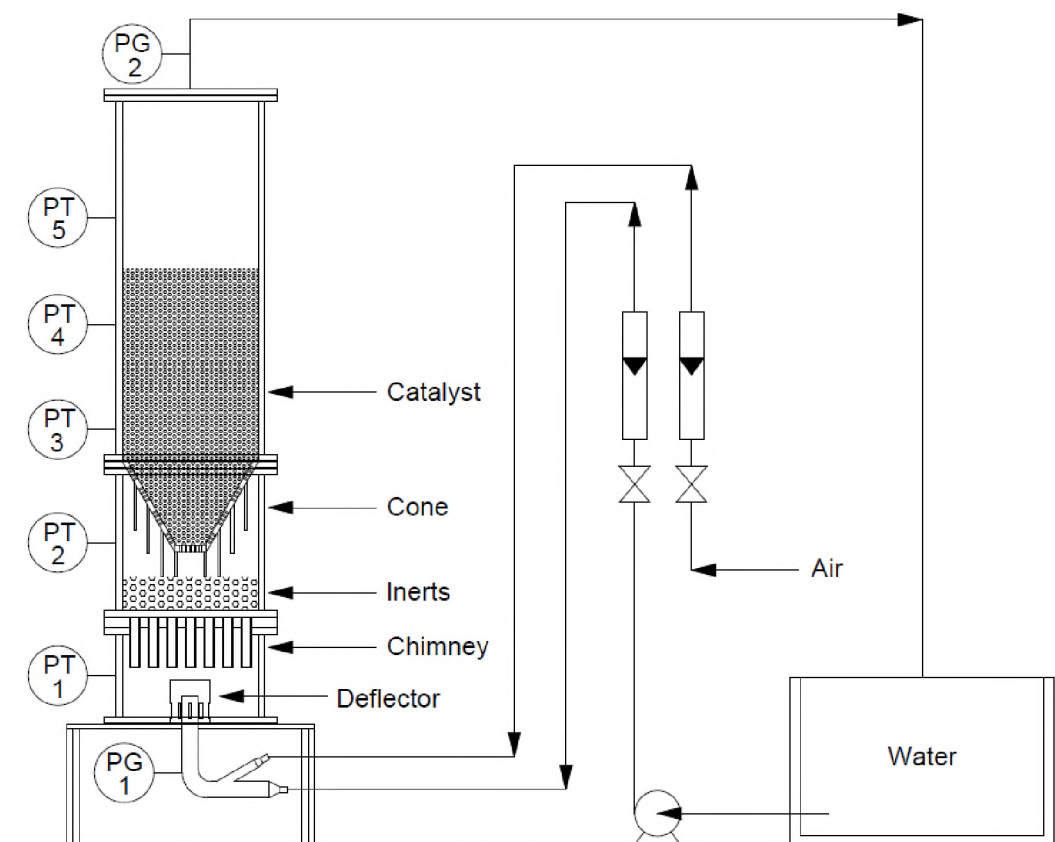


Figure 12. Schematic of experimental setup

Table 4. MBR information and operation conditions

Item	Remark
Reactor diameter [cm]	27.94
Total reactor height [cm]	150
Bed height (including cone) [cm]	70
Air superficial velocity [m / s]	0.78
Water superficial velocity [m / s]	0.13

5. RESULTS AND DISCUSSION

In CFD results as shown in Figure 13, it can be overserved that a gas pocket was generated around the chimneys, which is beneficial to create stable gas flowrate and pressure drop, as well as uniform gas distribution. However, there is more gas mixed with liquid flowing through center chimney pipes than that close to the wall, which can also be seen from the cone section that more gas flows through the column center.

From the experimental observation, the same gas pocket was identified around the chimneys. Even though the deflector contributed significantly to ejecting the fluid flow towards the wall for better distribution, there was still more gas flowing around the center which was similar to the phenomena in CFD simulation. The expansion of the catalyst bed was clearly observed. However, in reality, the expansion was not static that all the catalysts stayed suspended as always, but the expansion process was more likely a pulsing behavior. The expansion was continuously transported from the bottom to the top of the catalyst bed and then repeated over. Particularly, the top layer of the catalyst bed was totally turbulent that some catalysts moved randomly with the fluid flow then sank down.

5.1. PRESSURE DROPS

As shown in Figure 12, the pressured drops from PT-1 to PT-5 (ΔP_{1-2} , ΔP_{2-3} , ΔP_{3-4} , ΔP_{4-5}) were measured to compare with the results from CFD as shown in Figure 13. The Absolute Relative Errors are 6.6%, 3.9%, 10.3%, and 53.3%, respectively. The pressure drop between port 4 and 5 (ΔP_{4-5}) was much lower than that from CFD simulation. As mentioned earlier, the top layer of the catalysts was fluidized due to the two-phase turbulent

flow that it could not be treated as packed bed or expanded packed bed anymore. However, this information was not included in our newly developed porosity distribution model leading to higher pressure drops along the packed bed in CFD simulation. By means of that, certain modification and optimization are required to improve the applicability of the porosity distribution model proposed in this work. However, the improvement procedure needs to be done by practical experimental quantification such as measuring the average porosity at the top layer of the fluidized catalysts. By far, no such advanced techniques can be found to obtain such information. Hence, the improvement and modification will not be addressed in this work.

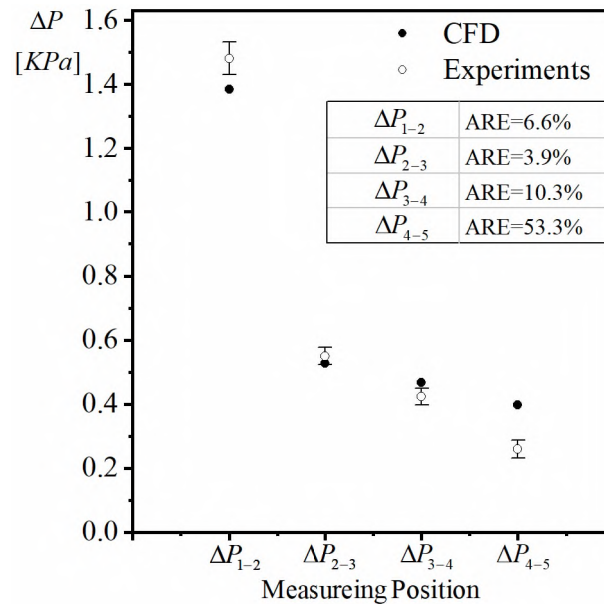


Figure 13. Pressure drops at different locations along the reactor in CFD and experiments

5.2. VELOCITY FIELD

Velocity field indicates the fluid flow orientation and magnitude inside the reactor.

The line integral convolution of the fluid velocity of one cut plane is shown in Figure 14.

It is noted that for VOF method, gas and liquid share the same velocity. It can be clearly seen that the air/water mixture is injected into the column horizontally through slots of the deflector that maximized the phase dispersion creating large eddies. Air and water separate around the chimneys where the gas pocket is generated so that air has equal chance to flow through the side holes to mix with the water flowing through the chimney pipes leading to better mixing and uniform distribution. In this way, the air/water mixture can flow passing through each cone section that is divided by skirts maintaining identical pressure drop and phase holdup. However, when air/water mixture flow through the holes on the cone, the flow orientation is always facing inward normal to the cone surface, that the fluid tends to flow towards to the center and at the same time, due to the gravity, air tends to flow upward regardless. When the phase mixture exits the catalyst bed region, it starts creates significant turbulent eddies.

5.3. GAS SATURATION

For VOF method, the total volume fraction of two phases is equal to 1 which represents the porous space excluding the solid phase in each computational cell in CFD simulation. Therefore, in other words, the volume fraction of each phase is the phase saturation (ϕ). Figure 16 shows the gas saturation at three different levels in the expanded catalyst bed. At $z/H = 0.3$, which is right above the cone, the gas saturation doesn't change significantly along the radius even though it is slightly higher in the center. As explained in the last section, the phase volume fractions are almost the same before the flow passing through the cone. Due to the tendency of flowing towards to the center, more gas accumulates in the center along the bed height as shown in Figure 15 and Figure 16.

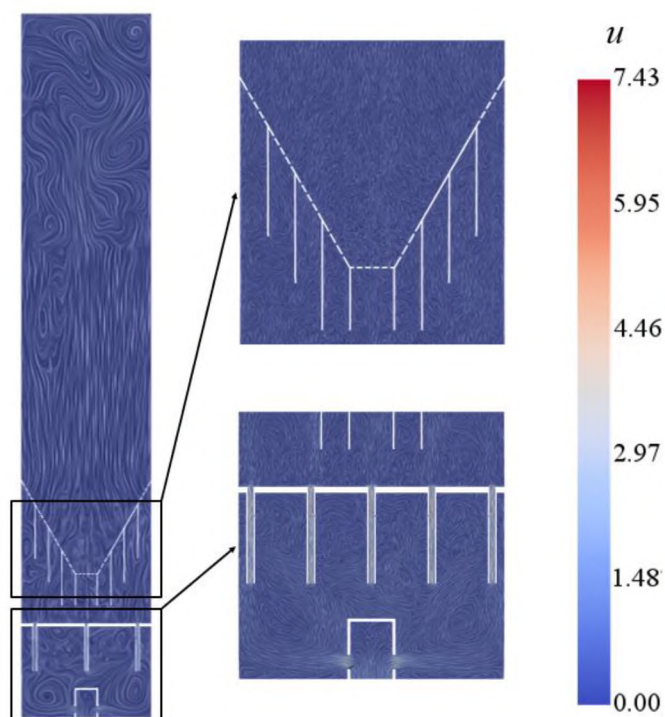


Figure 14. Velocity field on a cut plane in CFD

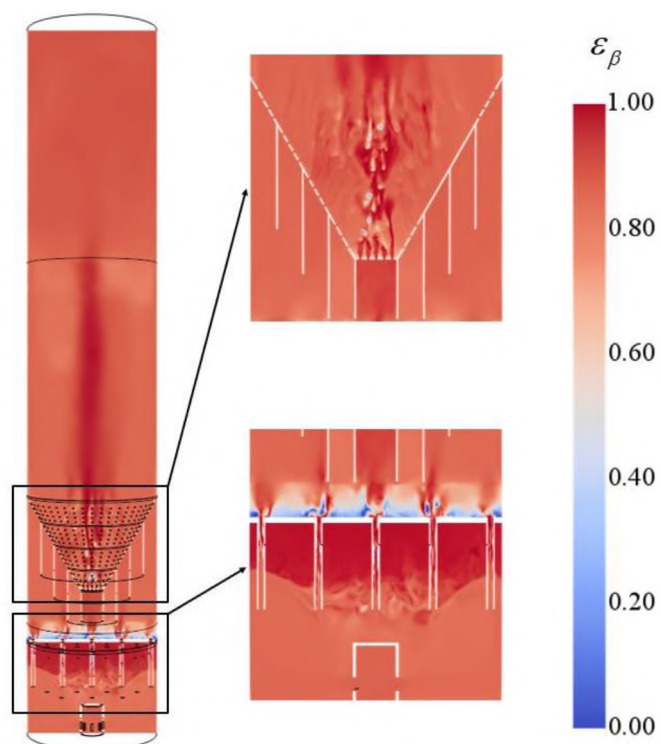


Figure 15. Gas saturation on a cut plane in CFD

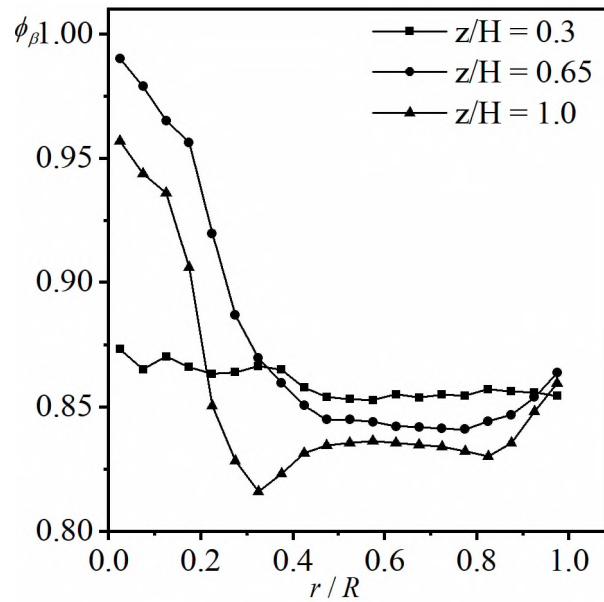


Figure 16. Gas saturation at different bed heights

5.4. GAS HOLDUP

In multiphase flow systems, gas holdup is preferred to present the hydrodynamics.

The holdup is the multiplication of saturation and porosity which can be expressed as:

$$\varepsilon = \varepsilon_B \phi \quad (34)$$

The average holdups at the level right above the cone, in the middle of the catalyst bed, and at the top of the bed are 0.41, 0.36, 0.49, respectively. The results exactly match the axial porosity distribution in Figure 8 (b) that with higher porosity, the gas holdup is higher. Figure 17 shows the gas profile in terms of radius that the gas is cross-sectionally uniformly distributed that demonstrates the advantage of the MBR design. However, due to the limitation of measurement techniques and methodologies, as so far, there is no proper way to validate the phase holdups for this special scenario that is presented as semi-packed and semi-fluidized reactor.

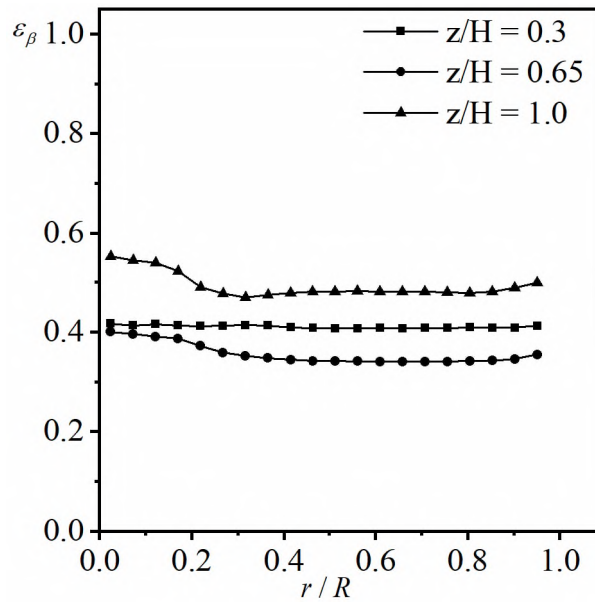


Figure 17. Gas holdup at different bed heights

6. REMARKS

A porosity distribution model was developed for different expansions in a packed bed with a cone distributor, based on DEM simulations using Eulerian-Lagrangian approach. It can be observed that the porosity distribution varies more in axial position than that in radial position for expanded beds. The overall porosity starts decreasing around 15% expansion which possibly indicates that the minimum fluidized expansion point is around 15%.

Despite that the analysis of the DEM results determined an oscillatory behaviour on the radial porosity distribution at different axial positions, these variations seemed to be lost on the overall radially and axially averaged porosity distributions. The proposed model is able to predict a smoothed local porosity distribution with good agreement to the average distributions determined by analysis of the DEM simulations results.

The model was implemented as the porosity distribution functions to describe the effective porous media in order to simplify the hydrodynamics simulation in these special expanded packed beds. From the overall experimental observation and pressure drop measurement, the CFD simulation incorporated with the newly developed model performed very well, even though the fluidized top layer information cannot be addressed due to the limitation of the techniques which might be solved in the near future.

FUNDING

This research did not receive any specific grant from funding agencies in the public, commercial, or not-for-profit sectors.

REFERENCES

- [1] Y. Liu, L. Gao, L. Wen, B. Zong, Recent Advances in Heavy Oil Hydroprocessing Technologies, Recent Patents Chem. Eng. 2 (2012) 22–36. doi:10.2174/2211334710902010022.
- [2] T. KRAMER, David, C., STANGELAND, Bruce, E., SMITH, David, S., BACHTEL, Robert, W., SCHEUERMAN, Georgieanna, L., MCCALL, James, Apparatus for an on-stream particle replacement system for countercurrent contact of a gas and liquid feed stream with a packed bed, US005302357A, 1994.
- [3] Georgieanna L. Scheuerman et al., Multistage moving-bed hydroprocessing reactor with separate catalyst addition and withdrawal systems for each stage, and method for hydroprocessing a hydrocarbon feed stream, US005916529A, 1999.
- [4] William B. Krantz et al., Balanced flow resistance OCR distributor cone, US006387334B1, 2002.
- [5] V. Alexander, Hydrodynamics Related Performance Evaluation of Upflow Moving Bed Hydrotreater Reactor (MBR) Using Developed Experimental Methods and CFD Simulation, Missouri University of Science and Technology, 2018.

- [6] A. Toukan, V. Alexander, H. AlBazzaz, M.H. Al-Dahhan, Identification of flow regime in a cocurrent gas – Liquid upflow moving packed bed reactor using gamma ray densitometry, *Chem. Eng. Sci.* 168 (2017) 380–390. doi:10.1016/j.ces.2017.04.028.
- [7] A. Toukan, Hydrodynamic of a Co-current Upflow Moving Packed Bed Reactor with a Porous Catalyst, Missouri Univeristy of Science and Technology, 2016.
- [8] V. Alexander, H. Albazzaz, M. Al-Dahhan, Gas phase dispersion/mixing investigation in a representative geometry of gas-liquid upflow Moving Bed Hydrotreater Reactor (MBR) using developed gas tracer technique and method based on convolution/regression, *Chem. Eng. Sci.* 195 (2019) 671–682. doi:10.1016/j.ces.2018.10.013.
- [9] P.A. Cundall, O.D.L. Strack, A discrete numerical model for granular assemblies, *Geotechnique*. (1979). doi:10.1680/geot.1979.29.1.47.
- [10] N.A. Patankar, D.D. Joseph, Modeling and numerical simulation of particulate flows by the Eulerian-Lagrangian approach, *Int. J. Multiph. Flow*. 27 (2001) 1659–1684.
- [11] M. Chiesa, V. Mathiesen, J.A. Melheim, B. Halvorsen, Numerical simulation of particulate flow by the Eulerian-Lagrangian and the Eulerian-Eulerian approach with application to a fluidized bed, *Comput. Chem. Eng.* 29 (2005) 291–304. doi:10.1016/j.compchemeng.2004.09.002.
- [12] N.A. Patankar, D.D. Joseph, Lagrangian numerical simulation of particulate flows, *Int. J. Multiph. Flow*. 27 (2001) 1685–1706. doi:10.1016/S0301-9322(01)00025-8.
- [13] G. Gouesbet, A. Berlemont, Eulerian and Lagrangian approaches for predicting the behaviour of discrete particles in turbulent flows, *Prog. Energy Combust. Sci.* 25 (1999) 133–159. doi:10.1016/s0360-1285(98)00018-5.
- [14] F. Durst, D. Milojevic, B. Schöning, Eulerian and Lagrangian predictions of particulate two-phase flows: a numerical study, *Appl. Math. Model.* 8 (1984) 101–115. doi:10.1016/0307-904X(84)90062-3.
- [15] F. Augier, M. Fourati, Y. Haroun, Characterization and modelling of a maldistributed Trickle Bed Reactor, *Can. J. Chem. Eng.* 95 (2017) 222–230. doi:10.1002/cjce.22618.
- [16] Z. Solomenko, Y. Haroun, M. Fourati, F. Larachi, C. Boyer, F. Augier, Liquid spreading in trickle-bed reactors: Experiments and numerical simulations using Eulerian-Eulerian two-fluid approach, *Chem. Eng. Sci.* 126 (2015) 698–710. doi:10.1016/j.ces.2015.01.013.

- [17] S. Uribe, B. Qi, M.E. Cordero, M. Al-Dahhan, Comparison between pseudohomogeneous and resolved-particle models for liquid hydrodynamics in packed-bed reactors, *Chem. Eng. Res. Des.* 166 (2021) 158–171. doi:10.1016/j.cherd.2020.12.001.
- [18] W. Du, J. Zhang, P. Lu, J. Xu, W. Wei, G. He, L. Zhang, Advanced understanding of local wetting behaviour in gas-liquid-solid packed beds using CFD with a volume of fluid (VOF) method, *Chem. Eng. Sci.* 170 (2017) 378–392. doi:10.1016/j.ces.2017.02.033.
- [19] S. Uribe, M. Al-Ani, M.E. Cordero, M. Al-Dahhan, Modelling and validation of TBR Hydrodynamics: Local comparison between CFD and experiments, *Fuel* 277 (2020) 118244. doi:10.1016/j.fuel.2020.118244.
- [20] J.J. Wortman, R.A. Evans, Young's modulus, shear modulus, and poisson's ratio in silicon and germanium, *J. Appl. Phys.* (1965). doi:10.1063/1.1713863.
- [21] G.E. Mueller, A simple method for determining sphere packed bed radial porosity, *Powder Technol.* 229 (2012) 90–96. doi:10.1016/j.powtec.2012.06.013.
- [22] H. Martin, Low peclet number particle-to-fluid heat and mass transfer in packed beds, *Chem. Eng. Sci.* (1978). doi:10.1016/0009-2509(78)85181-1.
- [23] Y. Cohen, A.B. Metzner, Wall effects in laminar flow of fluids through packed beds, *AIChE J.* (1981). doi:10.1002/aic.690270502.
- [24] G.E. Mueller, Prediction of radial porosity distributions in randomly packed fixed beds of uniformly sized spheres in cylindrical containers, *Chem. Eng. Sci.* (1991). doi:10.1016/0009-2509(91)80032-T.
- [25] O. Bey, G. Eigenberger, Fluid flow through catalyst filled tubes, *Chem. Eng. Sci.* (1997). doi:10.1016/S0009-2509(96)00509-X.
- [26] A. De Klerk, Voidage Variation in Packed Beds at Small Column to Particle Diameter Ratio, *AIChE J.* 49 (2003).
- [27] D. Vortmeyer, J. Schuster, Evaluation of Steady Flow Profiles in Rectangular and Circular Packed Beds by a Variational Method, *Chem. Eng. Res. Des.* 38 (1983) 1691–1699.
- [28] F. Al Falahi, M. Al-Dahhan, Experimental investigation of the pebble bed structure by using gamma ray tomography, *Nucl. Eng. Des.* 310 (2016) 231–246. doi:10.1016/j.nucengdes.2016.10.009.
- [29] C.W. Hirt, B.D. Nichols, Volume of Fluid (VOF) Method for the Dynamics of Free Boundaries, *J. Comput. Phys.* 39 (1981) 201–225.

- [30] Y. Wang, J. Chen, F. Larachi, Modelling and simulation of trickle-bed reactors using computational fluid dynamics: A state-of-the-art review, *Can. J. Chem. Eng.* 91 (2013) 136–180. doi:10.1002/cjce.20702.
- [31] B.G.M. van Wachem, A.E. Almstedt, Methods for multiphase computational fluid dynamics, *Chem. Eng. J.* 96 (2003) 81–98. doi:10.1016/j.cej.2003.08.025.
- [32] H. Huang, J. Ayoub, Applicability of the Forchheimer equation for non-Darcy flow in porous media, *SPE J.* (2008). doi:10.2118/102715-PA.
- [33] R.B. Bird, W.E. Stewart, E.N. Lightfoot, *Transport Phenomena*, 2002.
- [34] J.U. Brackbill, D.B. Kothe, C. Zemach, A continuum method for modeling surface tension, *J. Comput. Phys.* 100 (1992) 335–354. doi:10.1016/0021-9991(92)90240-Y.
- [35] Š. Šikalo, H.D. Wilhelm, I. V. Roisman, S. Jakirlić, C. Tropea, Dynamic contact angle of spreading droplets: Experiments and simulations, *Phys. Fluids.* 17 (2005) 1–13. doi:10.1063/1.1928828.
- [36] K. Yokoi, D. Vadiello, J. Hinch, I. Hutchings, Numerical studies of the influence of the dynamic contact angle on a droplet impacting on a dry surface, *Phys. Fluids.* 21 (2009). doi:10.1063/1.3158468.

SECTION

3. CONCLUSIONS AND RECOMMENDATIONS

3.1. CONCLUSIONS

The following conclusions and remarks can be made to summarize the work.

3.1.1. Maldistribution and Liquid Holdup in Trilobe Catalyst. The dynamic liquid distribution and holdup of porous quadrilobe catalyst in a TBR are for the first time being studied using advanced gamma-ray CT. The quantification and mapping of the maldistribution are discussed. The dynamic liquid holdup is modelled using deep neural network (DNN) as well as the pseudo-3D model. Here are the main remarks of this study:

- (1) A 32-compartment module is used to quantify the maldistribution factor. The maldistribution factors decrease from the higher level to lower level which means more uniform distribution show up at lower bed heights. There is a transition region from maldistribution to uniform distribution depending on the flowrates.
- (2) The 3D mapping figures of the dynamic liquid distribution are presented showing that there is more dynamic liquid in the center of the column at high levels. With decreasing the level height, the liquid proportion difference reduces gradually to maximize the uniform distribution.
- (3) There is no high correlation between the average dynamic liquid holdup and the bed height. If the gas flowrate increases while keeping the liquid flowrate fixed, the average dynamic liquid holdup decreases. However, if the gas flowrate is fixed, there is no dominant increasing or decreasing trend showing up.

- (4) The empirical model using deep neural network and the pseudo-3D model are developed and compared with the experimental data. Both show high accuracy for predicting the local dynamic liquid holdup with regard to bed height, radius, and flowrates.

3.1.2. Hybrid Pressure Drop and Liquid Holdup Model. Based on volume averaged equations for the two-phase flow on a porous media, a phenomenological model to estimate dimensionless pressure drop or liquid holdup of a Trickle Bed Reactor packed with extrudate particles, cylinders, trilobes and quadrilobes was developed. The model included three closure terms, the bed permeability (K), a gas-liquid ($K_{\beta\gamma}$) and a liquid-gas ($K_{\gamma\beta}$) viscous drag parameter. In this sense, the bed permeability captures the resistances to the momentum transfer imposed by the porous media over the fluids; while the viscous drag parameters capture, in a certain extent, the multiphase interactions. The permeability was approximated according to the generally accepted Kozeny-Carman model; while the viscous drag parameters were estimated according to experimentally determined liquid holdup and pressure drops. Furthermore, an empirical model based on the experimentally estimated viscous drag parameters was developed.

In order to develop a hybrid phenomenological model that can simultaneously predict pressure drops and liquid holdup, expressions from the extended slit model reported on literature [36], were coupled with the expression developed by means of the results of averaging procedure. The predictive quality of the hybrid model was tested by comparing with experimental measurements of dimensionless pressure drops and liquid holdup in a column of 0.14 m in diameter and 2 m in height. The proposed model shows a high predictive

quality to estimate the dimensionless pressure drop, with an overall AARE of 9.81%, and an overall MSE as low as 1.47%; while the model predictions liquid holdups also exhibits a high predictive quality, with an overall AARE of 7.52%, and an overall MSE as low as 0.07%. The observed deviations show a remarkable enhancement in the quality of the predictions in comparison with currently available models reported in literature. Furthermore, as shown by the comparison with other experimental data reported on literature, and due to the fact that both of the models coupled in the hybrid model development are based on a phenomenological development, the hybrid model has a wide range of applicability with high accuracy. A model with these characteristics is desirable for design and scale up tasks.

It should be noted that the developed hybrid model, as presented, is only applicable for extruded catalysts. The model was developed in this way due to the vast industrial applications and interest on extruded catalysts over spherical catalysts. Nevertheless, the model could be adapted for spherical packings, provided that experimental liquid holdup and pressure data is available to obtain fitting parameters for the viscous drag parameter.

3.1.3. CFD Simulations in Random Packed Trilobe Catalyst Bed. An efficient packing scheme was implemented to randomly pack a vast number of trilobe catalyst to represent the TBR based on the rigid body approach. The generated geometry was used to define the computational domain for the two-phase hydrodynamics simulation based on the volume of fluids (VOF) approach. The main remarks of this study are:

- (1) The pressure drops in CFD simulations have been validated by experiments that the maximum absolute relative error is 10.5%.

- (2) The azimuthally averaged liquid saturations in terms of radius in CFD simulations were compared with time averaged liquid saturations from 2-tip optical probe measurements, showing 19.18% average absolute relative error. However, the cross-sectional average liquid saturations in CFD simulations show maximum 15.56% absolute relative error from experimental data.
- (3) The kernel density estimation was used to describe the positive and negative velocities probability distributions. The modal number of experimental velocities are higher than the average velocities in CFD simulations. However, the overall velocity distribution range of CFD simulations are within the experimental velocity distribution range.

3.1.4. Heavy Metal Contaminants Accretion. A new method has been developed to seek the coordinates of the radioactive particle mimicking the heavy metal accretion inside a trickle bed hydrotreating reactor, using a modified dynamic radioactive particle tracking system (DRPT). The resolution obtained by the coarse and fine coordinates is high enough to clearly identify the location of the radioactive particle and to validate the capacity and reliability of this newly developed DRPT system. We have identified the location of the radioactive using a study on different catalysts shapes by accurately determining:

- (1) The probability density distributions by using kernel density estimator (KDE). The results show that in terms of:
- Radius: all the catalysts have similar probability density distribution, and the highest probability is at around $r = 20 \text{ mm}$.
 - Height: the spherical catalyst has larger distribution range than the other types do.

- (2) The heavy metal accretion is directly related to the pressure drops along the bed height which indicate the bed porosity and intricate bed structure in catalyst packed beds. Heavy metals have more chance to deposit at higher levels of packed beds with higher pressure drops for the extrudate catalyst shapes such as cylinder, trilobe, and quadrilobed.

3.1.5. Mathematical Modeling and CFD Simulation in Moving Bed Reactor.

A porosity distribution model was developed for different expansions in a packed bed with a cone distributor, based on DEM simulations using Eulerian-Lagrangian approach. It can be observed that the porosity distribution varies more in axial position than that in radial position for expanded beds. The overall porosity starts decreasing around 15% expansion which possibly indicates that the minimum fluidized expansion point is around 15%.

Despite that the analysis of the DEM results determined an oscillatory behaviour on the radial porosity distribution at different axial positions, these variations seemed to be lost on the overall radially and axially averaged porosity distributions. The proposed model is able to predict a smoothed local porosity distribution with good agreement to the average distributions determined by analysis of the DEM simulations results.

The model was implemented as the porosity distribution functions to describe the effective porous media in order to simplify the hydrodynamics simulation in these special expanded packed beds. From the overall experimental observation and pressure drop measurement, the CFD simulation incorporated with the newly developed model performed very well, even though the fluidized top layer information cannot be addressed due to the limitation of the techniques which might be solved in the near future.

3.2. RECOMMENDATIONS

(1) The pseudo-3D dynamic liquid holdup prediction model can be used to assess the other shapes of catalysts and modified accordingly based on the experimental data. The corrected models can be evaluated for different scales and implemented in CFD simulations to separate the dynamic liquid and static liquid.

(2) The hybrid pressure drop and liquid holdup phenomenological model can be redeveloped to be feasible for spherical catalyst shape. This model can be implemented in CFD simulations to compare with the other phase interactions models.

(3) The heavy metal contaminants accretion locations in different fluids with different physical properties such as density and viscosity at different flowrates can be investigated. The probability density information can be coupled with the packed bed porosity distribution function giving more realistic bed structure so that the flow behavior or hydrodynamics in the beds with catalyst coking or sintering scenarios can be investigated.

(4) The Eulerian multifluid multiphase model can be used to simulate the random packed trilobe bed in transient state to obtain local liquid velocity and local liquid velocity, respectively, and to compare the results with VOF method. The wetting efficiency can be assessed through image processing.

(5) The methodology to quantify the fluidized region in a moving bed reactor can be developed and a comprehensive porosity distribution model can be developed to further improve the accuracy of porosity prediction. A fast response local information measurement technique should be developed to validate the phase holdups.

BIBLIOGRAPHY

- [1] V. V. Ranade, R. V. Chaudhari, P.R. Gunjal, Introduction, Trickle Bed React. React. Eng. Appl. (2011) 1–23. <https://doi.org/10.1016/b978-0-444-52738-7.10001-4>.
- [2] M.E. Trivizadakis, D. Giakoumakis, A.J. Karabelas, A study of particle shape and size effects on hydrodynamic parameters of trickle beds, Chem. Eng. Sci. 61 (2006) 5534–5543. <https://doi.org/10.1016/j.ces.2006.03.025>.
- [3] E. Palmisano, P.A. Ramachandran, K. Balakrishnan, M. Al-Dahhan, Computation of effectiveness factors for partially wetted catalyst pellets using the method of fundamental solution, Comput. Chem. Eng. (2003). [https://doi.org/10.1016/S0098-1354\(03\)00033-4](https://doi.org/10.1016/S0098-1354(03)00033-4).
- [4] D. Janecki, A. Burghardt, G. Bartelmus, Parametric sensitivity of a CFD model concerning the hydrodynamics of trickle-bed reactor (tbr), Chem. Process Eng. - Inz. Chem. i Proces. 37 (2016) 97–107. <https://doi.org/10.1515/cpe-2016-0010>.
- [5] G.S. Honda, P. Gase, D.A. Hickman, A. Varma, Hydrodynamics of trickle bed reactors with catalyst support particle size distributions, Ind. Eng. Chem. Res. (2014). <https://doi.org/10.1021/ie403491x>.
- [6] S. Sundaresan, Role of hydrodynamics on chemical reactor performance, Curr. Opin. Chem. Eng. (2013). <https://doi.org/10.1016/j.coche.2013.06.003>.
- [7] R. Lange, M. Schubert, T. Bauer, Liquid holdup in trickle-bed reactors at very low liquid reynolds numbers, Ind. Eng. Chem. Res. 44 (2005) 6504–6508. <https://doi.org/10.1021/ie048906r>.
- [8] M. Bazmi, S.H. Hashemabadi, M. Bayat, CFD simulation and experimental study of liquid flow mal-distribution through the randomly trickle bed reactors, Int. Commun. Heat Mass Transf. 39 (2012) 736–743. <https://doi.org/10.1016/j.icheatmasstransfer.2012.03.005>.
- [9] M. Bazmi, S.H. Hashemabadi, M. Bayat, Flow Maldistribution in Dense- and Sock-Loaded Trilobe Catalyst Trickle-Bed Reactors: Experimental Data and Modeling Using Neural Network, Transp. Porous Media. 97 (2013) 119–132. <https://doi.org/10.1007/s11242-012-0114-x>.
- [10] G. Boccardo, F. Augier, Y. Haroun, D. Ferré, D.L. Marchisio, Validation of a novel open-source work-flow for the simulation of packed-bed reactors, Chem. Eng. J. 279 (2015) 809–820–820. <https://doi.org/10.1016/j.cej.2015.05.032>.
- [11] V. V. Ranade, R. V. Chaudhari, P.R. Gunjal, Hydrodynamics and Flow Regimes, 2011. <https://doi.org/10.1016/b978-0-444-52738-7.10002-6>.

- [12] F. Mousazadeh, Hot spot formation in trickle bed reactors, 2013.
- [13] C. Marcandelli, A.S. Lamine, J.R. Bernard, G. Wild, Liquid Distribution in Trickle-Bed Reactor, *Oil Gas Sci. Technol.* (2000). <https://doi.org/10.2516/ogst:2000029>.
- [14] Z. Solomenko, Y. Haroun, M. Fourati, F. Larachi, C. Boyer, F. Augier, Liquid spreading in trickle-bed reactors: Experiments and numerical simulations using Eulerian-Eulerian two-fluid approach, *Chem. Eng. Sci.* 126 (2015) 698–710. <https://doi.org/10.1016/j.ces.2015.01.013>.
- [15] A. SAPKOTA, M. TAKEI, M. NISHIO, J. HARUTA, T. EDA, Experimental Study on Liquid Spread and Maldistribution in the Trickle Bed Reactor Using Electrical Resistance Tomography, *J. Power Energy Syst.* 7 (2013) 94–105. <https://doi.org/10.1299/jpes.7.94>.
- [16] G. Liu, J. an Lan, Y. Cao, Z. Huang, Z. Cheng, Z. Mi, New insights into transient behaviors of local liquid-holdup in periodically operated trickle-bed reactors using electrical capacitance tomography (ECT), *Chem. Eng. Sci.* 64 (2009) 3329–3343. <https://doi.org/10.1016/j.ces.2009.04.008>.
- [17] C. Boyer, A. Koudil, P. Chen, M.P. Dudukovic, Study of liquid spreading from a point source in a trickle bed via gamma-ray tomography and CFD simulation, in: *Chem. Eng. Sci.*, 2005. <https://doi.org/10.1016/j.ces.2005.03.049>.
- [18] M. Schubert, G. Hessel, C. Zippe, R. Lange, U. Hampel, Liquid flow texture analysis in trickle bed reactors using high-resolution gamma ray tomography, *Chem. Eng. J.* (2008). <https://doi.org/10.1016/j.cej.2007.10.006>.
- [19] Z. Kuzeljevic, Hydrodynamics of Trickle Bed Reactors: Measurements and Modeling, Washington University, 2010. <http://dx.doi.org/10.7936/K7WQ01V5>.
- [20] M.K. Al Mesfer, A.J. Sultan, M.H. Al-Dahhan, Impacts of dense heat exchanging internals on gas holdup cross-sectional distributions and profiles of bubble column using gamma ray Computed Tomography (CT) for FT synthesis, *Chem. Eng. J.* 300 (2016) 317–333. <https://doi.org/10.1016/j.cej.2016.04.075>.
- [21] M.H. Al-Dahhan, M.P. Duduković, Pressure drop and liquid holdup in high pressure trickle-bed reactors, *Chem. Eng. Sci.* 49 (1994) 5681–5698. [https://doi.org/10.1016/0009-2509\(94\)00315-7](https://doi.org/10.1016/0009-2509(94)00315-7).
- [22] S.A. Gheni, M.H. Al-Dahhan, Assessing the Feasibility of Optical Probe in Phase Holdup Measurements and Flow Regime Identification, *Int. J. Chem. React. Eng.* (2015). <https://doi.org/10.1515/ijcre-2014-0147>.
- [23] F. Larachi, A. Laurent, N. Midoux, G. Wild, Experimental study of a trickle-bed reactor operating at high pressure: two-phase pressure drop and liquid saturation, *Chem. Eng. Sci.* (1991). [https://doi.org/10.1016/0009-2509\(91\)85051-X](https://doi.org/10.1016/0009-2509(91)85051-X).

- [24] M. Bazmi, S.H. Hashemabadi, M. Bayat, Extrudate Trilobe Catalysts and Loading Effects on Pressure Drop and Dynamic Liquid Holdup in Porous Media of Trickle Bed Reactors, *Transp. Porous Media.* 99 (2013) 535–553. <https://doi.org/10.1007/s11242-013-0199-x>.
- [25] R.A. Holub, M.P. Dudukovic, P.A. Ramachandran, A Phenomenological Model for Pressure Drop, Liquid Holdup, and Flow Regime Transition in gas-liquid Trickle Flow, *Chem. Eng. Sci.* 47 (1992) 2343–2348.
- [26] R.A. Holub, M.P. Duduković, P.A. Ramachandran, Pressure drop, liquid holdup, and flow regime transition in trickle flow, *AIChE J.* 39 (1993) 302–321. <https://doi.org/10.1002/aic.690390211>.
- [27] I. Iliuta, F. Larachi, M.H. Al-Dahhan, Double-slit model for partially wetted trickle flow hydrodynamics, *AIChE J.* 46 (2000) 597–609. <https://doi.org/10.1205/026387600528256>.
- [28] A. Attou, G. Ferschneider, A two-fluid hydrodynamic model for the transition between trickle and pulse flow in a cocurrent gas-liquid packed-bed reactor, *Chem. Eng. Sci.* 55 (2000) 491–511. [https://doi.org/10.1016/S0009-2509\(99\)00344-9](https://doi.org/10.1016/S0009-2509(99)00344-9).
- [29] A.E. Sáez, R.G. Carbonell, hydrodynamic parameters for gas-liquid cocurrent flow in packed beds, *AIChE J.* (1985). <https://doi.org/10.1002/aic.690310105>.
- [30] M.J. Al-ani, Hydrodynamics of trickle bed reactors (TBRs) packed with industrial catalyst using advanced measurement techniques, Missouri University of Science and Technology, 2019.
- [31] P. Dufresne, Hydroprocessing catalysts regeneration and recycling, *Appl. Catal. A Gen.* 322 (2007) 67–75. <https://doi.org/10.1016/j.apcata.2007.01.013>.
- [32] M.D. Argyle, C.H. Bartholomew, Heterogeneous catalyst deactivation and regeneration: A review, *Catalysts.* 5 (2015) 145–269. <https://doi.org/10.3390/catal5010145>.
- [33] P.W. Tamm, H.F. Harnsberger, A.G. Bridge, Effects of Feed Metals on Catalyst Aging in Hydroprocessing Residuum, *Ind. Eng. Chem. Process Des. Dev.* 20 (1981) 262–273. <https://doi.org/10.1021/i200013a014>.
- [34] B.M. Vogelaar, S. Eijssbouts, J.A. Bergwerff, J.J. Heiszwolf, Hydroprocessing catalyst deactivation in commercial practice, *Catal. Today.* 154 (2010) 256–263. <https://doi.org/10.1016/j.cattod.2010.03.039>.
- [35] M.J. Saxton, K. Jacobson, Single-particle tracking: Applications to membrane dynamics, *Annu. Rev. Biophys. Biomol. Struct.* 26 (1997) 373–399. <https://doi.org/10.1146/annurev.biophys.26.1.373>.

- [36] H.G. Maas, A. Gruen, D. Papantoniou, Particle tracking velocimetry in three-dimensional flows - Part 1. Photogrammetric determination of particle coordinates, *Exp. Fluids*. 15 (1993) 133–146. <https://doi.org/10.1007/BF00190953>.
- [37] V. Khane, M.H. Al-Dahhan, Hybrid dynamic radioactive particle tracking (RPT) calibration technique for multiphase flow systems, *Meas. Sci. Technol.* 28 (2017). <https://doi.org/10.1088/1361-6501/aa5c27>.
- [38] V. Khane, I.A. Said, M.H. Al-Dahhan, Experimental investigation of pebble flow dynamics using radioactive particle tracking technique in a scaled-down Pebble Bed Modular Reactor (PBMR), *Nucl. Eng. Des.* (2016). <https://doi.org/10.1016/j.nucengdes.2016.03.031>.
- [39] V.B. Khane, M.H. Al-Dahhan, Study of solids movement in pebble bed/moving bed reactors using radioactive particle tracking (RPT) technique, in: 7th World Congr. Ind. Process Tomogr., 2014.
- [40] V. Khane, I.A. Said, M.H. Al-Dahhan, Assessment of performing experimental investigation on a pebble bed modular reactor (PBMR) as a static packed bed approximation, *Ann. Nucl. Energy*. (2017). <https://doi.org/10.1016/j.anucene.2016.11.020>.
- [41] M.K. Al Mesfer, A.J. Sultan, M.H. Al-Dahhan, Study the effect of dense internals on the liquid velocity field and turbulent parameters in bubble column for Fischer–Tropsch (FT) synthesis by using Radioactive Particle Tracking (RPT) technique, *Chem. Eng. Sci.* (2017). <https://doi.org/10.1016/j.ces.2016.12.001>.
- [42] T. Al-Juwaya, N. Ali, M. Al-Dahhan, Investigation of hydrodynamics of binary solids mixture spouted beds using radioactive particle tracking (RPT) technique, *Chem. Eng. Res. Des.* (2019). <https://doi.org/10.1016/j.cherd.2019.05.051>.
- [43] P.S. Balusu, B. Mohanty, CFD Simulation of Multiphase Flow in Trickle Bed Reactor, *Int. J. Comput. Appl. Eng. I* (2011) 454–461.
- [44] R.J.G. Lopes, V.S.L. de Sousa, R.M. Quinta-Ferreira, CFD and experimental studies of reactive pulsing flow in environmentally-based trickle-bed reactors, *Chem. Eng. Sci.* 66 (2011) 3280–3290. <https://doi.org/10.1016/j.ces.2011.01.058>.
- [45] D. Nemec, J. Levec, Flow through packed bed reactors: 2. Two-phase concurrent downflow, *Chem. Eng. Sci.* 60 (2005) 6958–6970. <https://doi.org/10.1016/j.ces.2005.05.069>.
- [46] M.E. Cordero, S. Uribe, L.G. Zárate, R.N. Rangel, A. Regalado-Méndez, E.P. Reyes, CFD Modelling of Coupled Multiphysics-Multiscale Engineering Cases, *Comput. Fluid Dyn. - Basic Instruments Appl. Sci.* (2018). <https://doi.org/10.5772/intechopen.70562>.

- [47] S. Uribe, B. Qi, M.E. Cordero, M. Al-Dahhan, Comparison between pseudohomogeneous and resolved-particle models for liquid hydrodynamics in packed-bed reactors, *Chem. Eng. Res. Des.* 166 (2021) 158–171. <https://doi.org/10.1016/j.cherd.2020.12.001>.
- [48] G.E. Mueller, A simple method for determining sphere packed bed radial porosity, *Powder Technol.* 229 (2012) 90–96. <https://doi.org/10.1016/j.powtec.2012.06.013>.
- [49] G.E. Mueller, Radial porosity in packed beds of spheres, *Powder Technol.* 203 (2010) 626–633. <https://doi.org/10.1016/j.powtec.2010.07.007>.
- [50] H. Martin, Low peclet number particle-to-fluid heat and mass transfer in packed beds, *Chem. Eng. Sci.* (1978). [https://doi.org/10.1016/0009-2509\(78\)85181-1](https://doi.org/10.1016/0009-2509(78)85181-1).
- [51] A. De Klerk, Voidage Variation in Packed Beds at Small Column to Particle Diameter Ratio, *AIChE J.* 49 (2003) 2022–2029.
- [52] C.G. Sun, F.H. Yin, A. Afacan, K. Nandakumar, K.T. Chuang, Modelling and simulation of flow maldistribution in random packed columns with gas-liquid countercurrent flow, *Chem. Eng. Res. Des.* (2000). <https://doi.org/10.1205/026387600527275>.
- [53] M.L. Hunt, C.L. Tien, Non-darcian flow, heat and mass transfer in catalytic packed-bed reactors, *Chem. Eng. Sci.* (1990). [https://doi.org/10.1016/0009-2509\(90\)87080-C](https://doi.org/10.1016/0009-2509(90)87080-C).
- [54] R.J.G. Lopes, R.M. Quinta-Ferreira, Numerical simulation of trickle-bed reactor hydrodynamics with RANS-based models using a volume of fluid technique, *Ind. Eng. Chem. Res.* 48 (2009) 1740–1748. <https://doi.org/10.1021/ie8014186>.
- [55] R.J.G. Lopes, R.M. Quinta-Ferreira, CFD modelling of multiphase flow distribution in trickle beds, *Chem. Eng. J.* 147 (2009) 342–355. <https://doi.org/10.1016/j.cej.2008.11.048>.
- [56] R.J.G. Lopes, R.M. Quinta-Ferreira, Assessment of CFD Euler-Euler method for trickle-bed reactor modelling in the catalytic wet oxidation of phenolic wastewaters, *Chem. Eng. J.* 160 (2010) 293–301. <https://doi.org/10.1016/j.cej.2010.03.024>.
- [57] R.J.G. Lopes, R.M. Quinta-Ferreira, Evaluation of multiphase CFD models in gas-liquid packed-bed reactors for water pollution abatement, *Chem. Eng. Sci.* 65 (2010) 291–297. <https://doi.org/10.1016/j.ces.2009.06.039>.
- [58] R.J.G. Lopes, R.M. Quinta-Ferreira, Numerical studies of catalyst wetting and total organic carbon reaction on environmentally based trickle-bed reactors, *Ind. Eng. Chem. Res.* 49 (2010) 10730–10743. <https://doi.org/10.1021/ie100563n>.

- [59] S. Whitaker, Flow in porous media II: The governing equations for immiscible, two-phase flow, *Transp. Porous Media.* 1 (1986) 105–125. <https://doi.org/10.1007/BF00714688>.
- [60] Y. Liu, L. Gao, L. Wen, B. Zong, Recent Advances in Heavy Oil Hydroprocessing Technologies, *Recent Patents Chem. Eng.* 2 (2012) 22–36. <https://doi.org/10.2174/2211334710902010022>.
- [61] T. KRAMER, David, C., STANGELAND, Bruce, E., SMITH, David, S., BACHTEL, Robert, W., SCHEUERMAN, Georgianna, L., MCCALL, James, Apparatus for an on-stream particle replacement system for countercurrent contact of a gas and liquid feed stream with a packed bed, US005302357A, 1994.
- [62] Georgianna L. Scheuerman et al., Multistage moving-bed hydroprocessing reactor with separate catalyst addition and withdrawal systems for each stage, and method for hydroprocessing a hydrocarbon feed stream, US005916529A, 1999.
- [63] William B. Krantz et al., Balanced flow resistance OCR distributor cone, US006387334B1, 2002.
- [64] V. Alexander, Hydrodynamics Related Performance Evaluation of Upflow Moving Bed Hydrotreater Reactor (MBR) Using Developed Experimental Methods and CFD Simulation, Missouri University of Science and Technology, 2018.
- [65] A. Toukan, V. Alexander, H. AlBazzaz, M.H. Al-Dahhan, Identification of flow regime in a cocurrent gas – Liquid upflow moving packed bed reactor using gamma ray densitometry, *Chem. Eng. Sci.* 168 (2017) 380–390. <https://doi.org/10.1016/j.ces.2017.04.028>.
- [66] A. Toukan, Hydrodynamic of a Co-current Upflow Moving Packed Bed Reactor with a Porous Catalyst, Missouri University of Science and Technology, 2016.
- [67] V. Alexander, H. Albazzaz, M. Al-Dahhan, Gas phase dispersion/mixing investigation in a representative geometry of gas-liquid upflow Moving Bed Hydrotreater Reactor (MBR) using developed gas tracer technique and method based on convolution/regression, *Chem. Eng. Sci.* 195 (2019) 671–682. <https://doi.org/10.1016/j.ces.2018.10.013>.
- [68] V. Specchia, G. Baldi, Pressure drop and liquid holdup for two phase concurrent flow in packed beds, *Chem. Eng. Sci.* (1977). [https://doi.org/10.1016/0009-2509\(77\)87008-5](https://doi.org/10.1016/0009-2509(77)87008-5).
- [69] A. Burghardt, G. Bartelmus, M. Jaroszyński, A. Kołodziej, Hydrodynamics and mass transfer in a three-phase fixed-bed reactor with cocurrent gas-liquid downflow, *Chem. Eng. J. Biochem. Eng. J.* (1995). [https://doi.org/10.1016/0923-0467\(94\)02956-3](https://doi.org/10.1016/0923-0467(94)02956-3).

- [70] W.J.A. Wammes, J. Middelkamp, W.J. Huisman, C.M. DeBass, K.R. Westerterp, Hydrodynamics in a cocurrent gas-liquid trickle bed at elevated pressures, *AIChE J.* (1991). <https://doi.org/10.1002/aic.690371210>.
- [71] B.I. Morsi, N. Midoux, A. Laurent, J.C. Charpentier, Hydrodynamics and interfacial areas in downward cocurrent gas-liquid flow through fixed beds. Influence of the nature of the liquid, *Int. Chem. Eng.* (1982).
- [72] M.J. Ellman, N. Midoux, G. Wild, A. Laurent, J.C. Charpentier, A new, improved liquid hold-up correlation for trickle-bed reactors, *Chem. Eng. Sci.* (1990). [https://doi.org/10.1016/0009-2509\(90\)87046-U](https://doi.org/10.1016/0009-2509(90)87046-U).
- [73] S.A. Al-Naimi, F.T.J. Al-Sudani, E.K. Halabia, Hydrodynamics and flow regime transition study of trickle bed reactor at elevated temperature and pressure, *Chem. Eng. Res. Des.* 89 (2011) 930–939. <https://doi.org/10.1016/j.cherd.2010.11.008>.

VITA

Binbin Qi was born in Jiangsu, China. He obtained his bachelor's degree in Chemical Engineering in 2012 from Changzhou University, China. During his undergraduate studies, he won the Gold Award in National College Student Chemical Engineering Design and Venture Competition. After that, he joined the Shanghai branch of Anhui Shihua Engineering and Technology Co., Ltd as a Process Engineer. In 2016, Binbin Qi decided to pursue Ph.D. degree and received admission to the Ph.D. program in Chemical and Biochemical Engineering Department at Missouri University of Science and Technology, where he joined Dr. Al-Dahhan's research group. In May 2021, Binbin Qi received his Ph.D. degree in Chemical Engineering from Missouri University of Science and Technology.